MODELLING, SIMULATING AND FORECASTING REGIONAL CLIMATE AND WEATHER

EDITED BY: Hans Von Storch, Frauke Feser, Martin Stendel, Yinlong Xu, René Laprise and Izuru Takayabu

PUBLISHED IN: Frontiers in Environmental Science and Frontiers in Earth Science

frontiers Research Topics

ISSN 1664-8714
ISBN 978-2-88963-997-7
DOI 10.3389/978-2-88963-997-7

About Frontiers

Frontiers is more than just an open-access publisher of scholarly articles: it is a pioneering approach to the world of academia, radically improving the way scholarly research is managed. The grand vision of Frontiers is a world where all people have an equal opportunity to seek, share and generate knowledge. Frontiers provides immediate and permanent online open access to all its publications, but this alone is not enough to realize our grand goals.

Frontiers Journal Series

The Frontiers Journal Series is a multi-tier and interdisciplinary set of open-access, online journals, promising a paradigm shift from the current review, selection and dissemination processes in academic publishing. All Frontiers journals are driven by researchers for researchers; therefore, they constitute a service to the scholarly community. At the same time, the Frontiers Journal Series operates on a revolutionary invention, the tiered publishing system, initially addressing specific communities of scholars, and gradually climbing up to broader public understanding, thus serving the interests of the lay society, too.

Dedication to Quality

Each Frontiers article is a landmark of the highest quality, thanks to genuinely collaborative interactions between authors and review editors, who include some of the world's best academicians. Research must be certified by peers before entering a stream of knowledge that may eventually reach the public - and shape society; therefore, Frontiers only applies the most rigorous and unbiased reviews.
Frontiers revolutionizes research publishing by freely delivering the most outstanding research, evaluated with no bias from both the academic and social point of view. By applying the most advanced information technologies, Frontiers is catapulting scholarly publishing into a new generation.

What are Frontiers Research Topics?

Frontiers Research Topics are very popular trademarks of the Frontiers Journals Series: they are collections of at least ten articles, all centered on a particular subject. With their unique mix of varied contributions from Original Research to Review Articles, Frontiers Research Topics unify the most influential researchers, the latest key findings and historical advances in a hot research area! Find out more on how to host your own Frontiers Research Topic or contribute to one as an author by contacting the Frontiers Editorial Office: researchtopics@frontiersin.org

MODELLING, SIMULATING AND FORECASTING REGIONAL CLIMATE AND WEATHER

Topic Editors:
Hans Von Storch, Helmholtz Centre for Materials and Coastal Research (HZG), Germany
Frauke Feser, Helmholtz Centre for Materials and Coastal Research (HZG), Germany
Martin Stendel, Danish Meteorological Institute (DMI), Denmark
Yinlong Xu, Institute of Environment and Sustainable Development in Agriculture (CAAS), China
René Laprise, Université du Québec à Montréal, Canada
Izuru Takayabu, Meteorological Research Institute (MRI), Japan

Citation: Von Storch, H., Feser, F., Stendel, M., Xu, Y., Laprise, R., Takayabu, I., eds. (2020). Modelling, Simulating and Forecasting Regional Climate and Weather. Lausanne: Frontiers Media SA. doi: 10.3389/978-2-88963-997-7

Table of Contents

frontiers in Environmental Science

EDITORIAL
published: 22 July 2020
doi: 10.3389/fenvs.2020.00099

Editorial: Modelling, Simulating and Forecasting Regional Climate and Weather

Hans von Storch[1]*, *Frauke Feser*[1], *Rene Laprise*[2], *Martin Stendel*[3] and *Izuru Takayabu*[4]

[1] Helmholtz Centre for Materials and Coastal Research (HZG), Geesthacht, Germany, [2] Department of Earth and Atmospheric Sciences, Université du Québec à Montréal, Montreal, QC, Canada, [3] Danish Meteorological Institute, Copenhagen, Denmark, [4] Department of Climate and Geochemistry Research, Meteorological Research Institute, Tsukuba, Japan

Keywords: modeling, simulating, forecasting, climate, weather

Editorial on the Research Topic

Modelling, Simulating and Forecasting Regional Climate and Weather

Originally, climatology was a regional science (von Storch, 1999)—and the global climate merely something put together from the real and challenging findings—the regional climate analyses. Also, weather forecasting was mostly considered a process, which was made possible by regional information, and was of interest only for a regional audience. This has massively changed since, say, the 1960s, when systems for assembling observations from all corners of the globe were set up, and when global atmospheric models appeared as the dynamically right way to describe the circulation of the atmosphere. Thus, the global view became the dominant one in climatology, and in forecasting.

However, a niche remains for the regional set-up. First, the regional model can provide much more spatial detail than a global model, given the same computer power. Historically, this was in particular of importance, when the issue was the regional manifestation, say in terms of precipitation, of a given circulation—in the spirit of Starr's (1942) two-step concept of forecasting—first the large scale-circulation, then the regional or local manifestation.

Initially the regional set-up was challenged by the fact that the boundary-initial value problem for the equations of motion for limited areas is not well posed—among others, there may be several solutions satisfying the boundary values. Also, the propagation of disturbances on the finite grid may be different from the observed propagation; when data from a coarser resolution global model is used, the same problem emerges. This was solved by a rather practical way with the "sponge-zone," suggested by Davies (1976).

For a long time, regional climate models were something like all-purpose tools, and little attention was paid to the question, what specific added value its usage would provide, apart from a general "greater spatial detail"-claim. This greater spatial detail was in particular useful for hydrological applications, and early efforts dealt with coupling of these components. At the same time, global modeling focused on coupling with the oceanic dynamics, and the sea ice dynamics. Obviously, these two components are also crucial for the skill of regional climate change. However, the efforts to extend atmospheric limited area models in this way, commenced seriously only in the last 10, or so, years (e.g., Ham et al., 2016). What was also overseen in the climate applications was the presence of unprovoked variability, sometimes named noise, which lead to intermittent divergence in phase space (Weisse et al., 2000), and which made a statistical evaluation of numerical experiments with regional models necessary, as was recognized by global modelers already in the 1970s. This need is still not recognized generally.

OPEN ACCESS

Edited and reviewed by:
Yuqing Wang,
University of Hawaii at Manoa,
United States

***Correspondence:**
Hans von Storch
hvonstorch@web.de

Specialty section:
This article was submitted to Atmospheric Science, a section of the journal Frontiers in Environmental Science

Received: *20 May 2020*
Accepted: *09 June 2020*
Published: *22 July 2020*

Citation:
von Storch H, Feser F, Laprise R, Stendel M and Takayabu I (2020) Editorial: Modelling, Simulating and Forecasting Regional Climate and Weather. Front. Environ. Sci. 8:99. doi: 10.3389/fenvs.2020.00099

This was the background of the editors for suggesting a volume of Modeling, Simulating and Forecasting Regional Climate and Weather. We wanted to push for further advanced but critical efforts on the different usages of limited area models—and we made some progress, albeit more work needs to be done.

The skill of regional climate models in providing **useful atmospheric states for studying climate impacts** is one aspect of our collection of papers:

- One case (Feng T. et al.) deals with extreme dry spells in Southwest China. A series of regional climate models was found capturing the intensity and duration of such events reasonably well. Also, the statistics of the maximum dry spell length would be reproduced properly. The authors concluded "This information is useful for model evaluation and improvement, future climate projections, and water resource risk management."
- Prein et al. look at the ability of regional models to simulate 12 hydrologically important weather types (WTs) in the contiguous United States. When interested in localized hydrological processes, it is important to get these weather types right, which the authors enforced by constraining the regional model to stay close to the large-scale state of the driving global analysis ("spectral nudging"). In this set-up they found that the choice of parametrizations and grid resolution had little effect—given the constraining. Instead they found it crucial to select global simulations with realistic synoptic-scale variability.
- The biophysical effect of de- and afforestation in Europe, conditional upon different parameterizations of albedo is examined. Afforestation was found to be a warming in winter (Tölle et al.). However, the net effect in summer was small because of canceling albedo and evapotranspiration effects. The summer temperature change is strongly sensitive to the albedo parameterization, which needs to account for different vegetation types.
- Bit outside of the scope of collection of papers is the article by Rath and Costa-Cabral, who constructed an advanced, cointegration-based forecast scheme for snowpack for the Eastern Sierra Nevada.

Regional models are often used for constructing high-resolution scenarios of climate change conditional upon a global climate change projection.

- Matte et al. analyzed "European seasonal temperature and precipitation climate change projections using pan-European regional climate model projections for the twenty-first century." They find that "[e]mploying a simple scaling with the global mean temperature change enables the identification of emerging robust signals of seasonal changes." Additionally, they study the climate change signals from transient experiments at the time of an emerging global temperature exceedance of e.g., 1, 2, or 3°C.
- Feng J. et al. deal with the issue of localized changes in the expected storm surge heights at 15 Chinese sites by combining local observed statistics and scenarios of mean sea level rise provided by global climate change scenarios.

Another class of applications dealt with using regional models in **process studies**, mostly hydrological process studies:

- Eghdami and Barros study Cold Air Intrusions (CAIs) along the eastern flanks of the tropical Andes. They found "significant precipitation enhancement from intense shallow convection at the CAI frontal boundary amplified by orographic lifting as it propagates northward latched to the slopes of Andes."
- Wang et al. have looked at the significance of initial soil moisture (ISM) conditions on the simulation of three severe heat wave events in eastern China. They found a positive feedback between atmospheric circulation, surface warming, and soil dryness, when the ISM is reduced—it "locally strengthens the surface warming and the further drying of the soil. …. The reduced ISM forces positive anomalies of geopotential height at mid-troposphere and negative anomalies at lower levels, leading to an enhanced thickness of the atmosphere."
- The question how an extreme precipitation event at Hiroshima in 2014 would unfold under climate change conditions was studied by Hibino et al. using a 500 m-grid resolution model. The main result is that the "effect of the water vapor increase on extreme precipitation is canceled out by the suppression of convection due to the thermal stability enhancement" so that the expected change is small.

A **conceptual look** at the downscaling paradigm, and its roots—synoptic dynamics and spatial interpolation—was done by von Storch and Zorita. Even if here the concept and history of the empirical variant of downscaling was discussed, these deliberations apply to the dynamical variant as well.

AUTHOR CONTRIBUTIONS

All authors listed have made a substantial, direct and intellectual contribution to the work, and approved it for publication.

REFERENCES

Davies, H. C. (1976). A lateral boundary formulation for multi-level prediction models. *Q. J. R. Meteorol. Soc.* 102, 405–418. doi: 10.1256/smsqj.43209

Ham, S., Yoshimura, K., and Li, H. (2016). Historical dynamical downscaling for East Asia with the atmosphere and ocean coupled regional model. *J. Meteorol. Soc. Jpn.* 94, 199–208. doi: 10.2151/jmsj.2015-046

Starr, V. P. (1942). *Basic Principles of Weather Forecasting*. New York, NY; London: Harper Brothers Publishers, 299.

von Storch, H. (1999). "The global and regional climate system," in *Anthropogenic Climate Change*, eds H. von Storch and G. Flöse (Heidelberg: Springer Verlag), 3–36.

Weisse, R., Heyen, H., and von Storch, H. (2000). Sensitivity of a regional atmospheric model to a sea state dependent roughness and the need of ensemble calculations. *Mon. Weather Rev.* 128, 3631–3642. doi: 10.1175/1520-0493(2000)128<3631:SOARAM>2.0.CO;2

Conflict of Interest: The authors declare that the research was conducted in the absence of any commercial or financial relationships that could be construed as a potential conflict of interest.

frontiers in Earth Science

ORIGINAL RESEARCH
published: 19 April 2018
doi: 10.3389/feart.2018.00035

Physical Responses of Convective Heavy Rainfall to Future Warming Condition: Case Study of the Hiroshima Event

Kenshi Hibino[1], Izuru Takayabu[2], Yasutaka Wakazuki[3] and Tomomichi Ogata[4]*

[1] Institute of Industrial Science, University of Tokyo, Kashiwa, Japan, [2] Atmospheric Environment and Applied Meteorology Research Department, Meteorological Research Institute, Tsukuba, Japan, [3] College of Science, Ibaraki University, Mito, Japan, [4] Application Laboratory, Japan Agency for Marine-Earth Science and Technology, Yokohama, Japan

An extreme precipitation event happened at Hiroshima in 2014. Over 200 mm of total rainfall was observed on the night of August 19th, which caused floods and many landslides. The rainfall event was estimated to be a rare event happening once in approximately 30 years. The physical response of this event to the change of the future atmospheric condition, which includes a temperature increase on average and convective stability change, is investigated in the present study using a 27-member ensemble experiment and pseudo global warming downscaling method. The experiment is integrated using the Japan Meteorological Research Institute non-hydrostatic regional climate model. A very high-resolution horizontal grid, 500 m, is used to reproduce dense cumulonimbus cloud formation causing heavy rainfall in the model. The future climate condition determined by a higher greenhouse gas concentration is prescribed to the model, in which the surface air temperature globally averaged is 4 K warmer than that in the preindustrial era. The total amounts of precipitation around the Hiroshima area in the future experiments are closer to or slightly lower than in the current experiments in spite of the increase in water vapor due to the atmospheric warming. The effect of the water vapor increase on extreme precipitation is found to be canceled out by the suppression of convection due to the thermal stability enhancement. The fact that future extreme precipitation like the Hiroshima event is not intensified is in contrast to the well-known result that extreme rainfall tends to be intensified in the future. The results in the present study imply that the response of extreme precipitation to global warming differs for each rainfall phenomenon.

Keywords: extreme precipitation, future change, ensemble experiment, pseudo global-warming downscaling method, convective instability, modified relative humidity, temperature lapse rate

OPEN ACCESS

Edited by:
Jing-Jia Luo,
Bureau of Meteorology, Australia

Reviewed by:
Rosmeri Porfirio Da Rocha,
Universidade de São Paulo, Brazil
Daoyi Gong,
Beijing Normal University, China

****Correspondence:***
Kenshi Hibino
khibino@iis.u-tokyo.ac.jp

Specialty section:
This article was submitted to Atmospheric Science, a section of the journal Frontiers in Earth Science

Received: *04 January 2018*
Accepted: *03 April 2018*
Published: *19 April 2018*

Citation:
Hibino K, Takayabu I, Wakazuki Y and Ogata T (2018) Physical Responses of Convective Heavy Rainfall to Future Warming Condition: Case Study of the Hiroshima Event. Front. Earth Sci. 6:35. doi: 10.3389/feart.2018.00035

1. INTRODUCTION

In August 2014, a heavy rainfall event happened around Hiroshima city (34.39°N, 132.46°E), Japan. The total amount of precipitation was observed to be over 200 mm in the northern part of Hiroshima city, and floods and landslides happened due to the intense precipitation, and 75 people were killed by these disasters (Hirota et al., 2016). Although such heavy rainfall events

do not happen frequently, they can cause severe disasters. How extreme precipitation changes in the future, particularly influenced by the anthropogenic global warming due to an increase in the concentration of greenhouse gases (GHGs), is of great concern for society.

As the IPCC AR5 (Stocker et al., 2013) reported that the extreme precipitation has intensified in many regions in the world, the assessment of its future change has become more important. There are two types of studies concerning the future change in extreme precipitation: one focusing on statistical or climatological change and one dealing with changes in individual meteorological phenomena, i.e., case studies, which should be distinguished. The latter type of studies is superior to the former type in that it enables us to analyze the actual mechanism with which meteorological phenomena respond to global warming, but is inferior in that any changes of case studies do not necessarily imply the climatological change in similar precipitation events, e.g., no information concerning a change in the frequency of extreme precipitation. The two types of researches should be integrated to overcome the weaknesses of each individual type.

Many studies have been done focusing mainly on the general and statistical characteristics (first type) of future change in extreme precipitation (e.g., Kharin et al., 2013; Ban et al., 2015; Mizuta et al., 2016). Almost all of them concluded that the amount of extreme precipitation has increased, which is consistent with the deduction that more moisture is converted into precipitation in a warmer atmosphere according to the Clausisus Clapeion (C-C) relationship: an increase of approximately 7 % per degree of warming. However, the precipitation amount does not necessarily follow the C-C relation completely (e.g., Prein et al., 2017) since it is affected by other factors, such as circulation pattern changes or moisture availability. In addition, when considering heavy rainfall phenomena in small spatial scales, the poor resolution of current climate models deteriorates the ability to reproduce them and evaluate their strength with high reliability (Wehner et al., 2010; Volosciuk et al., 2015).

There are also various studies focusing on a particular meteorological phenomenon relating heavy rainfall and investigating the effect of future climate change on it (e.g., Pall et al., 2017). Takayabu et al. (2015) examined typhoon Haiyan and showed that its expected strength has been intensified by global warming from pre-industrial period until the current day. A similar approach was applied to heat wave events to elucidate the effect of anthropogenic global warming (e.g., Shiogama et al., 2014).

To investigate the future change of a specified meteorological phenomenon, environmental condition involving the meteorological phenomenon needs to be changed as what is expected in the future. One of the methods is the pseudo global-warming downscaling (PGWD) method (Kimura and Kitoh, 2007; Takayabu et al., 2015), in which the climatological change of temperature is superimposed to the current atmospheric or ocean conditions. The global warming level is usually obtained from general circulation models, e.g., Coupled Model Intercomparison Project Phase 5 (CMIP5) (Stocker et al., 2014), or prescribed with an arbitrary level e.g., 4.0 degree warming from the pre-industrial level (Mizuta et al., 2016).

Atmosphere warming accompanies an increase in the air moisture level providing that the other atmospheric conditions, such as circulation and stratification, are the same as before. The moisture increase does not only increase the total amount of precipitation linearly but also can change the flow field of particular meteorological phenomena, e.g., intensification of tropical cyclones (Takayabu et al., 2015), which suggests the possibility that more moisture from the surrounding areas is provided and converted to rainfall (Kanada et al., 2017). Therefore, in the case of tropical cyclones, the associated precipitation amount is expected to increase over the C-C relation. However, there is a possibility that extreme precipitation derived from other types of meteorological phenomena does not increase so much, i.e., under the C-C relation, or even decreases due to the different physical response to the future atmospheric warming from that of tropical cyclones. Although Utsumi et al. (2016) examined the future changes in three types of meteorological phenomena (tropical cyclones, extratropical cyclones including fronts, and others), their analyses were performed from the global point of view, and thus the rainfall events that are smaller-scale but intense enough to cause disasters have not been fully investigated.

Therefore, the target meteorological event in the present study is the Hiroshima heavy rainfall event explained before. In section 2, a detailed explanation of our ensemble simulation is given. The results of the simulations are shown in section 3. A discussion regarding the effect of future atmospheric environment change (temperature and moisture) on extreme precipitation and the conclusion of the present study are given in section 4.

2. METHODOLOGY

First, the extreme precipitation in Hiroshima is simulated in the current climate condition; this experiment is referred to as the current experiment. After checking the performance of the experiments to reproduce the precipitation amount and its spatial pattern, future experiments with warmer environmental conditions are performed using the PGWD method. The precise simulation of the precipitation event is vital for its comparison in the current and future environments.

The numerical model in the present study is the Meteorological Research Institute non-hydrostatic regional climate model (MRI-NHRCM) (Sasaki et al., 2008) in the Japan Meteorological Agency (JMA), and the computational domain is shown in **Figure 1**. The horizontal grid resolution is 500 m, and there are 50 vertical grids with irregular intervals starting from the surface to 21,801 m. Because of the high resolution, no convection scheme is necessary, and precipitation output is determined through the cloud microphysics scheme by Ikawa et al. (1991), in which mixing ratios of water vapor, cloud water, cloud ice, snow, rain, and graupel are calculated. The simulation period is 15 h: from 1800 Japan Standard Time (JST) on August 19th to 0900 JST on August 20th, 2014, which includes the heaviest rainfall period in the current experiments. The initial

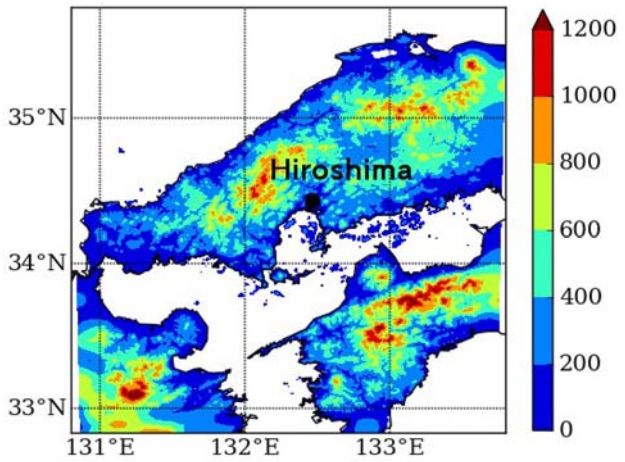

FIGURE 1 | Spatial distribution of altitude in the simulation domain.

and boundary conditions of the model are obtained from the JMA meso-scale analysis data of every 3 h with 5 km horizontal resolution.

The heavy rainfall in the Hiroshima event was caused by a back-building type rain-band (Bluestein and Jain, 1985), which involves consecutively formed cumulonimbus on the windward side. Because the terrain of mountainous region to the north of Hiroshima at which heavy rainfall was observed is complex (**Figure 1**), small perturbations in terms of environmental conditions can cause large differences in the precipitation amount. In addition, the generation of cumulonimbus is sensitive to the small initial perturbations due to its chaotic nature. Therefore, ensemble simulation is performed to cover such uncertainties and to find robust characteristics regarding the future change in the Hiroshima event.

For the ensemble members for the experiment, we use the ensemble meteorological data in the One-week Ensemble Prediction System (hereinafter called "weekly ensemble"), which is distributed operationally by JMA (Sakai, 2009). The perturbation of the weekly ensemble is calculated based on the singular vector method (Buizza and Palmer, 1995), which has a maximum growth rate for a prescribed optimization time: 48 h for the Northern hemisphere and 24 h for the tropics. We select the weekly ensemble generated at the time 0900 JST on August 19th and used its growing perturbation at the simulation starting time, i.e., 1800 JST of the same day, to construct the initial condition of the simulations. The variables from the weekly ensemble dataset are wind, temperature, pressure, and specific humidity. Because the horizontal resolution of the weekly ensemble is approximately 40 km and much coarser than that of the model in the present study (500 m), only the perturbations of weekly ensemble members, the number of which is 26, are used and superimposed to the initial condition derived form the JMA meso-scale analysis with a higher resolution. The experiment free from the weekly ensemble perturbations is referred to as the control experiment, and thus the total number of ensemble experiment members in the present study is 27.

For the three variables except specific humidity: wind, temperature, and pressure, weekly ensemble perturbation is added to each variable. If specific humidity perturbation is added similarly, the relative humidity exceeds 100% and artificial saturation and cloud formation can happen. To avoid this problem and to reproduce the heavy rainfall event with a small lead time, atmospheric humidity is converted to the modified relative humidity (MRH) (Wakazuki, 2013). The values of humidity in the control experiment and the weekly ensemble perturbations are both converted to MRH and summed, which is re-converted afterward to the specific humidity used in the simulations. Finally, 27 ensemble experiment members with different initial and boundary conditions are performed.

The PGWD method to change the environmental condition in the Hiroshima event to a future one is adopted with the temperature vertical profile change δT. Although there are various types in the PGWD method, horizontally-uniform temperature increase i.e., $\delta T(z)$ is used to avoid changing the wind patterns according to the thermal wind relation. This PGWD method helps maintain the environment condition in which heavy rainfall tends to occur, and the direct effect of the environmental warming can be analyzed. The value of δT is obtained from huge climate dataset d4PDF (Mizuta et al., 2016), which has order thousands of samples. The d4PDF dataset is constructed by the ensemble experiments of past periods (1951–2011) based on observation and future periods whose climate condition determined by a higher greenhouse gas concentration is prescribed to the model, in which the surface air temperature globally averaged is 4 K warmer than that in the preindustrial time. The difference between future and past experiments averaged in August and over the computational region in the present study is extracted as the future change δT and averaged over the whole d4PDF simulation years and over all d4PDF ensemble members. The red line in **Figure 2A** shows the vertical profile of δT and is added to the current temperature on whole model grids to change the current environment to a future one. In addition, the future change in the sea surface temperature and land surface temperature is homogeneous horizontally, the value of which is adopted from the lowest layer of $\delta T(z)$ i.e., 4 K to avoid the temperature discontinuity between sea or land surface and atmosphere in the future experiments.

The relative humidity in the future is the same as the current conditions to simulate the future moisture increase in the atmosphere according to the degree of the warming. **Figure 2B** shows the vertical profiles of specific humidity in the (blue) current and (red) future experiments, which are an averaged over the whole computational domain, simulation period, and ensemble members in our experiments. Future environment humidity is largely increased due to the atmospheric warming, although the humidity is concentrated in the troposphere, i.e., below 10,000 m.

The total precipitation accumulated in 6 h from 0000 JST to 0600 JST on August 20th and is area-averaged indicated by the red box in **Figure 3B** is calculated as an indicator to represent the rainfall intensity of the Hiroshima event. Hereafter, the total precipitation, analysis period, and analysis domain are referred to as AP_{6h}, the target period, and the target domain, respectively.

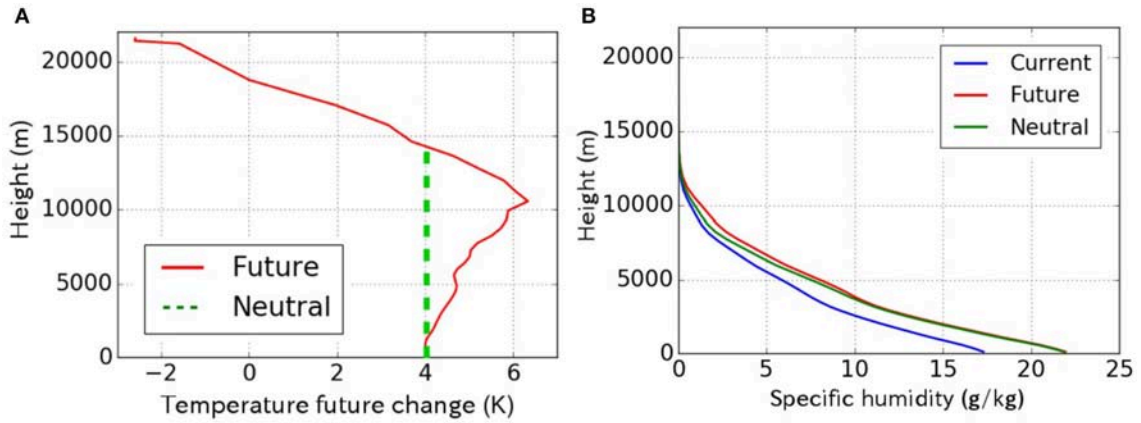

FIGURE 2 | (A) Future change (red line) of temperature vertical profile δT (K) obtained from d4PDF dataset, and temperature profile for the neutral experiments (green dashed line). **(B)** Vertical profiles of specific humidity (g/kg) in current (blue), future (red), and neutral (green) experiments, which are obtained by averaging the specific humidity over the whole computation domain, simulation periods, and ensemble experiment members.

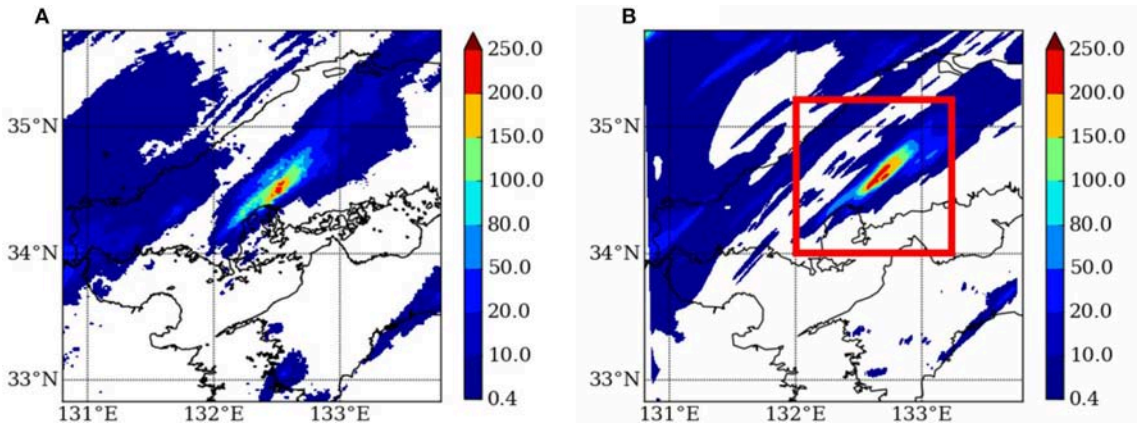

FIGURE 3 | Geographical distribution of the total precipitation (mm) from 0000 JST to 0006 JST on August 20th obtained from **(A)** the Radar-AMeDAS observation data and **(B)** the current control experiment. This figure domain is identical to the simulation domain, and the red square region is the target domain to calculate the value of AP_{6h}.

The target period includes the most intense precipitation timing (**Figure 4**), and the domain covers almost all fluctuations of heavy rainfall location in all ensemble experiment members (Figures S1–S3). The change in AP_{6h} between current and future climates is also examined.

3. RESULTS

In the observed precipitation event in Hiroshima, total precipitation over 200 mm through this event was observed in the northern part of the city. **Figure 3A** shows the spatial pattern of Radar-AMeDAS precipitation, which is a combined observation product based on the Automated Meteorological Data Acquisition Systems (AMeDAS) rain gauge data and radar precipitation (Makihara et al., 1996). This intense precipitation is reproduced in the current control experiment, as shown in **Figure 3B**; the results except for the control case are provided in Figure S1 for current experiments and Figure S2 for future experiments. Comparing the observation and model results, the high reproducibility of our model is revealed; their spatial patterns and the intensity of precipitation are quite similar, although the peak of precipitation in the model is located in a slightly north-eastward position.

Next, we examined the moisture inflow into the heavy rainfall region around Hiroshima. According to the report by MRI in Japan (MRI, 2014), one of the significant factors causing this heavy rainfall was the large southerly moisture inflow near the ground to the region around Hiroshima. The large amount of moisture over the ocean was transported to the mountainous region to the north of Hiroshima and lifted to form the cumulonimbus clouds and the rain-band. This moisture inflow is also represented in the current control experiment as shown by the moisture flux intensity at 975 hPa in the beginning of the target period, i.e., 0000 JST on 20th (**Figure 5A**). Leaving the

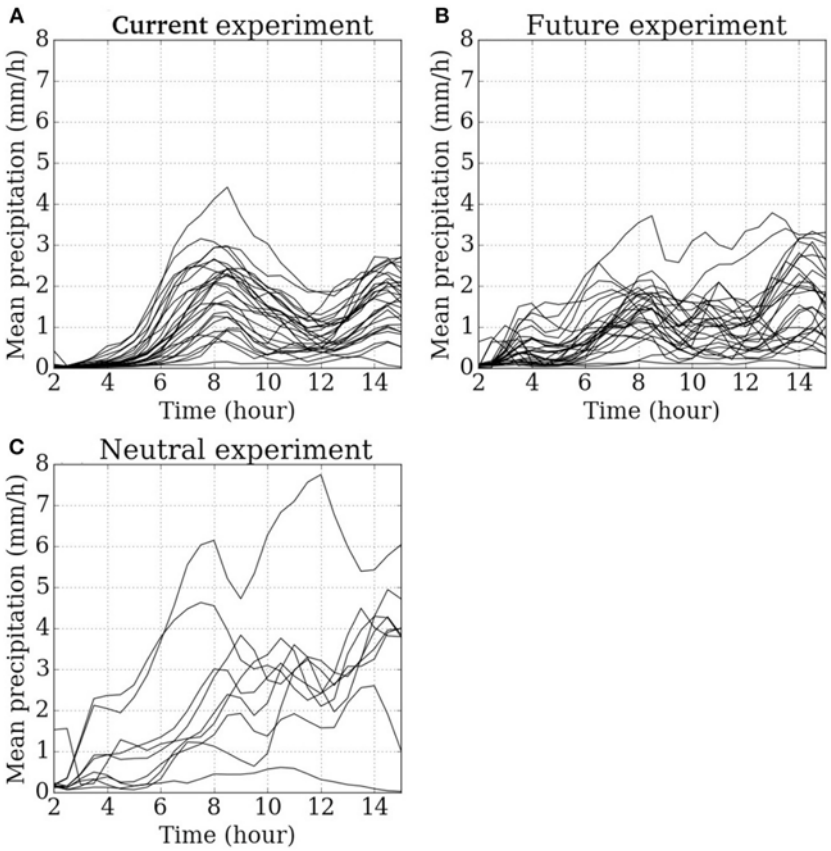

FIGURE 4 | Time series of the precipitation amount averaged in the target domain. The values are hourly cumulative precipitation until that time. Each line represents the result of each ensemble member in **(A)** the current experiments, **(B)** the future experiments, and **(C)** the neutral experiments. The simulation period is 15 h from 1800 Japan Standard Time (JST) on August 19th to 0900 JST on August 20th.

vicinity of the ground, south-easterly wind blows at the lower troposphere, the height of 850 hPa, (**Figure 5B**), and the rain-band formed is extended in the north-eastward direction along the wind at this level, which is consistent with the explanation by MRI (2014).

With these comparisons between the current control experiment and observation in terms of total precipitation amount, spatial pattern of heavy rainfall, and moisture inflow, we can conclude that the heavy precipitation event at Hiroshima was reproduced realistically by the model. Because similar results are obtained for the other ensemble members (Figures S1, S4, and S5), the mechanism causing the heavy rainfall can be suitable for most of the ensemble members, but the small environmental differences among the members determine rainfall severity. Note that the Hiroshima event has an aspect of orographic precipitation since moist air over the ocean is transported onto land and the mountainous region around Hiroshima, generating heavy rainfall.

From now on in this paper, we show the values of AP_{6h} to investigate the intensity of extreme precipitation in the Hiroshima event (**Figure 6**). The values of AP_{6h} in current and future experiments are closely correlated to each other ranging from very small precipitation (nearly 0 mm/6 h) to large precipitation (approximately 20 mm/6 h). The intensity of the heavy rainfall events is found to be mainly determined by the difference of ensemble members or large-scale flow pattern prescribed by the weekly ensemble perturbation and to have large prediction uncertainty or spread. The value of the Radar-AMeDAS observation is 12.68, as shown in **Figure 6**, which is included in the uncertainty of the current climate experiments.

Comparing the current and future values of AP_{6h} in **Figure 6**, most of the ensemble member results lie on the diagonal line showing AP_{6h}(future) = AP_{6h}(current), which implies that the future rainfall of the Hiroshima event is not intensified. This result looks contradictory to the fact that humidity in the future atmosphere has increased, as shown in **Figure 2B**. If the whole atmospheric motion including both horizontal and vertical velocities is identical between the current and future experiments, the resulting precipitation should be larger in the future model by the amount of additional water vapor due to the atmospheric warming. Seeing the time series of spatially-averaged precipitation in the target domain (**Figure 4**), clear intensification of precipitation in the future is not obtained, although the time variations are somewhat different between the

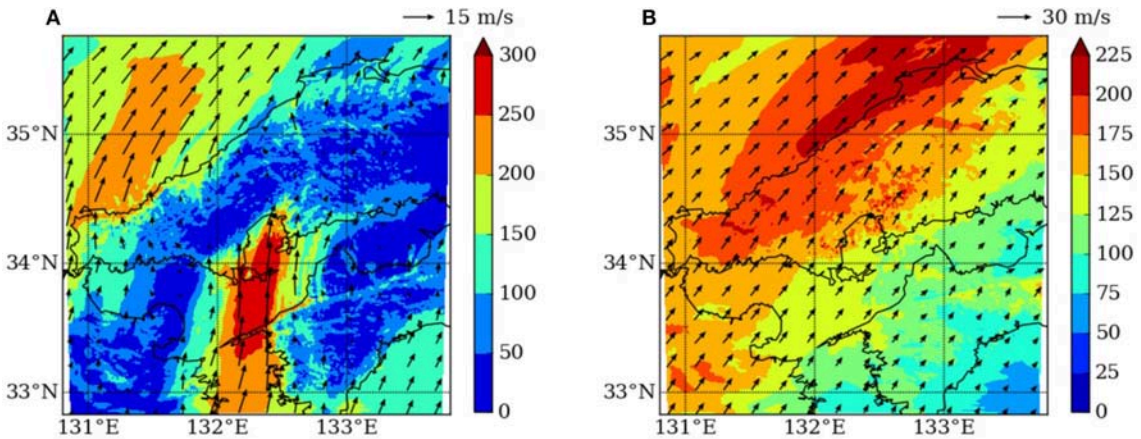

FIGURE 5 | Geographical distribution of the moisture flux intensity (shaded) and wind field (arrows) **(A)** near the ground (975 hPa) and **(B)** at the lower troposphere (850 hPa) obtained from the current control experiment.

current and future experiments; rainfall in the future experiments (**Figure 4B**) initiates earlier, and shows no clear peak time around $t = 8$, unlike the current experiments (**Figure 4A**).

To investigate the reason that the future precipitation in the Hiroshima event does not increase in a moister atmosphere, we examine the stabilizing effect of future temperature change profile δT in the troposphere (see **Figure 2A**). The value of δT increases with height corresponding to the decrease in the temperature lapse rate (Tett et al., 1996), which is based on the fact that the moist adiabatic lapse rate decreases with atmosphere warming. The characteristic regarding vertical temperature structure was found to reduce the non-extreme precipitation in mid-latitudes (Kröner et al., 2016). To evaluate the depression effect on extreme precipitation like the Hiroshima event, we performed additional ensemble experiments that we call "neutral experiments." In the neutral experiments, the profile of future temperature increase δT is changed from the actual future one; the new profile is shown by the green dashed line in **Figure 2A** as well as the profile of the specific humidity by the green line in **Figure 2B**. The temperature change over a height of approximately 14,000 m and the other model settings are the same as those of future experiments. Because the profile of the neutral experiments has a neutral effect on the convective instability of the troposphere, the comparison between the results of future and neutral experiments is expected to evaluate the stabilizing effect of δT in the future. We perform 9 member experiments due to the computational limit, which covers as much uncertainty as possible in terms of the rainfall intensity AP_{6h}, shown by the blue points in **Figure 6**.

All of the values of AP_{6h} in the neutral experiments are increased from those of the current and future experiments when comparing them in terms of each ensemble member; the intensification of rainfall in the neutral experiments is also revealed with its time series result (**Figure 4C**). Because the difference in the environmental conditions between the future and neutral experiments is only the temperature warming profile, the large decrease in precipitation in the future experiments compared with the neutral experiments is caused by the effect of thermal stability enhancement.

To analyze the future and neutral experiments' differences in greater detail, the strength of vertical or convective motion in the heavy rainfall region is examined. **Figure 7** is a scatter diagram of the maximum vertical velocity at 500 hPa plains (x-axis) of the target domain and the target period relating to the values of AP_{6h} (y-axis). Before extracting the maximum value, a running mean over 9 x 9 grids of vertical velocity is performed to smooth out the very small-scale noisy pattern. Such maximum velocity values precisely represent the convection strength, as its correlation to precipitation intensity AP_{6h} is actually higher than that without the smoothing operation; the correlation coefficient is 0.742 in **Figure 7**.

At the middle troposphere heights of 500 hPa, current and future results are scattered in close proximity, while the results of neutral experiments are separated from those of the current and future experiments. The statistical significance of the results is verified by the Mann–Whitney U-test (Wilks, 2011): 1% level significance between the results of the current and neutral experiments, but the significance even for the level of 10 % cannot be obtained between the results of current and future experiments. Thus, the convection in the current and future experiments has approximately the same strength and yields a closer amount of precipitation as a result. On the other hand, the neutral experiments show strong convection and large precipitation, which implies that the vertical motion is accelerated due to the condensation heating of the increased moisture in the atmosphere.

In the future experiments, the convective clouds in their early stage of growing yield the larger precipitation compared with the current experiments due to the large amount of moisture in the atmosphere, which is shown by an earlier increase in the AP_{6h} values (**Figure 4B**) and spatial distribution of precipitation in the early period, e.g., $t = 4$ (Figures S6, S7). However, the vertical acceleration associated with the condensation

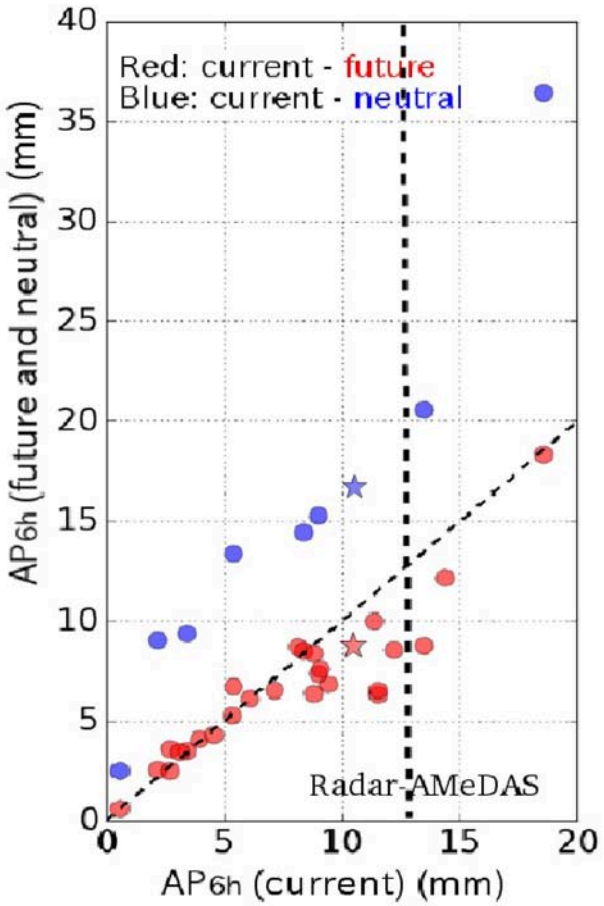

FIGURE 6 | Scatter diagram of the values of AP_{6h} showing the relation between the current experiments (*x*-axis) and future (*y*-axis; red points) and neutral (*y*-axis; blue points) experiments. The results from the control experiments are shown as stars. The black inclined dashed line is a line of $y = x$, the points on which show that the future or neutral experiments yield the same amount of precipitation intensity as that of current experiments. The value of AP_{6h} of Radar-AMeDAS precipitation is 12.68 and shown by a black vertical line.

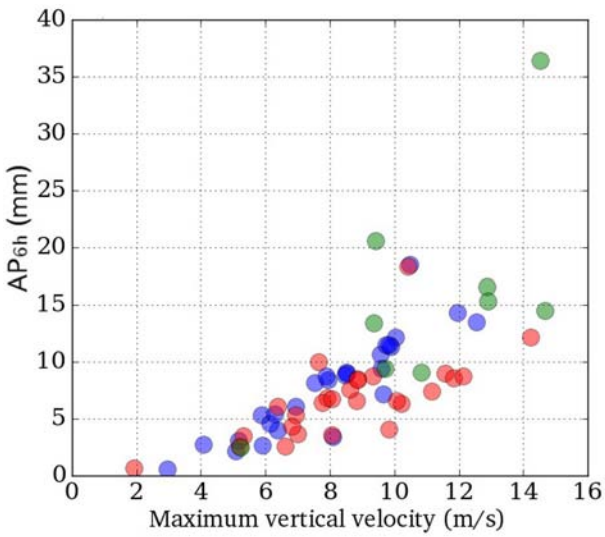

FIGURE 7 | Scatter diagram showing the relation between the extreme precipitation index in the present study, AP_{6h} and the maximum vertical velocity at a height of 500 hPa, which are obtained for the target domain (red square region in **Figure 3B**) and the target period (from 0000 JST to 0600 JST on August 20th). Blue, red, and green points represent the results of current, future, and neutral experiments, respectively.

heating is suppressed by the stabilizing effect of the change in the temperature profile in the troposphere. As a result, the convection and precipitation in the future experiments are not intensified and are thus closer to the current experiments.

4. DISCUSSION AND CONCLUSION

In this study, we examined the future change in the heavy rainfall event happened at Hiroshima by performing numerical experiments with the pseudo global warming downscaling method. There have been no previous studies using the ensemble experiment with very-high resolution, such as 500 m to investigate the future change in extreme precipitation event. The very-high resolution simulation in the present study demonstrates the high reproducibility of the heavy convective rainfall, and robust results regarding the future change in extreme precipitation are obtained thanks to the ensemble experiment. The main conclusion in the present study is that the extreme precipitation in the event is not increased even in the 4 K warmer environmental condition accompanying larger amounts of water vapor. This result looks contradictory to the many previous studies showing the intensification of extreme precipitation in the future (e.g., Kharin et al., 2013; Ban et al., 2015; Mizuta et al., 2016). Our main conclusion is derived from the cancellation between the destabilizing effect of a water vapor increase and the stabilizing effect of a temperature lapse rate decrease in future environmental conditions.

Kröner et al. (2016) showed that a future decrease in the temperature lapse rate reduces the non-extreme precipitation in Europe and Northern Africa. The present study shows that the similar precipitation suppression is effective for extreme precipitation to the extent that it can offset the thermodynamic aspect of a moisture increase. Because the decrease in the temperature lapse rate or the stabilizing characteristic is projected to be dominant from tropics to mid-latitudes in the future (IPCC AR5, Stocker et al., 2013), the suppression of extreme precipitation we found is expected to prevail in these regions.

In the Hiroshima event, thunderstorms with continuously generated cumulonimbus caused the heavy rainfall (MRI, 2014). The fact that this rainfall system is not intensified is in marked contrast to the previous studies focusing on the effect of global warming on tropical cyclones (e.g., Kanada et al., 2017), which revealed that tropical cyclones and associated rainfall intensify in the future. This difference strongly suggests that the physical responses of meteorological phenomena causing heavy

rainfall to a warmer climatic condition differ depending on their types and physical mechanisms. One of the hypotheses that tropical cyclones can be strengthened against the stabilization effect of temperature profile change but the rainfall of the Hiroshima event cannot is that tropical cyclones have a strong non-linear mechanism in which increased water vapor due to atmosphere warming enables them to gather more water vapor from the surrounding atmosphere. This characteristic of tropical cyclones amplifies the effect of a moisture increase in terms of convective instability and enables them to grow by overcoming the stabilizing effect of stratification. On the other hand, the extreme precipitation event at Hiroshima bearing the aspect of orographic precipitation does not have such a strong nonlinear effect, in other words, the thunderstorms and cumulonimbus systems in this event only perturb the flow field and do not change the environmental condition determining the severity of rainfall due to their relatively small spatial scale of the phenomena.

The present study cannot provide any knowledge concerning the future change in frequency of appearance of thunderstorms causing extreme precipitation because of the limitation of a case study. However, the possibility that these thunderstorm events cannot be intensified even in the warmer and wetter conditions due to the temperature lapse rate change in the troposphere leads to the further studies combined with climatological or statistical studies focusing on the frequency of extreme precipitation.

AUTHOR CONTRIBUTIONS

KH played a major role for the present study, including model simulation, analyses, and writing the paper. IT proposed the analysis of future change of the Hiroshima heavy rainfall event using pseudo global-warming downscaling method and coordinated the whole study. YW introduced the concept of "modified relative humidity" for our experiments and also determined the model setting and model initial condition with KH. TO gave the perspective based on interactions between large and small scale meteorological phenomena. He also made an analysis of synoptic-scale flow field including our simulation domain, the results of which are not used directly in the paper but affected our research.

ACKNOWLEDGMENTS

This research was supported by SOUSEI and TOUGOU Programs of Ministry of Education, Culture, Sports, Science, and Technology of Japan.

SUPPLEMENTARY MATERIAL

The Supplementary Material for this article can be found online at: https://www.frontiersin.org/articles/10.3389/feart.2018.00035/full#supplementary-material

REFERENCES

Ban, N., Schmidli, J., and Schär, C. (2015). Heavy precipitation in a changing climate: does short-term summer precipitation increase faster? *Geophys. Res. Lett.* 42, 1165–1172. doi: 10.1002/2014GL062588

Bluestein, H. B., and Jain, M. H. (1985). Formation of mesoscale lines of precipitation: severe squall lines in Oklahoma during the spring. *J. Atmos. Sci.* 42, 1711–1732.

Buizza, R., and Palmer, T. (1995). The singular-vector structure of the atmospheric global circulation. *J. Atmos. Sci.* 52, 1434–1456.

Hirota, N., Takayabu, Y. N., Kato, M., and Arakane, S. (2016). Roles of an atmospheric river and a cutoff low in the extreme precipitation event in Hiroshima on 19 August 2014. *Month. Weather Rev.* 144, 1145–1160. doi: 10.1175/MWR-D-15-0299.1

Ikawa, M., Mizuno, H., Matsuo, T., Murakami, M., Yamada, Y., and Saito, K. (1991). Numerical modeling of the convective snow cloud over the sea of japan. *J. Meteorol. Soc. Jpn. Ser. II* 69, 641–667.

Kanada, S., Takemi, T., Kato, M., Yamasaki, S., Fudeyasu, H., Tsuboki, K., et al. (2017). A multimodel intercomparison of an intense typhoon in future, warmer climates by four 5-km-mesh models. *J. Clim.* 30, 6017–6036. doi: 10.1175/JCLI-D-16-0715.1

Kharin, V. V., Zwiers, F., Zhang, X., and Wehner, M. (2013). Changes in temperature and precipitation extremes in the CMIP5 ensemble. *Clim. Change* 119, 345–357. doi: 10.1007/s10584-013-0705-8

Kimura, F., and Kitoh, A. (2007). *Downscaling by Pseudo Global Warming Method*. The Final Report of ICCAP, 4346. Research Institute for Humanity and Nature (RIHN), Kyoto.

Kröner, N., Kotlarski, S., Fischer, E., Lüthi, D., Zubler, E., and Schär, C. (2016). Separating climate change signals into thermodynamic, lapse-rate and circulation effects: theory and application to the european summer climate. *Clim. Dyn.* 48, 3425–3440. doi: 10.1007/s00382-016-3276-3

Makihara, Y., Uekiyo, N., Tabata, A., and Yoshiyuki, A. (1996). Accuracy of radar-AMeDAS precipitation. *IEICE Trans. Commun.* 79, 751–762.

Mizuta, R., Murata, A., Ishii, M., Shiogama, H., Hibino, K., Mori, N., et al. (2016). Over 5000 years of ensemble future climate simulations by 60 km global and 20 km regional atmospheric models. *Bull. Am. Meteorol. Soc.* 98, 1383–1398. doi: 10.1175/BAMS-D-16-0099.1

MRI (2014). *The Generation Mechanism of Extreme Precipitation Event at Hiroshima in 20th August, 2014 - Rainband Stagnation and Accumulation of Water Vapor in Bungo Channel (in Japanese)*. Press release, 26. Available online at: http://www.mri-jma.go.jp/Topics/H26/260909/Press_140820hiroshima_heavyrainfall.pdf

Pall, P., Patricola, C. M., Wehner, M. F., Stone, D. A., Paciorek, C. J., and Collins, W. D. (2017). Diagnosing conditional anthropogenic contributions to heavy colorado rainfall in september 2013. *Weather Clim. Extrem.* 17, 1–6. doi: 10.1016/j.wace.2017.03.004

Prein, A. F., Rasmussen, R. M., Ikeda, K., Liu, C., Clark, M. P., and Holland, G. J. (2017). The future intensification of hourly precipitation extremes. *Nat. Clim. Change* 7, 48–52. doi: 10.1038/nclimate3168

Sakai, R., Kyouda, M., Yamaguchi, M., and Kadowaki, T. (2008). *A New Operational One-Week Ensemble Prediction System at Japan Meteorological Agency*. CAS/JSC WGNE research activities in atmospheric and oceanic modelling, 38.

Sasaki, H., Kurihara, K., Takayabu, I., and Uchiyama, T. (2008). Preliminary experiments of reproducing the present climate using the non-hydrostatic regional climate model. *SOLA* 4, 25–28. doi: 10.2151/sola.2008-007

Shiogama, H., Watanabe, M., Imada, Y., Mori, M., Kamae, Y., Ishii, M., et al. (2014). Attribution of the June-July 2013 heat wave in the southwestern United States. *SOLA* 10, 122–126. doi: 10.2151/sola.2014-025

Stocker, T., Qin, D., Plattner, G., Tignor, M., Allen, S., Boschung, J., et al. (2013). *IPCC, 2013: Climate Change 2013: The Physical Science Basis. Contribution of Working Group I to the Fifth Assessment Report of the Intergovernmental Panel on Climate Change.*

Stocker, T. F., Qin, D., Plattner, G. K., Tignor, M., Allen, S. K., Boschung, J., et al. (2014). *Climate Change 2013: The Physical Science Basis*. Cambridge, UK; New York, NY: Cambridge University Press.

Takayabu, I., Hibino, K., Sasaki, H., Shiogama, H., Mori, N., Shibutani, Y., et al. (2015). Climate change effects on the worst-case storm surge: a case study of Typhoon Haiyan. *Environ. Res. Lett.* 10:064011. doi: 10.1088/1748-9326/10/8/089502

Tett, S. F., Mitchell, J. F., Parker, D. E., and Allen, M. R. (1996). Human influence on the atmospheric vertical temperature structure: detection and observations. *Science* 274:1170.

Utsumi, N., Kim, H., Kanae, S., and Oki, T. (2016). Which weather systems are projected to cause future changes in mean and extreme precipitation in cmip5 simulations? *J. Geophys. Res.* 121, 10,522–10,537 doi: 10.1002/2016JD 024939

Volosciuk, C., Maraun, D., Semenov, V. A., and Park, W. (2015). Extreme precipitation in an atmosphere general circulation model: impact of horizontal and vertical model resolutions. *J. Clim.* 28, 1184–1205. doi: 10.1175/JCLI-D-14-00337.1

Wakazuki, Y. (2013). Modified relative humidity based on the Johnson's SB distribution function. *SOLA* 9, 111–114. doi: 10.2151/sola.2013-025

Wehner, M. F., Smith, R. L., Bala, G., and Duffy, P. (2010). The effect of horizontal resolution on simulation of very extreme US precipitation events in a global atmosphere model. *Clim. Dyn.* 34, 241–247. doi: 10.1007/s00382-009-0656-y

Wilks, D. S. (2011). *Statistical Methods in the Atmospheric Sciences*. Amsterdam: Academic Press.

Conflict of Interest Statement: The authors declare that the research was conducted in the absence of any commercial or financial relationships that could be construed as a potential conflict of interest.

frontiers in Earth Science

ORIGINAL RESEARCH
published: 15 May 2018
doi: 10.3389/feart.2018.00054

A Snowpack Forecasting Model for the Eastern Sierra Nevada Based on Cointegration With the North Pacific High Sea-Level Pressure Anomaly

John S. Rath[1] *and Mariza Costa-Cabral*[2]*

[1] Tetra Tech Inc., R&D, Lafayette, CA, United States, [2] Northwest Hydraulic Consultants Inc., Seattle, WA, United States

A cointegrated relationship has been identified between the January sea level pressure anomaly at the climatological location of the North Pacific High (NPH) and seasonal precipitation throughout California (Costa-Cabral et al., 2016). This cointegration can be used for forecasting precipitation or snowpack indices at California locations. Here we develop a cointegration model, termed Vector Error Correcting Model (VECM), for issuing a forecast, in early February, for April 1 snow water content (SWC) at snow stations in the Eastern Sierra Nevada mountain range of California. We additionally develop a categorical model for forecasting the April 1 SWC category (dry, normal, or wet) based on the VECM forecast. Snowmelt from this region flows into the Owens River and serves as a major source of freshwater for the Los Angeles metropolitan area. The VECM relies on the cointegration between three variables: the January NPH sea level pressure, the February 1 SWC, and the April 1 SWC. Forecasts based on this VECM model have higher measures of skill compared to linear correlation methods. The statistical tool presented can be applied to other California watersheds and may provide reservoir operators the needed insight for making storage decisions in early February.

Keywords: cointegration, forecasting, North Pacific High, Owens valley, VECM models, categorical models

OPEN ACCESS

Edited by:
Hans Von Storch,
Helmholtz-Zentrum Geesthacht Zentrum für Material- und Küstenforschung, Germany

Reviewed by:
Manolis G. Grillakis,
Technical University of Crete, Greece
Andras Bardossy,
University of Stuttgart, Germany

***Correspondence:**
Mariza Costa-Cabral
mcabral@nhcweb.com

Specialty section:
This article was submitted to Atmospheric Science, a section of the journal Frontiers in Earth Science

Received: *03 December 2017*
Accepted: *23 April 2018*
Published: *15 May 2018*

Citation:
Rath JS and Costa-Cabral M (2018) A Snowpack Forecasting Model for the Eastern Sierra Nevada Based on Cointegration With the North Pacific High Sea-Level Pressure Anomaly. Front. Earth Sci. 6:54. doi: 10.3389/feart.2018.00054

INTRODUCTION

Precipitation in the Sierra Nevada mountain ranges of California occurs primarily in the winter months, in the form of snow and rain (Pandey et al., 1999). Meltwaters from accumulated snow, modulated by surface water reservoirs, serve as a source of water supply over the summer months. Snow accumulation over the winter months is carefully tracked to provide an estimate of future snowmelt volumes in the spring and summer months. Typically, reservoirs are operated to maintain sufficient flood storage capacity for the anticipated snowmelt and rain events later in the wet season. Excess runoff is released to maintain flood storage capacity. Advance knowledge of total precipitation during a wet season can allow adjustments in the flood storage capacity to maximize the water stored in the reservoirs.

Here we develop a model, to be used in early February of each year, for forecasting the snow water content (SWC) 2 months later, on April 1, at key Eastern Sierra snow stations on Owens Valley tributary watersheds. Freshwater from this watershed, transported more than 300 miles via aqueducts, is one of the most important water sources for over 4 million people in the Los Angeles metropolitan area (Costa-Cabral et al., 2012). Runoff is managed through reservoirs to support Los Angeles' water supply as well as in-valley uses.

The impetus for this work was the finding by Costa-Cabral et al. (2016) that seasonal precipitation totals in California and other parts of the southwestern United States have a considerably strong relationship with the high-pressure center off the coast of California known as the North Pacific High (NPH). Large-scale climatic indices have been used as predictors of precipitation totals and extremes in many studies and are used operationally in weather forecasts to circumvent the difficulty in obtaining robust dynamical simulations of precipitation.

Establishing a statistical association between observed large-scale climate patterns and precipitation to come in the months ahead is an approach that has been used at many world locations for forecasting precipitation and anticipating water resources availability (for example, Fernando et al., 2015). Such statistical associations have also been used extensively to obtain forecasts of future precipitation based on simulated forecasts of the large-scale climate patterns. Future projections of precipitation have also been obtained on the basis of such statistical associations with large-scale climate patterns (for example, Kharin et al., 2013; Costa-Cabral et al., 2016).

The El Niño-Southern Oscillation (ENSO) phenomenon has been identified as a major driver of climate variability worldwide, and arises from the coupled ocean-atmosphere system of the Pacific basin. Several studies have examined the influence of ENSO on precipitation and temperature over North America, and have documented associations between the strength and phase of ENSO and precipitation frequency and intensity over different regions—particularly the southwestern United States—due to ENSO's influence on the East Asian jet stream position. Thus, California has an increased likelihood of storms, precipitation extremes, and precipitation totals under El Niño conditions (see for example, Chikamoto et al., 2015).

Roughly half the time, however, ENSO is in a neutral phase. Such neutral conditions are not an indication of average meteorology over California. The recent multi-year drought in California provides an example of an extreme meteorological drought occurring at a time when both ENSO and the Pacific decadal oscillation (PDO; Mantua et al., 1997; Zhang et al., 1997) are in near-neutral states. In part due to the oft-neutral state of ENSO, the association of ENSO indices (including the atmospheric-pressure-based SOI index and sea surface temperature-based ENSO3.4 and other indices) with precipitation totals in California is near or below statistical significance level, as is also the case for the PDO as shown e.g., in Costa-Cabral et al. (2016). Rather than ENSO indices, it is the sea level pressure anomaly at the NPH that better reflects the local influence of ENSO, as well as additional variability specific to the North Pacific region.

The strength and position of the NPH, expressed as sea level pressure anomalies and geopotential height anomalies over the northeast Pacific region, affect the position of the jet stream and associated storm tracks. As shown in Costa-Cabral et al. (2016), the positive mode of the NPH is associated with a strong high-anomaly sea level pressure region over the northeastern Pacific. Abnormal northeastern Pacific high pressure ridges that extend from lower- to upper-atmospheric levels can prevent storm systems from reaching California. The role of such high-pressure ridges was discussed during the recent multiyear drought in California, which exhibited the strongest and longer lasting ridge ever observed (e.g., Swain et al., 2014; Wang et al., 2014, 2015; Stevenson et al., 2015). Costa-Cabral et al. (2016) showed that these exceptional high pressure conditions associated with the recent drought fit into a broader pattern documented in reanalysis data.

Costa-Cabral et al. (2016) demonstrated that winter precipitation totals over much of the Southwestern United States hold a special relationship, known as a "cointegration," with the sea level pressure at the normal location of the NPH. A cointegrated relationship between two stochastic variables exists when, although they appear to vary independently, the cumulative departure from the mean of the two variables tends to remain within a limited distance (Engle and Granger, 1987).

By exploiting the cointegrated relationship between SWC and the NPH anomaly, two models were developed to estimate seasonal precipitation for the Owens River watershed, and provide advance information to support reservoir operations in the Owens Valley:

- The *VECM Model* Vector Error Correcting Model (VECM) is designed to forecast, in early February, the April 1 SWC value. The VECM model uses the observed annual time series of three variables: (a) the observed January mean of the NPH anomaly, (b) the observed February 1 SWC, and (c) the April 1 SWC at each location of interest. The VECM model exploits the cointegrated relationship between these three variables, and provides a forecast for April 1 SWC based on a linear function of the values of the cumulative sum over time of standardized anomalies of all three variables.
- The *Categorical Model* is designed to determine the probability, in early February, of the April 1 SWC value falling into the dry, normal, and wet category. The thresholds between these categories are defined by a 20% deviation from the average April 1 SWC value. The Categorical Model uses the forecast value produced by the VECM model.

The mathematical formulation, parameter fitting, validation, and application of the models are described in sections Methods and Results and Model Evaluation Based on Hindcasts. The performance of both models in hindcasts (1951–2016) is also evaluated in sections Methods and Results and Model Evaluation Based on Hindcasts. The VECM model hindcasts of April 1 SWC are compared against those obtained by linear regression from observed February 1 SWC, showing significantly higher skill.

As a test, the January mean 850 hPa geopotential height over the NPH region was used in the VECM model instead of the sea level pressure, achieving comparable results in the hindcasts (Figures S-2 to S-9). For some of the stations, geopotential height performed slightly better in hindcasts, while at other stations (including Mammoth Pass) it performed slightly less well compared to sea level pressure. Also, the p-value representing the Phillips-Ouliaris cointegration test (Phillips and Ouliaris, 1990; Hamilton, 1994) is higher when geopotential height is used ($p > 0.01$) compared to sea level pressure ($0.01 < p < 0.05$), which may indicate that the cointegrated nature of the relationship with

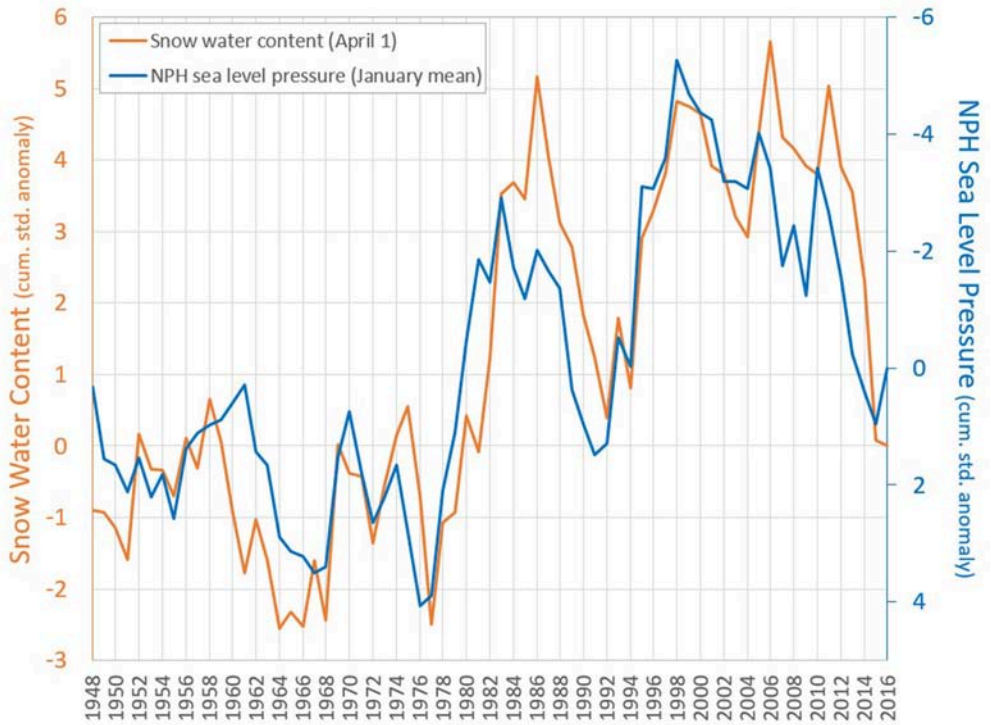

FIGURE 1 | Cumulative standardized anomaly of April 1 snow water content at Mammoth Pass (orange) and January mean sea level pressure at the North Pacific High region [NCEP/NCAR grid cell centered at (35°N, 232.5°E)] (blue). The blue line refers to the vertical axis on the right, where values are in reverse order to aid comparison between the two variables, given that they are inversely correlated.

geopotential height is less dependable. For these reasons, sea level pressure was selected for use.

The hindcasts reveal that the VECM model has considerable forecast skill. In the case of the Categorical Model, a much larger sample size would be required for evaluating the probability values that it provides, but the hindcast for the available sample size appears consistent with the calculated probabilities.

METHODS

Figure 1 shows the cumulative standardized anomalies of Mammoth Pass April 1 snow water content (SWC) and the January mean sea level pressure anomaly at a location near the NPH (1948–2016) (from the NCEP/NCAR Reanalysis). There is an apparent tendency for the two lines to remain within a limited distance of each other. The cumulative standardized anomalies of the two variables show higher linear correlation ($R = 0.88$) than the (non-cumulative) standardized anomalies ($R = 0.54$) (Figure S-1).

The Owens Valley snow water content (SWC) on April 1 depends mainly on seasonal precipitation totals but also on factors that influence snowmelt, including temperature, solar radiation and wind. Elevation is sufficiently high that nearly all winter precipitation at the sites of interest is in the form of snow. Years in which snowmelt occurs early will have diminished SWC on April 1. The model presented here does not account for these factors, but relies on the cointegrated relationship between SWC and NPH anomalies.

The cointegrated relationship between SWC and NPH anomalies is explored in the VECM model described in section The VECM Model, for Forecasting the April 1 SWC. The categorical model is described in section the Categorical Model, for Estimating Probability of Dry, Normal, or Wet Categories.

The VECM Model, for Forecasting the April 1 SWC

VECM Model Formulation

Vector Autoregression (VAR) is a type of model that represents multivariate time series using linear relationships between each variable and p of its own lags and the lags of the other variables. If the k x 1 vector y_t denotes the values of the k variables in the multivariate time series at time t, then a $VAR(p)$ model is:

$$y_t = a + A_1 y_{t-1} + A_2 y_{t-2} + \cdots + A_p y_{t-p} + \varepsilon_t \quad (1)$$

Here the vector a (intercept term) and the k x k matrices A_i (coefficients) are estimated model parameters and the vectors ε_t are random errors.

The year-specific vector at time t is given by the difference between the cumulative vectors at times t and $t - 1$:

$$\Delta y_t = y_t - y_{t-1} \quad (2)$$

Combining Equation (1) and (2) and writing $B_i = -(A_{i+1} + \cdots + A_p)$ for each $i = 1, \cdots, p-1$ and $\Pi = -\left(I - A_1 - \cdots - A_p\right)$ gives:

$$\Delta y_t = a + B_1 \Delta y_{t-1} + \cdots + B_{p-1} \Delta y_{t-p+1} + \Pi y_{t-1} + \varepsilon_t \quad (3)$$

Cointegration is a property that multivariate time series may exhibit. If the individual components of y_t are non-stationary (in particular, they have a unit root) while some (non-zero) linear combination $\beta' y_t$ is stationary, then y_t is said to be cointegrated. More intuitively, although the components of y_t are non-stationary and vary randomly, the distance between them tends to stay within a fixed distance. In fact, there may be up to $h < k$ linearly independent cointegrated relations among the y_t.

In Equation (3), if y_t is cointegrated then Π has reduced rank $h < k$ and can be factored as $\Pi = \alpha\beta'$, where α is $k \times h$ and β' is $h \times k$, such that $\beta' y_t$ is a stationary $h \times 1$ vector. Then inference proceeds by first estimating the cointegrated relations β'–either by ordinary least squares (OLS) or maximum likelihood (ML) methods—and then estimating the remaining parameters a, α and β_i by OLS. This type of *VAR* with reduced rank restrictions when y_t is cointegrated is known as a *Vector Error Correction Model (VECM)*. See Hamilton (1994) and Johansen (1995) for further details.

Data Sets

The observed snow water content (SWC) on February 1 and April 1 of each year, starting 1948, at the four Owens Valley snow stations of interest—Mammoth Pass, Rock Creek #2, Sawmill, and Cottonwood #1—were provided by LADWP and are used as predictor variables in the VECM model.

Also used as a predictor variable in the VECM model is the January mean sea level pressure at a location near the climatological position (i.e., the average position over time) of the NPH. The monthly mean sea level pressure data from the National Center for Environmental Prediction, National Center for Atmospheric Research (NCEP-NCAR) reanalysis dataset (originally described in Kalnay et al., 1996) were used. The data were downloaded from the National Oceanic and Atmospheric Administration's web site[1]. This data set was selected for this study because it goes back in time to 1948, covering the entire period of LADWP snow records; has a resolution of 2.5° of latitude and longitude, which is sufficiently fine-scale but not so fine as to have excessive variability over time; and is updated online by NOAA daily, with only a 2-day delay. The grid cell centered at {35°N, 232.5°E} is used.

Reanalysis datasets, such as the ones used in this work, are based on simulations by dynamic climate models combined with observations. Such datasets represent estimates subject to uncertainty, characterized, for example, in Bosilovich et al. (2008), Guirguis and Avissar (2008), and Janowiak et al. (1998).

Because the VECM model uses cumulative standardized anomalies, the raw variables are first transformed into standardized anomalies, by subtracting the series mean then dividing by the standard deviation. The mean and standard deviation values used are for the entire record period, 1948–2016. The standardized anomalies are then added successively over time to obtain the cumulative standardized anomalies.

Parameter Fitting

For fitting, the following steps were followed:

1) Clip the time series to the calibration period.
2) Specify number of lags. This study used $p = 3$, i.e., the *VECM* uses two lag terms (years) and the underlying *VAR* model is *VAR*(3).
3) Estimate β' by Full Information Maximum Likelihood (FIML; Johansen, 1995).
4) Estimate parameters a, α and β_i by OLS. Calculate parameters A_i from those.

For prediction, the following steps were followed:

5) Convert back to *VAR* representation $((\beta_i, \Pi) \mapsto A_i)$.
6) Use Equation (1) to calculate the forecasted cumulative value $\hat{y}_t$ using data from the preceding 3 time periods and with $\varepsilon_t = 0$.
7) Use Equation (2) to obtain the desired forecasted value $\Delta\hat{y}_t = \hat{y}_t - y_{t-1}$.

Model verification will be described in section VECM Model.

The Categorical Model, for Estimating Probability of Dry, Normal, or Wet Categories

Categorical Model Formulation

The Categorical Model was developed as a complement to the VECM model. The two models are distinct in intent and formulation. The purpose of the Categorical Model is to estimate in early February the probability of the upcoming April 1 SWC falling into each of the three categories, dry, normal, or wet. These probabilities can be denoted p_d, p_n, and p_w, respectively.

The only input to the Categorical Model is the April 1 SWC value forecast by the VECM model. As with any forecast, there is uncertainty in the value forecast by the VECM model, and this implies that in a general sense no one of the three categories—dry, normal, or wet—can be ruled out as a possible outcome. Instead, each category has some non-zero probability of occurring.

Figure 2 shows the forecast for year 2010, as an example. The forecast is indicated by the red line. The red dashed lines indicate the 95% confidence interval, assuming the errors are normally distributed about the forecast value. There is a 5% chance (or 1 in 20 chance) that the observed April 1 SWC will be outside the 95% confidence interval. The blue line is the Gaussian probability density function (PDF), with mean equal to the forecast value and standard error estimated from the 1951–2016 forecasts. The green line is the normal value (the average for 1966–2015), and the dashed green lines indicate a 20% deviation from the normal value. The probability of each category is determined by the area under the Gaussian blue line, lying within the range of values of that category.

Once the VECM model was fit for each location, the Categorical Model estimates the probability that the April

[1]http://www.esrl.noaa.gov/psd/data/gridded/data.ncep.reanalysis.derived.surface.html (file name: **slp.mon.mean.nc**)

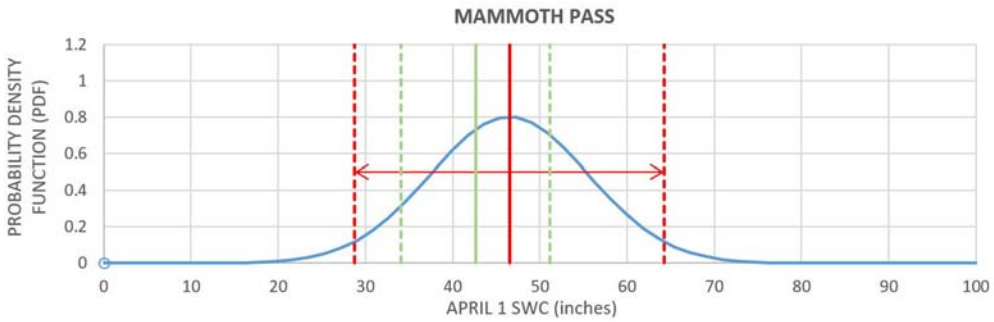

FIGURE 2 | Mammoth Pass April 1 SWC forecasts for year 2010 (red line). The red dashed lines indicate the 95% confidence interval, assuming the errors are normally distributed about the forecast value. The blue line is the Gaussian probability density function (PDF), with mean equal to the forecast value and standard error estimated from the 1951–2016 forecasts. The green line is the normal value (the average for 1966–2015), and the dashed green lines indicate the category boundaries defined by a 20% deviation from the normal value.

1 SWC value would fall into one of a pre-specified set of water year classes, using the categorical distribution (see for example Murphy, 2012). If there are K categories, the categorical distribution is parametrized by a K-vector $\theta = (\theta_1, \ldots, \theta_K)$ with entries summing to 1. θ_k gives the probability that an observation y falls into category k.

The Categorical model uses the VECM-forecast April 1 SWC value, x, as a predictor for θ via the regression

$$\theta_k = a_k + b_k \cdot x, \text{ for } k = 1, \ldots, K \tag{4}$$

The entries of θ are rescaled to sum to 1 via the softmax function:

$$\theta_k = \frac{\exp \theta_k}{\sum_i \exp \theta_i} \tag{5}$$

Parameter Fitting

Using Bayesian inference, the model parameters (a_k, b_k) are fit with Markov Chain Monte Carlo (MCMC) to draw samples from the model posterior distribution. All years were used in the model fitting. The following prior distributions were used:

$$\begin{cases} a_k \sim N(0, 5) \\ b_k \sim N(0, 1) \end{cases} \tag{6}$$

RESULTS AND MODEL EVALUATION BASED ON HINDCASTS

VECM Model

Model Verification

Parameter fitting was described in methods section Parameter fitting. For model verification, 10 years (2007–2016) were excluded from parameter fitting, to be used for model verification. This 10-year period includes a few wet and some very dry years, thus offering a range of different conditions for verification. In Figures S-10, S-12, S-14, and S-16, the cumulative time series of predictand and predictor variables are plotted (top panel) and the p-value on the top left corner tests the rejection of the null hypothesis that no cointegration is present in the vector time series via the Phillips-Ouliaris-Hansen test (Phillips and Ouliaris, 1990; Hamilton, 1994). The p-values are low for all the stations, indicating that the presence of cointegration cannot be rejected. Figures S-11, S-13, S-15, and S-17 show the observed (black) and VECM-model predicted April 1 SWC (green for the calibration period, 1951–2006, and blue for the verification period, 2007–2016), with the cumulative values on the top panels, and the regular values on the bottom panels. Examination of these figures indicates that the forecasts of the last 10 years have similar deviations from the observations as do those of the years used in parameter fitting.

Final Model Parameters

For the final model parameters, we repeated the parameter fitting, this time including all available years, 1948–2016. The results for Mammoth Pass are displayed in **Figure 3**. Results for all snow stations are shown in Figures S-18 to S-25.

VECM Model Performance Evaluation Using Hindcasts for 1951–2016

The VECM model is evaluated in this section using hindcasts for the period from 1951 through 2016. Because each forecast relies on data from the preceding three years (we have $p = 3$ in Equation (1) and the record starts in 1948, the first possible forecast is for 1951.

Observations are plotted against forecasts in **Figure 4**. Values of the coefficient of determination, R^2, are reported on each figure panel and in **Table 1**. Dashed lines have been added to each panel of **Figure 4** to indicate the 95% confidence interval. Confidence intervals were calculated based on the assumption that the forecasts' deviations from the observations are normally distributed, and characterized by the standard error calculated by comparing forecasted and observed values for all years (1951–2016) (Table S-1).

By definition of 95% confidence interval, 5% of the points (i.e., 1 in 20 points) are expected to fall outside the interval in a large sample of points. Here, the sample size of 66 years (1951–2016)

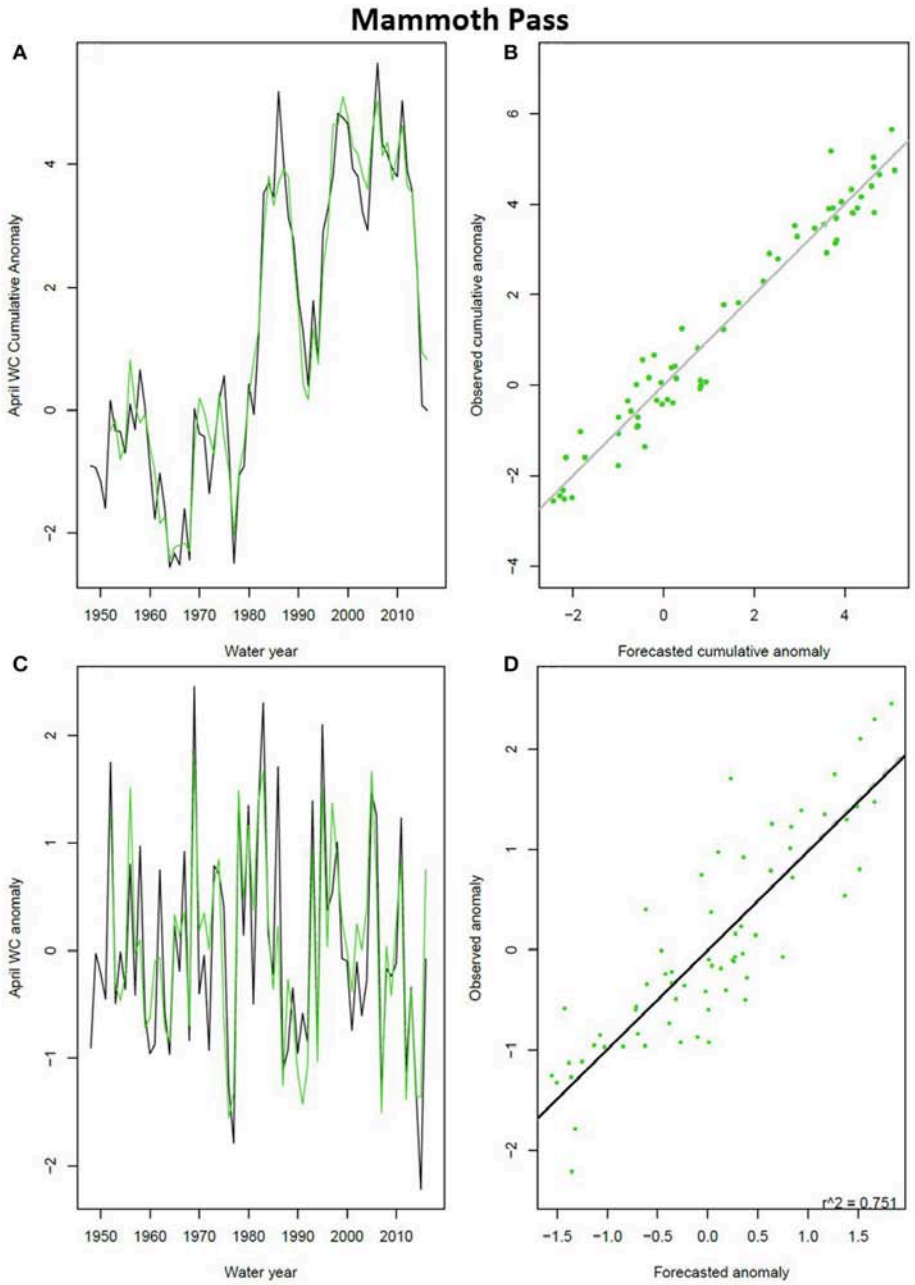

FIGURE 3 | VECM model predictions for Mammoth Pass, using the final parameters. **(A)** Cumulative April 1 SWC anomalies; **(B)** Scatter plot of the data in panel A; **(C,D)** As in panels **(A,B)** but for the anomalies (not cumulative). Time series lines in black are observed data. Green lines and points indicate VECM model forecasts (1951–2016).

is relatively small, so we expect the number of points outside the 95% confidence interval to be in the vicinity of 3.3. The number of points lying outside the 95% confidence interval bounds in **Figure 4** is indeed in the vicinity of 3.3: 2 points for Mammoth Pass, 4 points for Rock Creek #2, 3 points for Sawmill, and 6 points for Cottonwood #1.

LADWP defines the normal SWC value at each site as the average of 50 recent years. The 50-year range is updated every 5 years. At the time of writing this manuscript, the 50-year period used by LADWP is 1966–2015, and the normal values are the following:

$$\textit{Normal values}: \begin{cases} \text{Mammoth Pass}: & 42.64 \text{ in} \\ \text{Rock Creek \#2}: & 10.19 \text{ in} \\ \text{Sawmill}: & 19.33 \text{ in} \\ \text{Cottonwood \#1}: & 12.54 \text{ in} \end{cases}$$

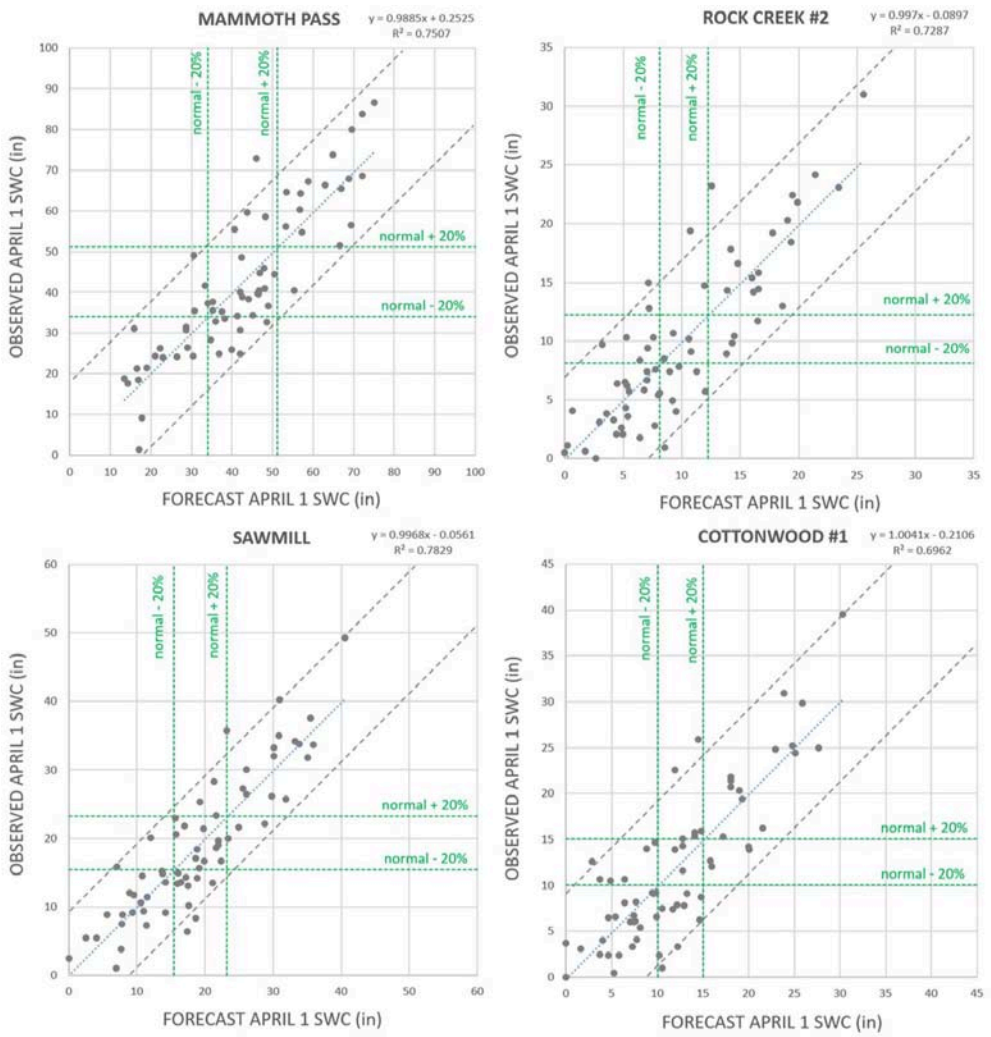

FIGURE 4 | Observed April 1 SWC each year in 1951–2016 plotted against the model's forecast value, for the four Owens Valley sites. Dashed gray lines indicate the 95% confidence interval. Dashed green lines indicate a 20% deviation from the normal value, separating between the categories dry, normal, and wet.

Of special importance to LADWP is an April 1 SWC forecast in the form of three categories:

April 1 SWC Categories:

- Dry : Less than 80% of the normal value
- Normal : Within 20% of the normal value
- Wet : More than 120% of the normal value

The observed frequency of these categories in the 66 years of record are: For Mammoth Pass, 24 dry, 22 normal, and 20 wet years; for Rock Creek #2, 32 dry, 13 normal, and 21 wet years; for Sawmill, 30 dry, 17 normal, and 19 wet years; and for Cottonwood #1, 33 dry, 13 normal, and 20 wet years.

Figure 4 and Table S-2 compares the forecast and observed value of April 1 SWC for each year, and also allows comparison of the forecast category and the observed category (dry, average, or wet). The number of years, from the total of 66 years, which were forecast in the wrong category, is given in **Table 1**. For Mammoth Pass, which is the most important station for LADWP, given its much larger snowpack, 50 of the 66 years (or 76%) had VECM model forecasts in the same category as observed. The remaining 16 years were misclassified in an adjacent category. For Mammoth Pass, Sawmill, and Cottonwood #1, there were no instances where the forecast value was in the category opposite the observed one, i.e., no dry year was forecast to be wet, and no wet year was forecast to be dry. For Rock Creek #2, there were two instances of opposite-category classifications. In both cases, the forecast was in the dry category, but the observation was in the wet category.

There is considerable agreement between observed categories across the four stations, and though there are several instances where a normal year at one station was dry or wet at another station, there are no instances where one station was dry and another wet in the same year, i.e., opposite categories were not observed across stations. The same is true of the VECM model

TABLE 1 | Measures of VECM model April 1 SWC forecast performance.

	Mammoth pass	Rock creek #2	Sawmill	Cottonwood #1
R^2 in **Figure 4**	0.751	0.729	0.783	0.696
No. of 10 wettest years misclassified	1[c]	1[c]	0	0
No. of 10 driest years misclassified	0	0	0	0
No. of opposite-category classifications[a]	0	2	0	0
No. of category misclassifications[b]	16	20	18	26
No. years over-predicted / No. under-predicted	34/32	36/30	35/31	35/31
Ave. deviation for over-predictions *(in)*	7.40	2.64	3.68	3.43
Ave. deviation for under-predictions *(in)*	−7.38	−2.90	−3.91	−3.77
Max. deviation for over-predictions *(in)*	17.06	7.64	11.09	9.51
Max. deviation for under-predictions *(in)*	−26.95	−10.63	−12.47	−11.42

[a]*An "opposite-category classification" is a dry year forecast to be wet, or a wet year forecast to be dry.*
[b]*A "category misclassification" is a year whose forecast value falls in a different category than observed (including adjacent and opposite categories).*
[c]*Year 1986 was forecast to be "normal" but turned out to be one of the 10 wettest years.*

predictions: in no year was one station predicted to be wet while another station was predicted to be dry. This can be seen in Figure S-26.

Additional measures of the VECM model performance are listed in **Table 1**. There is no evidence for model bias toward either over-predicting or under-predicting. For Mammoth Pass, the number of over-predicted years, 34, is close to the number of under-predicted years, 32; the average deviation of forecasts to observations is ∼ 0 (0.24 in), showing that positive and negative deviations approximately cancel each other out; and the slope of the regression line is ∼1.0. For the 34 over-predicted years, the average difference between forecast and observed values is 7.40 in, while for the 32 under-predicted years it is −7.38 in. The largest deviation is 17.06 in for the over-predicted years, and −26.95 in for the under-predicted years.

The year with the largest under-prediction for Mammoth Pass was 1986, where the forecast was for 45.9 in (108% of normal) and the observation was 72.9 in (171% of normal). The year with the largest over-prediction was 2015, where the forecast was for 17.1 in (40% of normal) and the observation was 1.4 in (3% of normal). This was a year when snowmelt occurred earlier than usual, depleting the snowpack before April 1.

Comparison Against Hindcasts Based on February 1 SWC Linear Regression

This section compares the VECM model performance in forecasting April 1 SWC against the results achieved using the historical linear regression equation relating observed April 1 SWC to February 1 SWC based on 1948–2016 observations for each station. The February linear regression method was available prior to this study, and represents a baseline against which the VECM model forecasting skill can be compared.

Skill forecasting the April 1 SWC value

The VECM model was more successful than the February linear regression, when comparing between **Table 2** and **Table 1** (and between Figures S-29 and S-27). For Mammoth Pass, the coefficient of determination (R^2) is 0.751 for the VECM model and 0.630 for the February linear regression. The forecast errors of the February linear regression, i.e., the differences between the forecast value and the observation on the same year, have higher average values and larger maximum values (positive and negative), compared to the VECM model. See also Figures S-28 and S-30.

Skill forecasting the April 1 SWC category (dry, normal, or wet)

The VECM model had no instances (for any station) where one of the 10 driest years was misclassified, while the February linear regression had one such instance for each station except Mammoth Pass (**Table 2**). The VECM model had one instance (for Mammoth Pass and Rock Creek #2) where a top 10 wettest year was misclassified (**Table 1**), while the February linear regression had one such instance for Mammoth Pass and Sawmill, two instances for Rock Creek #2 and three instances for Cottonwood #1 (**Table 2**). The VECM model had no instances of a top 10 dry year being misclassified (**Table 1**), while the February linear regression had one such instance for Rock Creek #2, Sawmill and Cottonwood #1 (**Table 2**).

Evaluation of the Categorical Model Results Using Hindcasts for 1951–2016

Given the probabilistic nature of the Categorical Model, it is expected that the observed April 1 SWC will often fall into a category (dry, normal, or wet) other than the one to which the model attributed the highest probability of the three. The observed April 1 SWC is expected to most often fall into the category assigned the highest probability, but to also often fall into the category assigned the second-highest probability, and occasionally to fall into the category assigned the lowest probability.

A rigorous evaluation of the Categorical Model's performance would require a much larger sample than the available 66 years (1951–2016). The available 66 years however does allow an approximate evaluation through the qualitative examination of **Figure 5**, where the probability assigned to category "wet" (p_w) is plotted against the probability assigned to "dry" (p_d). Each point

TABLE 2 | Performance measures for forecasts based on the February linear regression equations.

	Mammoth pass	Rock creek #2	Sawmill	Cottonwood #1
R^2	0.631	0.589	0.675	0.559
No. of 10 wettest years misclassified	1	2	1	3
No. of 10 driest years misclassified	0	1	1	1
No. of opposite-category classifications[a]	0	1	1	2
No. of category misclassifications[b]	16	23	21	26
No. years over-predicted / No. under-predicted	34/32	38/28	38/28	38/28
Ave. deviation for over-predictions *(in)*	8.54	3.05	4.09	3.84
Ave. deviation for under-predictions *(in)*	−8.89	−3.87	−5.51	−5.29
Max. deviation for over-predictions *(in)*	24.93	9.54	11.75	12.10
Max. deviation for under-predictions *(in)*	−32.61	−14.65	−17.29	−16.23

Compare against ***Table 1****, for the VECM model.*

[a]*An "opposite-category classification" is a dry year forecast to be wet, or a wet year forecast to be dry.*

[b]*A "category misclassification" is a year whose forecast value falls in a different category than observed (including adjacent and opposite-category classifications).*

represents a year between 1951 and 2016. Given $p_w + p_d + p_n = 1$, rearranging that equation we can write $p_n = 1–(p_w + p_d)$, which gives the probability assigned to category "normal" (p_n) is a function of the probabilities plotted in **Figure 5**. The graph area labeled "most likely wet" corresponds to p_w being larger than either p_d or p_n; "most likely dry" corresponds to $p_d > p_w, p_n$; and "most likely normal" corresponds to $p_n > p_w, p_d$.

In **Figure 5**, the actual observed category each year is indicated by the color of the point, keyed in the figure legend. The distribution of colors appears consistent with the probabilities, with most wet years having been attributed a high probability of being wet, and most dry years having been attributed a high probability of being dry. Because the model provides probabilities rather than predicted values, none of the outcomes represent model failures.

The Categorical Model is designed specifically for assigning probabilities to each of the three categories, not to provide a forecast. If it were used to forecast the category directly, this model would do somewhat less well than the VECM model, especially because of a larger number of opposite-category forecasts (i.e., wet years forecast to be dry, and dry years forecast to be wet) in the period 1951–2016. Therefore, the VECM model forecast April 1 SWC value should be used to forecast the category, and the Categorical Model should be used to evaluate the uncertainty pertaining to the category.

Example: The Probabilities Calculated for 2010

As an example, **Figure 6** displays the probabilities determined by the Categorical Model for 2010. The observed SWC values on April 1, 2010, fell into the normal category for all four stations. Even though in the case of Rock Creek #2 and Cottonwood #1 the normal category did not have the highest of the three probabilities (the wet category was assigned higher probability), it nevertheless had considerable probability values: 25.2% for Rock Creek #2, and 9.6% for Cottonwood #1.

FORECASTS FOR 2017 AND 2018

The VECM model and the Categorical model were parameterized using observations for 1948-2016 (section Methods). The models were completed and delivered to LADWP in January of 2017. Since then, the model has been used to forecast April 1 snow water content (SWC) in 2017 and 2018. These were actual forecasts as opposed to hindcasts. The forecast April 1 SWC is compared against the observed value in **Figure 7**. The red dots represent 2017 and the orange dots represent 2018. Gray dots are hindcasts for 1951–2016 and were previously shown in **Figure 4**.

Year 2017 had among the largest snowpack of the period plotted, especially at the most important station, Mammoth Pass. On February 1, the observed SWC was already almost double the normal (i.e., average) value for that date at Mammoth Pass and Sawmill, and more than triple the normal value at Rock Creek #2 and Cottonwood #1. By April 1, the observed SWC was about double the normal value for that date at Mammoth Pass and Sawmill, and about 2.5 times the normal at Rock Creek #2 and Cottonwood #1. The VECM model provided April 1 SWC forecasts that were mildly over-estimated for Mammoth Pass and Sawmill, and slightly under-estimated for Rock Creek #2 and Cottonwood #1 (**Figure 7**). The Categorical model correctly identified "wet" (i.e., more than 20% above the normal value) as the most likely category for April 1 SWC at all four stations.

Year 2018 was a more complex year, representing a good test case. SWC was very low on February 1 but, thanks to late-season storms in February and March, it reached near-normal values on April 1. The VECM model correctly forecast these near-normal values. For example, on February 1, the SWC at Rock Creek #2 was at 10% of the normal value for that date; but on April 1 had reached 40% of the normal value for that date. The VECM model correctly forecast the substantial SWC increase that occurred in February and March, producing approximate forecasts for the four stations (**Figure 7**). The Categorical model correctly identified "dry" (i.e., more than 20% below the normal value) as the most likely category for April 1 SWC at all four stations, with "normal" also having reasonable probability. For example, at Mammoth Pass, the probability of "dry" was 77.9% and the probability of "normal" was 21.9%. The observed April 1 SWC was "dry" but near "normal."

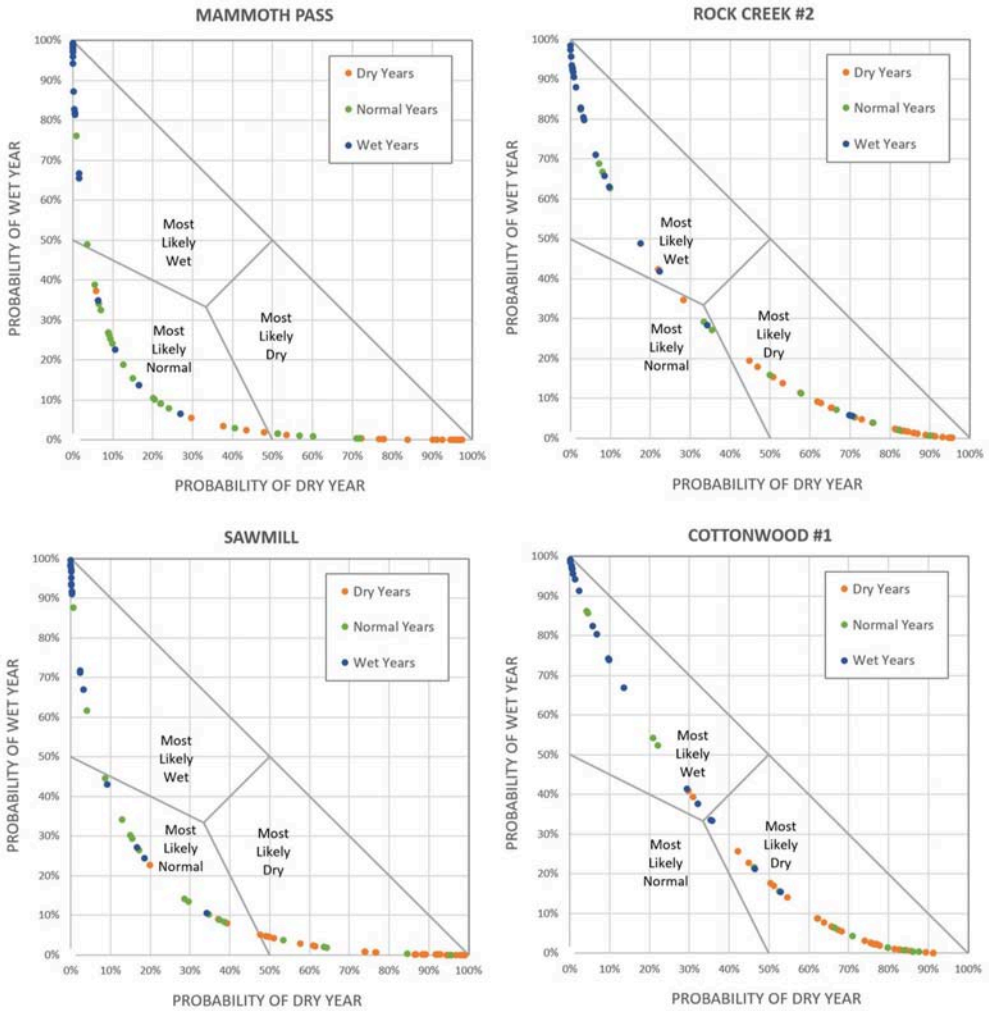

FIGURE 5 | Probability assigned to categories "dry" (x axis) and "wet" (y axis) each year in 1951–2016. The actual observed category each year is indicated in color, according to the legend. The distribution of colors appears consistent with the probabilities.

CONCLUSIONS

The VECM model developed and tested in this study has proven to have considerable skill forecasting Owens Valley April 1 SWC in early February. Its performance in hindcasts (1951-2016) was shown to surpass the skill of the pre-existing alternative, which consisted of using a linear regression to forecast April 1 SWC based on the observed February 1 SWC. The VECM model's performance was clearly superior to the February linear regression on every measure, including a higher coefficient of determination (R^2), smaller average and maximum errors (defined as the forecast value minus observed value), fewer misclassifications of years, defined as a year when the forecast and observed April 1 SWC are not in the same category (dry, normal, or wet), and fewer severe misclassifications of years (i.e., years forecast to be in the category opposite the observed one, especially when those were extreme years such as among the 10 wettest or 10 driest).

As a complement to the VECM model, the Categorical Model was developed to express forecast uncertainty by estimating the probability that April 1 SWC would fall into each of the three categories—dry, normal, and wet. While the sample size of the hindcast (66 years: 1951-2016) is too small for rigorous testing of the Categorical Model, the probabilities it produced for these hindcast years appear consistent with the observations. The VECM model forecast April 1 SWC value should be used to also forecast the category, and the Categorical Model should be used to evaluate the uncertainty pertaining to the category.

Since the model was completed, using 1948-2016 observations, it model has been used to forecast April 1 snow water content (SWC) in 2017 and 2018. These were actual forecasts as opposed to hindcasts. The 2017 and 2018 forecasts were compared against the observed April 1 SWC values, showing to have been successful and having deviated no more from observations than most years in the hindcast period. The Categorical model also attributed the highest probability

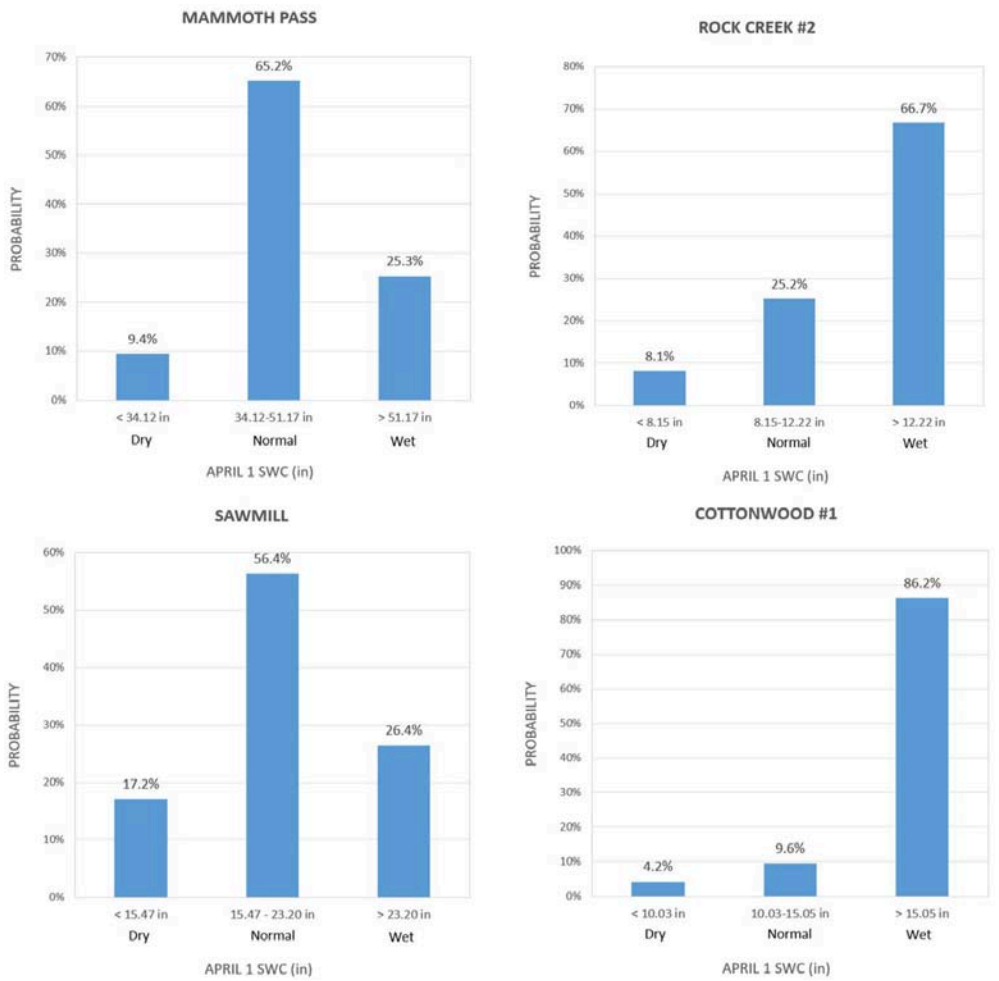

FIGURE 6 | Probability of April 1 SWC falling into each of the categories – dry, normal, or wet – issued by the Categorical Model for 2010.

to the category that was observed on April 1. The 2017 was an exceptionally wet year, and 2018 was overall a dry year but which received late-season storms in February and March. The successful forecast in both 2017 and 2018 adds confidence in the VECM model and the Categorical model.

While the VECM model was shown to provide considerable forecast skill for April 1 SWC, there is significant uncertainty associated with its forecast in any individual year. This is the case with any meteorological or hydrological forecast model. Model uncertainty was clearly characterized in this report using hindcasts. Future forecasts may incur smaller or larger errors than those seen in the hindcasts or the two forecast years of 2017 and 2018. Forecast uncertainty must therefore be taken into account by LADWP in its decision making.

WIDER SIGNIFICANCE OF THIS WORK, AND FUTURE RESEARCH

Many water supply reservoirs in California capture snowmelt in spring for supply later in summer. Under current operations, some reservoir storage is set aside for future floods over the course of the wet season—the flood control volume varying by month—and excess runoff is released downstream (e.g., Willis et al., 2011). The statistical tool presented in this work, relating NPH anomaly to precipitation or snowpack indices, can be applied to other California watersheds, where it may allow reservoir operators additional insight, on a year-to-year basis, on whether some of the flood storage could be utilized for water supply storage. This additional insight could be of great value in coming decades, where operators must make the most from a potentially more variable precipitation season, as well as declining snowpack due to higher temperatures and a partial shift from snowfall to rainfall, and greater peaks in runoff in wet years (Fissekis, 2008; Brekke et al., 2009; Hanak and Lund, 2012).

The forecasting tool presented in this paper allows issuing forecasts in early February for the remainder of the wet season, i.e., through April 1. The tool is based on the sea-level pressure anomaly at the climatological location of the NPH measured in mid-January.

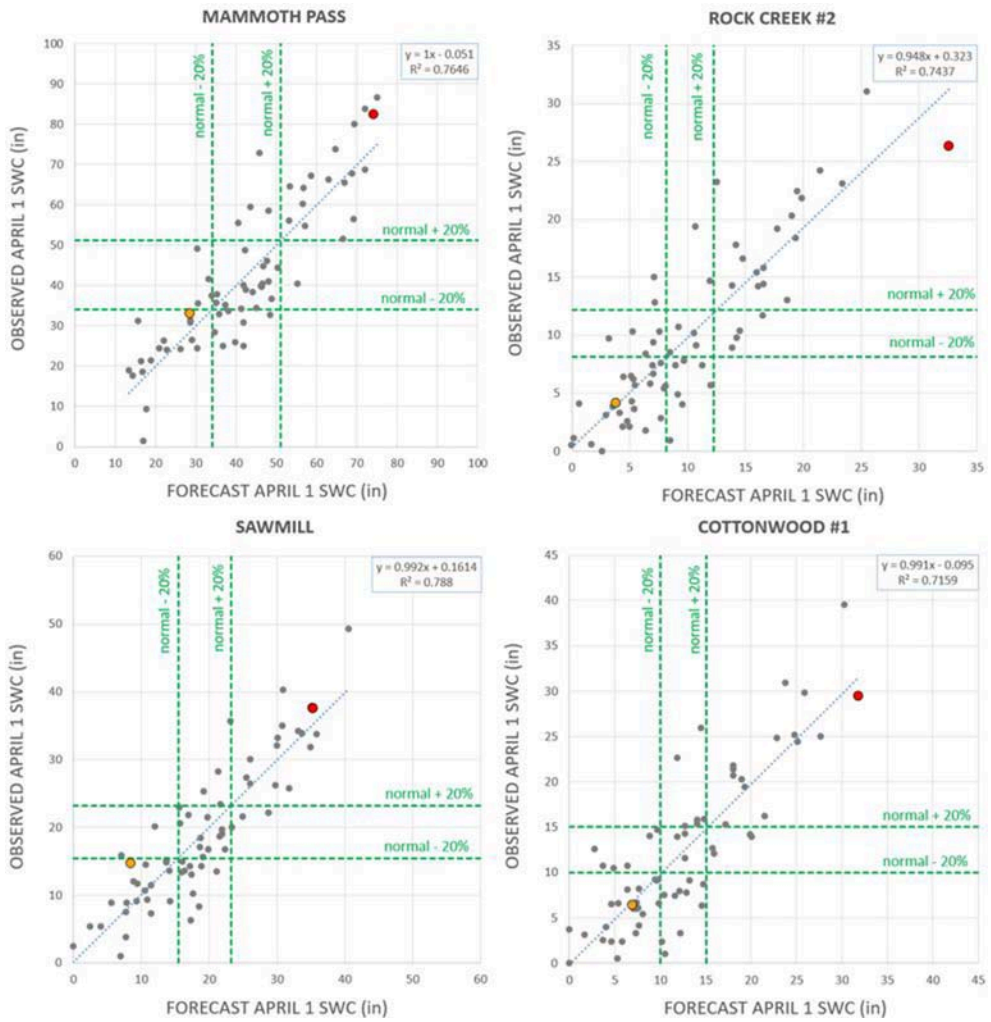

FIGURE 7 | Forecast for years 2017 (red) and 2018 (orange) plotted against the respective observations, for the four Owens Valley sites. The gray points represent 1951–2016 hindcasts, previously shown in **Figure 4**.

The forecast lead time may potentially be increased if the mid-January NPH sea level pressure anomaly can be accurately forecasted, whether by statistical or dynamical models. The NPH exhibits a closer relationship with precipitation throughout California compared to the ENSO indices (see Costa-Cabral et al., 2016). This may be because, in addition to tropical forcing, the NPH also receives influence from internal midlatitude variability. However, the question remains whether this internal midlatitude variability may or may not be forecastable.

This work demonstrates that advancements in forecasts of NPH are expected to have significant benefits for water resources, agriculture, energy, insurance, drought preparedness, and flood risk management in California. We hope that future research will investigate the present ability of the different models in the North American Multi-Model Ensemble (NMME; Kirtman et al., 2014) suite [which includes NOAA's National Weather Service Climate Forecast System, version 2 (CFSv2; Saha et al., 2014)] to anticipate the NPH anomaly in mid-January at different lead times.

This work may also contain important hints for future research by climate scientists. The cointegrated relationship identified means that the principal relationship between these 2 variables (NPH anomalies and California precipitation) is between their integrals. This suggests that the climate processes involved have characteristics analogous to reservoirs, which are integrals of stochastic inputs and outputs. This line of thinking, if further explored, might bear fruit in understanding the low-frequency variability in climate, such as decadal variability. Precipitation depends on ocean surface temperatures (SST) at different locations. Temperature measures heat content, a reservoir type variable which may be at the origin of cointegrated relationships between climatic variables.

AUTHOR CONTRIBUTIONS

MC-C led this study and had the idea of using cointegration as the basis for the forecasting model; JR suggested the VECM

model and the categorical model mathematical frameworks, fitted the model parameters, and encoded these models in Excel for operational use; MC-C conducted the hindcasts and model evaluation, and respective graphics, and wrote most of the text of this manuscript.

ACKNOWLEDGMENTS

This work was commissioned and funded by the Los Angeles Department of Water and Power (LADWP). We thank LADWP for the opportunity of developing this forecasting approach and applying it to the Owens Valley watershed. Sujoy B. Roy provided comments that improved the quality of this manuscript, and his contribution is gratefully acknowledged. Two reviews contributed to clarity and a more expanded discussion in this paper, and are gratefully acknowledged. The preparation of this manuscript was funded by the employers of the two authors, Northwest Hydraulic Consultants Inc, and Tetra Tech Inc.

SUPPLEMENTARY MATERIAL

The Supplementary Material for this article can be found online at: https://www.frontiersin.org/articles/10.3389/feart.2018.00054/full#supplementary-material

REFERENCES

Brekke, L. D., Maurer, E. P., Anderson, J. D., Dettinger, M. D., Townsley, E. S., Harrison, A., et al. (2009). Assessing reservoir operations risk under climate change. *Water Resour. Res.* 45:W04411. doi: 10.1029/2008WR006941

Bosilovich, M., Chen, J., Robertson, F. R., and Adler, R. F. (2008). Evaluation of global precipitation in reanalyses. *J. Appl. Meteor. Climatol.* 47, 2279–2299. doi: 10.1175/2008JAMC1921.1

Chikamoto, Y., Timmermann, A., Luo, J. J., Mochizuki, T., Kimoto, M., Watanabe, M., et al. (2015). Skilful multi-year predictions of tropical trans-basin climate variability. *Nat. Commun.* 6:6869.doi: 10.1038/ncomms7869

Costa-Cabral, M., Rath, J. S., Mills, W. B., Roy, S. B., Bromirski, P. D., and Milesi, C. (2016). Projecting and forecasting winter precipitation extremes and meteorological drought in California using the North Pacific High sea-level pressure anomaly. *J Clim*. 29, 5009–5026. doi: 10.1175/JCLI-D-15-0525.1

Costa-Cabral, M., Roy, S. B., Maurer, E. P., Mills, W. B., and Chen, L. (2012). Snowpack and runoff response to climate change in owens valley and mono lake watersheds. *Clim. Change* 116, 97–109. doi: 10.1007/s10584-012-0529-y

Engle, R. F., and Granger, C. W. J. (1987). Co-integration and error correction: representation, estimation and testing. *Econometrica* 55, 251–276.

Fernando, D. N., Fu, R., Solis, R. S., Mace, R. E., Sun, Y., Yang, B., et al. (2015). *Early Warning of Summer Drought Over Texas and the South Central United States: Spring Conditions as a Harbinger of Summer Drought*. Technical Note 15-02, Texas Water Development Board.

Fissekis, A. (2008). *Climate Change Effects on the Sacramento Basin's Flood Control Projects*. M. S. thesis, Department of Civil and Environmental Engineering, University of California, Davis, CA, 150 pp.

Guirguis, J., and Avissar, R. (2008). An analysis of precipitation variability, persistence, and observational data uncertainty in the western United States. *J. Hydrometeor*. 9, 843–865, doi: 10.1175/2008JHM972.1

Hamilton, J. D. (1994). *Time Series Analysis*. Princeton, NJ: Princeton University Press.

Hanak, E., and Lund, J. R. (2012). Adapting California's water management to climate change. *Clim. Change* 111, 17–44. doi: 10.1007/s10584-011-0241-3

Janowiak, J., Gruber, A., Kondragunta, C. R., Livezey, R. E., and Huffman, G. J. (1998). A comparison of the NCEP–NCAR reanalysis precipitation and the GPCP rain gauge–satellite combined dataset with observational error considerations. *Clim. J.* 11, 2960–2979. doi: 10.1175/1520-0442(1998)011<2960:ACOTNN>2.0.CO;2

Johansen, S. (1995). *Likelihood-based Inference in Cointegrated Vector Autoregressive Models*. Oxford, UK: Oxford University Press.

Kalnay, E., Kanamitsu, M., Kistler, R., Collins, W., Deaven, D., Gandin, L., et al. (1996). The NCEP/NCAR 40-year reanalysis project. *Bull. Amer. Meteor. Soc.* 77, 437–471. doi: 10.1175/1520-0477(1996)077<0437:TNYRP>2.0.CO;2

Kharin, V. V., Zwiers, F. W., Zhang, X., Hegerl, G., and Wehne, M. (2013). Changes in temperature and precipitation extremes in the CMIP5 ensemble. *Clim. Change* 119, 345–357. doi: 10.1007/s10584-013-0705-8

Kirtman, B. P., Min, D., Infanti, J. M. (2014). The North American multimodel ensemble. phase-i seasonal-to-interannual prediction; phase-ii toward developing intraseasonal prediction. *Bull. Amer. Meteor. Soc.* 95, 585–601. doi: 10.1175/BAMS-D-12-00050.1

Mantua, N. H., Hare, S. R., Zhang, Y., Wallace, J. M., and Francis, R. C. (1997). A Pacific interdecadal climate oscillation with impacts on salmon production. *Bull. Amer. Meteor. Soc*. 78, 1069–1079. doi: 10.1175/1520-0477(1997)078<1069:APICOW>2.0.CO;2

Murphy, J. P. (2012). *Machine Learning: a Probabilistic Perspective*. Cambridge, MA: MIT press.

Pandey, G. R., Cayan, D. R., and Georgakakos, K. P. (1999). Precipitation structure in the Sierra Nevada of California during winter. *J. Geophys. Res.* 104, 12019–12030. doi: 10.1029/1999JD900103

Phillips, P. C. B., and Ouliaris, S. (1990). Asymptotic properties of residual based tests for cointegration. *Econometrica J. Econometric Soc.* 58, 165–193. doi: 10.2307/2938339

Saha, S., Moorthi, S., Wu, X., Wang, J., Nadiga, S., Tripp, P., et al. (2014). The NCEP climate forecast system version 2. *Clim. J.* 27, 2185–2208. doi: 10.1175/JCLI-D-12-00823.1

Stevenson, S., Timmermann, A., Chikamoto, Y., Langford, S., and DiNezio, P. (2015). Stochastically generated North American megadroughts. *J Climate*, 28, 1865–1880. doi: 10.1175/JCLI-D-13-00689.1

Swain, D. L., Tsiang, M., Haugen, M., Singh, D., Charland, A., Rajaratnam, B., et al. (2014). Explaining extreme events of 2013 from a climate perspective.. *Bull. Amer. Meteor. Soc.* 95, S1–S104. doi: 10.1175/1520-0477-95.9.S1.1

Wang, S.-Y., Hipps, L., Gillies, R. R., and and, J.-,Yoon, H. (2014). Probable causes of the abnormal ridge accompanying the 2013-2014 California drought: ENSO precursor and anthropogenic warming footprint. *Geophys. Res. Lett*. 41, 3220–3226. doi: 10.1002/2014GL059748

Wang, S.-Y., Huang, W.-R., and Yoon, J.-H. (2015). The North American winter 'dipole' and extremes activity: a CMIP5 assessment. *Atmos. Sci. Lett.* 16, 338–345. doi: 10.1002/asl2.565

Willis, A. D., Lund, J. R., Townsley, E. S., and Faber, B. A. (2011). Climate change and food operations in the Sacramento Basin, California. *San Francisco Estuary Watershed Sci.* 9, 1–18, doi: 10.15447/sfews.2011v9iss2art3

Zhang, U., Wallace, J. M., and Battisti, D. S. (1997). ENSO-like interdecadal variability: 1900–93. *Clim. J.* 10, 1004–1020. doi: 10.1175/1520-0442(1997)010<1004:ELIV>2.0.CO;2

Conflict of Interest Statement: The authors declare that the research was conducted in the absence of any commercial or financial relationships that could be construed as a potential conflict of interest.

frontiers in Environmental Science

ORIGINAL RESEARCH
published: 20 November 2018
doi: 10.3389/fenvs.2018.00123

Sensitivity of European Temperature to Albedo Parameterization in the Regional Climate Model COSMO-CLM Linked to Extreme Land Use Changes

Merja H. Tölle[1]*, *Marcus Breil*[2], *Kai Radtke*[3] and *Hans-Jürgen Panitz*[2]

[1] Department of Geography, Climatology, Climate Dynamics and Climate Change, Justus-Liebig University Giessen, Giessen, Germany, [2] Institute of Meteorology and Climate Research–Troposphere Research, Karlsruhe Institute of Technology, Eggenstein-Leopoldshafen, Germany, [3] Chair of Environmental Meteorology, Brandenburg University of Technology, Cottbus-Senftenberg, Senftenberg, Germany

OPEN ACCESS

Edited by:
Izuru Takayabu, Meteorological Research Institute (MRI), Japan

Reviewed by:
Asuka Suzuki-Parker, Rissho University, Japan
Tomonori Sato, Hokkaido University, Japan

***Correspondence:**
Merja H. Tölle
merja.toelle@geogr.uni-giessen.de

Specialty section:
This article was submitted to Atmospheric Science, a section of the journal Frontiers in Environmental Science

Received: *09 July 2018*
Accepted: *28 September 2018*
Published: *20 November 2018*

Citation:
Tölle MH, Breil M, Radtke K and Panitz H-J (2018) Sensitivity of European Temperature to Albedo Parameterization in the Regional Climate Model COSMO-CLM Linked to Extreme Land Use Changes. Front. Environ. Sci. 6:123. doi: 10.3389/fenvs.2018.00123

Previous studies based on observations and models are uncertain about the biophysical impact of af- and deforestation in the northern hemisphere mid-latitude summers, and show either a cooling or warming. The spatial distribution, magnitude and direction are still uncertain. In this study, the effect of three different albedo parameterizations in the regional climate model COSMO-CLM (v5.09) is examined performing idealized experiments at 0.44° horizontal resolution across the EURO-CORDEX domain during 1986–2015. De- and af-forestation simulations are compared to a simulation with no land cover change. Emphasis is put on the impact of changes in radiation and turbulent fluxes. A clear latitudinal pattern is found, which results partly due to the strong land cover conversion from forest- to grassland in the high latitudes and open land to forest conversion in mid-latitudes. Afforestation warms the climate in winter, and strongest in mid-latitudes. Results are indifferent in summer owing to opposing albedo and evapotranspiration effects of comparable size but different sign. Thus, the net effect is small for summer. Depending on the albedo parameterization in the model, the temperature effect can turn from cooling to warming in mid-latitude summers. The summer warming due to deforestation to grassland is up to 3°C higher than due to afforestation. The cooling by grass or warming by forest is in magnitude comparable and small in winter. The strength of the described near-surface temperature changes depends on the magnitude of the individual biophysical changes in the specific background climate conditions of the region. Thus, the albedo parameterization need to account for different vegetation types. Furthermore, we found that, depending on the region, the land cover change effect is more important than the model uncertainty due to albedo parameterization. This is important information for model development.

Keywords: land cover change, biophysical effect, albedo parameterization, evapotranspiration, regional climate model, climate, de-/afforestation, surface energy balance

INTRODUCTION

Future strategies for climate change mitigation envision extensive afforestation to stabilize temperature rise due to their role in the global carbon cycle (Popp et al., 2017). A change in forest cover has widespread consequences to the society, economy, and ecology influencing climate and air quality. Forest cover changes exert strong influences on the energy and water balance by modifying the solar and long wave radiation, and atmospheric turbulence. This results in alterations in the fluxes of momentum, heat, water vapor, and CO_2 as well as other trace gases, and both anorganic and biogenic aerosols including dust between vegetation, soils, and the atmosphere (Pielke et al., 2011).

In terms of biogeophysical modulations of forest cover change, a major change occurs to the net radiation due to albedo alterations. Depending on the physiological control of the vegetation connected with the environmental conditions in the atmosphere and soil, this net radiation is partitioned between the turbulent fluxes (sensible and latent heat). The amount of energy transferred to the atmosphere depends on the changes in the aerodynamic roughness of the land surface, and ultimately influences the atmospheric boundary layer and climate. Forests have a lower surface albedo, and higher evapotranspiration compared to open lands (Lee et al., 2011; Swann et al., 2012). The outcome of the competition between albedo warming and evapotranspiration cooling, and the specific background climate exerts the climate of the region (Duveiller et al., 2018). The strength of both effects, thus the direction of change, depend on the type of change, and on the interactions with soil conditions (Pielke et al., 2011). As a result, landscape changes due to forests affect the regional/local near-surface air temperature patterns (Tölle et al., 2014), and can be different for mean vs. extreme quantities (Alkama and Cescatti, 2016).

The consequences due to land use changes between latitudes and regions are discussed controversial in the literature based on modeling and observational studies. There are still major uncertainties regarding climate responses in climate models to past land cover changes (Pitman et al., 2009). Not only the magnitude, but also the sign of the land conversion on temperature varies between models on regional and global scales. The impact due to forest cover changes may vary regionally and with latitude based on observation and modeling studies (Davin and de Noble-Ducoudré, 2010; Lee et al., 2011; Li et al., 2015). Increases in near-surface temperature were found due to large-scale deforestation in the tropics (Snyder et al., 2004), whereas a decrease in temperature in the mid- and high-latitudes was found (Li et al., 2016a). The warming in the tropics is explained by reduced evapotranspiration (Tölle et al., 2017). The albedo is increased in temperate and boreal regions leading to reduced shortwave radiation absorption in the cleared land, which explains the cooling there in summer (Cherubini et al., 2018). In addition, the reduction in the snow-masking effect enhance the cooling in the regions, where snow occurs in winter (Bonan et al., 1992). Others based on observational studies considered the impact of afforestation in the northern temperate regions as a weak cooling (Li et al., 2016b). In seasonal terms, Li et al. (2015) found that temperate forests exert a moderate cooling in summer season, in which vegetation is most active in terms of evapotranspiration, and moderate warming in winter. Tang et al. (2018) showed contradictory results based on remote sensing that afforestation warms northeastern Europe north of 45°N and leads to a cooling in other European regions. Thus, there are major uncertainties in mid-latitudes in the spatial distribution, magnitude and direction of climate response due to land cover changes (Alkama and Cescatti, 2016; Perugini et al., 2017).

A robust quantification of biogeophysical impact of land cover change on local and regional scale is hampered by the uncertainty of the different regional climate model responses of such changes. For this, a coordinated effort is formed by the EURO-CORDEX initiative LUCAS ("Land Use and Climate Across Scales") to benchmark the biogeophysical role of land use changes by various regional climate model and land surface model combinations using standard configurations. The effect of land cover change will be examined in detail with the LUCAS initiative over Europe. Extreme land use change scenarios help to estimate the maximal impact and elucidate processes. The work described here is part of LUCAS.

There is consensus in the scientific community about the impact of land cover change on climate in winter by the snow-masking effect in high latitudes (Bonan et al., 1992). Albeit debated is the spatial distribution, the magnitude and direction of this biogeophysical effect in summer. High uncertainties occur in mid and southern Europe, where the forest proportion is relatively small. Here, afforestation could have a potential high impact. The climatic extent of afforestation in these areas depends on the ratio between the increased net shortwave radiation and the increased aerodynamic roughness/evapotranspiration of forest. This proportion, however, strongly depends on the used regional climate model (RCM) and its model uncertainties. The question, whether these model uncertainties are higher than the potential impact of land cover change, has not yet been investigated. Therefore, we compare the regional climate response due to different albedo parameterizations in the state-of-the-art regional climate model COSMO-CLM (v5.09) with the impact of extreme land use change scenarios. The standard operational albedo configuration is considered in this study, and two modified versions of it. We quantify and compare the relative strength of seasonal and latitudinal biophysical effects from a surface energy balance perspective on the temperature response. Therefore, extreme (drastic) land use transitions are performed across the Euro-CORDEX domain at 0.44° horizontal resolution by converting the land cover to grass- or forestland. The land cover change experiments are compared to the control run with no land cover change. Simulations are carried out during 1986-2015, and the model is forced by ERA-Interim reanalysis data. Results are presented for the summer and the winter season over Europe in section 3, and the manuscript ends with a discussion and conclusion section.

MATERIALS AND METHODS

Model Description

The climate version COSMO-CLM of the state-of-the-art weather prediction model COSMO in its version 5.09 is used in this study (Rockel et al., 2008). It is a non-hydrostatic limited-area atmospheric model designed for applications for the meso-β to the meso-γ scale (Steppeler et al., 2003). The model describes compressible flow in a moist atmosphere, thereby relying on the primitive thermo-dynamical equations. These equations are solved numerically on a three-dimensional Arakawa-C grid (Arakawa and Lamb, 1977) based on rotated geographical coordinates and a generalized, terrain following height coordinate (Doms and Baldauf, 2015). The model applies a Runge-Kutta time-stepping scheme (Wicker and Skamarock, 2002). The parameterization of precipitation is based on a four-category microphysics scheme that includes cloud, rainwater, snow, and ice (Doms et al., 2011). The physical parameterizations include a radiative transfer scheme (Ritter and Geleyn, 1992), and a turbulent kinetic energy-based surface transfer and planetary boundary layer parameterization.

The lower boundary of COSMO-CLM is the soil-vegetation-atmosphere model TERRA-ML (Schrodin and Heise, 2002). It controls the surface energy and water balances at the land surface and in the ground based on first principles of conserving mass and energy. With that, it provides the surface temperature and humidity as lower boundary conditions for computing the energy and water fluxes between surface and atmosphere (Doms et al., 2011). Evapotranspiration includes bare soil evaporation, plant transpiration, evaporation from the interception storage, and the sublimation of snow. Stomatal conductance is Biosphere-Atmosphere Transfer Scheme (BATS)-based after Dickinson (1984). Radiation fluxes are based on grid scale albedo and temperature. COSMO-CLM requires the leaf area index as input and the vegetation albedo to compute the fraction of photosynthetically active radiation absorbed by vegetation to obtain transpiration. The soil temperature is calculated by the heat conduction equation. The soil hydrology is described by the Richards' equation, which is solved for the multi-layer soil column. It accounts for surface runoff and subsurface runoff when the layer is at field capacity. Ten unevenly spaced vertical soil layers with a total depth of 11.50 m are used. The lowest layer temperature acts as lower boundary condition of the heat conduction equation and is set to a climatological annual mean value. Five snow layers are used for snow calculations. TERRA-ML accounts for partial coverage of snow. Every surface grid is assigned to one single land cover type. Surface input data required for each grid cell include soil type and land cover type. Each vegetation type is assigned a set of time-invariant parameters: optical properties (albedo), morphological properties (roughness, leaf area index, plant coverage, root depth). The leaf area index and root depth follow a seasonal cycle.

Experiment Design

The regional climate model COSMO-CLM runs across the EURO-CORDEX domain at a resolution of 0.44° × 0.44° with 40 atmospheric levels for the period 1986 to 2015 with a spin-up starting at 1979 to achieve balanced soil temperatures and water contents. Hereby, the ERA-Interim reanalysis from the European Centre for Medium Range Weather Forecasts serves as initial and lateral boundary conditions and as the lower boundary over sea (Dee et al., 2011). The configuration is adapted from the EURO-CORDEX initiative (Kotlarski et al., 2014), where the model was evaluated. The time step is set to 300 s, and the convection scheme of Tiedtke is applied (Tiedtke, 1989). For all experiments the same lateral boundary conditions are used. The experiments impose an idealized change to the distribution of trees and grasses across the EURO-CORDEX domain, which are compared to the control run with no land cover change. The control run is called EVALUATION in subsequent analysis.

In the FOREST experiments, all areas in the map of present day vegetation between 30°N and 72°N are converted to forestland (i.e., broad-leaf deciduous or needle-leaf evergreen trees), where trees can grow (**Figure 1B**). The land transition experiments extract information from the MODIS present-day land cover map at 0.5° geographical resolution (Lawrence and Chase, 2007). This map provides a global distribution of percentages of 17 Plant Functional Types (PFTs). The MODIS map is modified to account for maximum forest cover in the following way. The forest PFTs are rescaled such that they occupy the non-bare soil area (i.e., crop, shrub, or grass) in all grid cells excluding glaciers. Hereby, the different forest type proportions and the fraction of bare soil (including desert areas) are conserved. A zonal average forest composition is chosen if no trees are initially present in a given grid cell. The total area consists of all forest classes together with bare soil and sum up to 100% in all grid cells. The same procedure is applied for the land conversion to grassland. Here, all forested areas from the FOREST map are converted to grassland. The GRASS simulation represents the theoretical maximum grass coverage if grass is allowed to grow all over the land area.

COSMO-CLM distinguishes between less plant categories than provided by the MODIS land cover map. Therefore, similar plant types are further combined into a single category to match the vegetation classification scheme of COSMO-CLM. For example, needle-leaf evergreen tree (temperate or boreal) are combined into a single needle-leaf evergreen tree category. The plant parameters of the new land cover type are derived from the global land cover database GLC2000 (Bartholomé and Belward, 2005). The plant parameters are kept constant throughout the simulation period to maximize model response (Tölle et al., 2014). Urban land units and lakes are not accounted for in the simulations.

Three forestland simulations are conducted, which allow three different types of shortwave albedo parameterizations. Therefore, the simulations are named FOREST1, FOREST2, and FOREST3, respectively. FOREST1 considers the standard operational albedo parameterization, where the albedo α depends on the soil type and soil moisture, and is further modified by plant and snow fraction:

$$\alpha = f_s\,\alpha_s + (1 - f_s)\,(f_v\,\alpha_v + (1 - f_v)\,\alpha_{so}(st, sm)), \qquad (1)$$

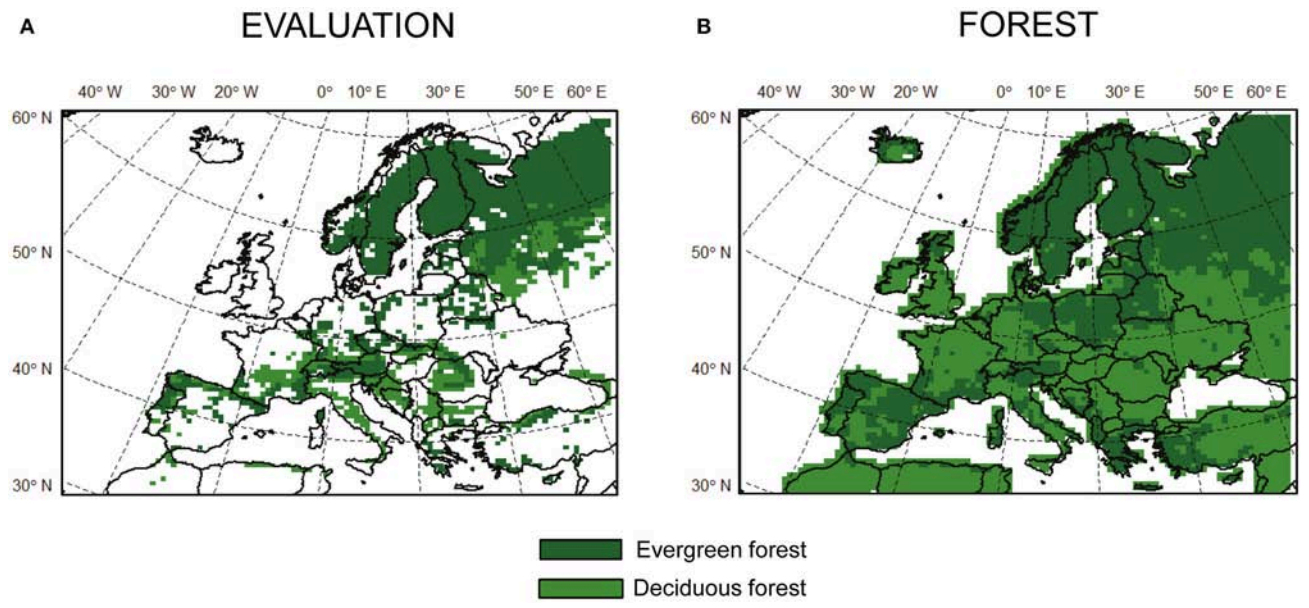

FIGURE 1 | Forest coverage over the EURO-CORDEX domain for the EVALUATION **(A)** and FOREST **(B)** simulations. Evergreen (dark green) and deciduous (light green) forest is shown for coverage greater than 50% in a grid cell.

where α_s, α_v, α_{so} are snow, vegetation and soil albedos. A constant background albedo value of 0.15 is applied for α_v with no distinction between different vegetation types. *st* is the soil type and *sm* is the soil moisture. f_s and f_v are the area fraction of snow and vegetation cover. FOREST2 assumes an albedo depending on soil type and moisture, and modified by snow coverage. Further, the albedo is modified by individual vegetation albedo values used for grass, evergreen, and deciduous forest. These categories depend further on the evergreen and deciduous forest fraction. Here, the following is assumed for α_v:

$$\alpha_v = f_{ve}\,\alpha_{ve} + f_{vd}\,\alpha_{vd} + (1 - f_{ve} - f_{vd})\,\alpha_{vg}, \qquad (2)$$

where f_{ve} and f_{vd} are area fractions of evergreen and deciduous forest cover respectively. $\alpha_{ve} = 0.1$ is the albedo for evergreen forest, $\alpha_{vd} = 0.15$ is the albedo for deciduous forest, and $\alpha_{vg} = 0.2$ is the albedo for grass. The difference of FOREST3 to FOREST2 is that the soil albedo α_{so} for FOREST3 does not depend on soil moisture *sm*. Here, the soil albedo varies between 0.2 and 0.3 depending on soil type. The standard operational albedo parameterization, see equation (1), is assumed for the EVALUATION and GRASS simulations.

The forest cover maps over the EURO-CORDEX domain along with the political boundaries are displayed in **Figures 1A,B** as used for the EVALUATION and FOREST simulations. If the coverage of either evergreen or deciduous forest is greater than 50% in a grid cell, the grid cell is marked as dark green or light green respectively. The grassland simulation considers grass in all the green grid points of **Figure 1B**. Obviously different from the EVALUATION simulation is the fraction of broad-leaf deciduous forest in the FOREST simulations, which covers now main open land areas over France, United Kingdom, Germany, Turkey, Hungary, Romania, Bulgaria, Ukraine, parts of western Russia, see **Figures 1A,B**. Spain, Poland, and Belarus are mainly converted to needle-leaf evergreen forest. Less conversion to forest is seen for the Scandinavian countries compared to the EVALUATION simulation since these countries are already forested. According to **Figure 1A** main vegetation transitions for GRASS occur over forested regions such as Scandinavia and northern Russia as well as parts of the western European countries.

The relative strength of seasonal and latitudinal biophysical effects is compared and quantified from a surface energy balance perspective on the temperature response. Therefore, anomalies of each energy balance component are calculated as the difference in climate variable between an experiment (FOREST1, FOREST2, FOREST3, GRASS) and control simulation without land cover change (EVALUATION), which is experiment minus control (Δ = experiment – control). The af- and deforestation experiments are extreme cases. Therefore, they do not represent a predicted or realistic scenario. It is intended to investigate how much of climate change is possible due to changes in European vegetation cover given the current configuration of continents. The experimental design with its sensitivity study on albedo gives an opportunity to identify the mechanisms controlling the interaction between climate and vegetation in Europe.

We suggest that the different biophysical forcing of conversion to forest- or grassland may depend on the climate zone. Therefore, we separately perform analysis for three climate zones: the boreal (58°-72°N) called NORTH, the temperate (43°-58°N) called MIDDLE, and Mediterranean (dry summer, 30°-43°N) region called SOUTH hereafter. Here, the fractional area with land cover change differs among the northern (1430 grid

points), middle (2178 grid points), and southern (987 grid points) regions.

RESULTS

Changes in Near-Surface Temperature

Contrasting effects occur between land conversion, latitudes, longitudes, and seasons (winter warming/cooling and summer indifferent/warming for changes to FOREST/GRASS), see **Figures 2A–D**. The largest climate impact of land conversion is depicted for GRASS during summer (**Figure 2D**, JJA), at a time of maximum incoming radiation. An overall mean increase in near-surface air temperature is about 1.6°C with largest changes up to 4°C over Hungary and Ukraine. Conversely, GRASS shows a cooling by −0.5°C in winter over regions, which experience snow coverage. Up to −1.5°C cooling over northern Russia is depicted. Contradictory, the western European countries turn warmer by +0.5°C in winter.

The largest change toward warmer air temperatures up to +2.5°C occurs in winter for all of the FOREST simulations mainly over the eastern states, west Russia, and Turkey, see **Figures 2A–C**, DJF). For Portugal and Spain, half a degree Celsius cooling is depicted. FOREST3 displays the strongest warming in winter, followed by FOREST2 and then FOREST1. The FOREST simulations yield similar patterns of change among each other in winter.

Most parts of the inner continental area of the mid-latitudes display minor cooling by half a degree Celsius for FOREST1 in summer. FOREST2 and FOREST3 display half degree warming over the same areas, while FOREST2 also shows +1°C warming in some coastal areas (Greece, western Turkey) and in the northern part (eastern Finland and northern Russia).

Seasonal Cycle of Albedo

The seasonality of the albedo is mainly driven by the seasonal snow coverage, and to a minor extent by the seasonal vegetation coverage, as the albedo values stay constant throughout the

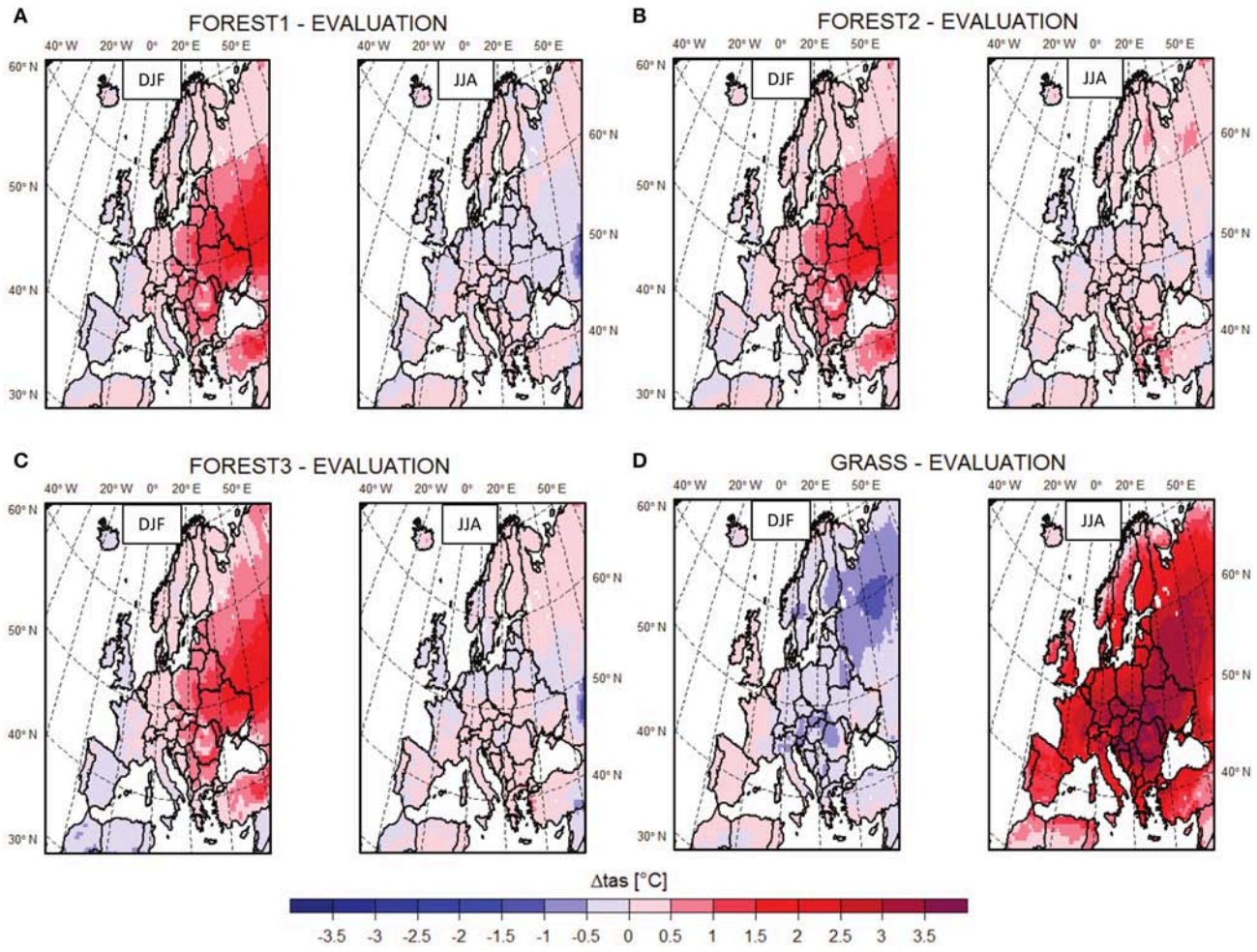

FIGURE 2 | Spatial distribution of mean seasonal near-surface air temperature changes over the EURO-CORDEX domain for the conversion to forest with three different albedo parameterizations [FOREST1 **(A)**, FOREST2 **(B)**, FOREST3 **(C)**], and to grassland [GRASS **(D)**] for winter (DJF, left) and summer (JJA, right) for 1986–2015. The difference between experiments and the EVALUATION simulation with no land cover change is displayed.

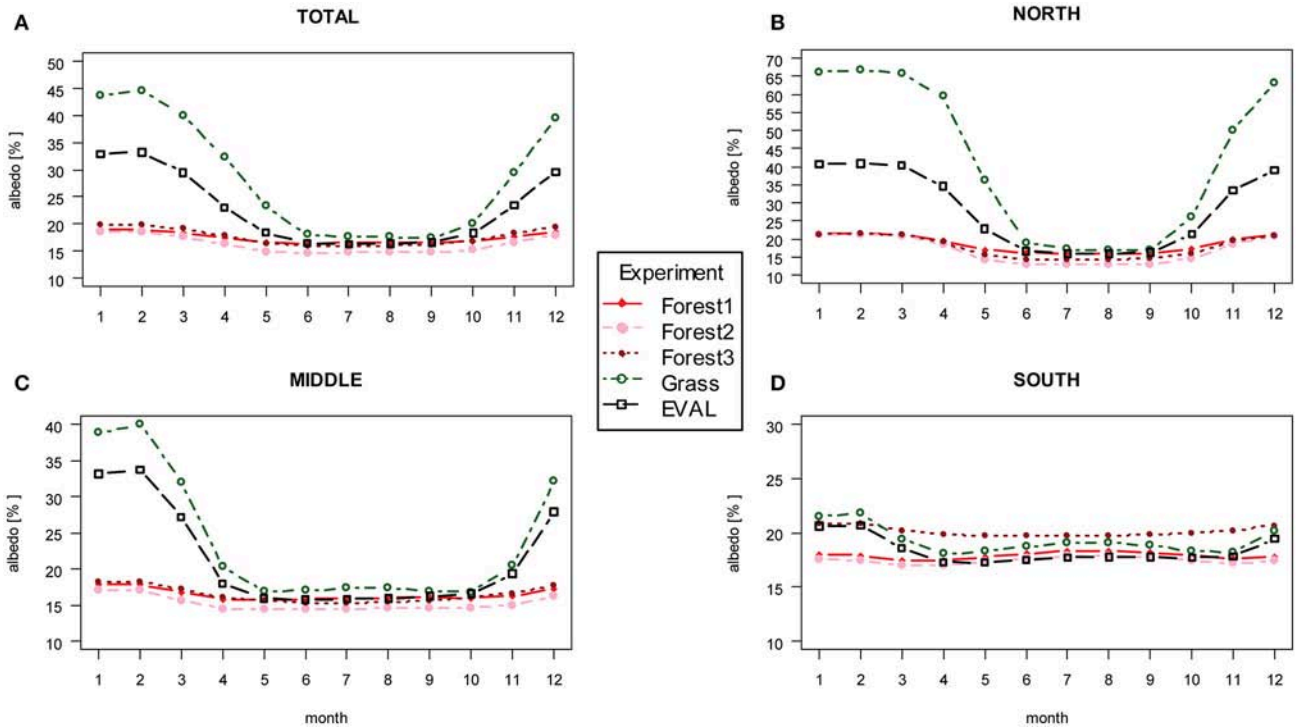

FIGURE 3 | Domain averaged long-term mean seasonal cycle of the albedo of FOREST1 (red), FOREST2 (rose), FOREST3 (dark red), GRASS (dark green), and EVALUATION (black) over all land points only for 1986–2015. Albedo values are displayed for the whole of the domain TOTAL **(A)**, and with latitudinal separation in NORTH **(B)** for high-latitudes (note the different y-axis scale), MIDDLE **(C)** for mid-latitudes, SOUTH **(D)** for the Mediterranean (note the different y-axis scale).

time [see Equations (1) and (2) and **Figure 3A**]. The albedo difference between all of the simulations is evident in all seasons (**Figures 3B–D**). Although major differences appear in winter (albedo increase for GRASS and decrease for FOREST compared to EVALUATION). The seasonal cycle of the albedo depends further on the latitudinal area (**Figures 3B–D**). Largest differences occur between the GRASS and the FOREST runs for the northern und mid-latitudes in winter, where the snow masking effect of trees is strongest. In summer, GRASS reflects the most of the incoming radiation followed by EVALUATION and FOREST1, FOREST3, and then FOREST2 (**Figure 3A**). The soil moisture is not considered in the albedo calculation of FOREST3. This leads to an overestimation of the albedo for moist soil. The albedo parameterization of FOREST1 is the operational one as used for the EVALUATION simulation, and does not depend on different vegetation types. Therefore, the simulated albedo of FOREST1 is similar to that of the EVALUATION simulation in mid-latitudes in summer (**Figure 3C**). This means that the observed changes in temperature realtive to the EVALUATION run are mainly the result of changes in surface roughness and turbulent flux partitioning. A lower albedo of 1 to 2 percent is depicted for FOREST3 and FOREST2 compared to EVALUATION in mid-Europe in summer (**Figure 3C**). The associated increase in available energy at the surface for FOREST3 and FOREST2 might contribute to the summer warming seen in **Figures 4B–C** for mid-latitudes. Further, the albedo differences are higher between the diverse albedo parameterizations than between the different land covers in southern Europe in summer (see FOREST vs. GRASS in **Figure 3D**). The albedo parameterization is here a high uncertainty factor to estimate the impact of land use/cover change.

To summarize, main albedo differences occur due to different vegetation types, and minor albedo differences occur due to the specified parameterization in the model. An exception is southern Europe, where the albedo parameterization is a high uncertainty factor.

Latitudinal and Seasonal Variations in Near-Surface Temperature

We recognize that there is also a west to east gradient, but do not account for this gradient in subsequent analysis, where the latitudinal dependence is discovered. Even though the effect of forests is expected to have high spatial variability within the same climate zone, we still see an overall cooling effect in the mid-latitudes for FOREST1 in summer (**Figure 4A**, JJA). This cooling effect turns into a warming for FOREST2 (**Figure 4B**, JJA), and is indifferent for FOREST3 (**Figure 4C**, JJA). The greatest warming of all regions occurs for FOREST2 in summer, and especially in high latitudes (+0.3°C). All of the FOREST runs display a warming in winter with greatest warming in mid-Europe (+0.7 to +1.0°C, **Figures 4A–C**, DJF). A minor winter cooling is depicted for FOREST3 in the Mediterranean area.

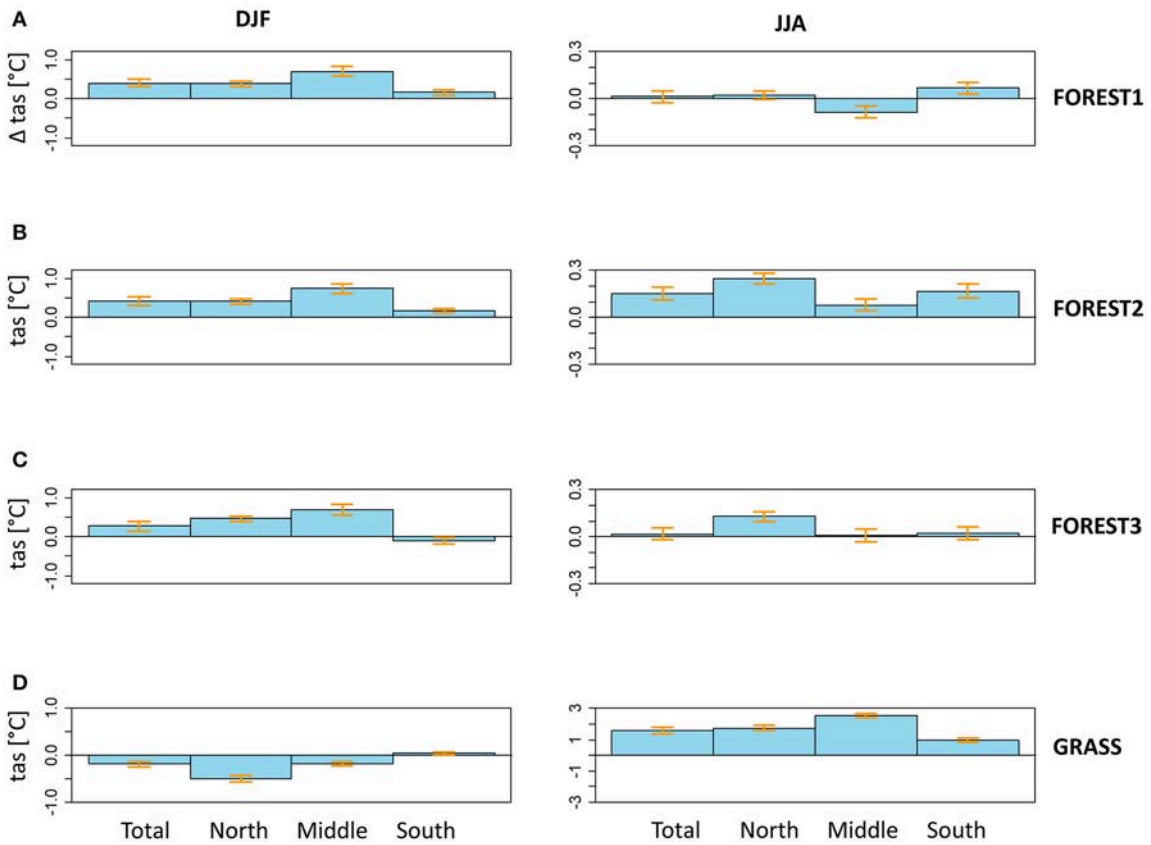

FIGURE 4 | Changes in mean near-surface air temperature compared to the EVALUATION simulation with no land cover change over the EURO-CORDEX domain of three afforestation experiments using a different albedo parameterizations [FOREST1 **(A)**, FOREST2 **(B)**, FOREST3 **(C)**] and deforestation experiment [GRASS **(D)**] for the whole of the domain (TOTAL), and with latitudinal separation in NORTH (58°-72°N) for high-latitudes, MIDDLE (43°-58°N) for mid-latitudes, SOUTH (30°-43°N) for the Mediterranean for winter (DJF) and summer (JJA) for 1986–2015. The errorbars represent ± two times the standard error around the mean. Plotted are differences over all land-points only. Note the different y-axis of GRASS in summer.

Grassland has the opposite effect in winter. Here, a cooling (−0.2 to −0.5°C) especially in the high-latitudes is seen (**Figure 4D**, DJF). No creditable difference is depicted for the Mediterranean. Major warming occurs in summer (up to 3°C in mid–Europe, JJA). The warming is much stronger than that of afforestation.

Seasonal Cycle of Diurnal Temperature Range

Change in the diurnal temperature range is greater for FOREST than for GRASS (**Figures A6a–d**) owing to the increased roughness length. During summer months, the diurnal cycle is increased for GRASS in the northern region (**Figure A6b**). Although changes in maximum and minimum temperatures are different among the three climatic zones and seasons (**Figures 5A–D**). In southern Europe, maximum temperature changes of GRASS is almost the same to that of FOREST. However, the decrease in minimum temperature of GRASS compared to EVALUATION is about 1°C less than that of FOREST in summer (**Figure 5D**). Changes in maximum and minimum temperatures are higher/lower in summer and to a lesser extent lower/higher in winter for GRASS compared to FOREST in mid-Europe, which explains the reduced diurnal cycle for GRASS here (**Figure 5C**). The maximum and minimum temperatures are slightly higher for FOREST2 followed by FOREST3 than for FOREST1 for the same region. A steeper seasonal gradient is found for GRASS in northern Europe. Here, the diurnal temperature range is greater for GRASS than for FOREST by half a degree Celsius in summer and to a minor extent in winter, too (see **Figure A6b**).

Changes in Turbulent Fluxes

Relative to the EVALUATION run, tree cover increases both latent and sensible heat fluxes, see **Figures 6**, **7**. Latent heat fluxes increase at up to +15 W/m^2 over the eastern countries in winter for the forestland simulations owing to the fact of major afforestation in these areas. All other parts display changes of +10 W/m^2. In summer, a mixture of increases over the continental areas and decreases over the maritime region is seen. Similarly,

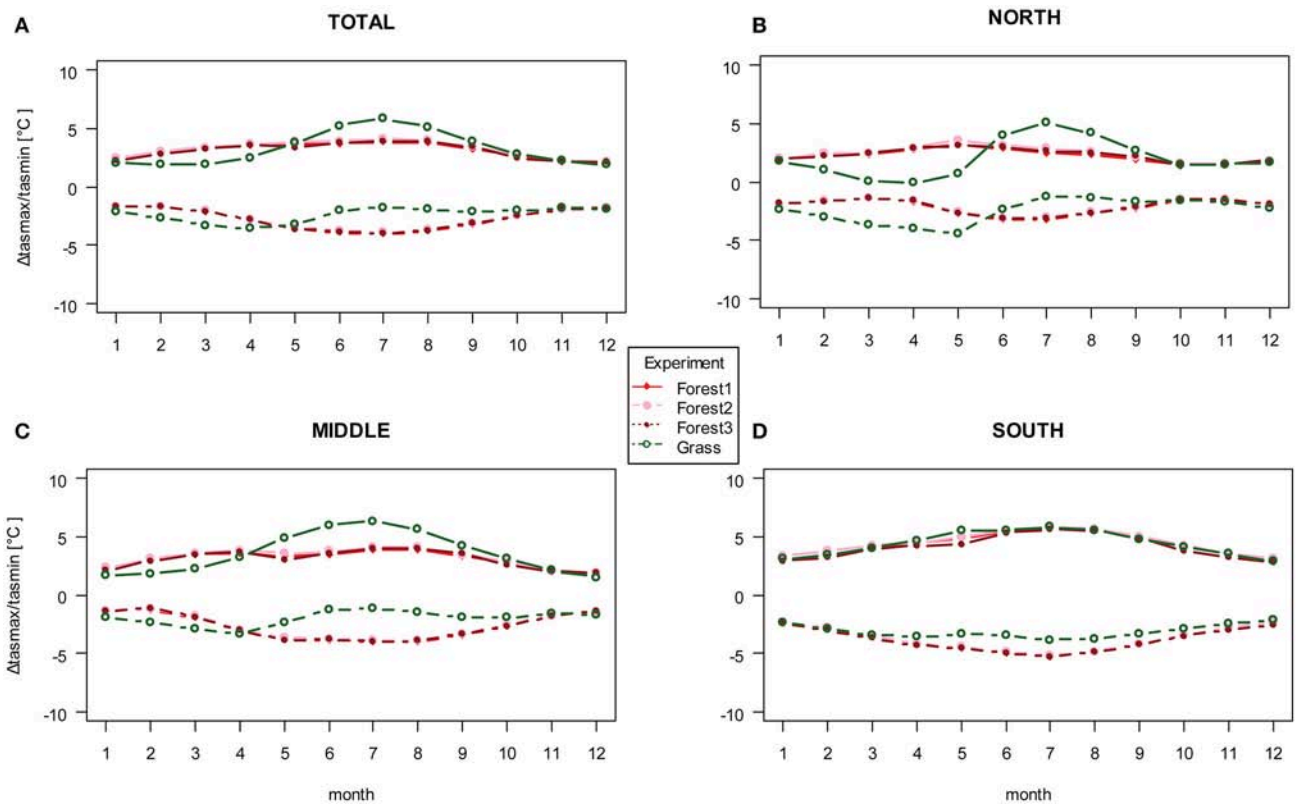

FIGURE 5 | Domain averaged long-term mean seasonal cycle difference of maximum and minimum near-surface temperature of FOREST1 (red), FOREST2 (rose), FOREST3 (dark red), GRASS (dark green) relative to EVALUATION over all land points only for 1986–2015. Values are displayed for the whole of the domain TOTAL **(A)**, and with latitudinal separation in NORTH **(B)** for high-latitudes, MIDDLE **(C)** for mid-latitudes, SOUTH **(D)** for the Mediterranean.

sensible heat fluxes are increased over all forestland simulations by +5 to +15 W/m^2.

The land cover change to forest is associated with biophysical vegetation characteristic changes via increases in the leaf area index, plant coverage, and roughness length. The actual flux change depends on the roughness length, which redistributes the energy through convection and evapotranspiration. Owing to their high aerodynamic roughness, forests dissipate sensible heat as efficiently to the atmospheric boundary layer as latent heat, see **Figures 6**, **7**. Due to the higher leaf area index and plant coverage, latent heat is increased and removed from the surface via turbulence, which is released above the atmospheric boundary layer by cloud condensation (see increase in total cloud coverage in **Figure A5a** compared to **Figures A5b** and **A5c**).

Major changes in the fluxes are seen for latent and sensible heat for GRASS in summer (**Figures 6D**, **7D**), where almost all over the domain a sharp decrease/increase of latent/sensible heat (up to −40/+20 W/m^2) is observed. Decreases of latent heat occur over the Mediterranean area in summer. In this case, reductions of surface roughness and leaf area index/plant coverage reduce the evapotranspirative potential (see reduced seasonal cycle of latent heat flux in **Figure A7d**). For GRASS, the partitioning between sensible and latent heat flux is different than for forestland (see **Figures A1**, **A7**, **A8** in the Appendix). Whereas FOREST have comparable latent and sensible heat fluxes, GRASS shows higher sensible than latent heat fluxes during the growing period (**Figures A7**, **A8**). This difference in flux portioning is especially apparent in the Mediterranean region (**Figures A7d**, **A8d**) due to the limitation of soil moisture availability.

To summarize, latent heat fluxes are increased for FOREST compared to GRASS, but sensible heat fluxes are additionally increased. Major changes occur over areas with strong land conversion. Major changes of the different albedo parameterizations occur during the summer time with strongest changes seen in FOREST2. Characteristic changes (decrease/increase of latent/sensible heat fluxes in summer and of less magnitude in winter) is seen for GRASS.

Changes in Radiation Fluxes

In the FOREST1 run, the net shortwave radiation is decreased by ∼4 W/m2 (**Figures 8A–C**), and the net longwave radiation is increased by ∼8 W/m2 (**Figures 9A–C**) in areas showing summer cooling (see Ukraine, Poland, Belarus, and western Russia in **Figure 2A**). Whereas for FOREST2, in Scandinavia and eastern countries the net shortwave radiation is increased and net longwave radiation is slightly decreased contributing to the summer warming in this area. This is for a lesser

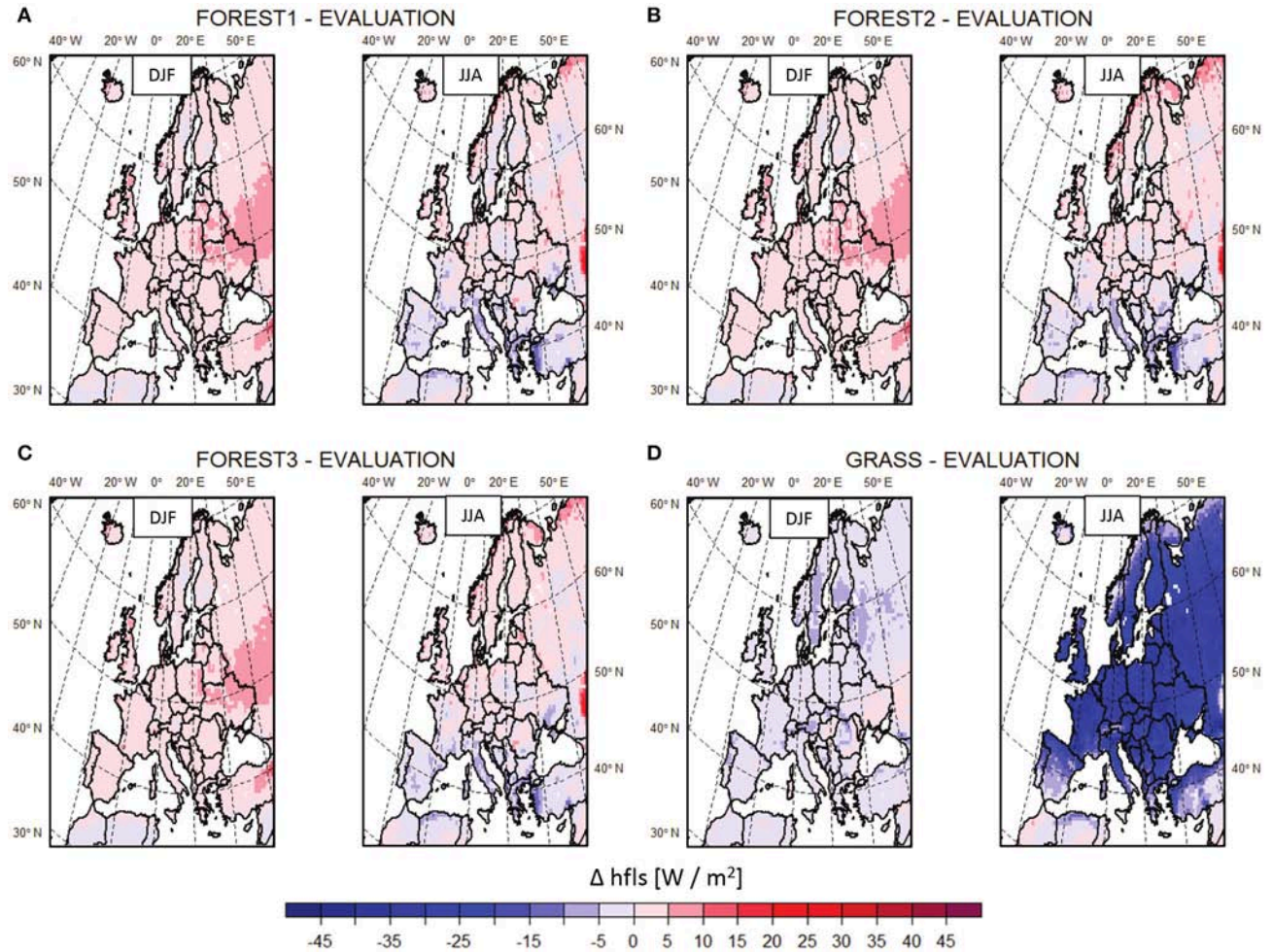

FIGURE 6 | Spatial distribution of mean latent heat flux changes over the EURO-CORDEX domain for the conversion to forest with three different albedo parameterizations [FOREST1 **(A)**, FOREST2 **(B)**, FOREST3 **(C)**], and to grassland [GRASS **(D)**] for winter (DJF, left) and summer (JJA, right) for 1986–2015. The difference between experiments and the EVALUATION simulation with no land cover change is displayed over land points only.

extent visible for FOREST3. The major warming in winter in the afforested areas results due to a sharp increase in net shortwave radiation in that area for all of the FOREST runs (**Figures 8A–C**).

Strongest radiation changes occur in the GRASS simulation, where the net shortwave radiation is decreased by 30 W/m^2 over the alpine area and northern high latitudes in winter (**Figure 8D**) obviously leading to the cooling seen in this region (**Figure 2D**). The replacement of forests with grass in northern latitudes increases surface albedo and reduces absorbed radiation (see **Figures A2**, **A3** in the Appendix). Since the snow-masking effect is less than for FOREST, the winter snow coverage is more effective in reflecting radiation over grassland resulting in a cooling effect. Major summer warming occurs for the conversion to grassland, because of major net shortwave increases and net longwave decreases. Although the albedo is higher for GRASS than for the EVALUATION simulation in summer, the increase in shortwave radiation can be explained by the decrease in total cloud coverage (see **Figure A5b**).

Changes in Ground Heat Fluxes

The relationship between net radiation and turbulent fluxes between the experiments and the EVALUATION simulation is displayed in **Figure 10** as differences of the ground heat flux. Here, the ground heat flux is the residuum of the radiation balance and the turbulent fluxes. If the residual differences between FOREST/GRASS and EVALUATION are positive, more radiative energy is absorbed than transferred to turbulent energy in the experiments relative to EVALUATION and vice versa. Changes in winter temperature for FOREST result due to changes in radiation processes, which are higher by 6 to 8 W/ m^2 than the turbulent flux changes (**Figures 10A–C**). Although turbulent flux changes dominate summer temperature differences. These results can be explained by the magnitude of the land conversion. The area, where the land conversion is the greatest (change of open

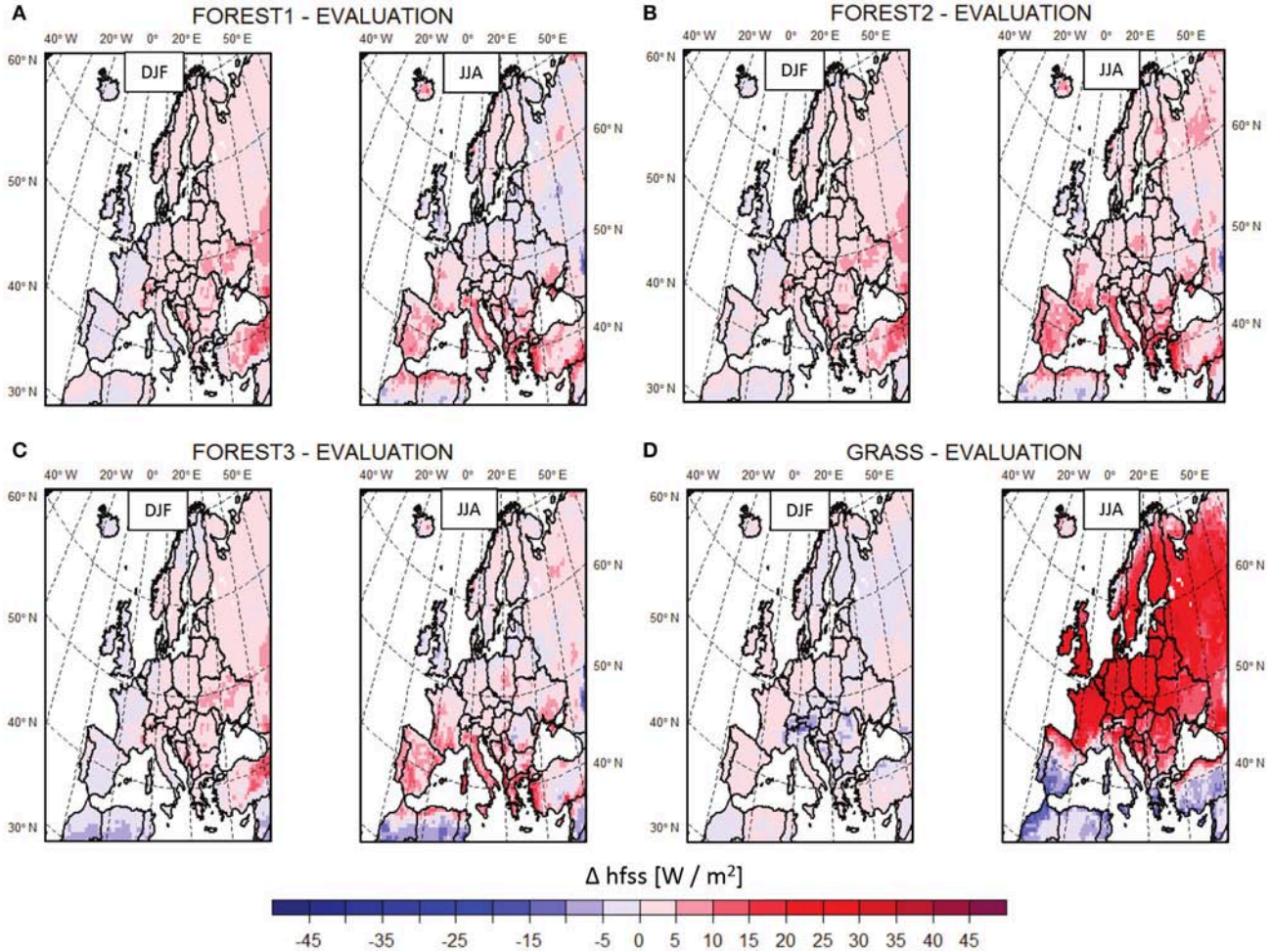

FIGURE 7 | Spatial distribution of mean sensible heat flux changes over the EURO-CORDEX domain for the conversion to forest with three different albedo parameterizations [FOREST1 **(A)**, FOREST2 **(B)**, FOREST3 **(C)**], and to grassland [GRASS **(D)**] for winter (DJF, left) and summer (JJA, right) for 1986–2015. The difference between experiments and the EVALUATION simulation with no land cover change is displayed over land points only.

land to forest in eastern countries), the difference in radiation dominates (see positive values of the change in the energy balance in **Figures 10A–C**) in winter resulting into a warming since forests have a lower albedo and consequent enhanced absorption of solar radiation. The turbulent flux changes dominate in summer. If soil moisture is present in suitable amounts, trees have a larger latent heat flux. They also dissipate sensible heat as efficiently to the atmospheric boundary layer as latent heat. The turbulent flux effect is here stronger for forestland than for grassland, especially in the higher latitudinal region. We acknowledge that the difference of the energy balance between forestland and grassland is positive in winter, meaning a stronger radiation effect of forest, and negative in summer (see **Figure A4** in the Appendix).

In the case of GRASS, turbulent flux differences are higher in winter and vice versa in summer (**Figure 10D**). Here, similar argumentation as before can be applied. That the turbulent flux differences are higher than the changes in radiation in winter applies mainly to the northern areas of Scandinavia and northern Russia, the area with former forest and thus greatest land conversion and associated changes in the biophysical characteristics. In summer, the transformation to grassland leads to an increase in net shortwave radiation, a decrease in net longwave radiation, a major decrease in latent heat flux and an increase in sensible heat flux.

DISCUSSION

The previous land cover must be considered in order to interpret the results. The former land cover determines the strength of the conversion to either forest or grass and with that the strength of the biophysical characteristic changes. This is also a function of the vegetation albedo, roughness length, and evapotranspiration potential, if different vegetation types are considered. The latitude is another determinant, which influences the climate change due to land conversion, because of the background climate and snow-masking effect.

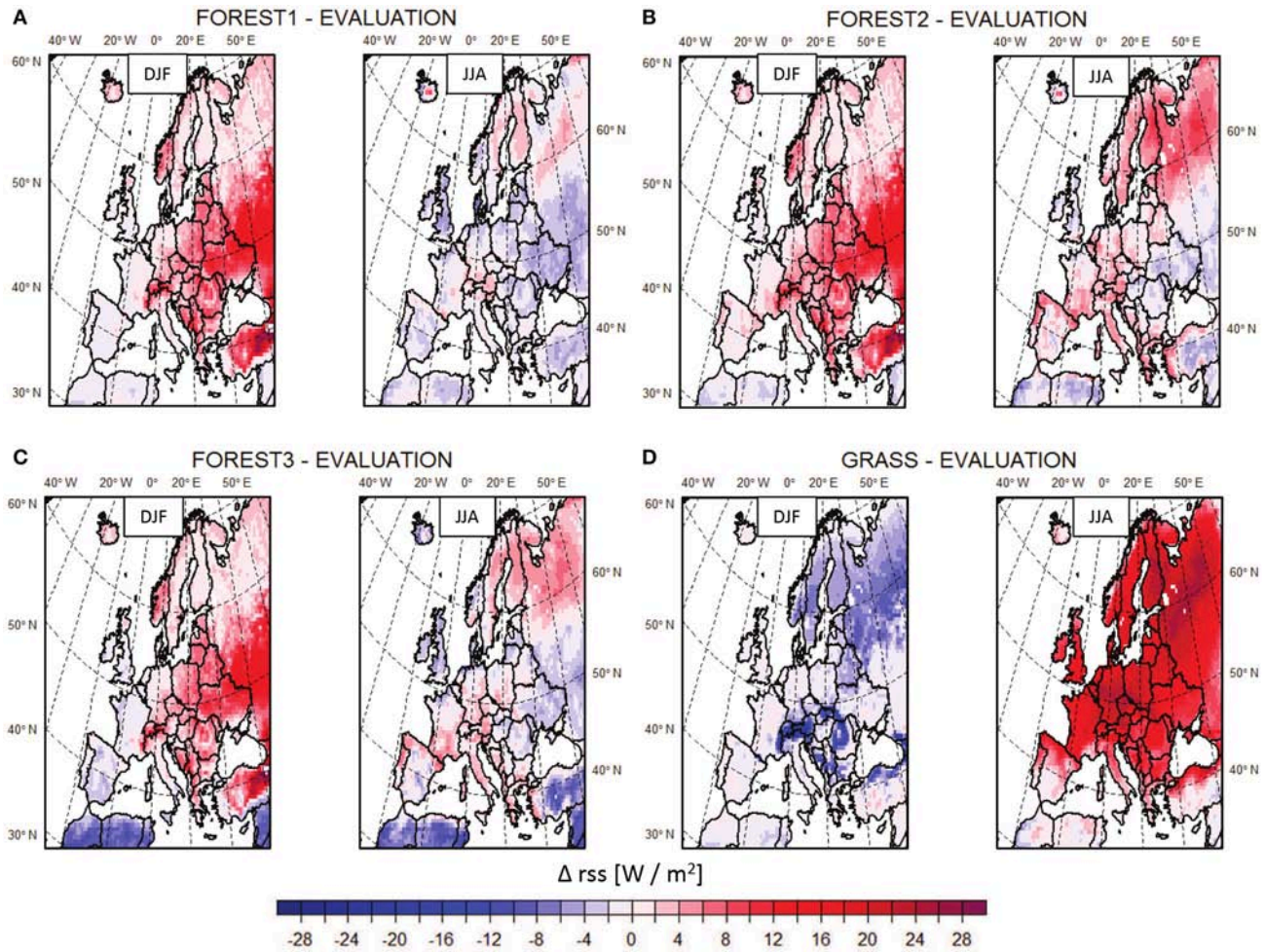

FIGURE 8 | Spatial distribution of mean net shortwave flux changes over the EURO-CORDEX domain for the conversion to forest with three different albedo parameterizations [FOREST1 **(A)**, FOREST2 **(B)**, FOREST3 **(C)**], and to grassland [GRASS **(D)**] for winter (DJF, left) and summer (JJA, right) for 1986–2015. The difference between experiments and the EVALUATION simulation with no land cover change is displayed over land points only.

Therefore, major winter warming (up to 2.5°C) of the FOREST simulations occurs over areas, which are extensively afforested compared to the EVALUATION simulation, which is true for the eastern countries, west Russia, and Turkey, see **Figures 1A,B**. Here, forests have a warming effect when the former major land cover was open land and not forest. The conversion to forest leads to a reduction of the albedo for all FOREST simulations in winter, which increases the available energy at the surface. The reflectivity is further reduced due to the snow-masking effect of forest in winter. This results in a winter warming of the eastern countries (Bonan et al., 1992; Bonan, 2008; Tang et al., 2018). Those remaining European regions, which experience snow cover in winter and where the forest fraction is increased, show also a warming effect since the radiative warming dominates the non-radiative cooling (Bright et al., 2017). Only in west-Europe, a winter cooling by half a degree Celsius is depicted, since more evapotranspiration of water occurs, and the sensible heat is decreased. In addition, the net incoming radiation is decreased due to more cloud coverage (see **Figure A5** in the Appendix) by higher evapotranspiration. Thus, the warmer regions can suppress the albedo warming effect of forest (Li et al., 2015). This effect is similar for FOREST1, FOREST2, and FOREST3.

A conversion to grassland can be regarded as a strong land cover change effect (deforestation) in the high latitudes. Thus, grassland has a winter cooling effect if the former land cover was forested like in the Scandinavian countries and northern Russia, see **Figures 1A,B**, and **Figure 2D**, DJF (Cherubini et al., 2018). These are regions, which experience snow coverage, and the decreased snow-masking effect enhance the cooling there in winter. The western European countries turn warmer in winter. Although the difference between forest and grass also implies the same direction (cooling by grass), see **Figure A1** in the Appendix. The regions, which experience snow coverage in winter, get cooler by half a degree Celsius due to the increase

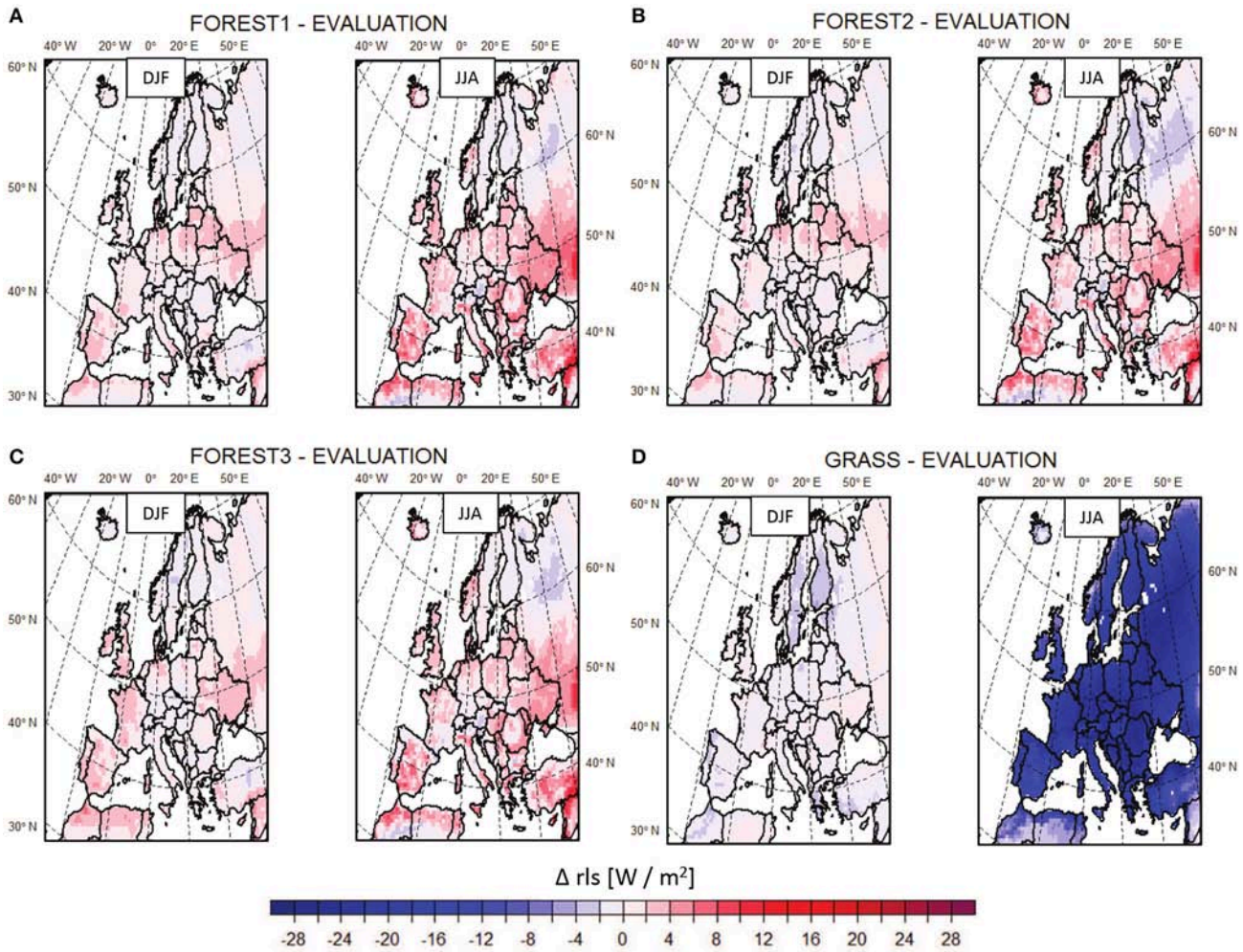

FIGURE 9 | Spatial distribution of mean net longwave flux changes over the EURO-CORDEX domain for the conversion to forest with three different albedo parameterizations [FOREST1 **(A)**, FOREST2 **(B)**, FOREST3 **(C)**], and to grassland [GRASS **(D)**] for winter (DJF, left) and summer (JJA, right) for 1986–2015. The difference between experiments and the EVALUATION simulation with no land cover change is displayed over land points only.

in reflectivity associated with the snow-masking effect. Alkama and Cescatti (2016) postulated a sharp reduction in high latitude temperatures due to large-scale deforestation. Although similar changes of temperatures are also seen over Scandinavia in our study, they are only moderate in magnitude. Also a surface cooling by deforestation of the mid and high latitudes of the northern hemisphere was reported before by Douville and Royer (1997). The western European areas turn warmer by half a degree Celsius in winter since the evapotranspiration is reduced and more sensible heat is produced.

Eastern and mid-Europe turn cooler for FOREST1 in summer. The operational albedo parameterization is used for FOREST1, and the summer albedo is similar to the albedo of the EVALUATION run in mid-latitudes, see **Figure 3C**. Thus, the simulated changes in temperature result from increases in surface roughness and turbulent fluxes. The higher evapotranspiration increases cloud coverage, strengthens the long-wave downward radiation, and reduces the direct incoming radiation, see **Figure A10**. This results in an additional cooling effect. The cooling effect due to afforestation in mid-Europe is in line with remote sensing and *in situ* observations (Alkama and Cescatti, 2016; Bright et al., 2017). Contradictory, these regions turn warmer for FOREST2 followed by FOREST3 with a different albedo parameterization depending on the vegetation type. A lower albedo is depicted for FOREST2 and FOREST3 compared to EVALUATION in mid-Europe in summer. The associated increase in available energy at the surface for FOREST2 and FOREST3 contributes to the summer warming in mid-latitudes. The soil moisture is not considered in the albedo calculation of FOREST3. This leads to an overestimation of the albedo for moist soil conditions of FOREST3 compared to FOREST2. Further, climatic changes depend on the strength of daytime warming and nighttime cooling, and is reflected by the differences in maximum and minimum temperature (**Figure 5D**, Cherubini et al., 2018). Summer warming by afforestation was pointed out by Bonan et al. (1992). The alternate albedo parameterization

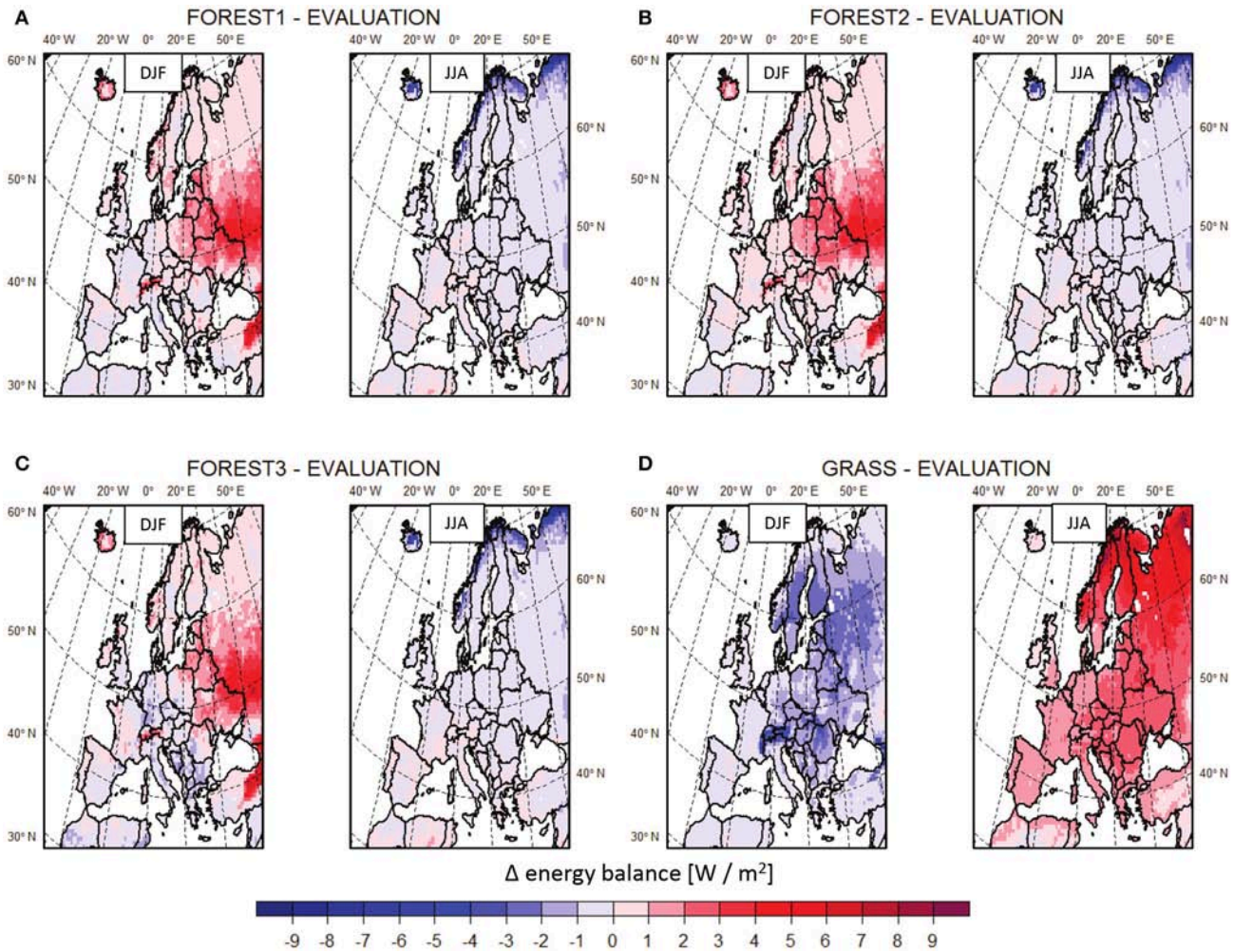

FIGURE 10 | Spatial distribution of temporal mean energy balance changes over the EURO-CORDEX domain for the conversion to forest with three different albedo parameterizations [FOREST1 **(A)**, FOREST2 **(B)**, FORESTS3 **(C)**], and to grassland [GRASS **(D)**] for winter (DJF, left) and summer (JJA, right) for 1986–2015. The difference between experiments and the EVALUATION simulation with no land cover change is displayed over land points only.

with vegetation albedo depending on vegetation type leads to a reduction of the albedo compared to FOREST1, and with that to increased net incoming radiation. It is thus how the albedo of the vegetation is treated in the model that determines the response of summer climate to afforestation in mid-latitudes.

All the forest simulations show a warming in southern Europe in summer. Despite the higher evapotranspiration potential due to the higher leaf area index of forest, there is less evapotranspiration. This may be translated to less soil moisture available for evaporation, which is also reduced (Swann et al., 2012). Thus, the Bowen ratio is increased, and more sensible heat is released to the atmosphere, see **Figure A9**. Sensible heat and net short-wave radiation fluxes show the most variability among the experiments. The results show that the differences in the various vegetation albedos (as for FOREST2 and FOREST3) are more important than the consideration of the soil moisture and type (as for FROEST1 and FOREST2).

For deforestation, the whole of Europe turns warmer by up to 3°C in summer since the latent/sensible heat fluxes are decreased/increased. The total cloud coverage decreases due to the reduced evapotranspiration (see **Figure A5b** in the Appendix), which is also seen in the reduced long-wave downward radiation. Thereby the net incoming radiation accelerates, see **Figures A9** and **A10**. Most climate models show an average regional cooling from deforestation (Perugini et al., 2017). This is generally confirmed in our study for regions, which experience snow coverage in winter. Although this winter cooling is offset by a dramatic warming in summer. Thus, grassland increases seasonal temperature variation compared to forest. These results highlight the fact that local biophysical processes triggered by afforestation can decrease seasonal temperature variations, further reducing the temperature trends driven by the increasing greenhouse gas concentrations.

Albedo differences turn out to be higher between the FOREST simulations due to the albedo parameterizations

than between the land cover types in southern Europe. The high temperature discrepancies between GRASS and the three FOREST simulations in this region thus stem primarily from differences in evapotranspiration rather than from the albedo effect. Therefore, the land cover change impact is higher in this region than the model uncertainty. Thus, an accurate land cover map with characteristic vegetation types is important to include for such kind of studies.

CONCLUSIONS

In this study, the effect of three different albedo parameterizations is examined for afforestation experiments at 0.44° horizontal resolution across the EURO-CORDEX domain during 1986-2015. Idealized de- and af-forestation simulations are compared to the simulation with no land cover change. Emphasis is put on the impact of changes in radiation and turbulent fluxes. A clear latitudinal pattern is found, which results partly due to the strong land cover conversion from forest- to grassland in the high latitudes and open land to forest conversion in mid-latitudes. Afforestation warms the climate in winter, strongest in mid-latitudes. Results are indifferent in summer owing to opposing albedo and evapotranspiration effects of comparable size but different sign. Thus, the net effect is small for summer. Depending on the albedo parameterization in the model, the temperature effect can turn from cooling to warming in mid-latitude summers. The summer warming due to deforestation is up to 3°C higher than due to afforestation due the reduced roughness and leaf area index cooling. The cooling by grass or warming by forest is in magnitude comparable and small in winter even though the albedo differences are high.

The strength of the land conversion and associated vegetation type with its biophysical characteristics is the major determinant in changing the climate. Different albedo parameterizations in the model either enhance or suppress the climate change due to land cover change. Even though the difference between the albedo parameterizations is small, they influence the model's outcome of summer climate due to afforestation being either a warming or cooling in the mid-latitudes. Here, we suggest that temperature changes are mainly influenced by the magnitude of individual biophysical changes and the specific background climate conditions, in which the land use change occurs. Thus, the albedo parameterization need to account for different vegetation types. Furthermore, the albedo parameterization is a high uncertainty factor to estimate the impact of land use/cover change in southern Europe. This is important information for model development.

Altering the surface boundary conditions resulted in changes of the total cloud cover amount in this study. Thus, land-atmosphere interactions affect the hydrological cycle, which indirectly feed back on the surface energy balance components. The contribution of horizontal/vertical advections to near-surface air temperature changes would be an important issue to look at next with reconsideration of the cumulus scheme in the model.

AUTHOR CONTRIBUTIONS

MT: conceptualization, methodology, software, formal analysis, writing-original draft preparation, writing-review & editing, supervision, project administration, funding acquisition, visualization; MT, MB: investigation, interpretation; MT, MB, KR, and H-JP: validation; MT, MB, and KR: data curation.

ACKNOWLEDGMENTS

Computational resources were made available by the German Climate Computing Center (DKRZ) through support from the Federal Ministry of Education and Research in Germany (BMBF). The FOREST and GRASS vegetation maps were created and provided by Edouard Davin in the context of the LUCAS initiative. We acknowledge the funding of the German Research Foundation (DFG) through grant nr. 401857120. Authors acknowledge the support from BMBF through MiKlip (FKZ: 01LP1518A). We have benefited from the CLM-community (www.clm-community.eu). We thank two reviewers for their useful comments to the manuscript.

SUPPLEMENTARY MATERIAL

The Supplementary Material for this article can be found online at: https://www.frontiersin.org/articles/10.3389/fenvs.2018.00123/full#supplementary-material

REFERENCES

Alkama, R., and Cescatti, A. (2016). Biophysical climate impact of recent changes in global forest cover. *Science* 351, 600–604. doi: 10.1126/science.aac8083

Arakawa, A., and Lamb, V. (1977). "Computational design of the basic dynamical processes in the UCLA general circulation model," in *Methods in Computational Physics: General Circulation Models of the Atmosphere,* ed J Chang (New York, NY: Academic Press) 17, 173–265. doi: 10.1016/B978-0-12-460817-7.50009-4

Bartholomé, E., and Belward, A. S. (2005). GLC: a new approach to global land cover mapping from earth observation data. *Int. J. Remote Sens.* 26, 1959–1977. doi: 10.1080/01431160412331291297

Bonan, G. B. (2008). Forests and climate change: forcings, feedbacks, and the climate benefits of forests. *Science* 320, 1444–1449. doi: 10.1126/science.1155121

Bonan, G. B., Pollard, D., and Thompson, S. L. (1992). Effects of boreal forest vegetation on global climate. *Nature* 359, 716–718.

Bright, R. M., Davin, E., O'Halloran, T., Pongratz, J., Zhao, K., and Cescatti, A. (2017). Local temperature response to land cover and management change driven by non-radiative processes. *Nat. Clim. Chang.* 7, 296–302. doi: 10.1038/nclimate3250

Cherubini, F., Huang, B., Hu, X., Tölle, M. H., and Strømman, H. A. (2018). Quantifying the climate response to extreme land cover changes in Europe with a regional model. *Environ. Res. Lett.* 13:074002. doi: 10.1088/1748-9326/aac794

Davin, E. L., and de Noble-Ducoudré, N. (2010). Climate impact of global-scale deforestation: radiative versus non-radiative processes. *J. Clim.* 23, 97–112. doi: 10.1175/2009JCLI3102.1

Dee, D. P., Uppala, S. M., Simmons, A. J., Berrisford, P., Poli, P., Kobayashi, S., et al. (2011). The ERA-Interim reanalysis: configuration and performance of

the data assimilation system. *Q. J. R. Meteorol. Soc.* 137, 553–597. doi: 10.1002/qj.828

Dickinson, R. E. (1984). "Modeling evapotranspiration for three-dimensional global climate models," in *Climate Processes and Climate Sensitivity*, eds J. E. Hansen and T. Takahashi (Washington, DC: American Geophysical Union), 58–72.

Doms, G., and Baldauf, M. (2015). *A Description of the Non-Hydrostatic Regional COSMO-Model, Part I: Dynamics and Numerics*. Offenbach, Germany: DWD.

Doms, G., Förstner, J., Heise, E., Herzog, H.-J., Mironov, D., Raschendorfer, M., et al. (2011). *A Description of the Non-Hydrostatic Regional COSMO-Model, Part II: Physical Parameterization*. Offenbach. Germany: DWD.

Douville, H., and Royer, J. F. (1997). Influence of the temperate and boreal forests on the Northern Hemisphere climate in the Meteo-France climate model. *Clim. Dyn.* 13, 57–74. doi: 10.1007/s0038200 50153

Duveiller, G., Hooker, J., and Cescatti, A. (2018). The mark of vegetation change on Earth's surface energy balance. *Nat. Commun.* 9:679. doi: 10.1038/s41467-017-02810-8

Kotlarski, S., Keuler, K., Christensen, O. B., Colette, A., Déqu,é, M., and Gobiet, A. (2014). Regional climate modeling on European scales: a joint standard evaluation of the EURO-CORDEX RCM ensemble. *Geosci. Model Dev.* 7, 1297–1333. doi: 10.5194/gmd-7-1297-2014

Lawrence, P. J., and Chase, T. N. (2007). Representing a new MODIS consistent land surface in the Community Land Model (CLM 3.0). *J. Geophys. Res.* 112:G01023. doi: 10.1029/2006JG000168

Lee, X., Goulden, M. L., Hollinger, D. Y., Barr, A., Black, T. A., Bohrer, G., et al. (2011). Observed increase in local cooling effect of deforestation at higher latitudes. *Nature* 479, 384–387. doi: 10.1038/nature10588

Li, Y., de Noblet-Decoudré, N., Davin, E. L., Motesharrei, S., Zeng, N., Li, S., et al. (2016a). The role of spatial scale and background climate in the latitudinal temperature response to deforestation. *Earth Syst. Dynam.* 7, 167–181. doi: 10.5194/esd-7-167-2016

Li, Y., Zhao, M., Mildrexler, D. J., Motesharrei, S., Mu, Q., Kalnay, E., et al. (2016b). Potential and actual impacts of deforestation and afforestation on land surface temperature. *J. Geophys. Res. Atmos.* 121, 14372–14386. doi: 10.1002/2016JD024969

Li, Y., Zhao, M., Motesharrei, S., Mu, Q., Kalnay, E., and Li, S. (2015). Local cooling and warming effects of forests based on satellite observations. *Nat. Commun.* 6:6603. doi: 10.1038/ncomms7603

Perugini, L., Caporaso, L., Marconi, S., Cescatti, A., Quesada, B., de Noblet-Ducoudré, N., et al. (2017). Biophysical effects on temperature and precipitation due to land cover change. *Environ. Res. Lett.* 12:053002. doi: 10.1088/1748-9326/aa6b3f

Pielke, Sr A., Pitman, A., Niyogi, D., Mahmood, R., McAlpine, C., Hossain, F., et al. (2011). R Land use/land cover changes and climate: modeling analysis and observational evidence. *WIREs Clim. Change* 2, 828–850. doi: 10.1002/wcc.144

Pitman, A. J., de Noblet- Decoudré, N., Cruz, F. T., Davin, E. L., Bonan, G. B., Brovkin, V., et al. (2009). Uncertainties in climate response to past land cover change: First results from the LUCID intercomparison study. *Geophys. Res. Lett.* 36:L14814. doi: 10.1029/2009GL039076

Popp, A., Calvin, K., Fujimori, S., Havlik, P., Humpenöder, F., Stehfest, E., et al. (2017). Land-use futures in the shared socio-economic pathways. *Glob. Environ. Change* 42, 331–345. doi: 10.1016/j.gloenvcha.2016.10.002

Ritter, B., and Geleyn, J. F. (1992). A comprehensive radiation scheme for numerical weather prediction models with potential applications in climate simulations. *Mon. Weather Rev.* 120, 303–325. doi: 10.1175/1520-0493(1992)120<0303:ACRSFN>2.0.CO;2

Rockel, B., Will, A., and Hense, A. (2008). The regional climate model COSMO-CLM (CCLM). *Meteorolog. Z.* 17, 347–348. doi: 10.1127/0941-2948/2008/0309

Schrodin, R., and Heise, E. (2002). *The Multi-Layer Version of the DWD Soil Model TERRA-LM, COSMO Tech. Rep. 2*. Offenbach: Deutscher Wetterdienst.

Snyder, P. K., Foley, J. A., Hitchman, M. H., and Delire, C. (2004). Analyzing the effects of complete tropical forest removal on the regional climate using a detailed three-dimensional energy budget: an application to Africa. *J. Geophys. Res.* 109:D21102 doi: 10.1029/2003JD004462

Steppeler, J., Doms, G., Schättler, U., Bitzer, H. W., Gassmann, A., Damrath, U.,et al. (2003). Meso-gamma scale forecasts using the non-hydrostatic model LM. *Meteorol. Atmos. Phys.* 82, 75–96. doi: 10.1007/s00703-001-0592-9

Swann, A. L. S., Fung, I. Y., and Chiang, J. C. H. (2012). Mid-latitude afforestation shifts general circulation and tropical precipitation. *PNAS* 109, 712–716. doi: 10.1073/pnas.1116706108

Tang, B., Zhao, X., and Zhao, W. (2018). Local effects of forests on temperatures across Europe. *MDPI Remote Sens.* 10:529. doi: 10.3390/rs100 40529

Tiedtke, M. (1989). A comprehensive mass flux scheme for cumulus parameterization in large-scale models. *Mon. Weather Rev.* 117, 1779–1800. doi: 10.1175/1520-0493(1989)117<1779:ACMFSF>2.0.CO;2

Tölle, M. H., Engler, S., and Panitz, H.-J. (2017). Impact of abrupt land cover changes by tropical deforestation on South-East Asian climate and agriculture. *J. Clim.* 30, 2587–2600. doi: 10.1175/JCLI-D-16-0131.1

Tölle, M. H., Gutjahr, O., Thiele, T., and Busch, G. (2014). Increasing bioenergy production on arable land: does the regional and local climate respond? Germany as a case study. *J. Geophys. Res. Atmos.* 119, 2711–2724. doi: 10.1002/2013JD020877

Wicker, L. J., and Skamarock, W. C. (2002). Time-splitting methods for elastic models using forward time schemes. *Mon. Weather Rev.* 130, 2088–2097. doi: 10.1175/1520-0493(2002)130<2088:TSMFEM>2.0.CO;2

Conflict of Interest Statement: The authors declare that the research was conducted in the absence of any commercial or financial relationships that could be construed as a potential conflict of interest.

frontiers in Environmental Science

CORRECTION
published: 30 January 2019
doi: 10.3389/fenvs.2019.00012

Corrigendum: Sensitivity of European Temperature to Albedo Parameterization in the Regional Climate Model COSMO-CLM Linked to Extreme Land Use Changes

Merja H. Tölle[1]*, *Marcus Breil*[2], *Kai Radtke*[3] and *Hans-Jürgen Panitz*[2]

[1] Department of Geography, Climatology, Climate Dynamics and Climate Change, Justus-Liebig University Giessen, Giessen, Germany, [2] Institute of Meteorology and Climate Research–Troposphere Research, Karlsruhe Institute of Technology, Eggenstein-Leopoldshafen, Germany, [3] Chair of Environmental Meteorology, Brandenburg University of Technology, Cottbus-Senftenberg, Senftenberg, Germany

Keywords: land cover change, biophysical effect, albedo parameterization, evapotranspiration, regional climate model, climate, de-/afforestation, surface energy balance

OPEN ACCESS

Approved by:
Frontiers in Environmental Science Editorial Office, Frontiers Media SA, Switzerland

***Correspondence:**
Merja H. Tölle
merja.toelle@geogr.uni-giessen.de

Specialty section:
This article was submitted to Atmospheric Science, a section of the journal Frontiers in Environmental Science

Received: *15 January 2019*
Accepted: *17 January 2019*
Published: *30 January 2019*

Citation:
Tölle MH, Breil M, Radtke K and Panitz H-J (2019) Corrigendum: Sensitivity of European Temperature to Albedo Parameterization in the Regional Climate Model COSMO-CLM Linked to Extreme Land Use Changes. Front. Environ. Sci. 7:12. doi: 10.3389/fenvs.2019.00012

A Corrigendum on

Sensitivity of European Temperature to Albedo Parameterization in the Regional Climate Model COSMO-CLM Linked to Extreme Land Use Changes
by Tölle, M. H., Breil, M., Radtke, K., and Panitz, H.-J. (2018). Front. Environ. Sci. 6:123. doi: 10.3389/fenvs.2018.00123

In the original article, we neglected to acknowledge Edouard Davin. A correction has therefore been made to the **Acknowledgements**:

"Computational resources were made available by the German Climate Computing Center (DKRZ) through support from the Federal Ministry of Education and Research in Germany (BMBF). The FOREST and GRASS vegetation maps were created and provided by Edouard Davin in the context of the LUCAS initiative. We acknowledge the funding of the German Research Foundation (DFG) through grant nr. 401857120. Authors acknowledge the support from BMBF through MiKlip (FKZ: 01LP1518A). We have benefited from the CLM-community (www.clm-community.eu). We thank two reviewers for their useful comments to the manuscript."

The authors apologize for this error and state that this does not change the scientific conclusions of the article in any way. The original article has been updated.

Conflict of Interest Statement: The authors declare that the research was conducted in the absence of any commercial or financial relationships that could be construed as a potential conflict of interest.

frontiers in Earth Science

ORIGINAL RESEARCH
published: 27 November 2018
doi: 10.3389/feart.2018.00216

Changes of Extreme Sea Level in 1.5 and 2.0°C Warmer Climate Along the Coast of China

Jianlong Feng[1], Huan Li[1], Delei Li[2,3], Qiulin Liu[1], Hui Wang[1] and Kexiu Liu[1]*

[1] National Marine Data and Information Service, Tianjin, China, [2] Key Laboratory of Ocean Circulation and Waves, Institute of Oceanology, Chinese Academy of Sciences, Qingdao, China, [3] Function Laboratory for Ocean Dynamics and Climate, Qingdao National Laboratory for Marine Science and Technology, Qingdao, China

Using hourly sea level data from 15 tide gauges along the Chinese coast and sea level data of three simulations of the Coupled Model Intercomparison Project Phase 5 (CMIP5), we assessed the changes and benefits of the extreme sea level of limiting warming to 1.5°C instead of 2.0°C. Observations show that the extreme sea level has risen with high confidence during the past decades along the coast of China, while the mean sea level change, especially the long-term change plays important roles in the changing process of extreme sea levels. Under the 1.5 and 2.0°C warming scenarios, the sea level will rise with fluctuations in the future, so will the return levels of the extreme sea levels. Compared with the 1.5°C warming condition, the return levels under the 2.0°C warming condition will rise significantly at all tide gauges along the Chinese coast. The results indicate that a 0.5°C warming will bring much difference to the extreme sea levels along the coast of China. It is of great necessity to limit anthropogenic warming to 1.5°C rather than 2.0°C, as proposed by the Paris Climate Agreement, which will greatly reduce the potential risks of future flood disasters along the coast of China and is beneficial for risk response management.

Keywords: extreme sea level, return sea level, sea level rise, projection, strom surge

OPEN ACCESS

Edited by:
Izuru Takayabu,
Meteorological Research Institute (MRI), Japan

Reviewed by:
Nobuhito Mori,
Kyoto University, Japan
Tomoki Tozuka,
The University of Tokyo, Japan

****Correspondence:***
Jianlong Feng
jianlongf@hotmail.com;
fjl181988@126.com

Specialty section:
This article was submitted to Atmospheric Science, a section of the journal Frontiers in Earth Science

Received: *31 July 2018*
Accepted: *07 November 2018*
Published: *27 November 2018*

Citation:
Feng J, Li H, Li D, Liu Q, Wang H and Liu K (2018) Changes of Extreme Sea Level in 1.5 and 2.0°C Warmer Climate Along the Coast of China. Front. Earth Sci. 6:216. doi: 10.3389/feart.2018.00216

INTRODUCTION

China has the largest coastal population in the world, with more than 40% people living in the coastal area, where the extreme sea level disasters occur frequently and have caused serious negative impacts. According to the China Marine Disaster Bulletin[1], the extreme sea level incidents have caused economic losses of 11.1 billion (RMB) and 49 deaths annually between 2000 and 2017.

Increases in the mean and extreme sea levels are regarded as one of the consequences of climate change (Church et al., 2013). In recent years, many studies have been done about the changes of extreme sea levels both regionally and globally (von Storch and Reichardt, 1997; Woodworth and Blackman, 2004; Méndez et al., 2007; Menéndez and Woodworth, 2010; Feng et al., 2015; Marcos and Woodworth, 2017). Substantial evidences have revealed the general increase in extreme sea level in the past decades worldwide. Many researches indicated that the changes of the extreme sea level, especially the long-term change, are highly correlated with the changes of mean sea level (Zhang et al., 2000; Woodworth and Blackman, 2004; Marcos et al., 2009; Menéndez and Woodworth, 2010; Tsimplis and Shaw, 2010). Meanwhile, statistical method and dynamical method

[1]http://www.soa.gov.cn/zwgk/hygb/

are utilized to study the future changes in extreme sea level. The extreme sea levels will increase as mean sea levels rise in the future according to the future projection (Langenberg et al., 1999; Busuioc et al., 2006; Woth et al., 2006; Grossmann et al., 2007).

Compared with the mean sea level (Ding et al., 2001; Yu et al., 2003; Zuo et al., 2007; Wang et al., 2018), fewer studies have been conducted to analyze the extreme sea levels along the China coast in the past. Chen and Wang (1993) found that the extreme sea level at Wusong and Huangpu Park increased between 1915 and 1985. Feng and Tsimplis (2014) and Feng et al. (2015) analyzed the changes of extreme sea levels using tide gauge data and indicated that the extreme sea level increased in the past decades, while the long-term change of extreme sea level was mainly affected by the change of mean sea level. Ma et al. (2016) discovered that the return levels of extreme sea level during 1980–2012 were higher than those during 1950–1979 at Tianjin. Due to the uneven distribution of tide gauges and data limitation, most studies above concentrated on the Yellow Sea, East China Sea, and the South China Sea. Besides, few work focuses on analyzing the future changes of extreme sea levels along the China coast.

The Paris Climate Agreement aims to hold global warming well below 2.0°C and to pursue efforts to limit it to 1.5°C above preindustrial temperature. Recently, increasing studies have been performed to investigate the extreme climate events at the 1.5 and 2°C warming levels and the superiority of limiting warming to 1.5°C rather than 2.0°C (Schleussner et al., 2016; Donnelly et al., 2017; Karmalkar and Bradley, 2017; King and Karoly, 2017; King et al., 2017; Lehner et al., 2017; Xu et al., 2017; Li et al., 2018). It is necessary to quantify the extreme sea levels changes under the 1.5 and 2.0°C warming scenarios and evaluate the differences between them.

In this paper, hourly sea level data from 15 tide gauges along the China coast and sea level data from three simulations of the Coupled Model Intercomparison Project Phase 5 (CMIP5) were used to answer the following questions: (1) How did the extreme sea level change during the past decades? (2) How will the extreme sea level change in future 1.5 and 2.0°C warming scenarios? (3) What will the extreme sea level differences be between 1.5 and 2.0°C warming climate?

DATA AND METHODSOLOGY

Data

Observed and numerical sea level data are applied in this study, including hourly sea level data from 15 tide gauges (Huludao, Qinhuangdao, Longkou, Yantai, Rizhao, Lusi, Dajishan, Zhenhai, Kanmen, Shansha, Xiamen, Shanwei, Zhapo, Haikou, and Beihai) along the China coast, and three CMIP5 simulations results downloaded from the online CMIP5 datasets (CNRM-CM5, BCC-CSMI-1, MIROC-ESM-CHEM).

The gauge data were obtained from the marine monitoring stations in China (**Figure 1**), dating from January, 1980 to December, 2016. All these data last for more than 30 years, which is essential to get the trends accurately (Feng et al., 2015). Careful quality control had been done to delete the data spikes and spurious records (Wang et al., 2013). In addition, data availability less than 60% were excluded in the analysis.

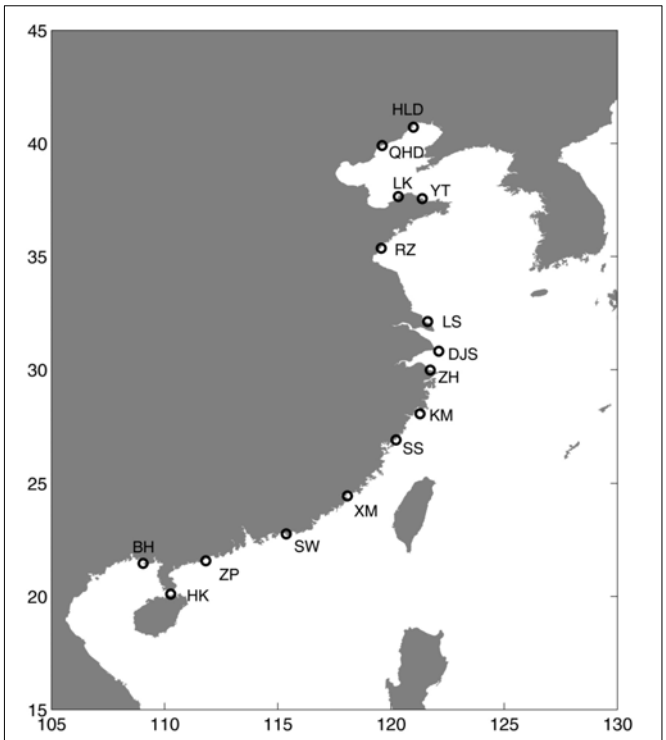

FIGURE 1 | Locations of 15 tide gauges along the coast of China used in this work: HLD, Huludao; QHD, Qinhuangdao; LK, Longkou; YT, Yantai; RZ, Rizhao; LS, Lusi; DJS, Dajishan; ZH, Zhenhai; KM, Kanmen; SS, Shansha; XM, Xiamen; SW, Shanwei; ZP, Zhapo; HK, Haikou; and BH, Beihai.

The sea-level projection in this study is based on CMIP5 numerical simulations. Three models were selected in this work (**Table 1**). The sea level data reached the warming limits of 1.5 and 2.0°C were used. Two oceanic data categories, i.e., "zostoga" (the global average sea-level change due to thermal expansion) and "zos" (the local steric and dynamic adjustment of sea-level change) are used to project the regional sea level change. The data were modified in each model through the following procedures: (I) perform a quadratic-fit as a function of time at each grid point of the piControl experiment; (II) remove the quadratic-fitted control drift from the corresponding grid point of the historical and RCPs (Representative Concentration Pathways) experiments; (III) subtract the global mean of the "zostoga" and "zos" field at each time step from each grid point (Slangen et al., 2014). The projected contributions from land ice and land water storage to local sea-level change are obtained by multiplying the

TABLE 1 | The selected CMIP5 simulations.

	Resolution	Period	Selected period
CNRM-CM5	0.6° × 1.0°	2006–2100	2006–2060
BCC-CSMI-1	0.8°° × 1.0°	2006–2100	2006–2050
MIROC-ESM-CHEM	0.7° × 1.2°	2006–2100	2006–2042

global mean estimates from IPCC AR5 by the regional scaling factors given by Slangen et al. (2014). All glaciers, ice caps and the ice sheets on Greenland and Antarctica are comprised in the land ice contribution. In addition, the glacier isostatic adjustment (GIA) is also included here (Slangen et al., 2014).

Sea level data from tide gauge and satellite located in the Xisha (111.51°N, 16.44°E) were used to validate the sea level data from three models (**Figure 2**). Results show that although there are some differences between the observations and the model results at the interannual and decadal time scales, all three models are in good agreement with the observations at the long-term time scale. These results enhance the confidence in the quality of the projected data got from the three climate models.

Methodology

The extreme sea levels defined as the maximum level during a selected period, usually a year, were mainly caused by the storm surges. It was usually the maximum water level during a storm surge event. To calculate the precise extreme sea level rise rates and to identify potential rate changes are of vital importance for this study. In general, the sea level change trend is estimated by analyzing its oscillatory behavior, which means extracting periodic components from original observations successively until there is no periodic component left (Jevrejeva et al., 2006; Ezer and Corlett, 2012; Breaker and Ruzmaikin, 2013). Due to the empirical, intuitive, direct and adaptive characteristics, the empirical mode decomposition (EMD) method is suitable for estimating the accurate long-term trend of the sea level data (Huang et al., 1998, 1999) and has been widely used to get the long-term change of the mean sea levels recently (Ezer and Corlett, 2012; Breaker and Ruzmaikin, 2013; Ezer et al., 2013; Uranchimeg et al., 2013).

The EMD method decomposes an arbitrary time series $X(t)$ into a finite and often small number of intrinsic mode functions (IMFs), which are defined as any function with an equal number of extreme and zero-crossing. Then $X(t)$ can be described as:

$$X(t) = \sum_{j=1}^{n} IMF_j + r_n$$

where n is the number of IMFs, and r_n is the residual. For more descriptions of the EMD method, refer to Huang et al. (1998).

Ensemble empirical mode decomposition (EEMD) is the improved method to obtain IMFs with more direct physical meaning and greater uniqueness (Wu and Huang, 2009). EEMD was estimated by averaging numerous EMD runs with the addition of some white noise. By averaging the different decompositions, the noise was averaged out and the true decomposition was calculated with a confidence estimate. The EEMD method was used to analyze the extreme sea levels in the study.

The risks associated with extreme sea levels can be assessed from the estimates of return levels and return periods. The return period of extreme sea level is defined as the sea level statistically expected to be equaled or exceeded every specific year. The Federal Emergency Management Agency [FEMA] (2004) recommended the frequency analysis metho3d to obtain the return levels. The traditional probability distribution methods, including the Gumbel, Weibull, Generalized Pareto Distribution (GPD), and Generalized Extreme Value (GEV) distributions, are typically used to analyze annual extreme sea levels. According to previous studies (Vogel et al., 1993; Huang et al., 2008; Feng and Jiang, 2015) the GEV distribution was used in this work to get the return levels of the extreme sea levels. As

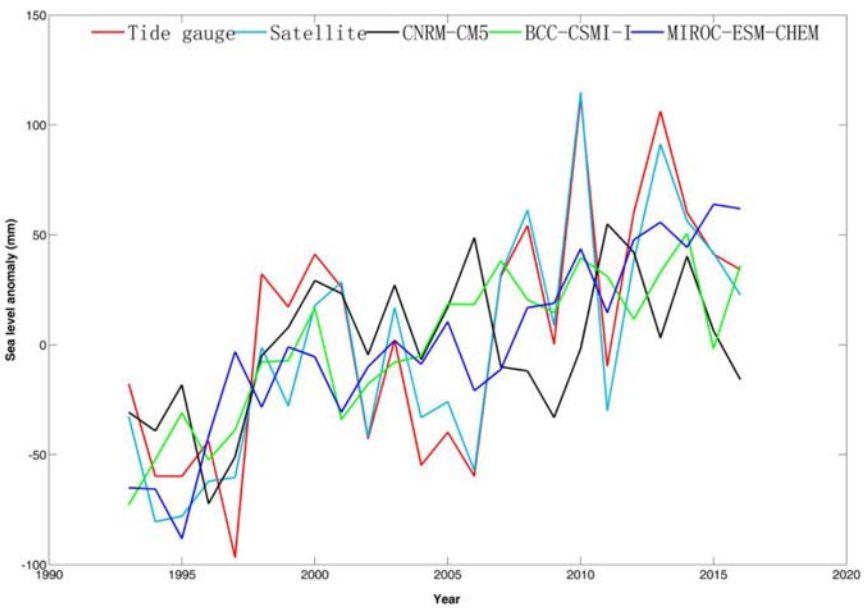

FIGURE 2 | The sea level anomaly calculated using the data from the tide gauge, the satellite, CNRM-CM5, BCC-CSMI-I, and MIROC-ESM-CHEM during 1993 and 2016.

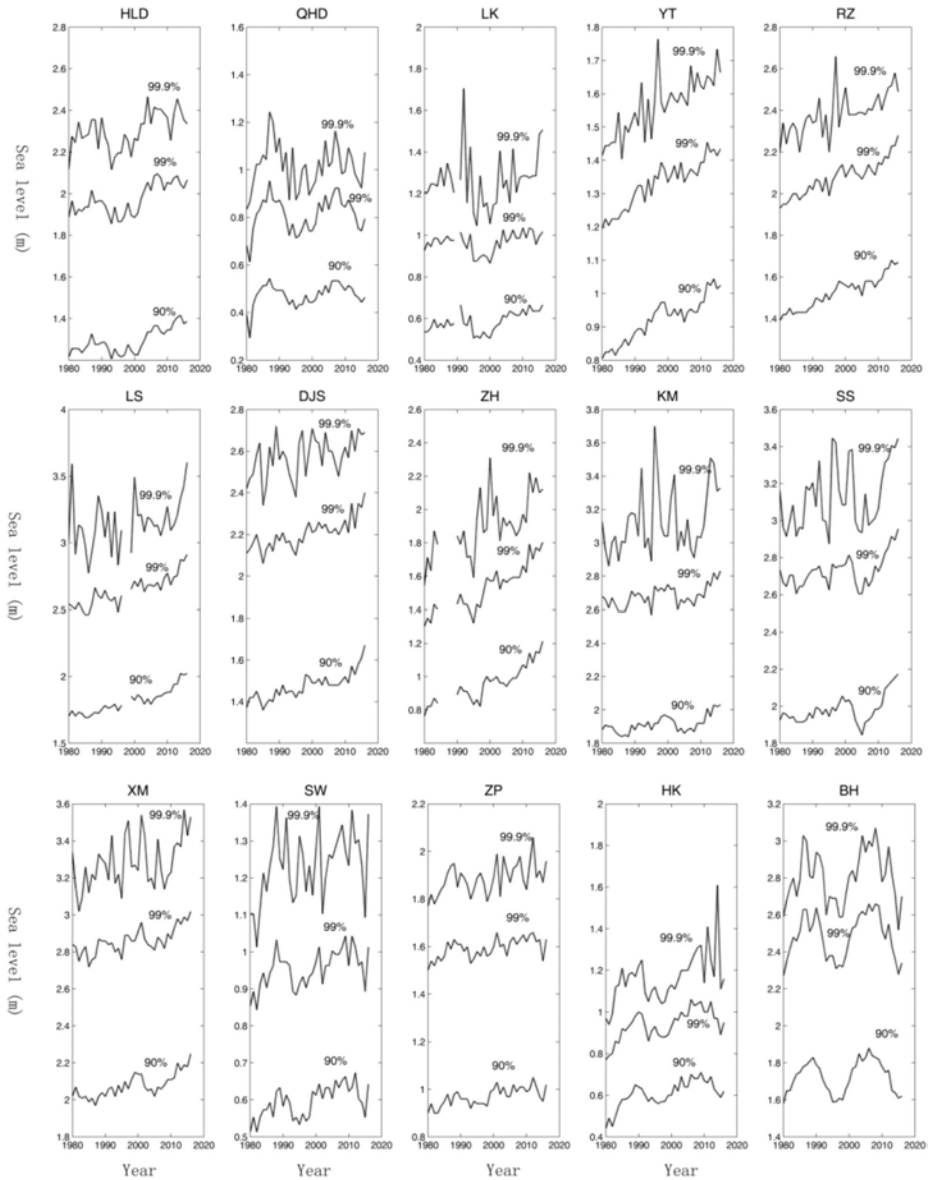

FIGURE 3 | 99.9, 99, and 90% values of the observed sea level at 15 tide gauges.

described in FEMA'S guideline (2014) the GEV distribution can be described by the probability density function (PDF) listed as follows:

$$f(x) = \frac{1}{b}\left\{1 + c\left(\frac{x-a}{b}\right)\right\}^{-\left[1/c-1\right]} e^{-\left(1+c(x-a)/b\right)^{-1/c}}$$

for $-\infty < x \leq a - \frac{b}{c}$ with $c < 0$

and $a - \frac{b}{c} \leq x < \infty$ with $c > 0$

$$f(x) = \frac{1}{b}\exp\left\{-\frac{(x-a)}{b} - \exp\left[-\frac{(x-a)}{b}\right]\right\}$$

for $-\infty \leq x < \infty$ with $c = 0$

where, a, b, and c are the location, scale and shape factors.

RESULTS AND DISCUSSION

Changes of the Extreme Sea Level

Percentile analysis method has been widely used to assess the extreme sea level changes (Menéndez and Woodworth, 2010; Feng et al., 2015; Marcos and Woodworth, 2017). 99.9, 99, and 90% levels of the observed sea level have been calculated at all 15 tide gauges (**Figure 3**). Results show that the three percentile levels of extreme sea level all rose with fluctuations at nearly all tide gauges except at QHD, SW, and BH. Also the long-term trend was not significant at the 95% confidence level at QHD, LK, SW, KM, and BH. Results also show that the increase rates are different at different percentile levels. Meanwhile clear decadal variations and interannual variations exist in the extreme sea

TABLE 2 | Correlation coefficient between the extreme sea level and mean sea level at 15 tide gauges (C1) and the correlations after detrending (C2), the P1/P2 are the *p*-value from *t*-test (where $p < 0.05$ means that the correlation was significant at 95% confidence level).

	C1	P1	C2	P2
HLD	0.33	0.04	−0.06	0.73
QHD	0.46	0.01	0.53	0.01
LK	0.28	0.09	0.28	0.09
YT	0.79	< 0.01	0.22	0.19
RZ	0.66	< 0.01	0.21	0.22
LS	0.43	0.01	0.28	0.10
DJS	0.61	< 0.01	0.43	0.01
ZH	0.68	< 0.01	0.39	0.02
KM	0.45	0.01	0.30	0.07
SS	0.66	< 0.01	0.56	< 0.01
XM	0.47	0.01	0.24	0.16
SW	0.41	0.01	0.12	0.47
ZP	0.49	< 0.01	0.19	0.24
HK	0.33	0.05	−0.32	0.05
BH	0.15	0.37	0.12	0.46

levels at all tide gauges. Especially the interannual variation was quite large at KM, SS, XM, and BH, where the amplitude of interannual variations were larger than 0.40 m.

Previous researches Feng and Tsimplis (2014) and Feng et al. (2015) show that the changes of extreme sea levels along the China coast were highly affected by the sea level change especially the long-term change. The correlations between the extreme sea level and mean sea level were calculated and shown in **Table 2**. Results show that the extreme sea levels were significantly correlated with the mean sea levels at most of the 15 tide gauges. The correlations were larger than 0.5 at YT, RZ, DJS, ZH, and SW. There are two tide gauges, LK and BH, where the extreme sea level was not significantly correlated with the mean sea level. Moreover, the correlation coefficients after detrending were also calculated. Results show that the correlations decrease after detrending. The correlation became non-significant at 95% significant level after detrending at HLD, YT, RZ, LS, XM, SW, ZP, and HK. Results indicate that the changes of mean sea level play important roles in the changes of extreme sea level along the China coast, and mean sea levels mainly affected the long-term change of the extreme sea levels. This conclusion coincides with previous studies, which indicated that the long-term trend of the extreme sea levels was mainly affected by the mean sea levels (Zhang et al., 2000; Woodworth and Blackman, 2004; Marcos et al., 2009).

Using the EEMD method the long term trends of the extreme sea levels along the Chinese coast were estimated in the study. **Figure 4** shows that the extreme sea levels along the Chinese coast show increase trend in general. Meanwhile the long term trends show various patterns at different tide gauges. At HLD, LK, KM, and BH the increase rate accelerates during the past years. At YT, RZ, DJS, ZH, XM, and SS the increase trends were nearly linear. At QHD, SW, and ZP the increase trends were not significant at 95% confidence level. At LS the increase rate first slowed down but after 2000 the increase rate accelerated. At HK the increase trend slowed down during the past years.

Projections of the Extreme Sea Level Return Levels

The projected sea levels from three simulations of the CMIP5 were used in the work (section Data). The sea level data reached the 1.5 and 2.0°C scenario of three models were shown in **Figure 5**. Results show that the sea level of the three selected models rise with fluctuations. The sea levels were much higher at the 2.0°C warming conditions than the 1.5°C warming conditions at all three models. Among the three

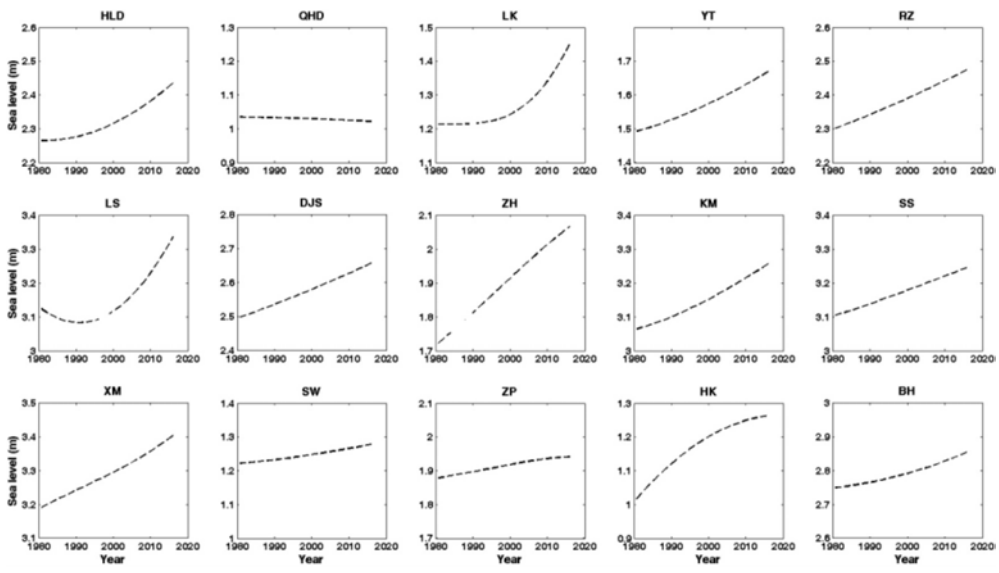

FIGURE 4 | Long term trends of the extreme sea levels at 15 tide gauges along the Chinese coast.

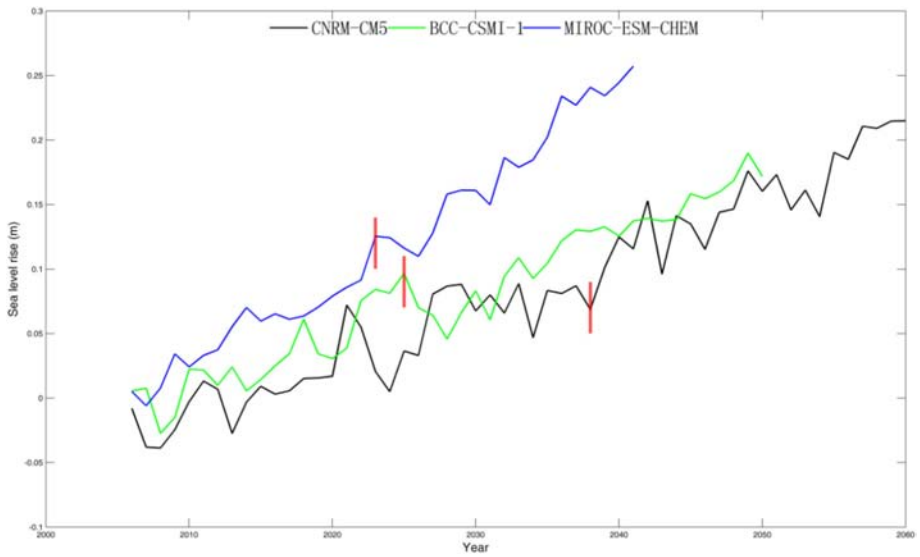

FIGURE 5 | The sea level rise (compared with the mean sea level from 1985 to 2016) of three models under RCP4.5 scenarios, the sea level rise reached the 2°C scenario (whole line), the sea level rise reached the 1.5°C scenario (2006- red line break).

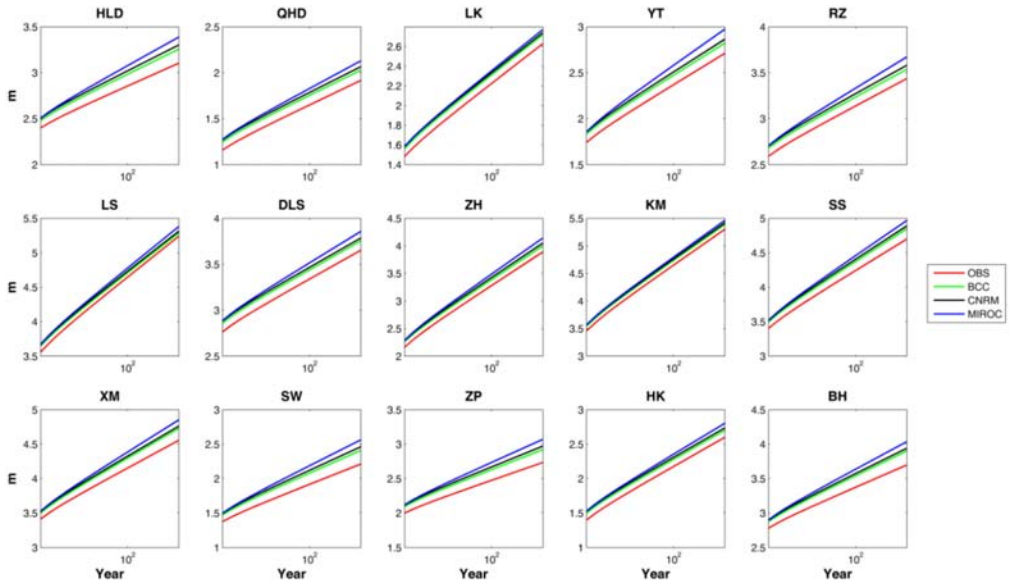

FIGURE 6 | Return levels of the extreme sea level at present (blue line), return levels of the extreme sea level under the 1.5°C temperature rise scenarios [BCC-CSMI-1(black line), CNRM-CM5(red line), MIROC-ESM-CHEM(green line)].

models the sea level of the MIROC-ESM-CHEM increased the fastest. The increase rate of the CNRM-CM5 and BCC-CSMI-1 is nearly the same. The CNRM-CM5 reached 1.5°C warming conditions in 2038 and reached 2.0°C warming conditions in 2060. The BCC-CSMI-1 and MIROC-ESM-CHEM reached 1.5 and 2.0°C warming conditions earlier than the CNRM-CM5.

Using the method described in section Methodology the return levels of the extreme sea level under the 1.5 and 2.0°C warming conditions were calculated. **Figures 6**, **7** show that the return levels of the extreme sea level changed under the 1.5 and 2.0°C warming conditions. And the differences between the 1.5 and 2.0°C scenarios were quite large. Under the 1.5°C warming condition the changes of the return levels were small. At some tide gauges there are nearly no changes in the return levels. Under 2.0°C warming condition the return levels of the extreme sea level of three models significant increased. In order to show the changes of the return levels more clearly, the 100-year return levels under three scenarios were calculated and shown in **Table 3**.

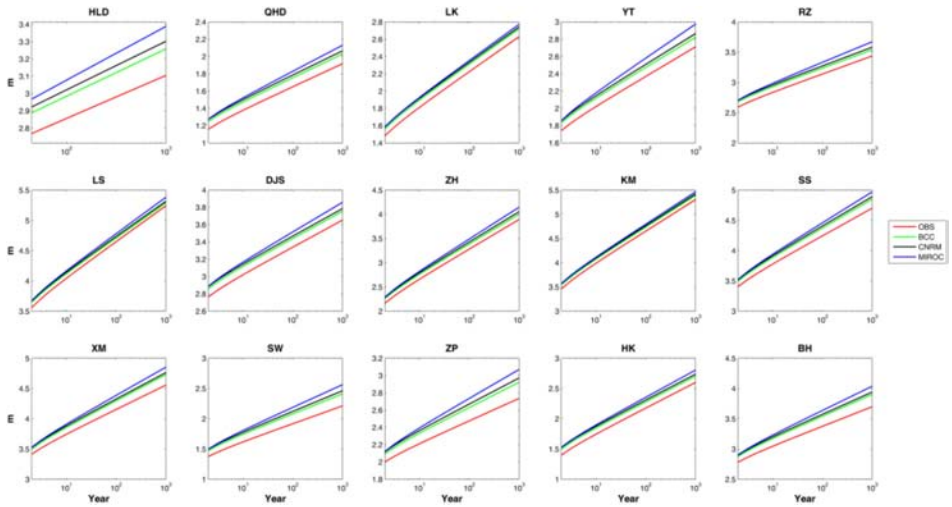

FIGURE 7 | Return levels of the extreme sea level at present (blue line), return levels of the extreme sea level under the 2.0°C temperature rise scenarios [BCC-CSMI-1(black line), CNRM-CM5(red line), MIROC-ESM-CHEM(green line)].

Compared with the present scenario, the 100-year return levels under the 1.5°C warming condition changed little at most tide gauges in BCC-CSMI-1 and CNRM-CM5. The 100-year return level changes ranged from -3 to 5 cm in BCC-CSMI-1. And in CRRM-CM5 the 100-year return level changes ranged from -4 to 4 cm. The changes of 100-year return levels in MIROC-ESM-CHEM ranged from -3 to 6 cm, and the 100-year return levels were larger than in the other two models at most tide gauges.

Under the 2.0°C warming condition, the changes of 100 year return levels were much larger than those under the 1.5°C warming condition in all three models. In BCC-CSMI-1 the 100-return level changes ranged from 8 to 20 cm, and the 100-year return levels correspond to the water levels of 140∼562 year return period under the present condition. Comparing to the 1.5°C warming condition the 100-year return levels increased about 4∼18 cm. In CNRM-CM5 the 100-return level changes ranged from 6 to 17 cm, and the 100 year return levels under the 2.0°C warming condition correspond to the water levels of 127∼394 return period under the present condition. Comparing to the 1.5°C warming condition the 100 year return levels increased about 8∼14 cm. In MIROC-ESM-CHEM the 100 return level changes ranged from 13 to 27 cm, and the 100 year return levels under the 2.0°C warming condition correspond to the water levels of 165∼998 year return period under the present condition. Comparing to the 1.5°C warming condition

TABLE 3 | Hundred-year return levels of the extreme sea level in present (unit is meter), under the 1.5 and 2°C scenario (from climate model) at 15 tide gauges, the return period (year) of the water levels in present scenario were listed in the bracket.

(m)	OBS	BCC-CSMI-1		CNRM-CM5		MIROC-ESM-CHEM	
		1.5°C	2.0°C	1.5°C	2.0°C	1.5°C	2.0°C
HLD	2.85	2.86 (102)	3.02 (460)	2.86 (102)	2.98 (327)	2.89 (134)	3.08 (777)
QHD	1.65	1.67 (117)	1.79 (322)	1.66 (105)	1.75 (244)	1.68 (131)	1.83 (467)
LK	2.22	2.26 (121)	2.33 (184)	2.24 (109)	2.31 (163)	2.25 (116)	2.35 (207)
YT	2.37	2.34 (85)	2.51 (255)	2.33 (80)	2.47 (201)	2.37 (100)	2.58 (415)
RZ	3.14	3.14 (100)	3.27 (255)	3.11 (95)	3.24 (212)	3.14 (100)	3.33 (445)
LS	4.65	4.64 (96)	4.73 (140)	4.62 (90)	4.71 (127)	4.62 (90)	4.78 (166)
DJS	3.34	3.35 (111)	3.47 (256)	3.34 (100)	3.44 (207)	3.35 (111)	3.52 (364)
ZH	3.28	3.27 (95)	3.42 (174)	3.27 (95)	3.39 (148)	3.30 (106)	3.49 (218)
KM	4.65	4.66 (103)	4.76 (148)	4.66 (103)	4.74 (135)	4.66 (103)	4.80 (165)
SS	4.24	4.26 (112)	4.41 (228)	4.26 (112)	4.37 (191)	4.28 (117)	4.46 (296)
XM	4.15	4.16 (105)	4.33 (269)	4.16 (105)	4.30 (227)	4.18 (119)	4.39 (377)
SW	1.92	1.94 (121)	2.12 (491)	1.95 (124)	2.08 (355)	1.96 (143)	2.19 (822)
ZP	2.48	2.49 (108)	2.67 (562)	2.49 (108)	2.63 (394)	2.52 (145)	2.74 (998)
HK	2.18	2.17 (97)	2.31 (207)	2.19 (108)	2.28 (174)	2.20 (110)	2.35 (263)
BH	3.37	3.42 (136)	3.57 (411)	3.41 (132)	3.54 (325)	3.43 (153)	3.64 (643)

the 100-year return levels increased about 10∼23 cm. Results indicated that a 0.5°C warming will make much difference in the extreme sea levels along the Chinese coast in all three models.

CONCLUSION

The growing concerns about climate change have motivated numerous researchers to study the effects of climate change in coastal areas. As one of the most important marine factors in coastal areas, extreme sea level has drawn more and more attentions in recent years. In this paper, we used hourly sea level data from 15 tide gauges along the China coast and numerical sea level data from three simulations of the CMIP5, to analyze the changes of extreme sea level in the past and under the 1.5 and 2°C warmer future scenarios.

The extreme sea levels rise with fluctuations at most tide gauges along the China coast, and the long term trends show various patterns. Quasi-linear trends are found at YT, RZ, DJS, ZH, XM, and SS, while no significant trends exists at QHD, SW, and ZP. The extreme sea level starts to rise since 2000 at LS, and the rise decelerates at HK during the past years. The mean sea level changes play important roles in the changes of extreme sea levels along the China coast, especially for the long-term change.

Under the 1.5 and 2.0°C warming scenarios, the sea level rise with fluctuations according to the simulation results by three selected models, and the sea levels are much higher under the 2.0°C warming scenarios. The return levels of the extreme sea level vary significantly under different warming scenarios, and there is considerable increase of the return levels at all tide gauges along the China coast under 2.0°C warming scenario compared with that under 1.5°C warming scenario. The results indicated that a 0.5°C warming will bring about major difference for the extreme sea levels along the China coast. It is reasonable to limit the anthropogenic warming to 1.5°C rather than 2.0°C based on this study, as proposed by the Paris Climate Agreement, and it is necessary and practical for future flood risk management and response along the coast of China.

There are also some caveats in this study. In order to meet the warming condition of 1.5 and 2.0°C, the data lengths of the three model here are different. And only three models are analyzed in this study and there may be some uncertainty in the results presented in this manuscript. Besides, only the results of the RCP4.5 scenario were applied in this work.

AUTHOR CONTRIBUTIONS

JF conceptualized the research and contributed to the discussion and interpretation of the results. HL gave the sea level rise results used in this work. DL, QL, HW, and KL prepared and conducted some of the data analysis in the work. All authors contributed to the revision and approved the manuscript.

FUNDING

This work was supported by the National Key Research Projects (Grant Nos. 2016YFC1401900, 2017YFC1404200, 2017YFA0604101, and 2017YFA0604102), and the National Natural Science Foundation of China (Grant Nos. 41706020 and 41406032) and Open Fund if the Key Laboratory of Research on Marine Hazards Forecasting and the National Natural Science Foundation of China (41706019).

REFERENCES

Breaker, L. C., and Ruzmaikin, A. (2013). Estimating rates of acceleration based on the 157-year record of sea level from San Francisco, California, U.S.A. *J. Coast. Res.* 29, 43–51. doi: 10.2112/JCOASTRES-D-12-00048.1

Busuioc, A., Giorgi, F., Bi, X., and Ionita, M. (2006). Comparison of regional climate model and statistical downscaling simulations of different winter precipitation change scenarios over Romania. *Theor. Appl. Climatol.* 86, 101–123. doi: 10.1007/s00704-005-0210-8

Chen, S., and Wang, B. (1993). Analysis of maximum water level in the Changjiang estuary. *J. East China Norm. Univ.* 3, 75–82.

Church, J., Clark, P., Cazenave, A., Gregory, J., Jevrejeva, S., Levermann, A., et al. (2013). "Sea level change," in *Climate Change 2013: The Physical Science Basis. Contribution of Working Group in the Fifth Assessment Report of the Intergovernmental Panel on Climate Change*, eds T. F. Stocker, D. Qin, G.-K. Plattner, M. Tignor, S. K. Allen, J. Boschung, et al. (Cambridge: Cambridge University Press).

Ding, X., Zheng, D., Chen, Y., Chao, J., and Li, Z. (2001). Sea level change in Hong Kong from tide gauge measurements of 1954-1999. *J. Geod.* 74, 683–689. doi: 10.1007/s001900000128

Donnelly, C., Greuell, W., Andersson, J., Gerten, D., Pisacane, G., Roudier, P., et al. (2017). Impacts of climate change on European hydrology at 1.5, 2 and 3 degrees mean global warming above preindustrial level. *Clim. Change* 143, 13–26. doi: 10.1007/s10584-017-1971-7

Ezer, T., Atkinson, L. P., Corlett, W. B., and Blanco, J. L. (2013). Gulf Stream's induced sea level rise and variability along the U.S. mid-Atlantic coast. *J. Geophys. Res.* 118, 685–697. doi: 10.1002/jgrc.20091

Ezer, T., and Corlett, W. B. (2012). Is sea level rise accelerating in the Chesaperake Bay? A demonstration of a novel new approach for analyzing sea level data. *Geophys. Res. Lett.* 39:L19605.

Federal Emergency Management Agency [FEMA] (2004). *Final Draft Guidelines for Coastal Flood Hazard Analysis and Mapping for the Pacific Coast of the United States*. Washington, DC: FEMA.

Feng, J., and Jiang, W. (2015). Extreme water level analysis at three stations on the coast of the Northwestern Pacific Ocean. *Ocean Dyn.* 65, 1383–1397. doi: 10.1007/s10236-015-0881-3

Feng, J., von Storch, H., Jiang, W., and Weisse, R. (2015). Assessing changes in extreme sea levels along the coast of China. *J. Geophys. Res. Ocean* 120, 8039–8051. doi: 10.1002/2015JC011336

Feng, X., and Tsimplis, M. N. (2014). Sea level extremes at the coasts of China. *J. Geophys. Res. Ocean* 119, 1593–1608. doi: 10.1002/2013JC009607

Grossmann, I., Woth, K., and von Storch, H. (2007). Localization of global climate change: storm surge scenarios for Hamburg in 2030 and 2085. *Die Küste* 71, 169–182.

Huang, N. E., Shen, Z., and Long, S. R. (1999). A new view of nonlinear water waves: the Hilbert spectrum. *Annu. Rev. Fluid Mech.* 31, 417–457. doi: 10.1146/annurev.fluid.31.1.417

Huang, N. E., Shen, Z., Long, S. R., Wu, M. C., Shih, E. H., Zheng, Q., et al. (1998). The empirical mode decomposition and the Hilbert spectrum for non stationary time series analysis. *Proc. R. Soc. Lond.* 454, 903–995. doi: 10.1098/rspa.1998.0193

Huang, W., Xu, S., and Nnaji, S. (2008). Evaluation of GEV model for frequency analysis of annual maximum water levels in the coast of United States. *Ocean Eng.* 35, 1132–1147. doi: 10.1016/j.oceaneng.2008.04.010

Jevrejeva, S., Grinsted, A., Moore, J. C., and Holgate, S. (2006). Nonlinear trends and multiyear cycles in sea level records. *J. Geophys. Res.* 11:C09012. doi: 10.1029/2005JC003229

Karmalkar, A. V., and Bradley, R. S. (2017). Consequences of global warming of 1.5°C and 2°C for regional temperature and precipitation changes in the contiguous United States. *PLoS One* 12:e0168697. doi: 10.1371/journal.pone.0168697

King, A. D., and Karoly, D. J. (2017). Climate extremes in Europe at 1.5 and 2 degrees of global warming. *Environ. Res. Lett.* 12:114031. doi: 10.1088/1748-9326/aa8e2c

King, A. D., Karoly, D. J., and Henley, B. J. (2017). Australian climate extremes at 1.5°C and 2°C of global warming. *Nat. Clim. Change* 7, 412–416. doi: 10.1038/nclimate3296

Langenberg, H., Pfi zenmayer, A., von Storch, H., and Sündermann, J. (1999). Storm related sea level variations along the North Sea coast: natural variability and anthropogenic change. *Cont. Shelf Res.* 19, 821–842. doi: 10.1016/S0278-4343(98)00113-7

Lehner, F., Coats, S., Stocker, T. F., Pendergrass, A. G., Sanderson, B. M., Raible, C. C., et al. (2017). Projected drought risk in 1.5°C and 2°C warmer climates. *Geophys. Res. Lett.* 44, 7419–7428. doi: 10.1002/2017GL074117

Li, D., Zhou, T., Zou, L., Zhang, W., and Zhang, L. (2018). Extreme high temperature events over East Asia in 1.5°C and 2°C warmer futures: analysis of NCAR CESM low-warming experiments. *Geophys. Res. Lett.* 45, 1541–1550. doi: 10.1002/2017GL076753

Ma, X., Zhang, G., Yuan, D., and Li, Y. (2016). Analysis of the characteristics of storm surges in Tianjin coastal area. *Adv. Mar. Sci.* 34, 516–522.

Marcos, M., Tsimplis, M. N., and Shaw, A. G. P. (2009). Sea level extremes in southern Europe. *J. Geophys. Res.* 114:C01007. doi: 10.1029/2008jc004912

Marcos, M., and Woodworth, P. L. (2017). Spatiotemporal changes in extreme sea levels along the coasts of the North Atlantic and the Gulf of Mexico. *J. Geophys. Res.* 122, 7031–7048. doi: 10.1002/2017JC013065

Méndez, F. J., Menéndez, M., Luceno, A., and Losada, I. J. (2007). Analyzing monthly extreme sea levels with a time-dependent GEV model. *J. Atmos. Ocean. Technol.* 24, 894–911. doi: 10.1175/JTECH2009.1

Menéndez, M., and Woodworth, P. L. (2010). Changes in extreme high water levels based on a quasi-global tide-gauge data set. *J. Geophys. Res.* 115:C10011. doi: 10.1029/2009JC005997

Schleussner, C.-F., Lissner, T. K., Fischer, E. M., Wohland, J., Perrette, M., Golly, A., et al. (2016). Differential climate impacts for policy-relevant limits to global warming: the case of 1.5°C and 2°C. *Earth Syst. Dyn.* 6, 2447–2505. doi: 10.5194/esdd-6-2447-2015

Slangen, A. B. A., Carson, M., Katsman, C. A., van de Wal, R. S. W., Köhl, A., Vermeersen, L. L. A., et al. (2014). Projecting twenty-first century regional sea-level changes. *Clim. Change* 124, 317–332. doi: 10.1007/s10584-014-1080-9

Tsimplis, M. N., and Shaw, A. G. P. (2010). Seasonal sea level extremes in the Mediterranean Sea and at the Atlantic European coasts. *Nat. Hazards Earth Syst. Sci.* 10, 1457–1475. doi: 10.5194/nhess-10-1457-2010

Uranchimeg, S., Cho, H. R., Kim, Y. T., Hwang, K. N., and Kwon, H. H. (2013). Estimating the accelerated sea level rise along the Korean Peninsula using multiscale analysis. *J. Coast. Res.* 75, 770–774. doi: 10.2112/SI75-155.1

Vogel, R. M., Tomas, W. J., and Mcmahon, T. A. (1993). Flood-flow frequency model selection in Southwestern United States. *J. Water Resour. Plan. Manage.* 119, 353–366. doi: 10.1061/(ASCE)0733-9496(1993)119:3(353)

von Storch, H., and Reichardt, H. (1997). A scenario of storm surge statistics for the German Bight at the expected time of doubled atmospheric carbon dioxide concentration. *J. Clim.* 10, 2653–2662. doi: 10.1175/1520-0442(1997)010<2653:ASOSSS>2.0.CO;2

Wang, H., Liu, K., Fan, W., and Fan, Z. (2013). Data uniformity revision and variations of the sea level of the western Bohai Sea. *Mar. Sci. Bull.* 32, 256–264.

Wang, H., Liu, K., Wang, A., Feng, J., Fan, W., Liu, Q., et al. (2018). Regional characteristics of the effects of the El Niño-Southern Oscillation on the sea level in the China Sea. *Ocean Dyn.* 68, 485–495. doi: 10.1007/s10236-018-1144-x

Woodworth, P. L., and Blackman, D. L. (2004). Evidence for systematic changes in extreme high water since the mid-1970s. *J. Clim.* 17, 1190–1197. doi: 10.1175/1520-0442(2004)017<1190:EFSCIE>2.0.CO;2

Woth, K., Weisse, R., and von Storch, H. (2006). Climate change and North Sea storm surge extremes: an ensemble study of storm surge extremes expected in a changed climate projected by four different regional climate models. *Ocean Dyn.* 56, 3–15. doi: 10.1007/s10236-005-0024-3

Wu, Z., and Huang, N. E. (2009). Ensemble empirical mode decomposition: a noise-assisted data analysis method. *Adv. Adapt. Data Anal.* 1, 1–41. doi: 10.1142/S1793536909000047

Xu, Y., Zhou, B.-T., Wu, J., Han, Z.-Y., Zhang, Y.-X., and Wu, J. (2017). Asian climate change under 1.5–4°C warming targets. *Adv. Clim. Change Res.* 8, 99–107. doi: 10.1016/j.accre.2017.05.004

Yu, Y., Yu, Y., and Zuo, J. (2003). Effect of sea level variation on tidal characteristic values for the East China Sea. *China Ocean Eng.* 17, 369–382.

Zhang, K., Douglas, B. C., and Leatherman, S. P. (2000). Twentieth-century storm activity along the U.S. east coast. *J. Clim.* 13, 1748–1761. doi: 10.1175/1520-0442(2000)013<1748:TCSAAT>2.0.CO;2

Zuo, J., Du, L., and Alvaro, P. (2007). The characteristic of near-surface velocity during upwelling season on the northern Portugal shelf. *J. Ocean Univ. China* 6, 213–225. doi: 10.1007/s11802-007-0213-4

Conflict of Interest Statement: The authors declare that the research was conducted in the absence of any commercial or financial relationships that could be construed as a potential conflict of interest.

frontiers in Environmental Science

ORIGINAL RESEARCH
published: 29 January 2019
doi: 10.3389/fenvs.2018.00163

Robustness and Scalability of Regional Climate Projections Over Europe

Dominic Matte[1,2]*, *Morten Andreas Dahl Larsen*[3], *Ole Bøssing Christensen*[2] and *Jens Hesselbjerg Christensen*[1,2,4]

[1] Physics of Ice, Department of Climate and Earth, Niels Bohr Institute, University of Copenhagen, Copenhagen, Denmark, [2] Danish Meteorological Institute, Copenhagen, Denmark, [3] Department of Management Engineering, Technical University of Denmark, Lyngby, Denmark, [4] NORCE Norwegian Research Centre AS, Bergen, Norway

Climate change projections for Europe consistently indicate a future decrease in summer precipitation over southern Europe and an increase over northern Europe. However, individual models substantially modulate these overarching precipitation change signals. Despite considerable model improvements as well as increasingly higher model resolutions in regional downscaling efforts, these apparent inconsistencies so far seem unresolved. In the present study, we analyze European seasonal temperature and precipitation climate change projections using all readily available pan-European regional climate model projections for the twenty-first century with model resolution increasing from ≈50 to ≈12 km grid distances from the CORDEX modeling project. This allows for an in-depth analysis of what may be the most robust projection of the future climate. Employing a simple scaling with the global mean temperature change enables the identification of emerging robust signals of seasonal changes in temperature and precipitation. Likewise, the "what-if" approach, i.e., analyzing the climate change signal from transient experiments at the time of an emerging global temperature exceedance of e.g., 1, 2, or 3 degrees offers a policy relevant approach to providing more accurate projections. A comparison of the projections from these two approaches has never before been done in a comprehensive manner and is the subject of the present paper.

Keywords: pattern scaling, climate change, EURO-CORDEX, robust information, regional climate model

OPEN ACCESS

Edited by:
Hans Von Storch,
Helmholtz Centre for Materials and Coastal Research (HZG), Germany

Reviewed by:
Silvina A. Solman,
Sea Research Center and Atmospheric Administration (CIMA), Argentina
Stefano Federico,
Italian National Research Council (CNR), Italy

***Correspondence:**
Dominic Matte
dominic.matte@nbi.ku.dk

Specialty section:
This article was submitted to Atmospheric Science, a section of the journal Frontiers in Environmental Science

Received: *31 October 2018*
Accepted: *31 December 2018*
Published: *29 January 2019*

Citation:
Matte D, Larsen MAD, Christensen OB and Christensen JH (2019) Robustness and Scalability of Regional Climate Projections Over Europe. Front. Environ. Sci. 6:163. doi: 10.3389/fenvs.2018.00163

1. INTRODUCTION

In the IPCC Special Report on Global Warming of 1.5°C (IPCC, 2018), a global warming of 1.5°C above pre-industrial levels is used as a target to understand how this warming will impact society and how drastic climate change mitigation actions are needed. At the current rate of change, this target is expected to be reached somewhere between 2030 and 2052. The geographical patterns of the ongoing change are indicators of what the near future may bring and how the longer-time average changes may manifest themselves. If no changes are made to moderate a *business-as-usual* societal development, it is very likely that a higher warming level will be reached increasing the risks for negative societal impacts.

To better understand the near-to-long-term climate change information, climate models are commonly used. Often, a "what-if" approach is used, analyzing climate simulations around the point in time where a target is crossed. For example, Vautard et al. (2014) used an ensemble of 30-year time slices around the point in time where the projected average global temperatures

reach 2°C. They pointed out that Europe will generally experience a higher warming than 2°C, even if mitigation keeps the global average change lower than 2°C. The Copenhagen Accord (UNFCCC, 2009) agreeing on a global 2°C warming target as compared to the pre-industrial value. This agreement has been found to be increasingly challenging to fulfill (Peters et al., 2012; Stocker, 2013; Knutti et al., 2016) and it is likely that a warming of 3 or 4°C will be reached by the end of the century with profound consequences (New et al., 2011). Sanderson et al. (2011) used the A2 scenario from the IPCC Fourth Assessment Report (IPCC, 2007) to study high-end (>4°C) and more moderate (<4°C) projections for the twenty-first century. For the European area, they show little difference between the two classes of global model sensitivity, other than a larger warming in Southern Europe during the summer per degree of global warming for the high-end projections.

Climate models continue to exhibit large inter-model differences due to, among other things, differences in cloud parameterization schemes (Van Weverberg et al., 2013), resolution (Evans and McCabe, 2013), physics (Schwartz et al., 2010), land-surface, water cycle representation (Larsen et al., 2016), and sea ice treatment (Rae et al., 2012). Furthermore, climate models have systematic biases, which further complicates the extraction of useful climate change information. To provide such information, Santer et al. (1990) proposed using a pattern scaling approach. This approach implies a linear relationship between patterns of regional climate change and the average global temperature change. The approach has the considerable advantage of providing climate change information for time periods or emission scenarios for which no simulation is available (Lustenberger et al., 2014). Since Santer et al. (1990), pattern scaling has been widely used (Huntingford and Cox, 2000; Mitchell, 2003; Sanderson et al., 2011; Lustenberger et al., 2014; Tebaldi and Arblaster, 2014; Christensen et al., 2015, 2019). It is worth noting that one of the major conclusions of Mitchell (2003) is the necessity to use a large ensemble to achieve a sufficiently large change signal when compared with the inter-model spread [also called the signal-to-noise ratio (S/N)] to identify a robust signal.

Many coordinated experiments such as CMIP3 (Meehl et al., 2007), CMIP5 (Taylor et al., 2012), PRUDENCE (Christensen et al., 2002; Christensen and Christensen, 2007), ENSEMBLES (Van der Linden and Mitchell, 2009; Christensen et al., 2010), and CORDEX (Giorgi and Gutowski, 2015; Gutowski et al., 2016) have offered the opportunity to deepen our understanding of pattern scaling by using model ensembles (Lustenberger et al., 2014; Tebaldi and Arblaster, 2014; Christensen et al., 2015, 2019). For the particular case of temperature and precipitation, Tebaldi and Arblaster (2014) analyzed the robustness of pattern scaling across time, Representative Concentration Pathways (RCP), and models using the third and fifth phases of the Coupled Model Intercomparison Project (CMIP3 and CMIP5). They concluded that the RCP2.6 scenario is not well suited for pattern scaling due to a weak signal. They also pointed out that pattern variability is explained by the inter-member variability rather than the RCP variability. Their results showed that the pattern scaling is insensitive to the choice of emission scenarios (RCP4.5 or RCP8.5). Overall, only small differences were noted, suggesting that pattern scaling might provide a robust type of information across RCPs. They have also shown a greater variability of the signal for precipitation compared to temperature, which is likely due to differences in parameterization of cumulus convection together with cloud formation (Santer et al., 1990). To better understand high-end scenarios, Christensen et al. (2015) investigated the European response to a global mean warming of 6°C. They showed that a such response was largely linear in global temperature change, comparing to the scaled patterns produced from previous experiments (ENSEMBLES and PRUDENCE), with extreme precipitation as a notable exception (extremes are outside the scope of this study).

Recently, Christensen et al. (2019) applied and compared pattern scaling from several coordinated experiment (PRUDENCE, ENSEMBLES and CORDEX). Their results show comparable patterns and ranges between these projects, suggesting that pattern scaling is robust across modeling initiatives over time. They also compared the scaled patterns of an observational dataset, here using CRU (Harris et al., 2014), and also here show a high correspondence with scaled patterns originating from the coordinated experiments. This result strongly supports that the linearity of pattern scaling is also observed and can be extended to, at least, the end of the twenty-first century. However, models tend to need time to stabilize, so scaled patterns might not emerge until a period of years or even decades. Some studies have analyzed the time dependence of pattern scaling using time-slice experiments (Mitchell, 2003; Lustenberger et al., 2014; Tebaldi and Arblaster, 2014), but the question has not previously been properly studied using a continuous timeline.

In general, the information provided by scaled patterns should be addressed with special attention to the robustness of the signal. It is commonly agreed that the climate change signal must exceed the inter-model spread to reflect proper robustness (Mitchell, 2003; McSweeney and Jones, 2013). In this paper, we wish to address this aspect on a pan-European scale as well as on smaller sub-regions, previously addressed in projects such as ENSEMBLES. The first part of this study shows scaled patterns of the EURO-CORDEX simulations (Jacob et al., 2014) and analyses their levels of robustness. In the second part of the study, the emergence of a significant signal in the scaled patterns is studied to enable a subsequent analysis comparing the what-if approach and the pattern scaling approach. The analysis on the emergence of robust change signals is necessary to enable the detection of patterns extracted from different time windows using the what-if approach. The final focus of the study is to address the robustness of emerging scaled patterns for precipitation and temperature using different metrics on signal, noise and variability. The methodology is explained in section 2 followed by the results in section 3 and finally a brief conclusions is given.

2. MATERIALS AND METHODS

2.1. Data and Sub-domains

The temperature and precipitation fields from the EURO-CORDEX experiment (Giorgi and Gutowski, 2015) at 0.11°

(EUR-11) and 0.44° (EUR-44) are used (see **Figure 1**) for RCP 4.5 and 8.5.

Figure 2 shows the EURO-CORDEX domain and the sub-domains used in this study, with subdomain 6 slightly modified compared to Christensen and Christensen (2007). The analysis on sub-domains is performed to enhance the understanding of regional-to-local signals. Only aggregated results combining RCP4.5 and RCP8.5 are shown; however, analyses suggest (not shown) that no significant differences exist between RCP4.5 and RCP8.5 after scaling, as also shown globally by Tebaldi and Arblaster (2014) and regionally for Europe, as in the present study, in Christensen et al. (2019).

2.2. Methods

2.2.1. The Pattern Scaling Approach

The pattern scaling is defined as the climate change of a 20-year mean (relative to 1985–2004) of the temperature and precipitation fields scaled by the global mean temperature change of the relevant GCM. In this study, the end-century scaled pattern is defined as the one calculated from 2080 to 2099, the latest period available for all models, divided by the time averaged global mean temperature change for the period.

2.2.2. The What-If Approach

The procedure used in the what-if approach is straightforward, as it extracts the year where the GCM in question, for all GCM-RCM combinations, crosses the selected climate change thresholds of 1, 2, and 3°C, respectively, at the first occurrence. We have not observed any multiple crossings, so this definition is unique here. Around the extracted years, a 20-year time average was then calculated from each model member combination followed by averaging all the members. Note that the scale of all patterns extracted by the what-if approach is adjusted to 1°C value (for example, the resulting 3°C pattern was divided by three).

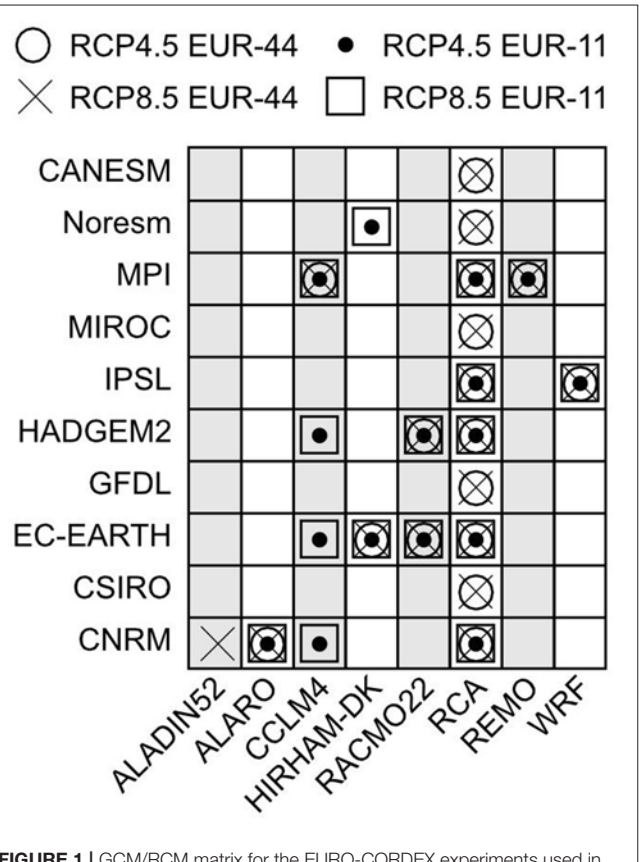

FIGURE 1 | GCM/RCM matrix for the EURO-CORDEX experiments used in this paper.

2.2.3. Signal-To-Noise Ratio

As presented in Christensen et al. (2019), the *S/N* is produced for each scaled pattern output combination and on the results from the what-if approach. The *S/N* is defined as:

$$S/N = \frac{< SP >}{\sigma_{SP}}, \quad (1)$$

where $<SP>$ is the scaled patterns average of all the members and σ_{SP} is the inter-member (32 members for EUR-11 and 35 members for EUR-44; see **Figure 1**) standard deviation of the scaled patterns from the net model results (i.e., there is no inter-annual variability component in this noise). The *S/N* is considered a good proxy of the robustness of the signal. When $S/N > 1$, the level of change is identified as significant change. It is worth noting that precipitation results are shown for relative changes (in %) unless stated otherwise.

3. RESULTS

3.1. Scaled Pattern at the End of the Century

The end-of-century scaled patterns for temperature in DJF (first two rows of **Figure 3**) are showing strong warming in the north-east of the domain with a smaller value over the Atlantic Ocean as also observed by other studies (Christensen et al., 2015, 2019). However, although some larger differences can be observed in the S/N, the percentage of grid points where S/N < 1 (shown in the upper-left corner of each figure) is quite small if not zero. Only the area over the Atlantic Ocean is affected by S/N < 1 due to a moderate climate change signal. Note that EUR-44 is slightly warmer than the EUR-11. This is caused by the slightly different model ensembles available. Employing only models and hence identical model ensembles for the two resolutions, the scaled patterns between EUR-11 and EUR-44 do not show differences in temperature (not shown).

The scaled patterns of the precipitation fields for DJF (last two rows of **Figure 3**) are showing, overall, a future with a wetter climate over northern Europe and drier conditions over the southern and north-western parts of the domain; the S/N ratio is quite similar. However, the percentage of grid points with S/N < 1 is considerably higher for precipitation (53, 63% for EUR-11 and EUR-44, respectively) indicating a higher disparity between ensemble members. In general, Northern European land areas have S/N larger than one. This is consistent with the global tendency of increased intensity of the hydrological cycle with global warming. The results show relatively low-level noise over

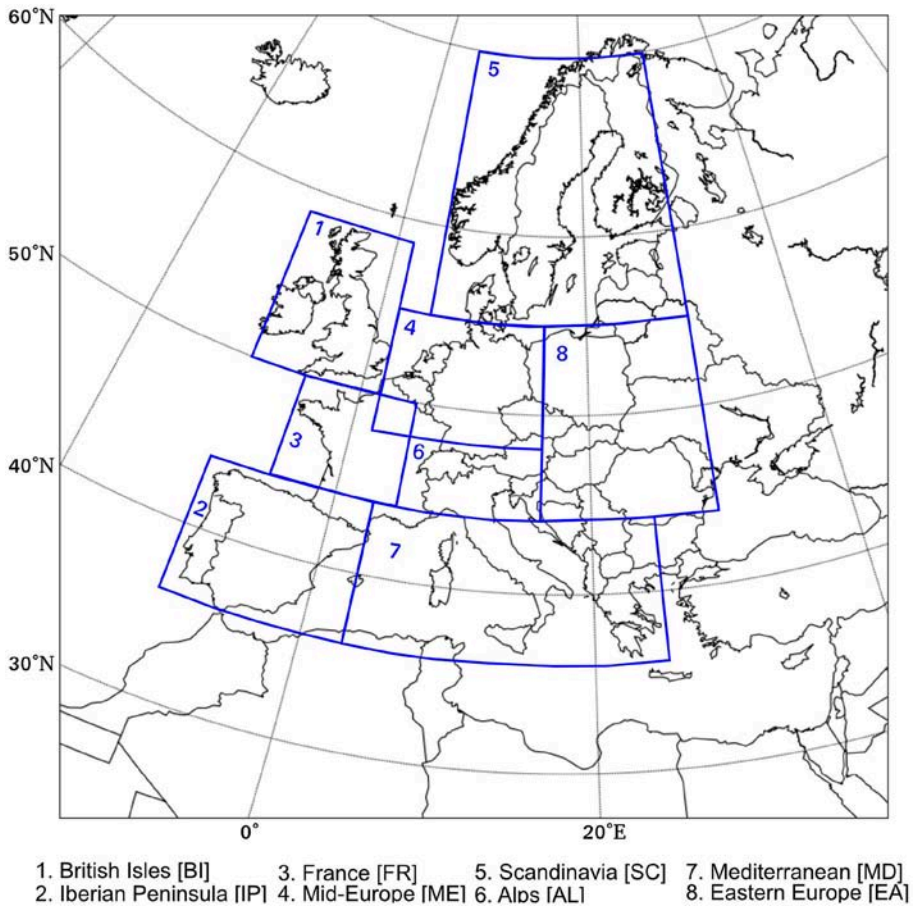

FIGURE 2 | Cordex domain for $\Delta x = 0.44^\circ$ and $\Delta x = 0.11^\circ$ and the associated sub-domains.

the European region and a larger signal over the Scandinavian and Russian area. The low-level noise over the European continent is likely due to the large-scale circulation constraint dominating this mid-latitude region in this season (stratiform precipitation from large low-pressure systems) (Sørland et al., 2018).

The scaled patterns of JJA temperature (**Figure 4**) is showing a more homogeneous warming over the domain than DJF with the highest warming rates in the southern and northeastern parts of the domain as also observed in Christensen et al. (2019). In general, the JJA scaled precipitation patterns have a smaller S/N than those for DJF. Due to large inter-member disparities as seen here for JJA, as likely affected by the reproduction of convective precipitation, the percentage of grid points with $S/N < 1$ is higher (78, 83% for EUR-11 and EUR-44, respectively) than for DJF. The area where $S/N > 1$ over the Iberian Peninsula it is due to a stronger signal. It is expected that noise levels are higher in summer than in winter, as weather is more locally generated, which also means that the role of the regional model for noise is higher than in winter; this was originally described by Déqué et al. (2007). Further discussions on the robustness in relation to S/N is seen in section 3.4. The large levels of noise for JJA and DJF in the southern parts of the domain are related to the use of relative rather than absolute changes. This is supported by both a small absolute signal and a small absolute noise for this region (see **Figure 12**).

The results presented in this section are similar to those presented in previous studies (Tebaldi and Arblaster, 2014; Christensen et al., 2015, 2019). In order to study the what-if approach, a deeper investigation of the evolution of the emerging scaled patterns is needed.

3.2. Emergence of the End-Of-Century Scaled Pattern

This section is focusing on the emergence of the scaled patterns. To depict the emergence of the scaled patterns, movies are available in the **Supplementary Material** showing the temporal evolution of the temperature and the scaled precipitation patterns for JJA and DJF (see **Supplementary Videos S1, S2**, respectively). **Figure 5** shows the main statistics of the annual evolution of the scaled patterns from 2005 to 2090 (i.e., the 2005 level is calculated from the 1995–2014 period and so forth). The main purpose is to show at which time the scaled patterns shown

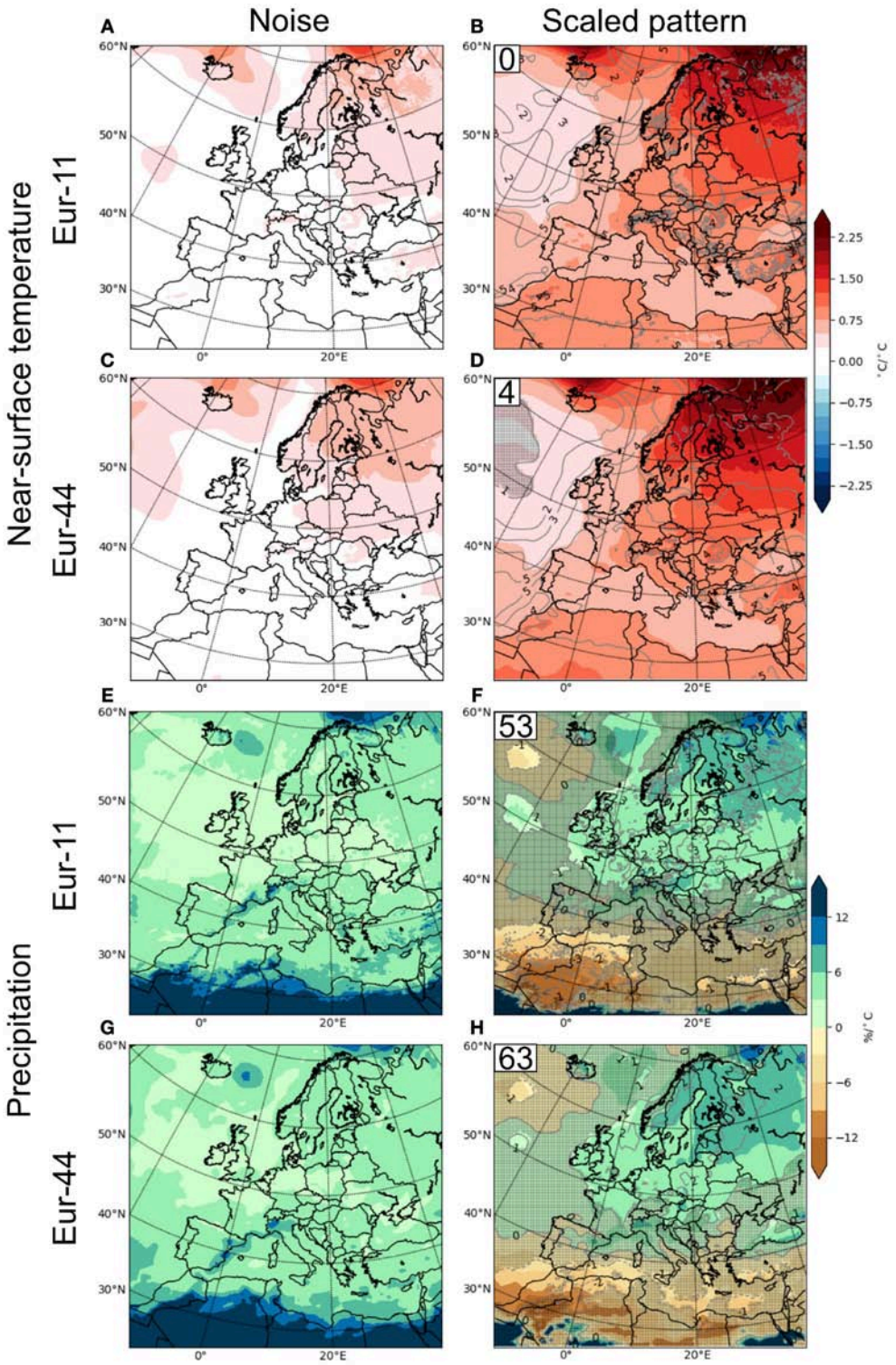

FIGURE 3 | Scaled 2080–2099 DJF patterns for combinations of temperature **(A–D)**/precipitation **(E–H)** and EUR-11 **(A,B,E,F)**/EUR-44 **(C,D,G,H)**. The left column shows the inter-member noise and the right column shows the 2080–2099 scaled patterns. The contour lines shown in the right column show the S/N ratio and the gray shading depicts areas of S/N < 1. The numbers in the upper left corner of the right column shows the percentage of grid points where S/N < 1. Note that both columns have the same unit.

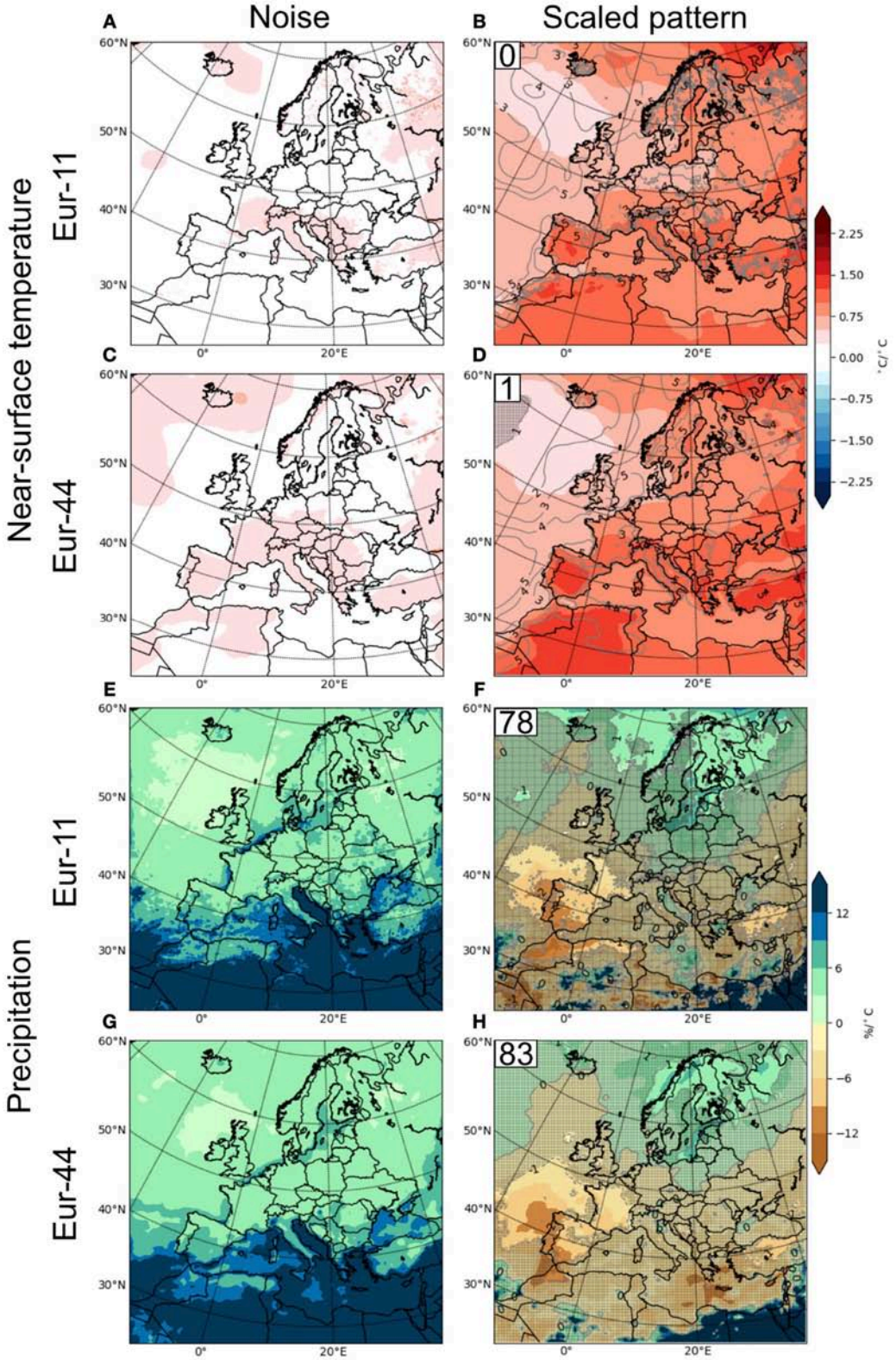

FIGURE 4 | As for **Figure 3** but for JJA.

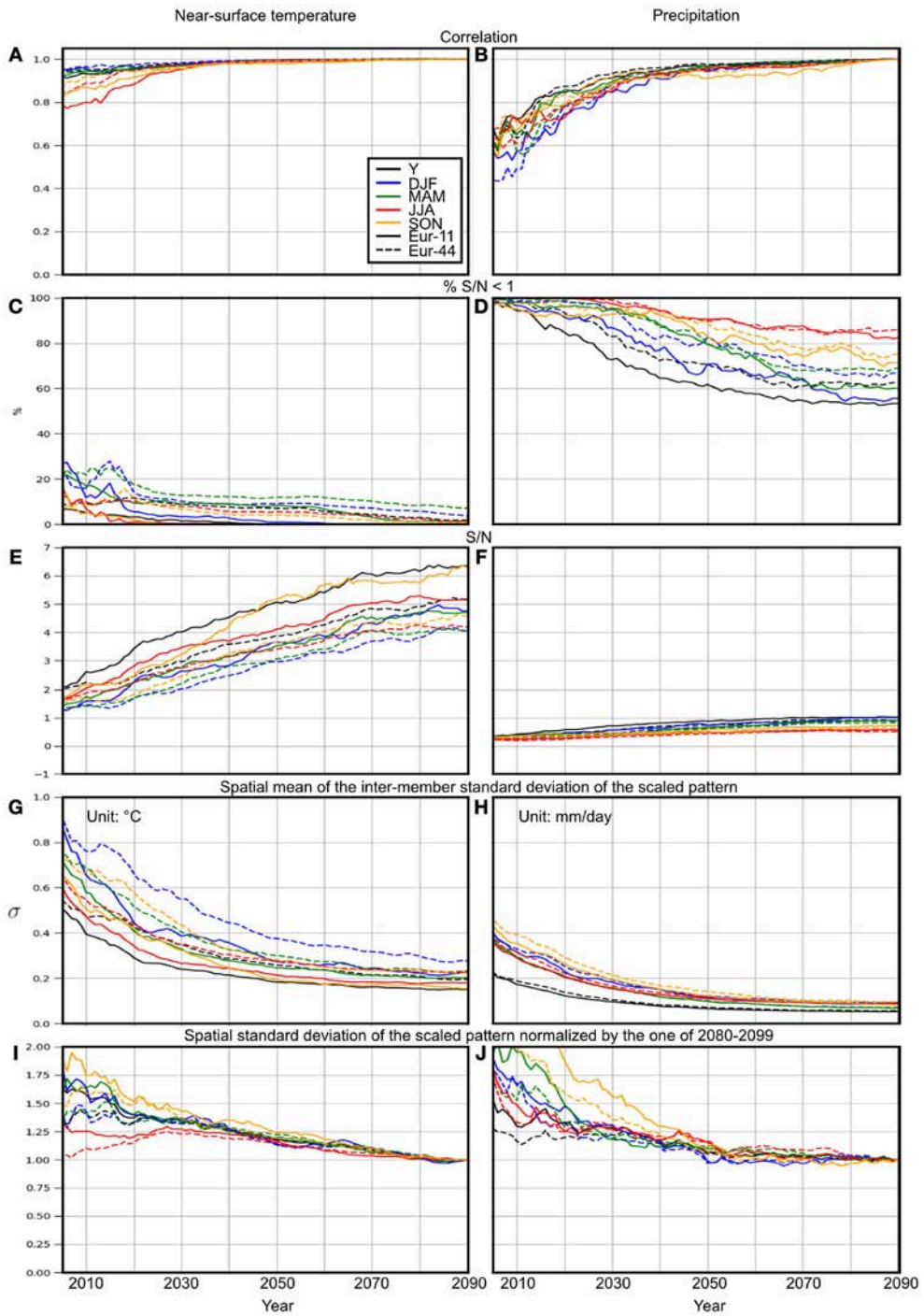

FIGURE 5 | Correlation between a running mean of 20-years scaled patterns from 2005 to 2090 (central year shown) against corresponding end-period levels (2080–2099) **(A,B)**. Percentage of grid points where S/N < 1 **(C,D)**. Spatial average of the S/N levels (using the absolute signal) of the scaled patterns **(E,F)**. Spatial average of inter-member standard deviation of the scaled patterns **(G,H)**. Spatial standard deviation of scaled patterns normalized by that of 2080–2099 **(I,J)**. The results are shown for both variables (temperature and absolute precipitation, left and right respectively), and across resolutions and seasons as well as annually.

in section 3.1 emerge at various geographical locations and scales.

The first row of **Figure 5** shows the spatial correlation between the scaled patterns calculated each year against the 2080–2099 scaled patterns (as shown in **Figures 3**, **4**). The spatial correlation for temperature (**Figure 5A**) reaches the asymptotic unit value for all seasons and for both resolutions early in the century (around 2035). The latest alignment to the asymptotic value is

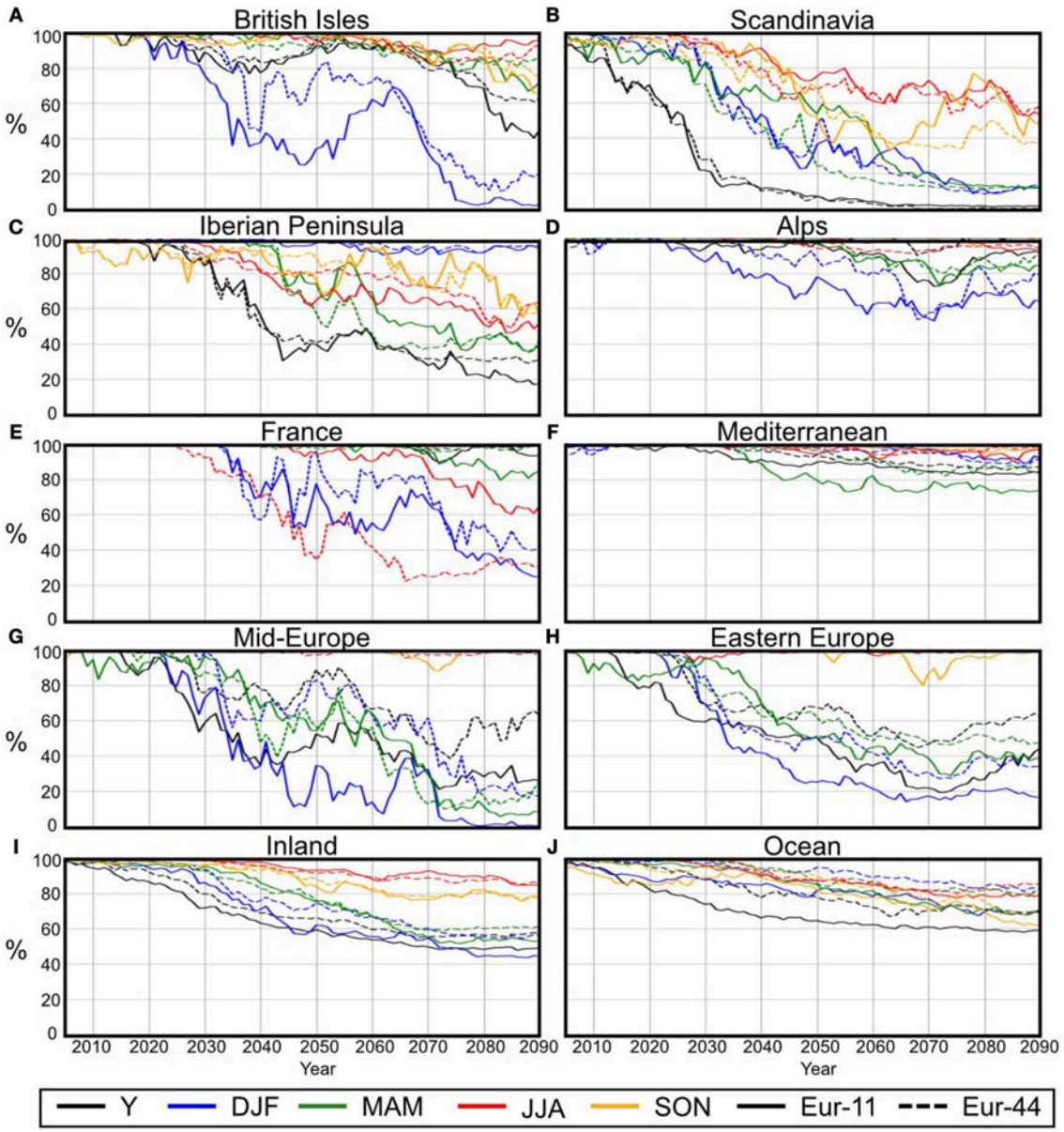

FIGURE 6 | Percentage of inland grid points where S/N<1 for absolute precipitation for each subdomain **(A–H)** and for land **(I)** and ocean **(J)** grid points in the full domain.

seen for the JJA season, which again is likely due to smaller-scale convective weather systems. For absolute precipitation change, the evolution of correlations (**Figure 5B**) is more divergent than for temperature, reaching unity at a later stage (around 2080). However, the correlation levels seem to stabilize around 2050. For precipitation, DJF is the last season to reach its asymptotic value.

The second and the third rows of **Figure 5** show the percentage of grid points where S/N $<$ 1 and the value of the spatial average of S/N, respectively. For temperature (**Figure 5C**), the percentage of grid points where S/N $<$ 1 is relatively low early in the period. For EUR-11, a level of 0% is reached around 2040 whereas EUR-44 decreases to around 2% at the end of the century. The scaled precipitation patterns differ substantially from those of temperature (**Figure 5D**), starting at approximately 100% for all seasons and resolutions, decreasing steadily to levels between 50 and 85% at the end of the century. Accordingly, the spatial average of S/N is increasing for both variables (**Figures 5E,F**). At the start of the period, spatially averaged temperature S/N levels are already $>$1 reaching values between 4 and 6.4 at the end of the century (across seasons and resolutions) for temperature. However, although S/N levels also increase in precipitation, the spatial average is comparatively lower and shows a slower increase toward the end of the century, suggesting a much noisier field for precipitation. Note

that the absolute signal has been used in order to avoid too large disparities due to use of relative value. The fourth row of **Figure 5** depicts the spatial mean of the inter-member standard deviation of the scaled patterns. It is seen that regardless of variable, season and resolution, the inter-member disparity of the scaled patterns is larger in the beginning of the period and converges at the end of the century, which is in agreement with the results of the first rows of **Figure 5**. The last row of **Figure 5** shows the spatial standard deviation of the ensemble mean scaled patterns normalized by the level at the end of the century. The results suggest that the spread between variables, seasons, and resolutions is higher early in the period, due to the large noise here, becoming increasingly similar toward the end of the century. The scaled precipitation patterns seem to converge to unity more rapidly than the temperature. This may be explained by the fact that warming over land is generally faster than the global average; therefore the mid-century is scaled by a smaller warming amplitude than the probably more relevant regional warming. As the sea catches up with the land during the century, this effect is diminished. Furthermore, the curves group together more rapidly than in the case of precipitation. In general, EUR-44 seems to differ somewhat from EUR-11 which is likely due to the slightly different sets of members between the EUR-11/EUR-44 model groups (not shown).

Although **Figure 5** gives a general idea of the robustness of the signal in scaled patterns, **Figure 6** shows that there are important local differences between the subregions. **Figures 6A–H** is showing the same as **Figure 5D**, but for land grid points of individual subregions (as shown in **Figure 2**), for all inland grid points (**Figure 6I**) and all water grid points (**Figure 6J**). Overall, all subdomains have more or less the same behavior; (1) levels of 100% is generally seen at the beginning decreasing toward the end of the century; (2) some large differences in seasons are seen with JJA showing the slowest decline; (3) DJF reaches the lowest levels (except for the Iberian Peninsula; **Figure 6C**).

The high value shown for the Alps (**Figure 6D**) and the Mediterranean (**Figure 6F**) area is due to a persistently stronger noise (not shown) likely to be produced by the complex topography of the Alps and land/sea effects from the vast coastlines of the Mediterranean. Despite some variations in the evolution of the statistics and relatively low S/N, the movies (**Supplementary Video S1**) suggest that the underlying emerging patterns are already recognizable from around 2020.

3.3. Comparison Between the Pattern Scaling and the What-If Worlds

The main purpose of this section is to analyze the robustness and persistence of the scaled patterns by comparison to the patterns resulting from the what-if approach.

Figure 7 shows the global average of the ensemble mean of the 2 m temperature from the CMIP5 datasets used to drive the RCMs of this study. The years shown in the legend represent the year where the selected threshold is crossed by the global average of the ensemble mean. The 1°C threshold is crossed in 2031 and 2026, the 2°C is crossed in 2070 and 2050 for RCP4.5 and RCP8.5, respectively, and the 3°C is crossed in 2068 (RCP8.5 only). Overall, we have shown in section 3.2 that the signal increasingly emerges from the noise as we go through the century, which should be considered when comparing the scaled patterns from the patterns resulting from the what-if approach.

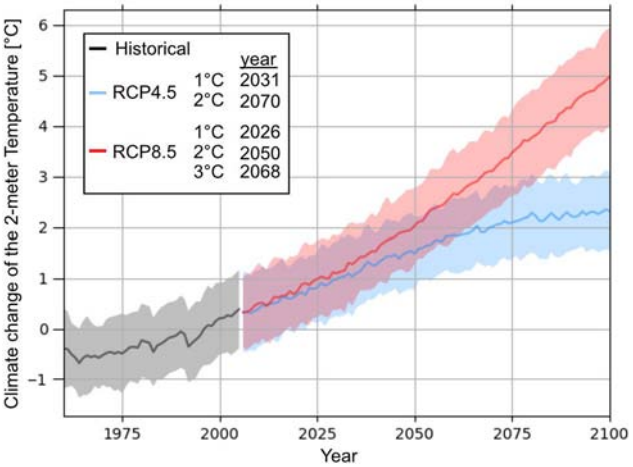

FIGURE 7 | Global average of the ensemble mean of the 2-m temperature from the CMIP5 model used as driving data for this study. The black, blue, and red lines are the historical, RCP4.5 and RCP8.5, respectively. The shadow represents the standard deviation of the model ensemble. The years in the legend represent the year where the i°C was crossed by the global ensemble mean.

The mean what-if result at 1°C warming for JJA temperature (second column of **Figure 8**) shows a good correspondence (correlation of 0.93 and 0.97) with the scaled patterns for both resolutions (for **Figures 8B,F**, respectively), which was expected since the scaled temperature patterns converge rapidly (see **Figure 5A**). The results from the other two thresholds are also similar (showing pattern correlations of 0.98 [0.99] and 0.99 [0.99], respectively, for the 2 and 3°C thresholds for EUR-11 [EUR-44]; **Figures 8C,D** [**Figures 8G,H**], respectively). The main difference is seen in the percentage of grid points where S/N < 1 since EUR-11 (**Figures 8A–D**) shows levels of 0–1% for all temperature thresholds whereas EUR-44 (**Figures 8E–H**) shows a decrease from 7 to 0% with the increasing threshold from 1 to 3°C as also expected from **Figure 5C**. This is mostly due to a combination of low change signal and a large noise (**Figures 4C,D**). However, it is worth noting that the number of available members (lower-left corner) decreases as the threshold increases, since some simulations never reach the higher thresholds.

For JJA precipitation (**Figure 9**), S/N is below 1 in 99% of the domain for the 1°C patterns making this scenario unusable (**Figures 9B–F**) for both resolutions. Also, the overall signal of the 1°C patterns differ from the scaled patterns [with correlations of 0.63 and 0.69 for EUR-11 and EUR-44, respectively (**Figures 9B–F**)] with the most notable differences south of the Baltic Sea, in the Mediterranean and in the southern parts of the domain. In contrast, the 2 and the 3°C patterns (third and fourth column of **Figure 9**) are showing a higher correlation than the 1°C pattern. However, in terms of correlation, little improvement is noted going from the 2°C to

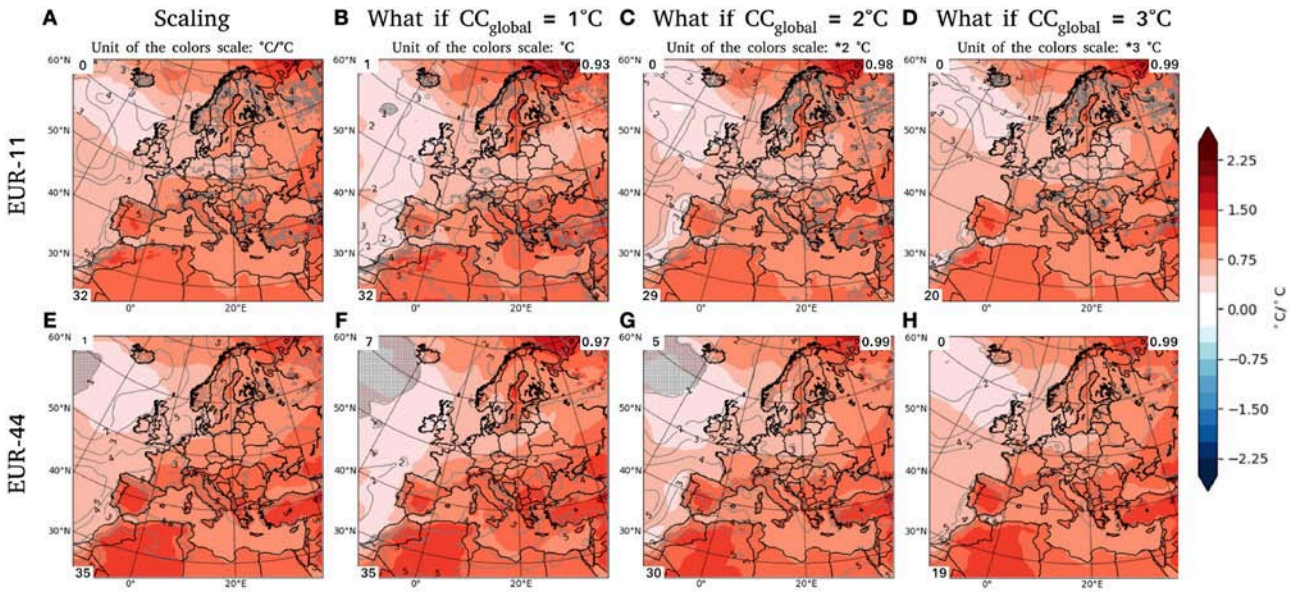

FIGURE 8 | JJA temperature. 2080–2099 scaled fields **(A,E)**, fields from the what-if approach for the 1°C **(B,F)**, 2°C **(C,G)**, and 3°C **(D,H)** for the EUR-11 domain and EUR-44 domain (**A–D** and **E–H**, respectively). The metrics shown in the corners of the figures include the percentage of grid points where S/N<1 (upper left), the number of model members (lower left) and the correlation between the scaled pattern and the what-if approach (upper right for the what-if subplots). It is worth noting that the scale of the what-if patterns have to be multiplied by their threshold values to obtain actual warming.

the 3°C level although some areas do improve such as the Baltic Sea and the Mediterranean area. The percentage of the S/N also decreases from 1, 2 to 3°C (99% [99%], 85% [86%], and 77% [76%], respectively for EUR-11 [EUR-44]) reflecting increasing confidence for a larger proportion of the domain. In summary, the 1°C patterns are likely unusable to reflect climate change patterns, leading to the conclusion that an analysis on 1°C should instead employ higher thresholds which are then subsequently adjusted to 1°C.

For DJF temperature (**Figure 10**), as in JJA, the what-if pattern is similar to the scaled pattern (both resolutions) with a decrease in the percentage of grid points where S/N < 1 as the threshold increases. The S/N levels below 1 in the North Atlantic region is due to a small signal and a medium-to-large noise (not shown).

The 1°C patterns for DJF precipitation (second column of **Figure 11**) shows that the correlation is already high for 1°C and increases very little over the highest thresholds (both resolutions). Yet, the min/max values are distinct and become even more comparable when increasing the thresholds. Unlike the JJA 1°C precipitation pattern of EUR-11 (**Figure 9B**), DJF is showing a relatively large region where S/N > 1 over Germany, North Atlantic, the Norwegian Sea and North Algeria. The 2°C precipitation patterns have a relatively large area where S/N > 1 increasing to levels similar to the scaled patterns for the 3°C threshold for both resolutions.

In summary, the results suggest that patterns extracted from 1°C threshold should not be used whereas the scaled patterns shows a much more robust signal, which is similar to the 2 and 3°C patterns.

3.4. The Trustworthy Change Signal

In this study, we have defined the trustworthy information as the one where the main signal is detectable from the inter-model spread (S/N > 1). This is quite straightforward with temperature since S/N is almost always >1, except occasionally for the North Atlantic area. However, the quantity of information judged untrustworthy for the precipitation patterns is larger. The S/N metric might be misleading since negligible or small change signals are more likely to be judged as untrustworthy although usable information can in fact be extracted. McSweeney and Jones (2013) discuss this issue by using the interannual variability as noise and claim that a clear distinction should be made between "no signal" and a signal overwhelmed by noise. In this section, we wish to present some additional thoughts on this issue.

To deepen our understanding, several other metrics were selected and applied on the absolute field of precipitation. The first column of **Figure 12** shows the inter-member noise of the scaled patterns. A bootstrap analysis with replacement using 1,000 samples was used to create 1,000 estimates of the noise. The resulting bootstrap average shows a similar, but weaker, pattern compared to those shown in **Figures 3**, **4**. Furthermore, the 25th–75th range is quite narrow. The results together suggest that a few outlier members have a considerable impact on the noise, especially in the Alps and Mediterranean areas (confirmed by a qualitative visual evaluation).

As stated, it is expected that areas with high noise relative to the change signal should be judged untrustworthy; in that sense the S/N metric (second column of **Figure 12**—as also shown in **Figures 9**, **11**) is suitable. But, using this metric, some regions are judged untrustworthy because of a combination of a

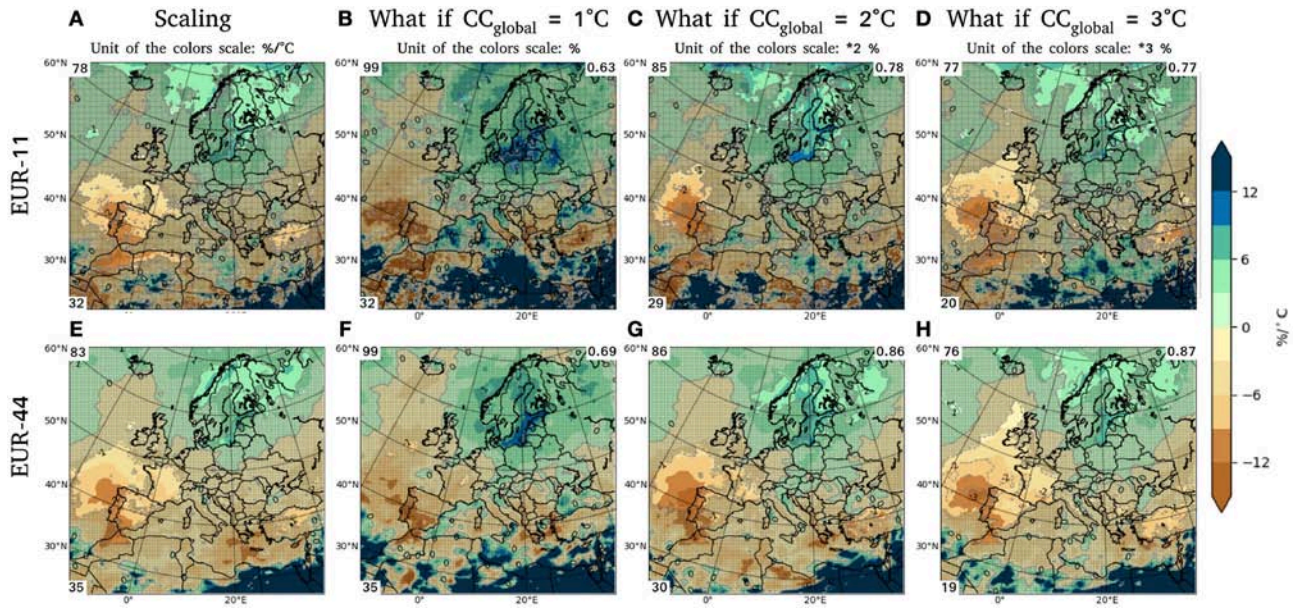

FIGURE 9 | JJA precipitation. Specifications and conventions as in **Figure 8**.

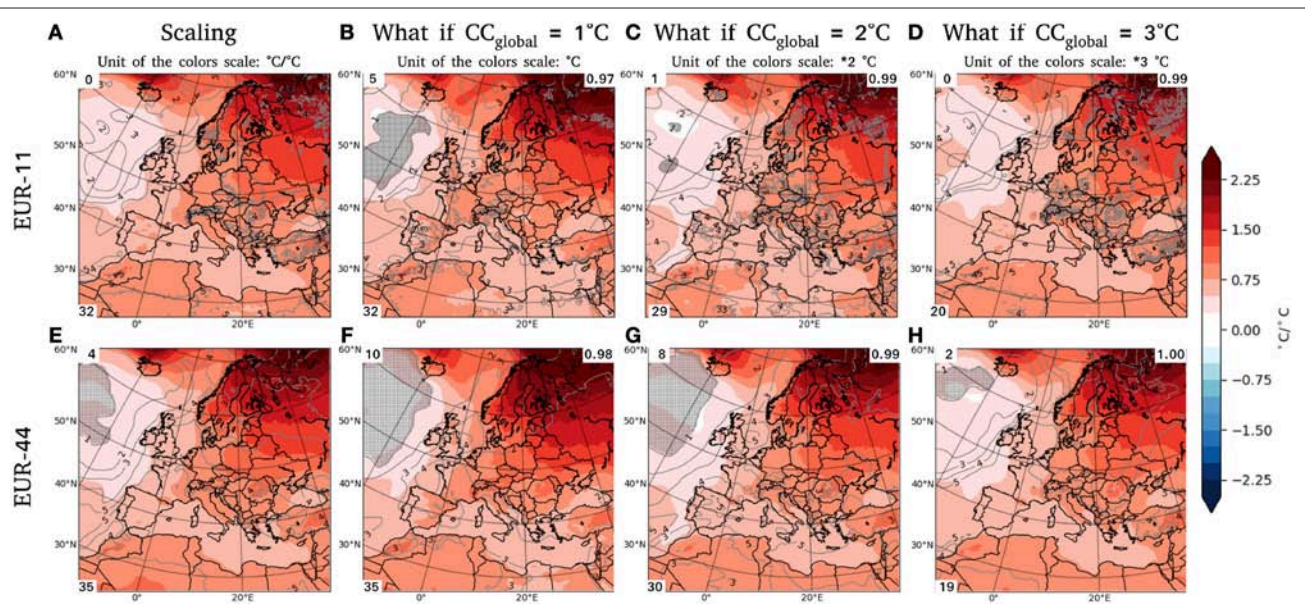

FIGURE 10 | DJF temperature. Specifications and conventions as in **Figure 8**.

weak signal and a weak noise (for example the Eastern part of the Mediterranean; subdomain 7 in **Figure 2**). Such weak noise should be considered when trying to extract a valuable signal. For the rest of the Mediterranean area the noise is large and the change signal weak, making it difficult to extract trustworthy information from this region.

The second metric used to judge the trustworthy information is to apply a quantitative threshold on the noise as shown here using 0.1 mm/day (third column of **Figure 12**), which in essence is a small change over a three month period (≈10 mm). By applying this threshold, numerous grid points become trustworthy in comparison with the conventional S/N approach (as shown by the decrease in the percentage of the untrustworthy grid points in the upper left of each figure) albeit still keeping all areas with high noise levels out of the trustworthy signal. The subjective selection of threshold level, however, might be disputable and it may also be region-specific.

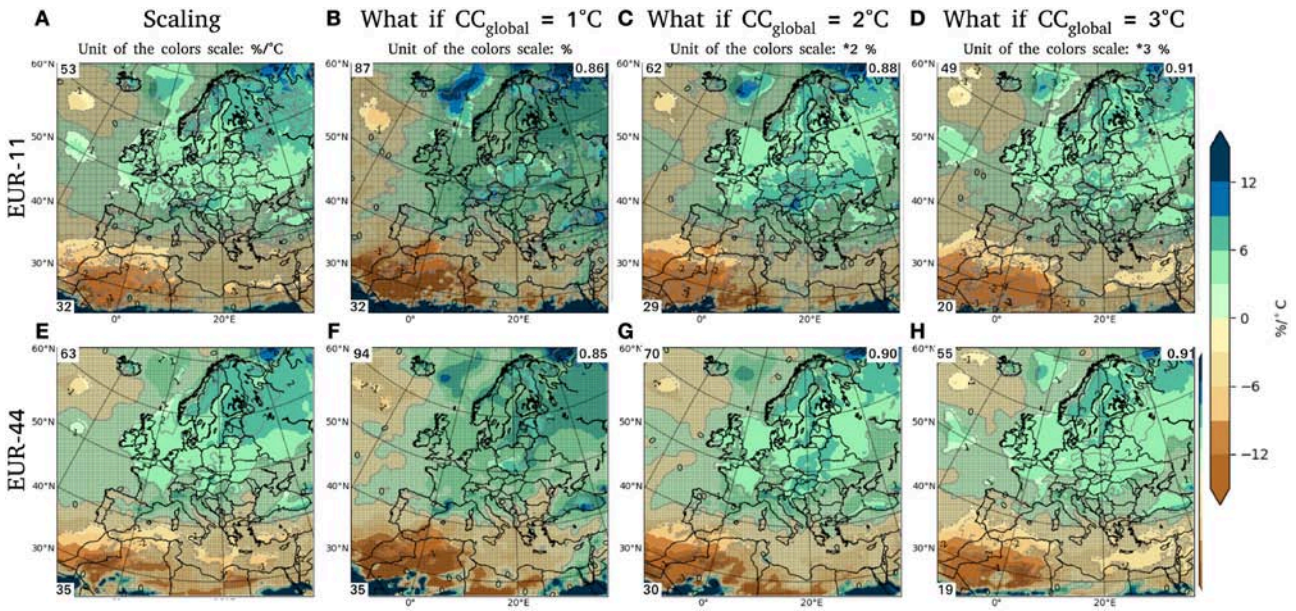

FIGURE 11 | DJF precipitation. Specifications and conventions as in **Figure 8**.

The third metric is based on the Variability of the Scaled Patterns (VSP). The VSP is calculated by splitting the last 50 years of the scaled patterns evolution (from 2041 to 2090) into five decades (i.e., 2041–2050 and so forth). Using these five times slices an inter-decadal variability was calculated and then temporally averaged. The five decades are basically treated in the same way as would have been done with perturbed members for an internal variability study (see Lucas-Picher et al., 2008, for example). We interpret the VSP as the "natural" variability of the scaled patterns. So, all noise smaller than the VSP should not be considered. In **Figure 12**, the fourth column shows the available signal when not considering noise <VSP. This method has the advantage to produce trustworthy information using grid points with a low signal. Such an approach could be further complemented with the conventional S/N > 1 metric, which as shown in the fifth column of **Figure 12**. One can see that the resulting percentage of the available signal is higher than using the S/N metric, but less than using the 0.1 mm/day threshold. It is worth noting that a better description of VSP is needed to understand uncertainties related to scaled patterns.

4. CONCLUDING REMARKS

In this study, the robustness and scalability of regional climate projections over Europe have been studied using the EURO-CORDEX dataset. In the first section, the 2080–2099 scaled patterns of temperature and precipitation for DJF and JJA have been shown. In winter, the land is warmer than the ocean with a south-to-north warming gradient. During summer, the land is overall still warmer than the ocean and the warming is more homogeneous than in winter. The noise is smaller for temperature than precipitation for both seasons. In general, the noise is higher in the North Atlantic for all seasons in combination with a weak change signal resulting in areas where S/N < 1. The noise in precipitation is larger for the Alps and the Mediterranean, but weaker for the North Atlantic Ocean.

The second section analyzes the emergence of the scaled patterns, as also visualized in an animation (**Supplementary Information**). It has been shown that the scaled temperature patterns emerge faster than the corresponding patterns for precipitation. For temperature, the areas of trust (grid points where S/N > 1) increase to 100% toward the end of the century whereas a stabilization of 50–60% is seen for precipitation around 2050. The large noise throughout the century related to the scaled precipitation pattern suggests that the precipitation pattern is not as linear as is the case with temperature. However, although the signal drowns in the inter-member noise (the ratio of which decreases through the century), the consistency in the scaled precipitation patterns from 2020 suggests that the precipitation field is actually scalable at longer timescales.

The third section of the results shows a comparison between the scaled patterns and the pattern extracted from a what-if approach, where thresholds of 1, 2, and 3°C were employed. It has been shown that the patterns from the 2 and 3°C of the what-if approach results were highly similar to the end of century scaled patterns of temperature and also largely to the scaled precipitation pattern. The 1°C what-if patterns differed due to a lack of signal as elaborated below. It could also be seen (for both variables/seasons/resolutions) that the percentage of trustworthy grid points was increasing from the 1 to 2°C results and that no major differences were seen between 2 and 3°C and the scaled pattern. This latter result corresponds to the

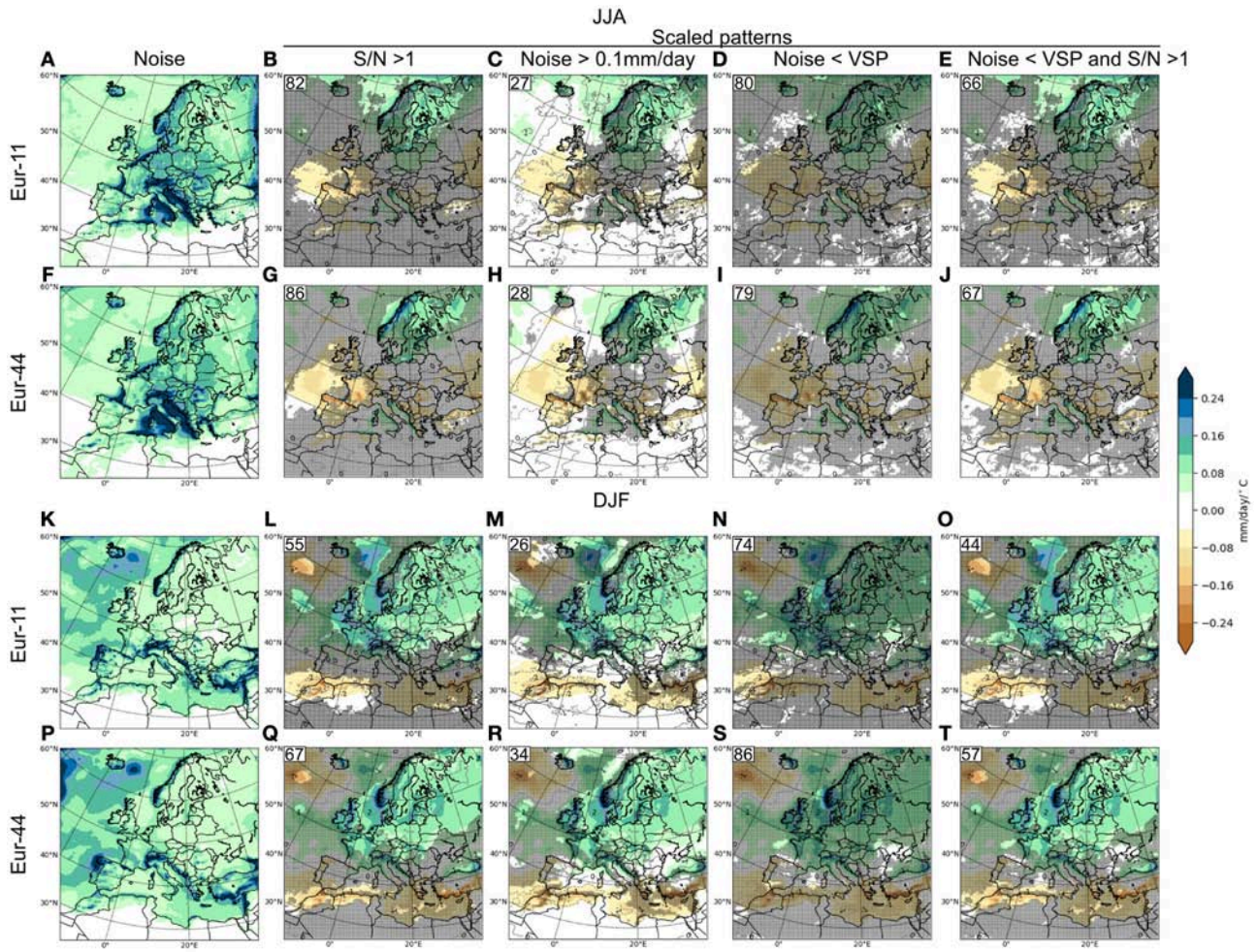

FIGURE 12 | Inter-member noise **(A,F,K,P)** of the 2080–2099 scaled precipitation patterns where different thresholds have been used: (1) S/N > 1 **(B,G,L,Q)**, (2) considering only grid points with Noise >0.1 mm/day **(C,H,M,R)**, considering only grid points with Noise < VSP **(D,I,N,S)** and (4) considering only grid points with S/N > 1 together with Noise < VSP **(E,J,O,T)**. The results are shown for JJA and DJF (**A–J** and **K–T**, respectively) and both resolutions for absolute precipitation. The contour lines show the S/N ratio and the gray shading depicts "low-trust" areas defined by the metric selected. In the upper left corner of each figure, the percentage of shaded grid points is shown.

finding that patterns were stabilized around 2050. Nonetheless, patterns are already recognizable as early as 2020. The major difference was noted while comparing the 1°C precipitation patterns with the scaled ones. The percentage of trustworthy information is almost 0 for the 1°C results and the patterns were poorly represented. This suggests that patterns extracted from analyses with a 1°C threshold should not be used, whereas scaled patterns provide a more robust signal, as do 2 and 3°C patterns. It is worth noting that, although the pattern scaling approach provided important and robust information about the future climate change, this approach does not take into account any non-linear feedback from global warming. Those feedbacks might have a non-negligible impact on pattern scaling whereas processes with longer time scales (e.g., soil processes and permafrost in particular; Christensen 1999; Stendel and Christensen 2002) might be a reason for caution for longer projections and scales of the presented results. In Christensen et al. (2015), the scalability of regional climate signals with global temperature change was studied, and only extreme precipitation showed any strong deviation from linearity in this connection. In taking a pattern scaling approach, as many simulated climate change signals as possible are included, which is a direct way to improve the signal-to-noise ratio suppressing low-frequency variability.

Finally, the last results section is an attempt to raise the challenging issue of the "level of trust" in using a multi-model ensemble climate change signal. At first, the conventional metric S/N was used. It has, however, been suggested that this latter metric might misjudge information where a low-level change signal is located. Therefore, to deepen our understanding, an arbitrary threshold was applied to the noise resulting in increased levels, or areas, of trustworthy information. Only high noise

regions, such as the Alps and the Mediterranean, remained below the trust level threshold. To overcome arbitrariness in the selection of this threshold, the variability of scaled patterns was calculated and used as a new threshold for the noise. It has been shown that when this threshold is combined with the conventional S/N, low-level signals, which were otherwise judged as unusable, become available as trustworthy change information. This study shows that pattern scaling can be used to analyze low- to high-level climate change signals with sufficient robustness for climate adaptation and mitigation for the likely climate evolution through the century.

DATA AVAILABILITY STATEMENT

All data used in this study are available on the Earth System Grid Federation website (https://esg-dn1.nsc.liu.se/projects/esgf-liu/).

AUTHOR CONTRIBUTIONS

JHC conceived the idea. DM led the study, processed the model data, performed the analysis, led the writing, and produced the figures. JHC, DM, MADL, and OBC analyzed the results, contributed to discussions, and the writing of the paper.

FUNDING

The research leading to these results has received funding from the European Research Council under the European Community's Seventh Framework Programme (FP7/2007-2013) ERC grant agreement 610055 as part of the ice2ice project. This work also received support by the European Union under the Horizon 2020 Grant Agreement 776613, the EUCP project.

ACKNOWLEDGMENTS

We acknowledge the World Climate Research Programme's CORDEX project for its role in making available the WCRP CORDEX multi-model data set, and we thank the climate modeling groups for producing and making available their model outputs. The authors are grateful to the two reviewers that helped improve this manuscript.

SUPPLEMENTARY MATERIAL

The Supplementary Material for this article can be found online at: https://www.frontiersin.org/articles/10.3389/fenvs.2018.00163/full#supplementary-material

REFERENCES

Christensen, J. H., Carter, T. R., and Giorgi, F. (2002). PRUDENCE employs new methods to assess European climate change. *EOS Trans. Am. Geophys. Union* 83:147. doi: 10.1029/2002EO000094

Christensen, J. H., and Christensen, O. (2007). A summary of the PRUDENCE model projections of changes in European climate by the end of this century. *Clim. Change* 81, 7–30. doi: 10.1007/s10584-006-9210-7

Christensen, J. H., Kjellström, E., Giorgi, F., Lenderink, G., and Rummukainen, M. (2010). Weight assignment in regional climate models. *Clim. Res.* 44, 179–194. doi: 10.3354/cr00916

Christensen, J. H., Larsen, M. A. D., Christensen, O. B., Drews, M., and Stendel, M. (2019). Robustness of European climate projections from dynamical downscaling. *Climate Dyn*.

Christensen, O. B. (1999). Relaxation of soil variables in a regional climate model. *Tellus A* 51, 674–685. doi: 10.3402/tellusa.v51i5.14486

Christensen, O. B., Yang, S., Boberg, F., Maule, C. F., Thejll, P., Olesen, M., et al. (2015). Scalability of regional climate change in europe for high-end scenarios. *Clim. Res.* 64, 25–38. doi: 10.3354/cr01286

Déqué, M., Rowell, D. P., Lüthi, D., Giorgi, F., Christensen, J. H., Rockel, B., et al. (2007). An intercomparison of regional climate simulations for Europe: assessing uncertainties in model projections. *Clim. Change* 81(Suppl. 1), 53–70. doi: 10.1007/s10584-006-9228-x

Evans, J. P., and McCabe, M. F. (2013). Effect of model resolution on a regional climate model simulation over southeast Australia. *Clim. Res.* 56, 131–145. doi: 10.3354/cr01151

Giorgi, F. and Gutowski, W. J. (2015). Regional dynamical downscaling and the CORDEX initiative. *Annu. Rev. Environ. Resour.* 40, 467–490. doi: 10.1146/annurev-environ-102014-021217

Gutowski, J. W. J., Giorgi, F., Timbal, B., Frigon, A., Jacob, D., Kang, H., Raghavan, K., et al. (2016). WCRP COordinated Regional Downscaling EXperiment (CORDEX): a diagnostic MIP for CMIP6. *Geosci. Model Dev.* 9, 4087–4095. doi: 10.5194/gmd-9-4087-2016

Harris, I., Jones, P. D., Osborn, T. J., and Lister, D. H. (2014). Updated high-resolution grids of monthly climatic observations-the CRU TS3. 10 Dataset. *Int. J. Climatol.* 34, 623–642. doi: 10.1002/joc.3711

Huntingford, C., and Cox, P. M. (2000). An analogue model to derive additional climate change scenarios from existing GCM simulations. *Clim. Dyn.* 16, 575–586. doi: 10.1007/s003820000067

IPCC (2007). *Climate Change 2007: Contribution of Working Group 1 to the Fourth Assessment Report of the Intergovernmental Panel on Climate Change.* eds S. Solomon, D. Qin, M. Manning, Z. Chen, M. Marquis, K. B. Averyt, M. Tignor, and H. L. Miller, Cambridge University Press.

IPCC (2018). *Special Report on the Impacts of Global Warming of 1.5 °C.*

Jacob, D., Petersen, J., Eggert, B., Alias, A., Christensen, O. B., Bouwer, L. M., et al. (2014). EURO-CORDEX: new high-resolution climate change projections for European impact research. *Reg. Environ. Change* 14, 563–578. doi: 10.1007/s10113-013-0499-2

Knutti, R., Rogelj, J., Sedláček, J., and Fischer, E. M. (2016). A scientific critique of the two-degree climate change target. *Nat. Geosci.* 9:13. doi: 10.1038/ngeo2595

Larsen, M. A., Christensen, J. H., Drews, M., Butts, M. B., and Refsgaard, J. C. (2016). Local control on precipitation in a fully coupled climate-hydrology model. *Sci. Rep.* 6:22927. doi: 10.1038/srep22927

Lucas-Picher, P., Caya, D., de Elía, R., and Laprise, R. (2008). Investigation of regional climate models internal variability with a ten-member ensemble of 10-year simulations over a large domain. *Clim. Dyn.* 31, 927–940. doi: 10.1007/s00382-008-0384-8

Lustenberger, A., Knutti, R., and Fischer, E. M. (2014). The potential of pattern scaling for projecting temperature-related extreme indices. *Int. J. Climatol.* 34, 18–26. doi: 10.1002/joc.3659

McSweeney, C. F., and Jones, R. G. (2013). No consensus on consensus: the challenge of finding a universal approach to measuring and mapping ensemble consistency in GCM projections. *Clim. Change* 119, 617–629. doi: 10.1007/s10584-013-0781-9

Meehl, G. A., Covey, C., Delworth, T., Latif, M., McAvaney, B., Mitchell, J. F. B., et al. (2007). The WCRP CMIP3 multimodel dataset: a new era in climate change research. *Bull. Am. Meteorol. Soc.* 88, 1383–1394. doi: 10.1175/BAMS-88-9-1383

Mitchell, T. D. (2003). Pattern scaling: an examination of the accuracy of the technique for describing future climates. *Clim. Change* 60, 217–242. doi: 10.1023/A:1026035305597

New, M., Liverman, D., Schroder, H., and Anderson, K. (2011). Four degrees and beyond: the potential for a global temperature increase of four degrees and its

implications. *Philos. Trans. R. Soc. Lond. A Math. Phys. Eng. Sci.* 369, 4–5. doi: 10.1098/rsta.2010.0304

Peters, G. P., Andrew, R. M., Boden, T., Canadell, J. G., Ciais, P., Le Quéré, C., et al. (2012). The challenge to keep global warming below 2°c. *Nat. Clim. Change* 3:4. doi: 10.1038/nclimate1783

Rae, J., Adalgeirsdóttir, G., Edwards, T., Fettweis, X., Gregory, G., Hewitt, H., et al. (2012). Greenland ice sheet surface mass balance: evaluating simulations and making projections with regional climate models. *Cryosphere* 6, 1275–1294. doi: 10.5194/tc-6-1275-2012

Sanderson, M. G., Hemming, D. L., and Betts, R. A. (2011). Regional temperature and precipitation changes under high-end (≥ 4 c) global warming. *Philos. Trans. R. Soc. Lond. A Math. Phys. Eng. Sci.* 369, 85–98. doi: 10.1098/rsta.2010.0283

Santer, B. D., Wigley, T. M. L., Schlesinger, M. E., and Mitchell, J. F. B. (1990). *Developing Climate Scenarios From Equilibrium GCM Results.* Report Max Planck Institut für Meteorologie, Max-Planck-Institut fr Meteorologie.

Schwartz, C. S., Kain, J. S., Weiss, S. J., Xue, M., Bright, D. R., Kong, F., et al. (2010). Toward improved convection-allowing ensembles: model physics sensitivities and optimizing probabilistic guidance with small ensemble membership. *Weather Forecast* 25, 263–280. doi: 10.1175/2009WAF2222267.1

Sørland, S. L., Schär, C., Lüthi, D., and Kjellström, E. (2018). Bias patterns and climate change signals in gcm-rcm model chains. *Environ. Res. Lett.* 13:074017. doi: 10.1088/1748-9326/aacc77

Stendel, M., and Christensen, J. (2002). Impact of global warming on permafrost conditions in a coupled gcm. *Geophys. Res. Lett.* 29, 10–11. doi: 10.1029/2001GL014345

Stocker, T. F. (2013). The closing door of climate targets. *Science* 339, 280–282. doi: 10.1126/science.1232468

Taylor, K. E., Stouffer, R. J., and Meehl, G. A. (2012). An overview of CMIP5 and the experiment design. *Bull. Am. Meteorol. Soc.* 93, 485–498. doi: 10.1175/BAMS-D-11-00094.1

Tebaldi, C., and Arblaster, J. M. (2014). Pattern scaling: its strengths and limitations, and an update on the latest model simulations. *Clim. Change* 122, 459–471. doi: 10.1007/s10584-013-1032-9

UNFCCC (2009). *Decision 2/cp.15 Copenhagen Accord.*

Van der Linden, P., and Mitchell, J. e. (2009). *ENSEMBLES: Climate Change and Its Impacts-Summary of Research and Results from the ENSEMBLES Project*. Exeter: Met Office Hadley Centre.

Van Weverberg, K., Vogelmann, A. M., Lin, W., Luke, E. P., Cialella, A., Minnis, P., et al. (2013). The role of cloud microphysics parameterization in the simulation of mesoscale convective system clouds and precipitation in the tropical western Pacific. *J. Atmos. Sci.* 70, 1104–1128. doi: 10.1175/JAS-D-12-0104.1

Vautard, R., Gobiet, A., Sobolowski, S., Kjellström, E., Stegehuis, A., Watkiss, P., et al. (2014). The European climate under a 2°C global warming. *Environ. Res. Lett.* 9:034006. doi: 10.1088/1748-9326/9/3/034006

Conflict of Interest Statement: The authors declare that the research was conducted in the absence of any commercial or financial relationships that could be construed as a potential conflict of interest.

frontiers in Environmental Science

ORIGINAL RESEARCH
published: 19 February 2019
doi: 10.3389/fenvs.2019.00018

The Sensitivity to Initial Soil Moisture for Three Severe Cases of Heat Waves Over Eastern China

Pinya Wang[1,2], *Qi Zhang*[1,2], *Yi Yang*[1,2] *and Jianping Tang*[1,2]*

[1] School of Atmospheric Sciences, Nanjing University, Nanjing, China, [2] Key Laboratory of Mesoscale Severe Weather, Ministry of Education, Nanjing University, Nanjing, China

Using Weather Research and Forecasting model (WRF) simulations with different initial soil moisture (ISM) conditions, we investigate the sensitivity to ISM for the three severe heat wave events that dominated eastern China in 2003, 2007, and 2013. The control simulations are able to reproduce the spatial distributions and the daily evolutions for each of the three heat waves but apparently underestimate their amplitudes, intensities, and spatial extensions. The decreased ISM could cause an enhancement on heat waves with increased amplitudes, extents and intensities, while it has insignificant influence on the spatial distributions and temporal variations. The responses of heat waves are generally decreasing with the increasing ISM, controlled by different regimes in the surface soil moisture-temperature relationship. Through enhanced sensible flux as well as reduced latent cooling, the initial soil dryness locally strengthens the surface warming and the further drying of the soil. The three heat waves were all dominated by high-pressure systems in the mid-troposphere. The reduced ISM forces positive anomalies of geopotential height at mid-troposphere and negative anomalies at lower levels, leading to an enhanced thickness of the atmosphere. Such a thickened atmosphere can strengthen the anomalous high-pressure systems, favoring the maintenance of severe heat waves. This acts as a positive feedback between atmospheric circulation, surface warming, and soil dryness.

Keywords: initial soil moisture, heat waves, WRF, soil moisture-temperature relationship, land-atmosphere interaction

OPEN ACCESS

Edited by:
Hans Von Storch,
Helmholtz Centre for Materials and Coastal Research (HZG), Germany

Reviewed by:
Juan Pedro Montávez,
University of Murcia, Spain
Stefan Hagemann,
Helmholtz Centre for Materials and Coastal Research (HZG), Germany

***Correspondence:**
Jianping Tang
jptang@nju.edu.cn

Specialty section:
This article was submitted to Atmospheric Science, a section of the journal Frontiers in Environmental Science

Received: *14 September 2018*
Accepted: *30 January 2019*
Published: *19 February 2019*

Citation:
Wang P, Zhang Q, Yang Y and Tang J (2019) The Sensitivity to Initial Soil Moisture for Three Severe Cases of Heat Waves Over Eastern China. Front. Environ. Sci. 7:18. doi: 10.3389/fenvs.2019.00018

INTRODUCTION

Characterized by a period of consecutive days with abnormally high temperatures, heat waves have been known as one of the typical extreme weather events across the world (Perkins, 2015). The severe 1995 Chicago heat wave, the 2003 European heat wave, and the 2010 Russian heat wave caused disastrous impacts on humans, socio-economic development and the ecological environment (Whitman et al., 1997; Conti et al., 2005; Dole et al., 2011). For example, the severe European heat wave in 2003 killed more than 25,000 people and caused enormous economic losses (García-Herrera et al., 2010; Alexander, 2011). With continuing global warming, such extreme heat wave events are expected to be more frequent and severe in the coming decades (Meehl and Tebaldi, 2004).

Great efforts have been made in understanding the underlying mechanisms of heat waves, which is instrumental for the short-term prediction of heat waves. It is widely accepted that heat waves are generally dominated by persistent high-pressure systems (e.g., Huth, 2000; Black et al., 2004; Tomczyk and Ewa, 2015). Under the control of blocking highs, warm air over mid-high latitudes cannot mix with cold air and warm air builds up, eventually causing the extreme warmth, such as the great heat wave in Russia in 2010 (Matsueda, 2011). Besides the typical blocking highs, anomalous high-pressure systems associated with Rossby wave propagations are also favorable for sustaining a heat wave (Pezza et al., 2012; Wang et al., 2017a). Although anomalous high-pressure systems are a fundamental ingredient for a heat wave to occur, the coupling with the land surface also plays a crucial role (Fischer et al., 2007a,b; Teuling et al., 2010). In general, soil moisture is mostly considered when investigating the impacts of land surface processes (Fischer et al., 2007b; Seneviratne et al., 2010). The impacts of soil moisture on surface air temperature are mostly expected to be induced by its role for evapotranspiration in soil moisture-limited regimes, depicted in the relationship between soil moisture and evaporative fraction (EF), the ratio of latent heat flux to the total available energy (Seneviratne et al., 2010; Berg et al., 2014). In general, characterized by EF, two evapotranspiration regimes exist. A soil moisture-limited regime in which the available surface energy is relatively abundant for evaporation or transpiration while the content of soil moisture is limited ($\theta < \theta_{CRIT}$, see the conceptual framework of Figure 5 in Seneviratne et al., 2010). In this case, EF increases when the content of soil moisture increases, and an energy-limited regime is one in which the soil moisture is abundant ($\theta > \theta_{CRIT}$) and EF is independent of the increasing soil moisture. Accordingly, three regimes of the soil moisture-temperature relationship are obtained based on the evapotranspiration regimes: the wet regime, the transitional regime and the dry regime. In the wet regime ($\theta > \theta_{CRIT}$), EF is independent of soil moisture. In the transitional regime ($\theta_{WILT} \leq \theta \leq \theta_{CRIT}$), EF reacts effectively to the changes of soil moisture. In this case, the dryness of the soil results in very low EF, with the constrained total energy used by the latent heat flux and more energy available for sensible heating. Thus, the near-surface air temperature would increase (Lorenz et al., 2010; Seneviratne et al., 2010; Alexander, 2011). However, in the dry regime ($\theta < \theta_{WILT}$), neither evapotranspiration will take place nor will any feedback. On the other hand, in the soil moisture-limited regime, the near-surface warming will amplify decreases in soil moisture, which induces a positive feedback cycle between atmospheric heating and further drying of soil conditions (Fischer et al., 2007b; Alexander, 2011). Moreover, the dry soil also favors the maintenance of upper-air anticyclonic circulations (Fischer et al., 2007b; Zampieri et al., 2009). Dry soil conditions along with persistent high-pressure systems would amplify the soil moisture-temperature feedback and enhance surface warming (Rohini et al., 2016).

The anomalies of soil moisture can last for weeks or even months (Koster and Suarez, 2001; Hu and Feng, 2004). Such long memory of the soil moisture and the resulting climate persistence are important for the prediction of extreme climate events like droughts and heat waves (Kim and Wang, 2007; Lorenz et al., 2010). Various studies investigated the impacts of soil moisture on temperatures through model simulations (e.g., Hirschi, 2011; Zeng et al., 2014; Vogel et al., 2017). It was reported that the model differences induced by initial soil moisture were far more important than those induced by various land surface physical parameterizations and the evolution of soil moisture itself (Trier et al., 2008). The intrinsic impacts of initial soil moisture on extreme temperatures have been revealed in previous studies. Through a northward propagation, drought in late spring from the Mediterranean regions can cause a further increase of high temperatures during summer in continental Europe (Zampieri et al., 2009). By perturbing the spring soil moisture, Fischer et al. (2007b) showed that the loss of soil moisture induced by precipitation deficit in preceding months contributed to the exceptionally high temperature anomalies in the European summer of 2003. Through numerical simulations, Ferranti and Viterbo (2006) demonstrated that the atmospheric response during the 2003 European summer to the initial soil water conditions extended up to 2 months, greatly exceeding the impact of the ocean boundary forcing.

Previous studies mostly concentrated on high temperatures from the whole summer (June, July, and August), whereas heat waves are usually defined as several consecutive days with abnormally high temperatures, dominating a large area, and characterized by different durations, impacted areas and intensities (e.g., Ren et al., 2012; Wang et al., 2017b). The impacts of initial soil moisture on the formation/occurrence and development of heat wave events, specifically on their characteristics including duration, impacted area and intensity, have received limited attention. Therefore, in this study, we focus on three extreme heat wave events in 2003, 2007, and 2013 in Eastern China, which are featured by different durations, spatial extents, and intensities, and all caused serious damage to the social economy (e.g., Tan et al., 2007; Sun X. et al., 2014; Xia et al., 2016). We investigate the impacts of initial soil moisture (hereafter ISM) on the heat wave characteristics through sensitivity experiments using the Weather Research and Forecast (WRF) model. In this study, heat waves are identified based on the definition in Wang et al. (2017b). The detailed information for the three heat waves will be given in section Methods and Data. Section Methods and Data introduces the methodology, data, and experimental design. Section Results documents the results and analyses. The last section presents the summary and conclusions of this research.

METHODS AND DATA

Study Area and the Three Heat Wave Events

Under the control of a subtropical high in summer, eastern China is vulnerable to frequent extreme high temperatures (Ding et al., 2010; Sun Y. et al., 2014; Wang et al., 2017a). Moreover, the heavy populations and the large urban areas in eastern China exacerbate the impacts of heat waves on society and human health (Freychet et al., 2017). More importantly, abundant

observational meteorological data are accessible in eastern China. Hence, this study aims to provide an insight into the effects of ISM on temperature responses in eastern China and as well as a broader region.

Extreme hot temperatures struck eastern China in the summers of 2003, 2007, and 2013, and caused severe consequences for society. The three high temperature events are identified according to the heat wave definition from Wang et al. (2017b), consisting of an absolute temperature metric of 35°C, a temporal duration of at least 3 days and a demanded spatial extension with more than 20 neighbored stations, any two of which are within a distance of 250 km. The three heat waves began on July 2, July 3, and August 4 and lasted for 41, 40, and 15 days, respectively. The maximum daily surface temperatures during the three heat wave processes were all beyond 40°C. Their detailed information is listed in **Table 1**.

Model and Experimental Design

In this study, the WRF model version 3.8 (Skamarock et al., 2008) was utilized for the numerical simulations. The following parameterizations were used: the two-stream correlated-k distribution Rapid Radiative Transfer Model (RRTMG; Iacono et al., 2008) for the radiation schemes, the Yonsei University (YSU) boundary layer parameterization scheme (Hong et al., 2006), the revised Monin–Obukhov surface layer (Jiménez et al., 2012), the cloud microphysics of WRF Single-Moment 5-class scheme (WSM5; Hong et al., 2004), the unified Noah land-surface model (Chen and Dudhia, 2001) and the cumulus parameterization based on the Kain–Fritsch scheme (Kain and Fritsch, 1990). The simulation domain is shown in **Figure 1** and includes 300 × 300 grid points with a horizontal resolution of 9 km. The vertical resolution is 34 non-uniform layers with 50 hPa at the top of the atmospheric columns.

Following Vivoni et al. (2009), to vary the initial soil moisture in WRF, we multiplied the initial soil moisture field by a factor (α) ranging from 0.25 to 1.25 (i.e., 0.25, 0.50, 0.75, 1.00, and 1.25; five sensitivity cases, from dry to wet condition). Compared to the control run (CTL, and $\alpha = 1$), simulations with $\alpha < 1$ represent dryer conditions while simulations with $\alpha > 1$ represent wetter conditions. For each of the heat wave events, five sensitivity experiments were conducted with the modified ISM (in total 15 simulations). There are four soil layers (0–5, 5–25, 25–70, and 70–150 cm thickness). The α factor is applied to the total volumetric soil moisture content at each grid point for each soil layer. For the model's spin up, five sensitivity simulations with different ISM conditions were set up about 10 days before the beginning date of each heat wave process (**Table 1**). Specifically, for the three heat waves, the initial dates were June 21 in 2003, June 23 in 2007, and July 12 in 2013.

TABLE 1 | Information of the three heat wave events in 2003, 2007, and 2013.

Year	Date	The Maximum daily Tmax (°C)	Duration (days)	Location
2003	July 2 to August 11	43.2	41	Southeast China
2007	July 3 to August 11	41.4	40	Southeast China
2013	August 4 to August 18	42.7	15	Middle to lower reaches of Yangtze River

The Data

The WRF simulations are driven by the National Centers for Environmental Prediction (NCEP) Final (FNL) Operational Global Analysis data (1° by 1° resolution) at 3 h intervals (00:00, 03:00, 06:00, 09:00, 12:00, 15:00, 18:00, and 21:00 UTC) for the initial and lateral meteorological boundary conditions. The initial soil moisture data are derived from the Global Land Data Assimilation System (GLDAS), which constrains multiple land surface models with ground and satellite observation-based datasets, with the goal of accurate simulation of water and energy cycle states and fluxes (e.g., Syed et al., 2008).

According to Wang et al. (2017b), heat waves are defined based on the maximum of daily surface air temperature (Tmax). The daily observed Tmax from meteorological sites are used to validate the WRF simulations. The dataset is provided by the China Meteorological Administration (CMA). The locations of observational stations are shown in **Figure 1** (black dots). For the simulations, we focus on the daily maximum of 2 m surface air temperature (T2m), which usually occurs at ∼14:00 or 17:00 Beijing Time (i.e., 06:00 and 09:00 UTC). To investigate the anomalies of upper-level atmospheric circulations during heat waves, a geopotential height of 500 hPa (H500) is used, derived from the new Japanese 55-year Reanalysis (JRA-55) at 1.25° × 1.25° resolution (Ebita et al., 2011).

RESULTS

Model Validation

In this section, we first evaluate the ability of the WRF model to simulate the observed heat wave events, and then investigate the impacts of changing ISM on the characteristics of the three heat waves. **Figure 2** shows the spatial distributions of the averaged Tmax during the three heat wave periods in the observation and in the five sensitivity simulations with different ISM conditions. The model temperatures are interpolated into the observation sites using the bilinear interpolation method. Heat waves in 2003 and 2007 dominated southeastern China (**Figures 2A,G**) and the 2013 heat wave was centered over the middle to lower reaches of Yangtze River, with an averaged Tmax above 35°C (**Figure 2M**). For each of the three events (**Figures 2B-F,H-L,N-R**), the spatial patterns of the simulated heat waves do not vary significantly to different ISM conditions, whereas the magnitude of the averaged Tmax and the spatial extension of high temperatures increase gradually with decreasing ISM. In addition, it is noted that for the three observed heat waves, the CTL simulations can reasonably capture their spatial distributions but generally underestimate the amplitudes of averaged Tmax (**Figures 2E,K,Q**).

The spatial correlations, biases in the number of high-temperature stations with averaged Tmax higher than 35°C (simulations minus the observations), and the root mean square errors (RMSEs) between the observed and the simulated averaged Tmax in five sensitivity experiments for the three

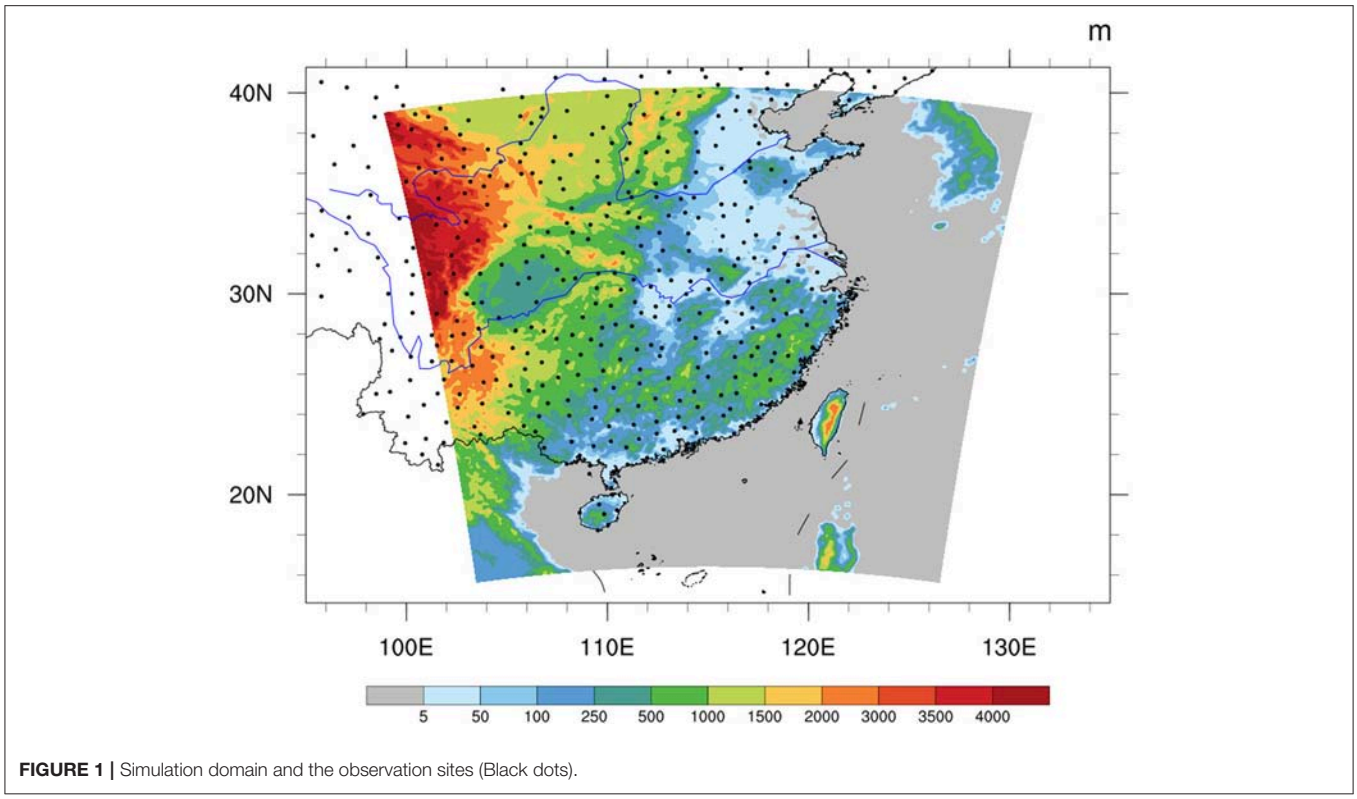

FIGURE 1 | Simulation domain and the observation sites (Black dots).

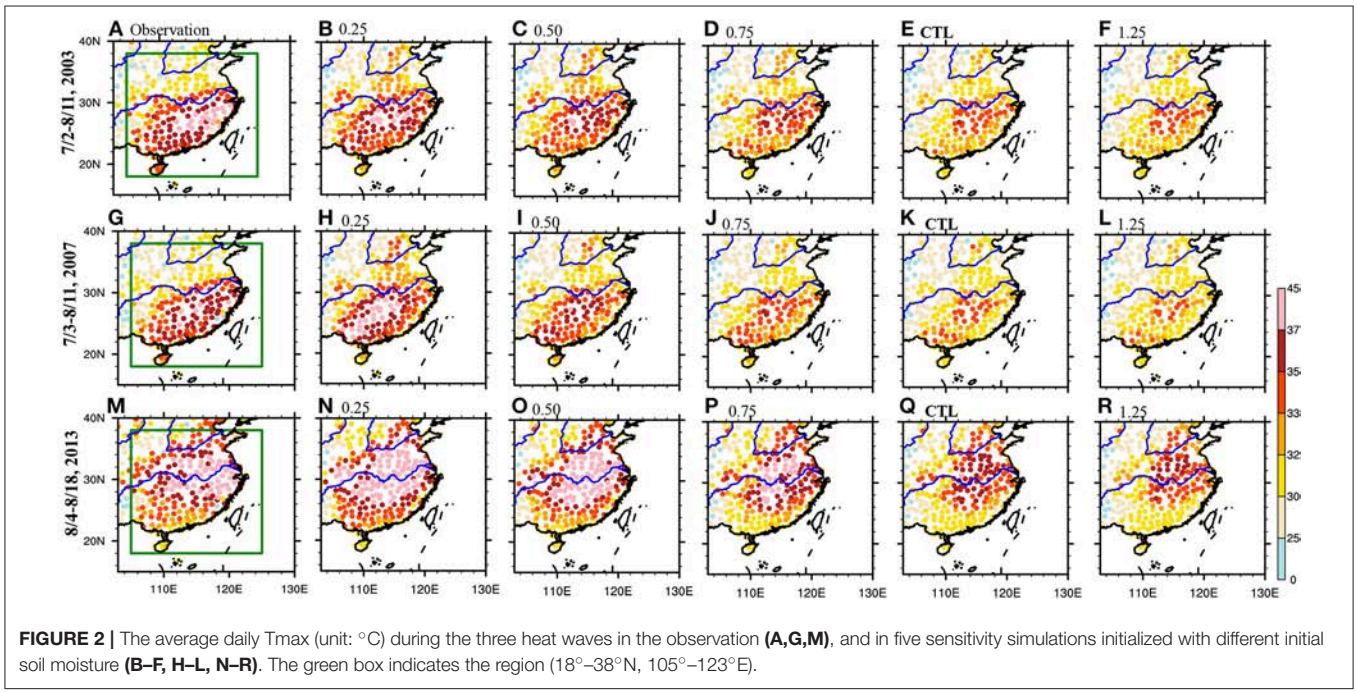

FIGURE 2 | The average daily Tmax (unit: °C) during the three heat waves in the observation **(A,G,M)**, and in five sensitivity simulations initialized with different initial soil moisture **(B–F, H–L, N–R)**. The green box indicates the region (18°–38°N, 105°–123°E).

heat waves are given in **Table 2**. All the statistical values herein and the following area-averaged results (e.g., in **Figure 5**) are derived from the bounded region (105°-125°E, 18°-38°N) in **Figure 2** (green box), which apparently covers the major regions of the three heat waves. For each of the three heat waves, the spatial correlations between the averaged Tmax in the observation and that in the sensitivity simulations with different ISM conditions are of similar values, which are all above 0.70 and significant at the 95% confidence level. The results indicate that all the five sensitivity simulations are able

TABLE 2 | The spatial correlations, the biases in the number of stations with averaged Tmax higher than 35°C (simulated results minus the observations) and the RMSEs between the observed and the simulated averaged Tmax in five sensitivity experiments for the three heat waves.

	Heat Waves / ISM(α)	2003	2007	2013
Spatial Correlations	0.25	0.79	0.71	0.74
	0.50	0.79	0.74	0.77
	0.75	0.79	0.77	0.78
	CTL	0.78	0.77	0.78
	1.25	0.79	0.76	0.78
Biases in the number of high temperatures	0.25	−17	5	21
	0.50	−39	−30	1
	0.75	−58	−53	−29
	CTL	−67	−55	−63
	1.25	−68	−55	−86
RMSEs	0.25	2.15	2.44	2.76
	0.50	2.20	2.18	2.34
	0.75	2.44	2.29	2.34
	1.00	2.68	2.50	2.80
	1.25	2.82	2.65	3.20

to reproduce the spatial pattern of the observed heat waves. However, biases are seen in the magnitudes and extensions of heat waves between the observation and the simulations. We can see that all three CTL simulations underestimate the number of high temperatures (average exceeding 35°C); in other words, the extension of high temperatures for the three observed heat waves are underestimated in the CTL simulations. This potentially indicates a certain overestimation of surface soil moisture with the GLDAS data, as Vivoni et al. (2009) suggested that the soil moisture initializations toward the dryer end ($\alpha < 1.0$) are considered more realistic with respect to field observations. For the three heat waves, the simulated number of high temperatures decreases gradually with increasing ISM. In addition, for the 2003 heat wave, the underestimation of the number of high temperatures is found in all five sensitivity simulations, indicating an overestimation of realistic surface soil moisture existing in all five sensitivity simulations. For the 2007 heat wave, the underestimation of the number of high temperatures is found in the four simulations with α from 1.25 to 0.50, but becomes negligible in the driest simulation ($\alpha = 0.25$). A similar phenomenon is found for the 2013 heat wave, whereby the underestimation of high temperatures is seen for the simulations with α from 1.25 to 0.75, whereas it becomes negligible in the simulation with $\alpha = 0.50$ and turns into overestimation in the simulation with $\alpha = 0.25$. Such results indicate a transition from overestimation to underestimation of the surface soil moisture. For the spatial distributions of averaged Tmax for the three heat waves in 2003, 2007, and 2013, the most realistic simulation among the five sensitivity experiments with the highest spatial correlation and the lowest RMSE is the simulation of $\alpha = 0.25$, 0.50, and 0.50, respectively.

Figure 3 shows the scatterplot and linear trend of the averaged Tmax and the surface soil moisture (0–5 cm) at the observational sites in the bounded region (105°-125°E, 18°-38°N) during the three heat waves. It is obvious that, overall, there is a decreasing trend in the averaged Tmax, with the increasing surface soil moisture for the three heat wave events (negative *R*-value in **Figures 3A–C**). In addition, the decreasing trends of the averaged Tmax decline gradually with increasing ISM in the 2003 and 2007 heat waves, implying a transition from the transitional regime to the wet regime in the soil moisture-temperature relationship (**Figures 3A,B**), whereas the decreasing rates of high temperature in the 2013 heat wave are very significant in all five simulations with different ISM conditions (**Figure 3C**). Furthermore, the linear trends of the averaged Tmax in the five sensitivity simulations for the 2013 heat wave are approximately twice those for the 2003 and 2007 heat waves. Therefore, it can be inferred that, with increasing ISM, the land surface in the 2003 and 2007 heat waves is more easily able to enter the wet regime than that in the 2013 heat wave. The surface soil moisture in the CTL simulations for the three heat waves is shown in **Figure 4**. The averaged surface soil moisture from the CTL simulation for the 2013 heat wave (**Figure 4C**) is apparently lower than that from the CTL simulations of the 2003 and 2007 heat waves over most of eastern China (**Figures 4A,B**), which strongly supports our above supposition. Therefore, the impacts of soil moisture on high temperatures on the CTL and wet simulations in the 2003 and 2007 heat waves should be obviously weaker compared to those from the 2013 heat wave and will be discussed in detail in the next.

To quantitatively characterize the daily variations of heat waves, we define three heat wave indices: heat wave mean temperature (HWMT), heat wave number (HWN) and heat wave accumulated intensity (HWI). For a specific date during a heat wave process, the HWMT means the area-averaged Tmax. The HWN means the number of stations with Tmax higher than 35°C. The HWI means the sum of deviations between Tmax and the 35°C threshold at all stations with Tmax higher than 35°C. The three indices are all calculated over the region (105°-125°E, 18°-38°N). **Figure 5** exhibits the daily HWMT, HWN HWN, and HWI in the observation and the five sensitivity simulations with different ISM conditions, respectively. For the daily HWMT in the 2003 heat wave (**Figure 5A**), the four simulations with α ranging from 0.50 to 1.25 underestimate the daily HWMT throughout the whole heat wave period, consistent with the underestimation of the number of high temperatures in **Table 2**, while the driest simulation with $\alpha = 0.25$ overestimates the daily HWMT during a short period of the heat wave. The magnitude of daily HWMT generally decreases during the heat wave period, with an increasing ISM of α ranging gradually from 0.25 to 1.25. On the other hand, all five sensitivity experiments show high capacity to capture the temporal variability of the daily HWMT, with temporal correlations higher than 0.85 (shown in **Table 3**). The results are similar for the daily HWN and HWMI in the 2003 heat wave (**Figures 5B,C**). The five sensitivity simulations with different ISM conditions show an ability to characterize the daily evolutions of HWN and HWI, with significant temporal correlations around 0.80 (**Table 3**). However, the underestimations of HWN and HWI during the heat wave period are also remarkable in the sensitivity

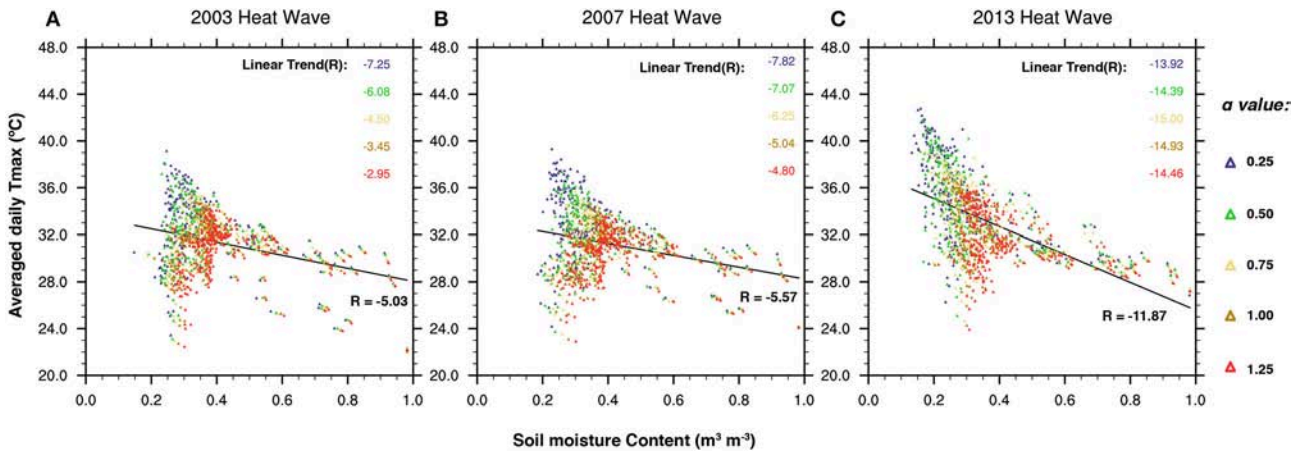

FIGURE 3 | The scatterplot and linear trend between the average daily Tmax and the average daily mean surface soil moisture (0–5 cm) at the observational sites over the region (18°-38°N, 105°-123°E) in the five sensitivity simulations with different ISM. **(A–C)** Represent the three heat wave events. The R values (unit: °C) in each panel represent the overall linear trend (black font) and the individual linear trend (colored fonts) in each sensitivity simulation, respectively.

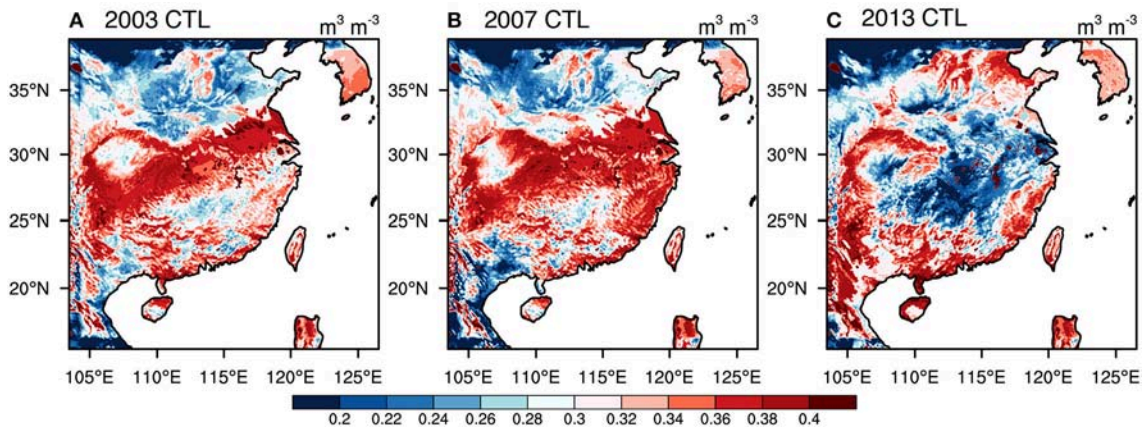

FIGURE 4 | The average surface soil moisture (0–5 cm, unit: m^3m^{-3}) at the CTL simulation during the three heat waves **(A–C)**.

experiments, and the underestimations increase gradually along with increasing ISM. The results indicate that the initial soil moisture shows insignificant effects on the temporal variability of heat waves, but pronouncedly affects their amplitudes, spatial extensions and intensities.

For the 2007 heat wave, the CTL simulation shows an underestimation for the daily HWMT throughout the heat wave period, indicating an overestimation of the surface soil moisture. Moreover, the three other simulations with $\alpha = 0.50$, 0.75, and 1.25 also demonstrate obvious underestimations of HWMT throughout the whole heat wave period, whereas the driest simulation with $\alpha = 0.25$ overestimates the daily HWMT during most of the heat wave period. Additionally, the magnitude of daily HWMT in five sensitivity experiments decreases gradually, with α ranging from 0.25 to 1.25. Particularly, all five simulations with different ISM conditions can reasonably simulate the temporal variability of daily HWMT for the 2007 heat wave, with significant correlations above 0.75 (**Table 3**). Similar results are found for the daily HWN and HWI during the 2007 heat wave (**Figures 5E,F**). All five sensitivity experiments with different ISM conditions can reasonably characterize the daily variations of HWN and HWI, with significant temporal correlations mainly above 0.6 and 0.4, respectively. Moreover, the CTL run and the simulations of $\alpha = 0.50$, 0.75 and 1.25 show apparent underestimations of the HWN and HWI. The underestimations are the worst in the CTL and the wet simulation with $\alpha = 1.25$, which fails to reproduce the existence of high temperatures above 35°C at several dates of the heat wave period. The driest simulation with $\alpha = 0.25$ overestimates the daily HWN and HWI during most of the heat wave period.

For the 2013 heat wave, the CTL simulation shows obvious underestimations of the HWMT, HWN, and HWI (**Figures 5G–I**). The wet simulation with $\alpha = 1.25$ and the dry simulation with $\alpha = 0.75$ also underestimate the magnitude of

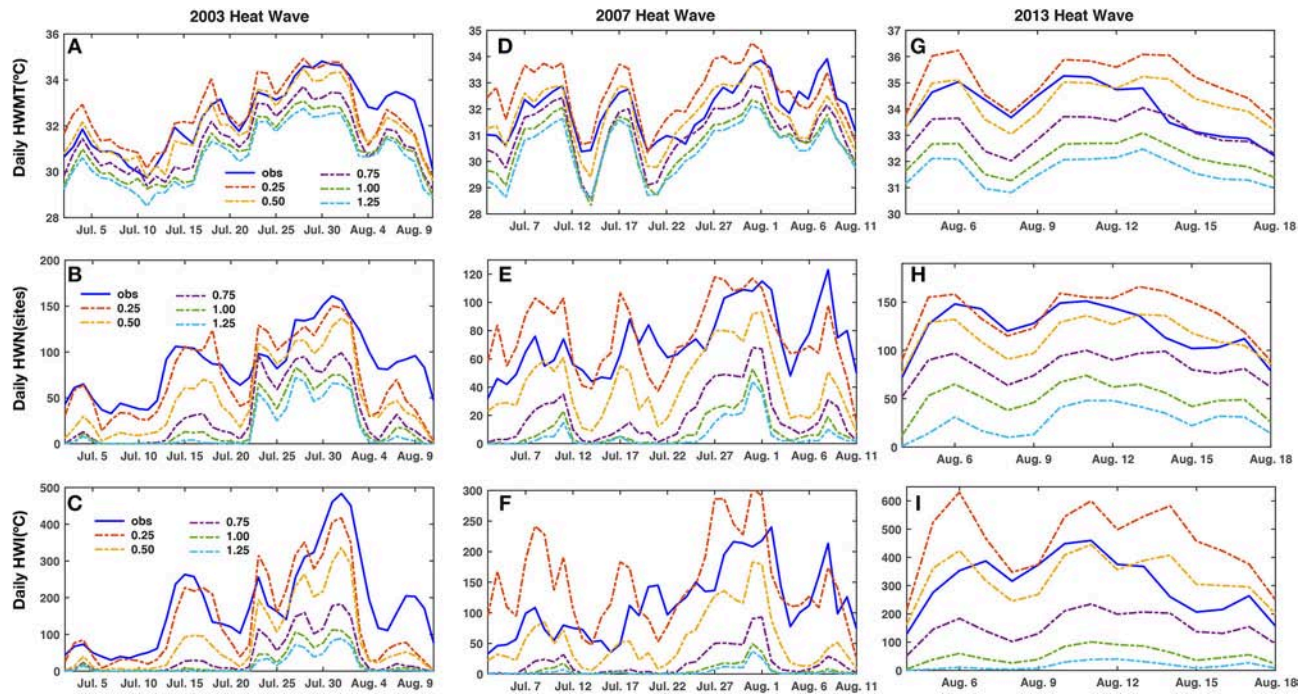

FIGURE 5 | The daily variations of area-averaged HWMT**(A,D,G)**, HWN **(B,E,H)**, and HWI **(C,F,I)** over the region (18°-38°N, 105°-123°E) in the observation and in the five sensitivity simulations during the three heat waves.

TABLE 3 | The temporal correlations between the observed and the simulated daily heat wave indices initialized with different soil moisture (α).

ISM(α) \ Heat Waves	2003			2007			2013		
	HWMT	HWN	HWI	HWMT	HWN	HWI	HWMT	HWN	HWI
0.25	0.85	0.83	0.85	0.78	0.57	0.38	0.71	0.74	0.67
0.50	0.91	0.87	0.88	0.81	0.67	0.41	0.64	0.72	0.71
0.75	0.91	0.82	0.83	0.87	0.72	0.47	0.65	0.77	0.75
CTL	0.93	0.79	0.79	0.90	0.70	0.45	0.69	0.90	0.76
1.25	0.94	0.77	0.78	0.92	0.66	0.48	0.68	0.62	0.57

HWMT, HWM and HWI, whereas the dry simulation with α = 0.50 shows both underestimations and overestimations for the three heat wave indices during the heat wave period, and the driest simulation with α = 0.25 tends to overestimate these heat wave characteristics during most of the heat wave period. Moreover, the temporal correlations between the simulated and observed daily HWMT, HWN and HWI are mainly above 0.60 in the five sensitivity experiments for the 2013 heat wave, significant at the 95% confidence level.

Sensitivity of Heat Waves to Soil Moisture Initialization

It was shown above that the CTL simulation is able to capture the spatial distributions and daily evolutions for each of the three heat waves but apparently underestimates their amplitudes, intensities and spatial extensions. Different ISM conditions show insignificant effects on the spatial distributions and temporal variations of heat waves, but they pronouncedly affect the magnitudes of high temperatures, spatial extensions and intensities. In this section, we will discuss the response of high temperatures to the different ISM conditions in detail.

Figure 6 illustrates the changes of averaged Tmax during the three heat waves caused by a decrease in the initial soil moisture between the two contiguous simulations, represented by 0.25–0.50 (α), 0.50–0.75 (α), 0.75–1.00 (α), 1.00–1.25 (α). During the three heat wave processes (three rows), prominent increases in Tmax with reduced initial soil moisture are mainly located within the heat wave territories. It is worth mentioning that the increases in Tmax imply an increase in both the amplitude and the extent of a heat wave, as shown in **Figure 2**. Moreover, for the three heat waves, the magnitudes and spatial extents of the temperature increases induced by reduced ISM are generally higher in 0.25–0.50 (α) and 0.50–0.75 (α) than those in 0.75–1.00 (α) and 1.00–1.25 (α), with the exception of the 2013

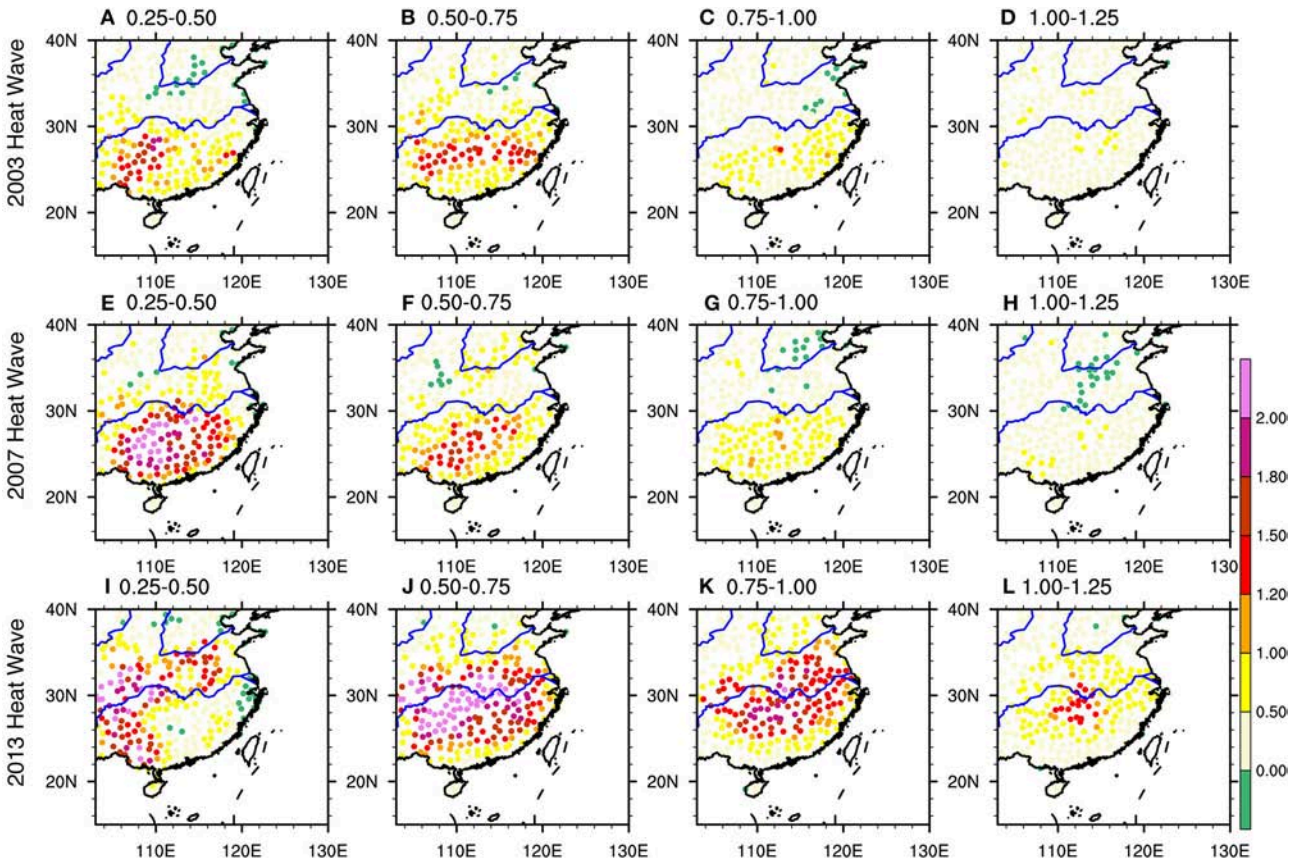

FIGURE 6 | The spatial distributions of changes in average daily Tmax for the three heat waves, with decreased initial soil moisture in two contiguous simulations (**A–D** for the 2003 heat wave, **E–H** for the 2007 heat wave and **I–L** for the 2013 heat wave).

heat wave, where the spatial extent of temperature changes in 0.75–1.00 (α) is comparable or slightly larger than that of temperature changes in the 0.25–0.50 (α). The root mean square deviations (RMSDs) for the averaged Tmax differences between two contiguous simulations over the region (18°-38°N, 105°-123°E) are shown in **Table 4**. Consistent with those depicted in **Figure 6**, the RMSDs in 0.25–0.50 (α) and 0.50–0.75 (α) are higher than those in 0.75–1.00 (α) and 1.00–1.25 (α) in the 2003 and 2007 heat waves, with the exception that the RMSD in 0.75–1.00 (α) is slightly higher than that in 0.25–0.50 (α) in the 2013 heat wave. As mentioned above, with increasing soil moisture, the soil moisture-temperature relationship during the three heat waves experiences a transition from the transitional regime to the wet regime, in which EF and surface temperature become less sensitive to the change of soil moisture content. Therefore, the changes in the averaged Tmax caused by reduced initial soil moisture generally decrease from dryer to wetter simulations. Additionally, as addressed above, the CTL and wet simulations for the 2003 and 2007 heat waves are more likely to enter the wet regime than those for the 2013 heat wave. Thus, the responses of high temperatures to the ISM conditions decreases in the 0.75–1.00 (α) and 1.00–1.25 (α) in the 2003 and 2007 heat waves are much weaker or negligible (**Figures 6C,D,G,H**) compared to those in the 2013 heat wave (**Figures 6K,L**).

TABLE 4 | The RMSD for the averaged Tmax between two contiguous sensitivity simulations with different ISM (α) over the region (18°-38°N, 105°-123°E).

Heat Waves / ISM(α)	2003	2007	2013
0.25–0.50	0.70	1.10	1.04
0.50–0.75	0.76	0.76	1.40
0.75–1.00	0.47	0.51	1.07
1.00–1.25	0.31	0.27	0.64

Figure 7 demonstrates the daily variations of the changes in HWMT, HWN, and HWI caused by ISM decreases between two consecutive simulations. Consistent with the results in **Figure 6**, for the three heat waves, the daily HWMT, HWN, and HWI changes caused by the ISM reductions are mostly higher in 0.25–0.50 (α) and 0.50–0.75 (α) than those in 0.75–1.00 (α) and 1.00–1.25 (α), with the exception that the changes of HWMT and HWN in 0.75–1.00 (α) are relatively higher than those in 0.25–0.50 (α) at several dates during the 2013 heat wave. In particular, the changes of HWMT, HWN, and HWI in the 2003 and 2007 heat waves (**Figures 7A–F**), and the changes of HWMT in the 2013 heat wave (**Figure 7G**) are negligible (close to zero) in the pairs of simulations [1.00–1.25 (α)]. Therefore, for the 2003 and 2007 heat waves, the correlations of all three heat wave indices

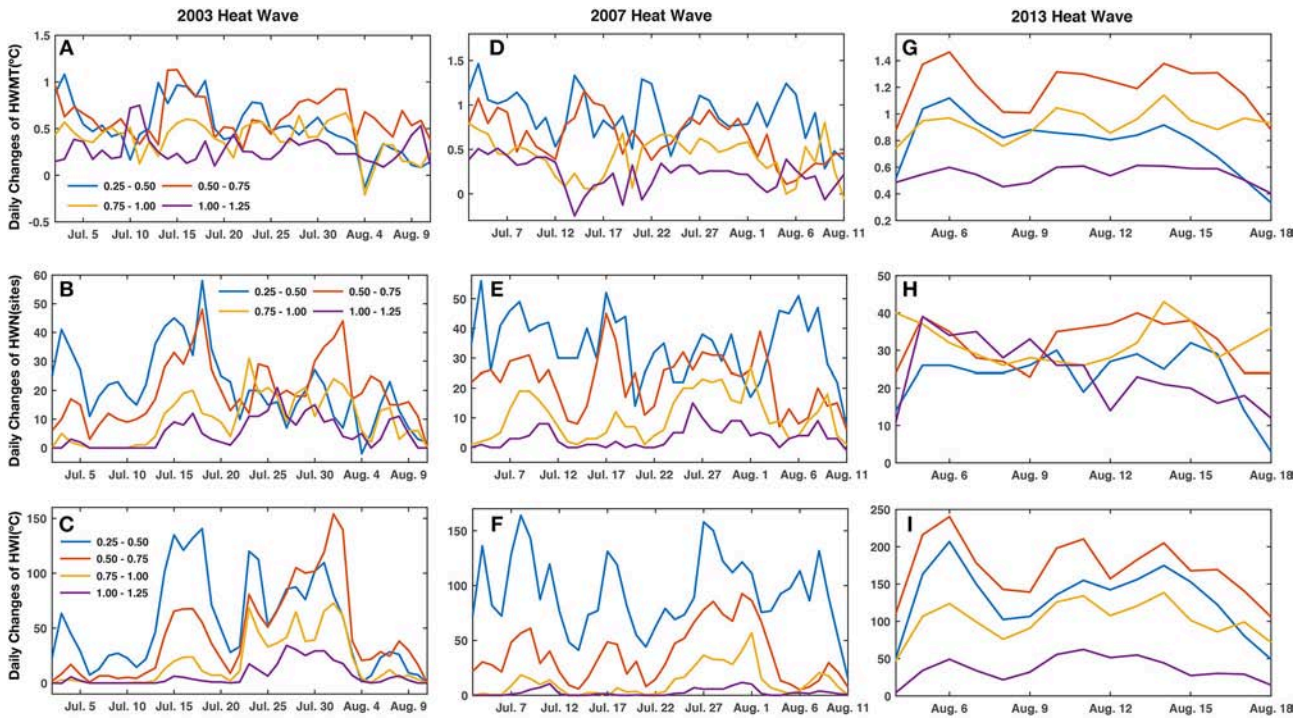

FIGURE 7 | The daily variations of the changes in area-averaged HWMT **(A,D,G)**, HWN **(B,E,H)** and HWI **(C,F,I)** over the region (18°-38°N, 105°-123°E) caused by initial soil moisture decreases in two contiguous simulations.

with the observations are of similar values in the CTL simulation and the wetter simulation, with $\alpha = 1.25$ (**Table 3**). The same happens for the HWMT for the 2013 heat waves (**Table 3**). However, the changes in heat wave indices induced by decreased ISM cannot be ignored in the dryer simulations (**Figure 7**), which are very likely to influence the temporal variations of heat wave indices. It's noted that compared with the CTL simulations, the correlations of HWMT in the 2003 heat wave and almost all the three heat wave indices from the 2007 and 2013 heat waves become lower in the dryer simulations with the decreasing ISM (**Table 3**).

In short, the above results demonstrate that different ISM conditions can significantly influence the amplitudes, spatial extensions, and intensities of heat wave events, whereas they show relatively fewer impacts on their spatial distributions and temporal variations. The response of heat waves to changing ISM is dominated by the different regimes in the soil moisture-temperature relationship, characterized by the varying behaviors of the evaporative fraction (Seneviratne et al., 2010).

It is increasingly argued that the internal variability (IV) of a regional model should be considered in the assessment of a climate change signal (Giorgi and Bi, 2000; Christensen et al., 2001). Here, to ascertain whether the IV has impacts on the high temperature changes induced by different ISM conditions, we designed a set of sensitivity experiments with a perturbation in their initial dates. That is, for each heat wave event, nine simulations with the more realistic surface soil moisture condition ($\alpha = 0.5$) were conducted with a varying initial date, i.e., a lead time of 8 to 0 days to the CTL simulation. For example, for the 2003 heat wave, with α fixed at 0.5, the nine sensitivity experiments were initialized from 13 to 21 June 2003, respectively. Comparative analyses on the nine simulations enable us to assess the impacts of IV. Taking the heat wave in 2003 for example, **Figure S1** exhibits the averaged (a-i) and maximum daily Tmax (j) during the heat wave period (**Table 1**) in the nine simulations with different initial dates. It was found that IV has insignificant effects on the spatial and temporal variations of high temperatures, as the spatial pattern and daily evolution of maximum Tmax show negligible differences among the nine simulations. Thus, it can be concluded that the results of the impacts of ISM on the three heat waves are robust.

Explanations for the Sensitivity

The above results provide robust evidence for the impacts of initial soil moisture on the three observed heat waves with different durations, extensions and intensities. In the following part, systematical analyses are made to discuss the related mechanisms.

Soil Moisture Changes

Figure 8 shows the spatial patterns for the decreases in averaged daily surface soil moisture (0–5cm) between two contiguous simulations [i.e., 0.25–0.50(α), 0.50–0.75 (α), 0.75–1.00 (α), 1.00–1.25 (α)] during the three heat wave events. We focus on the

surface soil moisture (first 5 cm), as it is more strongly correlated to heat fluxes than the total column moisture (Berg et al., 2014). The soil moisture changes in the other soil layers (i.e., at 5–25 cm, 25–70 cm, and 70–150 cm thickness) show similar patterns to the surface layer but with higher magnitudes (**Figures S2–S4**). For the three heat waves (three rows in **Figure 8**), the spatial distributions of the decreases in soil moisture coincide with those of the increases in Tmax (**Figure 6**), consistent with the soil moisture-temperature feedback loop whereby higher temperatures tend to cause more evaporation demand, and thus lead to further drying of the soil (Seneviratne et al., 2010; Alexander, 2011). Additionally, due to the coupling with the upper-level high-pressure system, the positive feedback between surface soil moisture loss, evapotranspiration decrease, and temperature increase can be amplified (Fischer et al., 2007a). **Figures 9A–C** show the anomalies of averaged H500 during the three heat waves (removing the summer climatology during 1971–2000) with JRA-55 reanalysis. It is clear that in the mid-troposphere, the three heat waves are dominated by positive H500 anomalies, which may strengthen the subtropical high. The anomalous upper-level circulations favor the maintenance of heat wave events and enhance the positive feedback between surface soil moisture loss and temperature increases (Fischer et al., 2007a; Pezza et al., 2012).

The corresponding daily variations of the regional averaged surface soil moisture differences between the two contiguous simulations during the three heat waves are shown in **Figure 10**. It is found that the surface soil moisture differences in the pair of simulations 1.00–1.25 (α) are clearly lower than the other pairs of simulations for the three heat waves, especially for the 2003 and 2007 heat waves (**Figures 10A,B**). Because of the wetter land surface in the 2003 and 2007 heat waves compared to the 2013 heat wave (**Figure 4**), the wet experiments for the 2003 and 2007 heat waves are more likely to reach the water-holding capacity. In this case, the soil moisture would be instantaneously removed from the grid box through runoff. Besides, the surface soil moisture differences in the pair of simulations 0.25–0.50 (α) are generally lower than those in the pair of simulations 0.50–0.75 (α) and 0.75–1.00 (α) for the three heat waves, even lower than the 1.25–1.00 (α) in the 2013 heat wave. This is possibly due to the precipitation during the three heat waves, captured in the model (**Figure S5**). Previous studies have suggested that the sensitivity of runoff with respect to soil moisture decreases with lower soil moisture content (i.e., Seneviratne et al., 2006). Accordingly, the precipitation-induced soil moisture anomalies increase with lower soil moisture content, which weakens the soil moisture differences caused by imposed perturbation in dryer simulations [i.e., 0.25–0.50 (α)]. Such a phenomenon is also seen in **Figure 8**.

Heat Flux Response

Most of the inferred impacts of soil moisture for the climate system are induced by its role for evapotranspiration E (or latent heat flux λE, where λ is the latent heat of vaporization) in soil moisture-limited regimes (e.g., Seneviratne and Stöckli, 2008; Seneviratne et al., 2010). The decreased evaporation with reduced soil moisture would lead to increased air temperature through affecting the land surface energy. According to Seneviratne et al. (2010), the land surface energy balance can be expressed as:

$$R_n = \lambda E + SH + G \tag{1}$$

where R_n is the net radiation, λE is the latent heat flux, SH is the sensible heat flux, and G is the ground heat flux at the surface. The net radiation R_n is defined as follows:

$$R_n = SW_{in} - SW_{out} + LW_{in} - LW_{out} \tag{2}$$

where the SW_{in} represents the incoming shortwave radiation, SW_{out} is the outgoing shortwave radiation (equals to $SW_{in} * \lambda$, *where* λ *is the albedo*), the LW_{in} is the incoming longwave radiation, and $LW_{out}$is the outgoing longwave radiation. LW_{out} from the surface is $\varepsilon\sigma T^4 - (1-\varepsilon)\,LWin$, sum of the surface emission and reflected down-welling long wave radiation incident on the surface. ε is the emissivity of the land surface. σ and T refer to the Stefan-Boltzmann constant ($5.67 \times 10^{-8}\mathrm{Wm^{-2}K^{-4}}$) and land surface temperature, respectively. Therefore, the land surface energy balance can be rewritten as:

$$\epsilon\sigma T^4 = (1-\lambda)SW_{in} + \varepsilon LW_{in} - \lambda E - SH - G \tag{3}$$

Equation (3) demonstrates that soil moisture plays a key role for the land surface energy balance and thus for the changes of land surface temperature through its impacts on the energy partioning at the surface. Therefore, the relative contribution of each item in the right hand of Equation (3) for the changes of surface air temperature can be obtained through analyzing their response to soil moisture.

Taking the 2013 heat wave as an example, **Figure 11** shows the changes of each energy component in Equation (3) caused by decreases in soil moisture between two dry simulations [0.25–0.50(α)]. The LH and G are multiplied by −1 for the convenience of comparison. It is demonstrated that the SW_{in} shows few changes over the heat wave territory but a negative tendency south of the heat wave territory (**Figure 11A**). The LW_{in} shows positive changes over the heat wave territory (**Figure 11B**) while its magnitude is much less than the LH changes (**Figure 11C**). The deficit of LH over heat wave territory can be largely compensated by increased SH (**Figure 11D**). Compared with the other energy components, the G shows insignificant changes over the research domain when soil moisture decreases (**Figure 11E**). Therefore, the results show that the impacts of soil moisture on the land surface energy balance are effectuated mainly by affecting the partioning of LH and SH. The soil moisture loss can limit the total energy used by the latent heat flux, and more energy is available for sensible heating. The increased SH enables the warming of the near-surface atmosphere (shown in **Figure 6I**), accompanied by increased LW_{out} over the heat wave territory (**Figure 11F**). It should be noted that the results are similar for the heat waves in 2003 and 2007. This suggests that the changes in Tmax (**Figure 6**) can be reasonably well-explained by the changes in land surface energy balance, induced by initial soil moisture decreases.

Furthermore, we investigate the temporal variations of regionally averaged LH and SH changes caused by the ISM

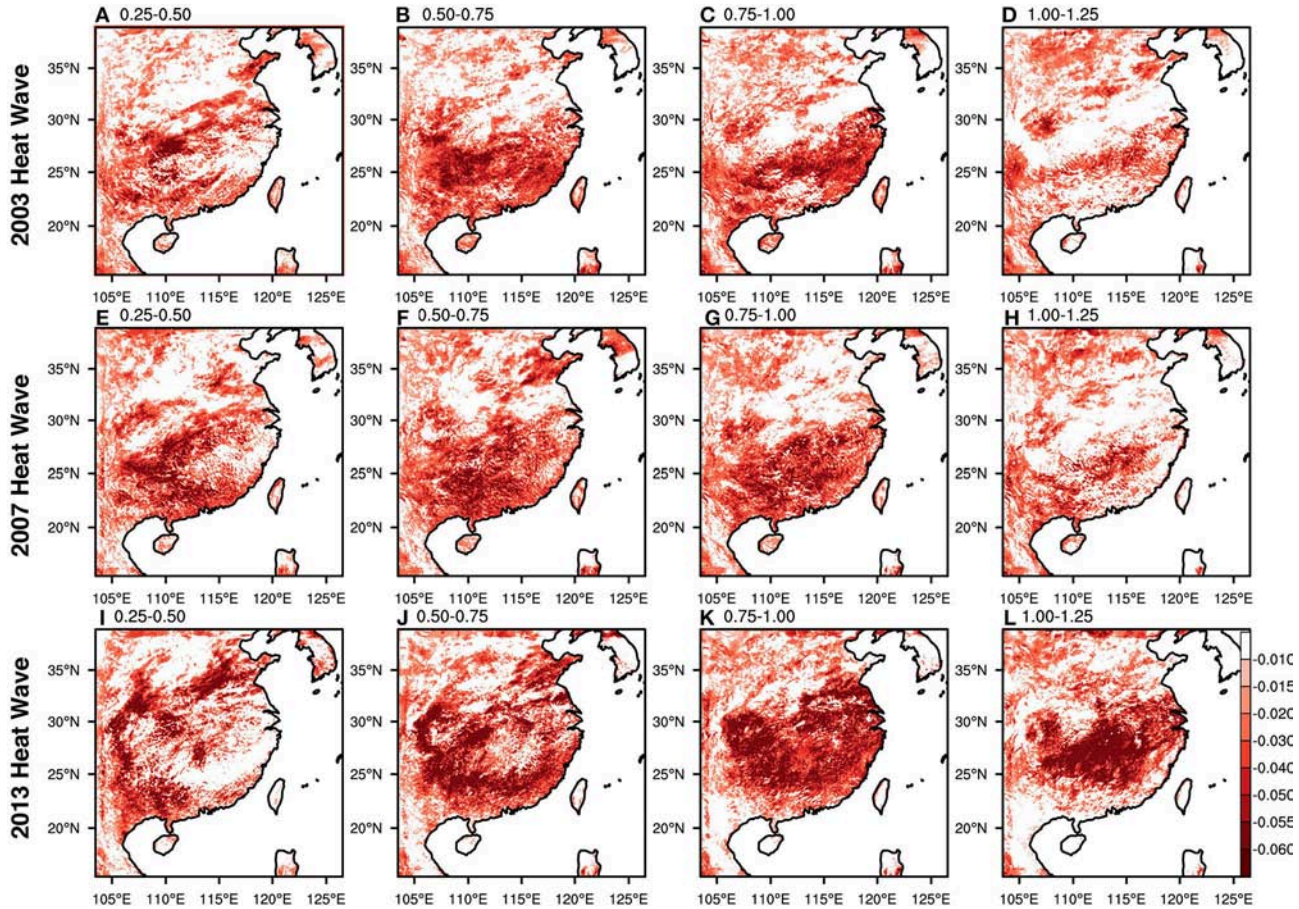

FIGURE 8 | Same as in **Figure 6** but for the average daily mean surface soil moisture (0–5cm: unit: m^3m^{-3}) during the three heat waves (**A–D** for the 2003 heat wave, **E–H** for the 2007 heat wave, and **I–L** for the 2013 heat wave).

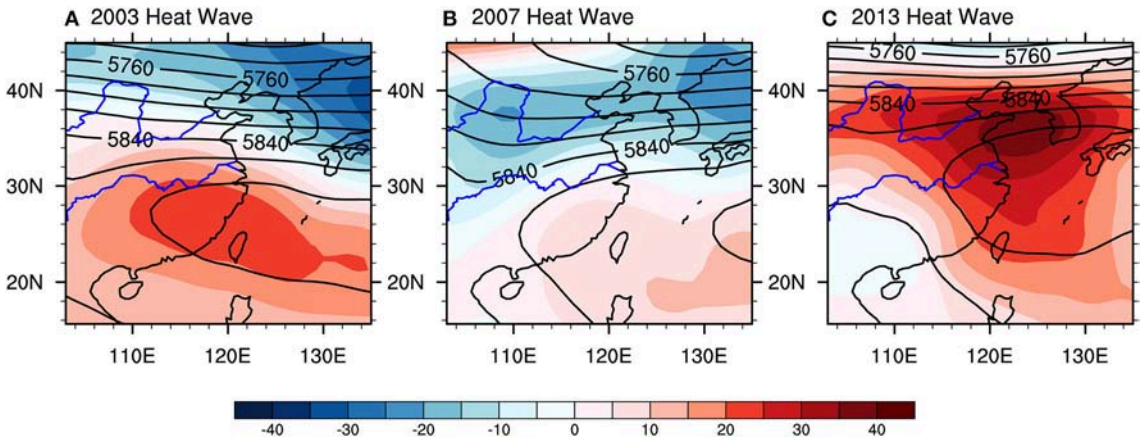

FIGURE 9 | The anomalies (units: m, shading) and the average of H500 (units: m, contour) during the three heat waves **(A–C)** in JRA-55 reanalysis (removing the summer climatology during 1971–2000).

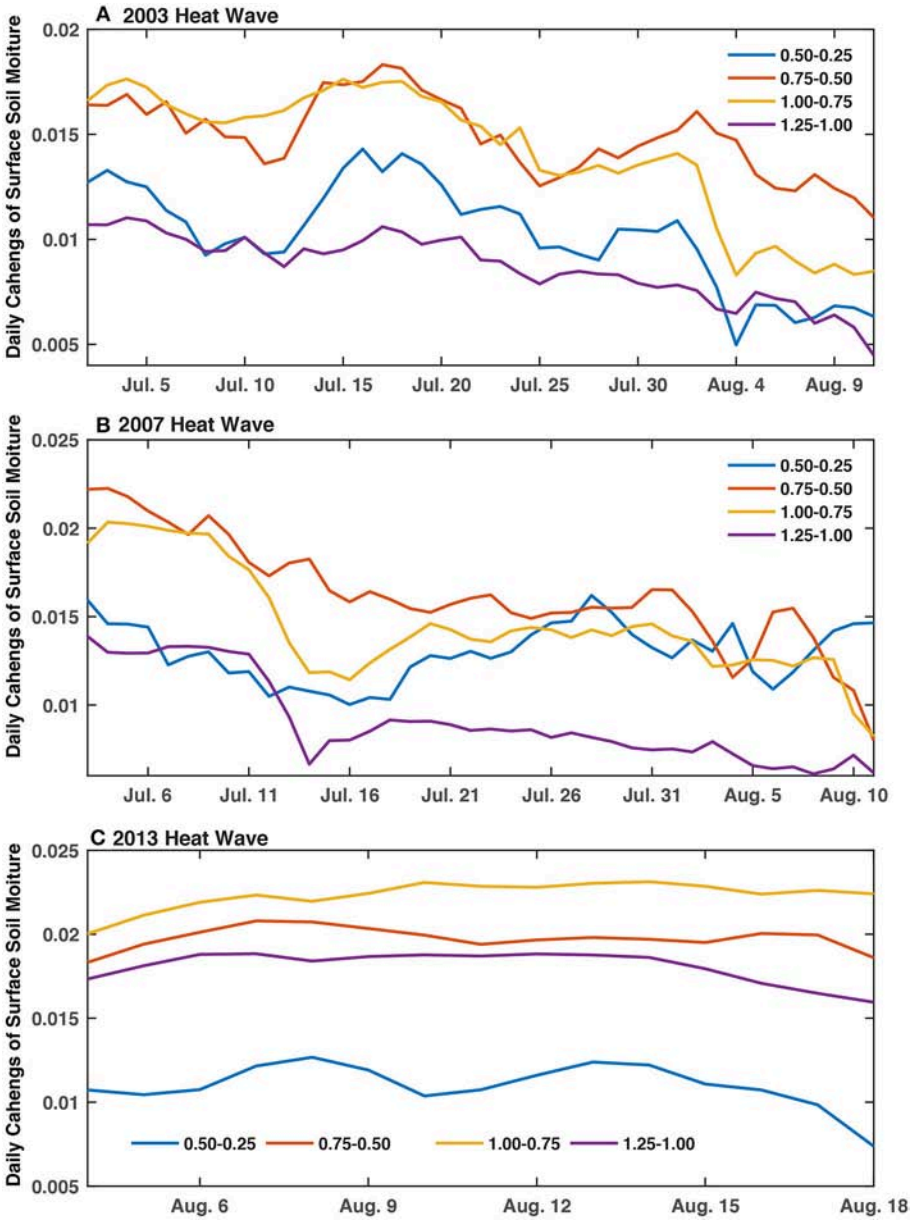

FIGURE 10 | Same as in **Figure 7**, but for daily mean surface soil moisture (0–5cm, unit: m^3m^{-3}). **(A–C)** Represent the three heat wave events.

decreases between two contiguous simulations during the three heat waves (**Figure 12**). The LH changes are multiplied by −1 for the convenience of comparison. For the three heat waves, the changes in LH and SH are higher in 0.25–0.50 (α) and 0.50–0.75(α), followed by the changes in 0.75–1.00(α), and the changes in 1.00–1.25(α) are the least, indicating the transition from a transitional regime to the wet regime in the land surface. Additionally, the spatial correlations between the changes of daily LH/SH and the changes of daily Tmax induced by reduced ISM are mainly significant and of higher values in the pairs of simulations 0.25–0.50 (α) and 0.50–0.75(α) than those in 0.75–1.00(α) and 1.00–1.25(α) during the three heat waves (not shown). The results indicate that the imposed impacts of ISM on high temperatures through affecting the land surface energy balance are weakened over wetter land surfaces.

Atmospheric Circulation Response

It has been demonstrated that high-pressure systems dominated eastern China during the three heat waves (**Figure 9**). Moreover, soil conditions are able to influence the continental-scale atmosphere circulation, leading to the domination of extreme high temperature events (Ferranti and Viterbo, 2006; Fischer

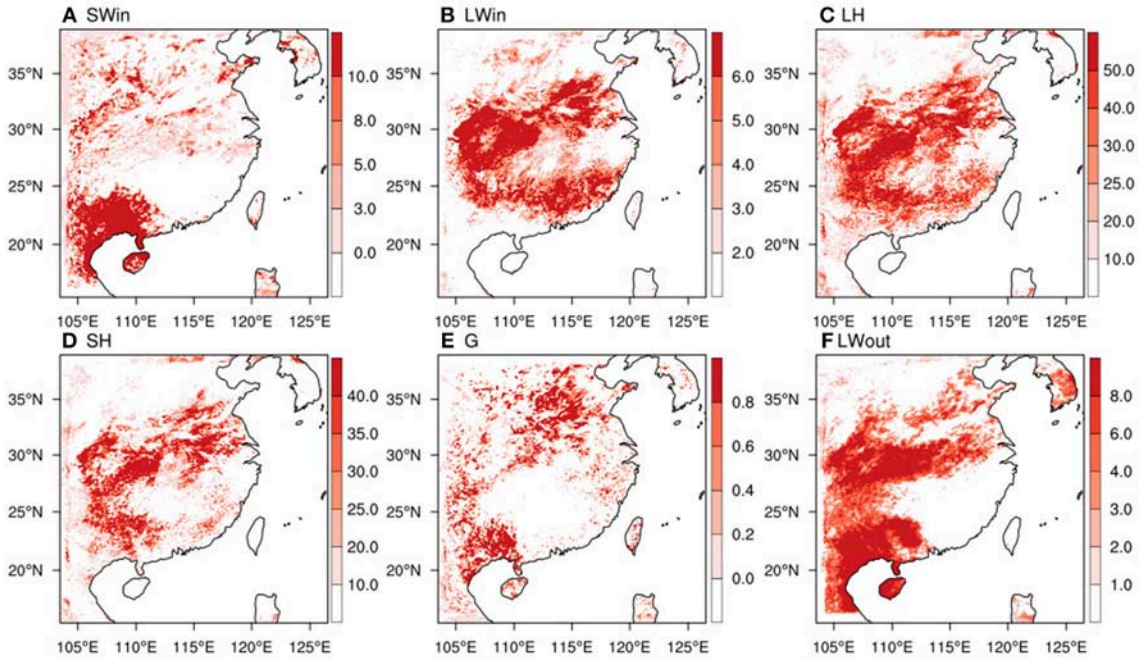

FIGURE 11 | Changes in average SWin **(A)**, LWin **(B)**, LH **(C)**, SH **(D)**, G **(E)**, and LW_{out} **(F)** during the 2013 heat wave caused by soil moisture reduction [0.25–0.50(α)].

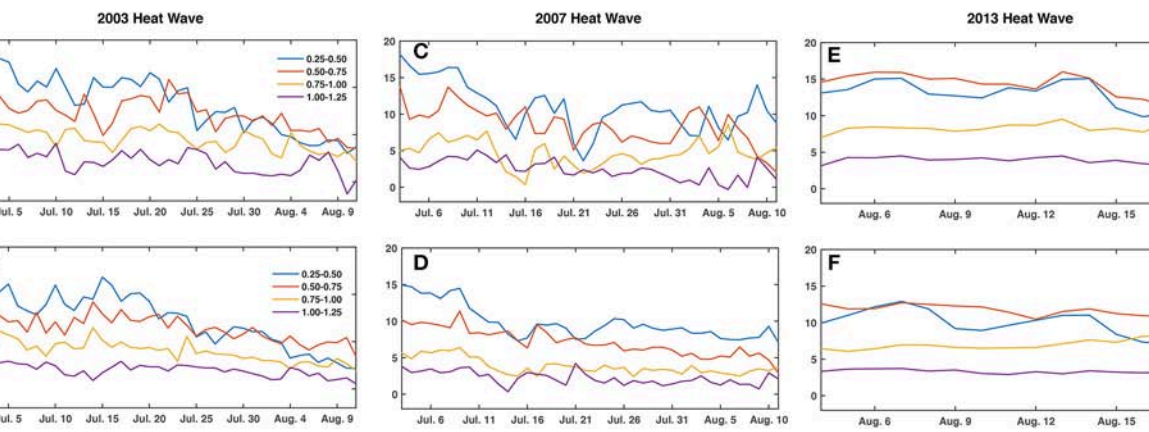

FIGURE 12 | Same as in **Figure 7**, but for the daily mean LH **(A,C,E)** and SH **(B,D,F)**.

et al., 2007b). Here, to broadly represent the response of atmospheric circulation to the initial soil moisture, **Figure 13** shows the 925 hPa (H925) and H500 anomalies caused by initial soil moisture reduction between the very dry and wet simulations [0.25–1.25 (α)]. It is shown that the soil moisture affects geopotential height from the surface to the mid-troposphere. With reduced ISM, the H925 is substantially reduced during each of the three heat waves, with varying magnitudes. The shape and location of the anomaly corresponds well to the changes in temperature shown in **Figure 4**, implying the existence of a surface heat low caused by strong surface heating (Ferranti and Viterbo, 2006; Fischer et al., 2007b). The expanded air induced by surface heating lifts the pressure levels in the middle and upper troposphere (Zeng et al., 2014). As shown in **Figures 13A–C**, H500 is generally enhanced by reduced initial soil moisture, with positive anomalies above the location of the surface heat low for the three heat waves. In turn, the enhanced thickness of the atmosphere from the surface to upper levels associated with soil dryness may strengthen the anomalous circulation pattern (**Figure 9**), and favor local warming (**Figure 6**) and the further drying of the soil, implying a positive feedback mechanism between soil moisture, upper-level circulation and surface temperatures (Fischer et al., 2007a).

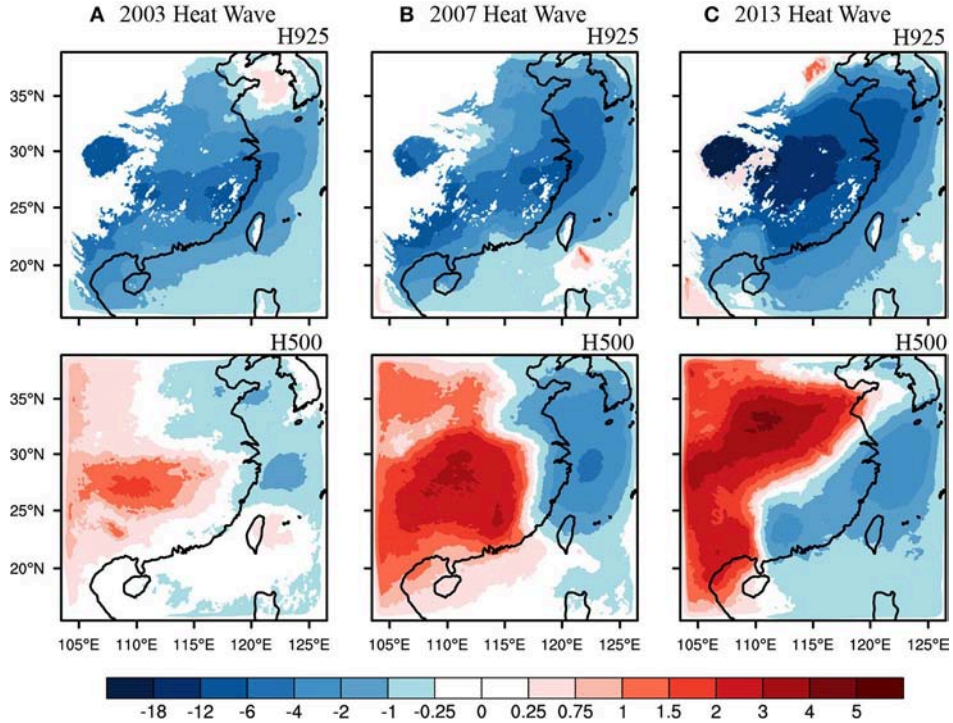

FIGURE 13 | The differences of average daily H500 and H925 (units: m) between the driest and wettest simulations [0.25–1.25 (α)] during the three heat waves **(A–C)**.

SUMMARY AND CONCLUSIONS

In this study, we investigated the impacts of initial soil moisture on the three severe observed heat wave events in 2003, 2007, and 2013 through WRF simulations. The observed heat waves in 2003 and 2007 dominated over southeastern China and the 2013 heat wave was centered over the middle and lower reaches of the Yangtze River. Results show that the CTL simulation is able to reproduce the spatial distributions and the daily evolutions for each of the three heat waves but apparently underestimates their amplitudes, intensities, and spatial extensions. Different ISM contents show insignificant impacts on the spatial distributions and temporal variations of heat waves but pronouncedly affect their magnitudes, spatial extensions, and intensities. Specifically, the average daily Tmax in the three heat waves increases gradually with alongside decreasing ISM. During the heat wave periods, the daily HWMT, HWN, and HWI show apparent increases with the decreased initial soil moisture. In addition, the responses of heat waves are decline gradually with increasing soil moisture, implying a transition from the transitional regime to the wet regime in the soil moisture-temperature relationship. The internal variability in the regional climate model shows insignificant effects on the spatial and temporal variations of high temperatures. Thus, it is concluded that the analyses of the impacts of ISM on the three heat waves are robust.

To explain the sensitivity of the three heat waves to ISM, we investigated the responses of land surface energy and atmospheric circulations to the different ISM contents. Results show that the surface energy balance, especially the partitioning of LH and SH flux, is changed by different ISM contents. With decreased ISM, LH is reduced, and the decrease of energy is compensated by the increased SH, which leads to near-surface warming and further dryness of land. However, such impacts are weakened over the wetter land surface.

The three heat waves were all dominated by anomalous high-pressure systems. The decreased soil moisture may enhance a positive anomaly of geopotential height at the upper levels and thus make the anomalous pattern more persistent. However, a negative anomaly is usually forced over the lower levels due to the strong surface heating. Thus, the thickness of the associated atmosphere is increased from the surface to upper levels. Such a thickened atmosphere associated with soil moisture dryness will further strengthen the local warming and drying.

AUTHOR CONTRIBUTIONS

JT provided the conceptualization. PW did the main computation and analyses. QZ and YY helped in polishing the manuscript.

FUNDING

This work is jointly funded by the National Key Research and Development Program of China (2018YFA0606003, 2016YFA0600303) and the National Natural Science Foundation of China (41375075, 91425304 and 41575099). This work is also supported by the Chinese Jiangsu Collaborative Innovation Center for Climate Change. The observational data of meteorological stations are provided by the China Meteorological Administration (CMA).

ACKNOWLEDGMENTS

The authors also acknowledge with thanks the organizations of NCEP and GLDAS for providing the driving fields in the simulations.

SUPPLEMENTARY MATERIAL

The Supplementary Material for this article can be found online at: https://www.frontiersin.org/articles/10.3389/fenvs.2019.00018/full#supplementary-material

REFERENCES

Alexander, L. (2011). Climate science: extreme heat rooted in dry soils. *Nat. Geosci.* 4, 12–13. doi: 10.1038/ngeo1045

Berg, A., Lintner, B. R., Findell, K. L., Malyshev, S., Loikith, P. C., and Gentine, P. (2014). Impact of soil moisture–atmosphere interactions on surface temperature distribution. *J. Clim.* 27, 7976–7993. doi: 10.1175/JCLI-D-13-00591.1

Black, E., Blackburn, M., Harrison, G., Hoskins, B, and, Methven, J. (2004). Factors contributing to the summer 2003 European heatwave *Weather* 59, 217–223. doi: 10.1256/wea.74.04

Chen, F., and Dudhia, J. (2001). Coupling an advanced land surface-hydrology model with the Penn State-NCAR MM5 modeling system part I: model implementation and sensitivity. *Mon. Wea. Rev.* 129, 569–585. doi: 10.1175/1520-0493(2001)129<0569:CAALSH>2.0.CO;2

Christensen, O., Gaertner, M. A., Prego, J. A., Polcher, J. Internal variability of regional climate models. *Climate Dyn.* (2001). 17, 875–887. doi: 10.1007/s003820100154

Conti, S., Meli, P., Minelli, G., Solimini, R., Toccaceli, V., Vichi, M., et al. (2005). Epidemiologic study of mortality during the Summer 2003 heat wave in Italy. *Environ. Res.* 98, 390–399. doi: 10.1016/j.envres.2004.10.009

Ding, T., Qian, W., and Yan, Z. (2010). Changes in hot days and heat waves in China during 1961–2007. *Int. J. Climatol.* 30, 1452–1462. doi: 10.1002/joc.1989

Dole, R., Hoerling, M., Perlwitz, J., Eischeid, J., Pegion, P., Zhang, T., et al. (2011). Was there a basis for anticipating the 2010 Russian heat wave? *Geophy. Res. Lett.* 38:L06702. doi: 10.1029/2010GL046582

Ebita, A., Kobayashi, S., Ota, Y., Moriya, M., Kumabe, R., and Onogi, K., et al. (2011). The Japanese 55-year reanalysis "JRA-55": an interim report. *Sola* 7, 149–152. doi: 10.2151/sola.2011-038

Ferranti, L., and Viterbo, P. (2006). The European summer of 2003: sensitivity to soil water initial conditions. *J. Clim.* 19, 3659–3680. doi: 10.1175/JCLI3810.1

Fischer, E. M., Seneviratne, S., Vidale, P., Lüthi, D., and Schär, C. (2007b). Soil moisture-atmosphere interactions during the 2003 European summer heat wave. *J. Clim.* 20, 5081–5099. doi: 10.1175/JCLI4288.1

Fischer, E. M., Seneviratne, S. I., Lüthi, D., and Schär, C. (2007a). Contribution of land-atmosphere coupling to recent European summer heat waves. *Geophy. Res. Lett.* 34, 125–141. doi: 10.1029/2006GL029068

Freychet, N., Tett, S., Wang, J., and Hegerl, G. (2017). Summer heat waves over Eastern China: dynamical processes and trend attribution. *Environ. Res. Lett.* 12:024015. doi: 10.1088/1748-9326/aa5ba3

García-Herrera, R., Díaz, J. R. M., Luterbacher, T. J., and Fischer, E.M. (2010). A review of the European summer heatwave of 2003. *Crit. Rev. Environ. Sci. Technol.* 40, 267–306. doi: 10.1080/10643380802238137

Giorgi, F., and Bi, X. (2000). A study of internal variability of a regional climate model. *J. Geophys. Res.* 105, 29503–29521. doi: 10.1029/2000JD900269

Hirschi, M. (2011). Observational evidence for soil-moisture impact on hot extremes in southeastern Europe. *Nat. Geosci.* 4, 17–21. doi: 10.1038/ngeo1032

Hong, S.Y., Dudhia, J., and Chen, S. H. (2004). A revised approach to ice microphysical pro- cesses for the bulk parameterization of clouds and precipitation. *Monthly Weather Rev.* 132, 103–120. doi: 10.1175/1520-0493(2004)132<0103:ARATIM>2.0.CO;2

Hong, S.Y., Noh, Y., and Dudhia, J. (2006). A new vertical diffusion pack- age with an explicit treatment of entrainment processes. *Monthly Weather Rev.* 134, 2318–2341. doi: 10.1175/MWR3199.1

Hu, Q., and Feng, S. (2004). A role of the soil enthalpy in land memory. *J. Clim.* 17, 3633–3643. doi: 10.1175/1520-0442(2004)017<3633:AROTSE>2.0.CO;2

Huth, R. (2000). A GCM simulation of heat waves, dry spells, and their relationships to circulation. *Clim. Change* 46, 29–60. doi: 10.1023/A:1005633925903

Iacono, M. J., Delamere, J. S., Mlawer, E. J., Shephard, M. W., Clough, S. A., and Collins, W. D. (2008). Radiative forcing by long-lived greenhouse gases: calculations with the AER radiative transfer models. *J. Geophys. Res.* 113:D13103. doi: 10.1029/2008jd009944

Jiménez, P. A., Dudhia, J., González-Rouco, J. F., Navarro, J., Montávez, J. P., and García-Bustamante, E. (2012). A revised scheme for the WRF surface layer formulation. *Monthly Weather Rev.* 140, 898–918. doi: 10.1175/MWR-D-11-00056.1

Kain, J.S., and Fritsch, J. M. (1990). A one-dimensional entraining/detraining plume model and its application in convective parameterization. *J. Atmos. Sci.* 47, 2784–2802

Kim, Y., and Wang, G. (2007). Impact of initial soil moisture anomalies on subsequent precipitation over North America in the coupled land atmosphere model CAM3 CLM3. *J. Hydrometeorol.* 8, 513–33. doi: 10.1175/JHM611.1

Koster, R.D., and Suarez, M. J. (2001). Soil moisture memory in climate models. *J. Hydrometeor.* 2, 558–570. doi: 10.1175/1525-7541(2001)002<0558:SMMICM>2.0.CO;2

Lorenz, R., Jaeger, E. B., and Seneviratne, S. I. (2010). Persistence of heat waves and its link to soil moisture memory. *Geophys. Res. Lett.* 37, 384–397. doi: 10.1029/2010GL042764

Matsueda, M. (2011). Predictability of euro-russian blocking in summer of 2010. *Geophys. Res. Lett.* 38:L06801. doi: 10.1029/2010GL046557

Meehl, G. A., and Tebaldi, C. (2004). More intense, more frequent, and longer lasting heat waves in the 21st century. *Science* 305, 994–997. doi: 10.1126/science.1098704

Perkins, S.E. (2015). A review on the scientific understanding of heatwaves—their measurement, driving mechanisms, and changes at the global scale. *Atmos. Res.* 164, 242–267. doi: 10.1016/j.atmosres.2015.05.014

Pezza, A.B., Rensch, P. V., and Cai, W. (2012). Severe heat waves in Southern Australia: synoptic climatology and large scale connections. *Clim. Dyn.* 38, 209–224. doi: 10.1007/s00382-011-1016-2

Ren, F., Cui, D., Gong, Z., Wang, Y., Zou, X., Li, Y., et al. (2012). An objective identification technique for regional extreme events. *J. Clim.* 25, 7015–7027. doi: 10.1175/JCLI-D-11-00489.1

Rohini, P., Rajeevan, M., and Srivastava, A. K. (2016). On the variability and increasing trends of heat waves over India. *Sci. Rep.* 6:26153. doi: 10.1038/srep26153

Seneviratne, S.I., Corti, T., Davin, E. L., Hirschi, M., Jaeger, E. B., Lehner, I., et al. (2010). Investigating soil moisture–climate interactions in a changing climate: a review. *Earth Sci. Rev.* 99, 125–161. doi: 10.1016/j.earscirev.2010.02.004

Seneviratne, S.I., Koster, R.D., Guo, Z., Dirmeyer, P.A., Kowalczyk, E., Lawrence, D., et al. (2006). Soil moisture memory in AGCM simulations: analysis of global land–atmosphere coupling experiment (GLACE) data. *J. Hydrometeorol.* 7, 1090–1112. doi: 10.1175/JHM533.1

Seneviratne, S.I., and Stöckli, R. (2008). "The role of land-atmosphere interactions for climate variability in Europe," in *Climate Variability and Extremes during the Past 100 years*, eds S. Bronnimann, J. Luterbacher, T. Ewen, H. F. Diaz , R. S. Stolarski, and U. Neu (Dordrecht: Springer), 179–193.

Skamarock, W. C., Klemp, J. B., Dudhia, J., Gill, D.O., Barker, D. M., Duda, M. G. et al. (2008). *A Description of the Advanced Research WRF Version 3*. NCAR Technical Notes, NCAR/TN-4751STR

Sun, X., Sun, Q., Zhou, X., Li, X., Yang, M., Yu, A., et al. (2014). Heat wave impact on mortality in Pudong New Area, China in 2013. *Sci. Total Environ.* 493, 789–794. doi: 10.1016/j.scitotenv.2014.06.042

Sun, Y., Zhang, X., Zwiers, F. W., Song, L., Wan, H., Hu, T., et al. (2014). Rapid increase in the risk of extreme summer heat in Eastern China. *Nat. Clim. Change* 4, 1082–1085. doi: 10.1038/nclimate2410

Syed, T. H., Famiglietti, J. S., Rodell, M., Chen, J., and Wilson, C. R. (2008). Analysis of terrestrial water storage changes from GRACE and GLDAS. *Water Resourc. Res*, 44, W02433:doi:10.1029/2006WR005779

Tan, J., Zheng, Y., Song, G., Kalkstein, L.S., Kalkstein, A.J., and Tang, X. (2007). Heat wave impacts on mortality in Shanghai, 1998 and 2003. *Int. J. Biometeorol.* 51, 193–200. doi: 10.1007/s00484-006-0058-3

Teuling, A.J., Seneviratne, S.I., Stöckli, R., Reichstein, M., Moors, E., Ciais, P., et al (2010). Contrasting response of European forest and grassland energy exchange to heatwaves. *Nat. Geosci.* 3, 722–727. doi: 10.1038/ngeo950

Tomczyk, A. M., and Ewa, B. (2015). Heat waves in Central Europe and their circulation conditions. *Int. J. Climatol.* 36, 770–782. doi: 10.1002/joc.4381

Trier, S. B., Chen, F., Manning, K. W., Lemone, M. A., and Davis, C. A. (2008). Sensitivity of the PBL and precipitation in 12-day simulations of warm-season convection using different land surface models and soil wetness conditions. *Monthly Weather Rev.* 136, 2321–2343. doi: 10.1175/2007MWR2289.1

Vivoni, E.R., Tai, K.W., and Gochis, D.J. (2009). Effects of initial soil moisture on rainfall generation and subsequent hydrologic response during the North American monsoon. *J. Hydrometeorol.* 10, 644–664. doi: 10.1175/2008JHM1069.1

Vogel, M. M., Orth, R., Cheruy, F., Hagemann, S., Lorenz, R., van den Hurk, B. J. J. M., et al. (2017). Regional amplification of projected changes in extreme temperatures strongly controlled by soil moisture-temperature feedbacks. *Geophys. Res. Lett.* 44, 1511–1519. doi: 10.1002/2016GL071235

Wang, P., Tang, J., Sun, X., Wang, S., Wu, J., Dong, X., et al. (2017a). Heatwaves in China: definitions, leading patterns and connections to large-scale atmospheric circulation and SSTs. *J. Geophys. Res. Atmos.* 122, 10679–10699 doi: 10.1002/2017JD027180

Wang, P., Tang, J., Wang, S., Dong, X., and Fang, J. (2017b). Regional heatwaves in china: a cluster analysis. *Clim. Dyn.* 1–17. doi: 10.1007/s00382-017-3728-4

Whitman, S., Good, G., Donoghue, E. R., Benbow, N., Shou, W., and Mou, S. (1997). Mortality in Chicago attributed to the July 1995 heat wave. *Am. J. Publ. Health* 87, 1515–1518. doi: 10.2105/AJPH.87.9.1515

Xia, J., Tu, K., Yan, Z., and Qi, Y. (2016). The super-heat wave in eastern China during July–August 2013: a perspective of climate change. *Int. J. Climatol.* 36, 1291–1298. doi: 10.1002/joc.4424

Zampieri, M., D'Andrea, F., Vautard, R., Ciais, P., Nobletducoudré, N. D., and Yiou, P. (2009). Hot European summers and the role of soil moisture in the propagation of Mediterranean drought. *J. Clim.* 22, 4747–4758. doi: 10.1175/2009JCLI2568.1

Zeng, X. M., Wang, B., Zhang, Y., Song, S., Huang, X., Zheng, Y., et al. (2014). Sensitivity of high-temperature weather to initial soil moisture: a case study using the WRF model. *Atmos. Chem. Phy.* 14, 9623–9639. doi: 10.5194/acp-14-9623-2014

Conflict of Interest Statement: The authors declare that the research was conducted in the absence of any commercial or financial relationships that could be construed as a potential conflict of interest.

frontiers in Environmental Science

REVIEW
published: 26 February 2019
doi: 10.3389/fenvs.2019.00021

The History of Ideas of Downscaling—From Synoptic Dynamics and Spatial Interpolation

Hans von Storch and Eduardo Zorita*

Institute of Coastal Research, Helmholtz Zentrum Geesthacht Geesthacht, Geesthacht, Germany

The history of ideas, which lead to the now matured concept of empirical downscaling, with various technical procedures, is rooted in two concepts, that of synoptic climatology and that of spatial interpolation in a phase space. In the former case, the basic idea is to estimate from a synoptic weather map the regional details, and to assemble these details into a regional climatology. In the other approach, a shortcut is made, in that samples of (monthly, seasonal, or annual) large-scale dynamical statistics (i.e., climate) are linked to a sample of local statistics of some variables of interest.

Keywords: downscaling, spatial interpolation, synoptic dynamics, history of ideas, empirical downscaling

OPEN ACCESS

Edited by:
Raquel Nieto, University of Vigo, Spain

Reviewed by:
Kei Yoshimura, The University of Tokyo, Japan
Enrique Sanchez, University of Castilla La Mancha, Spain

****Correspondence:***
Hans von Storch
hvonstorch@web.de

Specialty section:
This article was submitted to Atmospheric Science, a section of the journal Frontiers in Environmental Science

Received: *24 September 2018*
Accepted: *05 February 2019*
Published: *26 February 2019*

Citation:
von Storch H and Zorita E (2019) The History of Ideas of Downscaling—From Synoptic Dynamics and Spatial Interpolation. Front. Environ. Sci. 7:21. doi: 10.3389/fenvs.2019.00021

ROOTS

When talking about "downscaling," a reference is made to the observation that it is possible to estimate small-scale states from the large-scale state. This expectation is included in all dynamical models, which describe the dynamics of the atmosphere and the ocean. The unavoidable truncation of the description, be it a grid point space or in a Galerkin (spectral) formulation, leads to disregarding the dynamics of unresolved scales. The concept, expressed in scales, is demonstrated in **Figure 1**. However, those unresolved scales, such as the boundary layer turbulence, are essential for the correct formation of the large scales. This seeming paradox is, however, routinely overcome by the use of "parametrizations," which is an empirically informed (and possibly dynamically motivated) shortcut to condition the expected influence of the small scales on the large scales, by the state of the large-scales themselves. Thus, the large-scale somehow "knows" with which small scales it is associated.

This observation was the key for modern weather forecasting, as was expressed by Starr (1942):

> "The General Nature of Weather Forecasting. The general problem of forecasting weather Conditions may be subdivided conveniently into two parts. In the first place, it is necessary to predict the state of motion of the atmosphere in the future; and, secondly, it is necessary to interpret this expected state of motion in terms of the actual weather which it will produce at various localities. The first of these problems is essentially of a dynamic nature, inasmuch as it concerns itself with the mechanics of the motion of a fluid. The second problem involves a large number of details because, under exactly similar conditions of motion, different weather types may occur, depending upon the temperature of the air involved, the moisture content of the, air, and a host of, local influences'."

First ideas along the lines of this article were presented in a conference proceeding by Von Storch (1999).

It may be useful to define, what we mean with the word "downscaling," and the "attributes" empirical" and "dynamical." The basic idea of downscaling is the observation that in amny case, the statistics of variables of interest at smaller scales may be skillfully estimated by relating it to

the state of larger scales. Thus, the state of large sclaes becomes the "predictor," or maybe better: the "conditioner" of the smaller scale statistics. The downscaling is empirical, when the link is empirically determined, in particular by fitting statistical models; it is dynamical, when the link is established by process-based models, in particular limited area models of the hydro- and thermodynamics of the atmosphere or the ocean. The main focus of our article is on the empirical part, but the dynamical one is also dealt with.

The purpose of this article is to present the roots of ideas, which were used to build the concept of downscaling, namely synoptic climatology and spatial interpolation. As such, the article dos not present new ideas of how to do downscaling, nor an improved systematic of the various avenues available to do downscaling. Instead it is an account of the history of ideas behind something like an "industry" in climate sciences, which began with first publications in the early 1990s, but exploited earlier work, such as that of the above-mentioned Victor Starr.

The technical aspects of implementing downscaling is subject to books and articles in encyclopedias, as will is listed below.

Empirical Procedures

The term "downscaling" was introduced by von Storch et al. (1991)—it refers to a statistical approach that relates statistics of large scales to statistics of small scales, or impacts

$$S_t^C = F(L_t^C, \eta_t^s) \tag{1}$$

with small scale climate states S_t^C, large-sale climate states L_t^C, and small-scale physiographic details η_t^S, which are external to the dynamics. The superscript C refers to "climate," and F represents a statistical model. This model, possibly based on a phenomenological motivation, is fitted to recorded samples of the statistics of the large scales and the small scales (or impacts). F can take various forms, but it is always a kind of interpolated map, with L_t^C as coordinates (more on this later). The time t is no longer a time instance, but represents monthly or annual means. For early reviews, refer to von Storch et al. (2000a) or Zorita and von Storch (1997).

The link (2) is not a direct dynamical link, i.e., it may be that the large-scale "predictor," say the monthly mean intensity of westerly, has nothing directly to do with the forming of the state of the predictand, such as the height of storm surges at a certain location. Instead the link exploits the empirically derived fact that in months with on average stronger westerly winds, higher storm surges are observed in Cuxhaven (by referring to a later example). The main wind does nothing with the water, but embedded in an intensified westerly wind, more and heavier storms travel. And these, the embedded storms, cause the accumulation of coastal waters (von Storch and Reichardt, 1997).

This indirect statistical link can be more explicitly resolved by including in S_t^C not only the expected mean of the small-scale variables (conditioned on the large-scale flow), but instead parameters that describe a full probability distribution or a stochastic process. These parameters are the ones that are conditioned on the large-scale dynamics (Wilby et al., 1999, 2002; Busuioc and von Storch, 2003).

In the following sections The Interpolation Problem and Example: Fitting surfaces, we address and illustrate the concept of extending a cloud of data into a mapping, in case of a 2-dimensional problem a surface, by interpolation. Before doing so we discuss the closely related concept of dynamical downscaling.

Dynamical Procedures

Empirical downscaling is related to dynamical downscaling, which grew from limited area modeling. However, in the conventional set-up this latter procedure is nor really "downscaling," i.e., deriving estimates of smaller-scale states from larger-sale states, but all scales along a lateral boundary zone. The introduction of large-scale constraints overcame this limitation, and allowed eventually global dynamical downscaling.

This principle describes downscaling "weather." In a formal nutshell, it may be expressed as

$$S_t^w = M(L_t^w, \eta_t^s) \tag{2}$$

With the large-scale weather state L_t^w, the small-scale weather state S_t^w, and some physiographic details η_t^s at small scales, which are external to the dynamics. M represents a dynamical model.

A "climate" downscaling may be obtained by applying the model (2) repeatedly to a sufficiently large number of large-scale states, which sample the "climate" (the statistics of weather) sufficiently completely.

In a pure form, this concept was implemented by the stochastic-dynamic method [SDM; e.g., (Frey-Buness et al., 1995)], which ran a limited area model covering, for instance, the Alps with a set of characteristic weather variables, such as wind direction or vertical stability. This approach was computationally efficient, as a large number of (short term) simulations were feasible, even if a very high resolution was as implemented.

Later this concept was replaced by running regular "limited area models" (LAM, Dickinson et al., 1989), originally derived from regional atmospheric forecast models. These models, forced along the lateral boundaries with time-variable atmospheric states (and lower boundary values), were run for sufficiently long time, so that statistics could be derived from the small-scales simulated by the LAM. The LAMs replaced the SDM method after more and more computing time became available, and the heavy computational costs needed for running LAMs for extended times became affordable.

Dynamical downscaling has been studied and extensively pursued in big internationally coordinated projects, such as the the European projects PRUDENCE (Christensen et al., 2002) and ENSEMBLES (Christensen et al., 2007) or the international CORDEX (Giorgi and Gutowski, 2015; Souverijns et al., 2019).

In the beginning the LAM method was not labeled as "downscaling," and indeed it does not represent a downscaling in a strict sense—the model does not process given large-scale states, but all scales along a narrow boundary ("sponge") zone. A consequence is that the state in the interior is not uniquely determined by the boundary values—a mathematical fact long known. If the area is relatively small, and the region is well-flushed (i.e., disturbances travel quickly through the region, as is the case with most mid-latitude regions), multiple solutions rarely emerge. However, if the region is large, say covering the

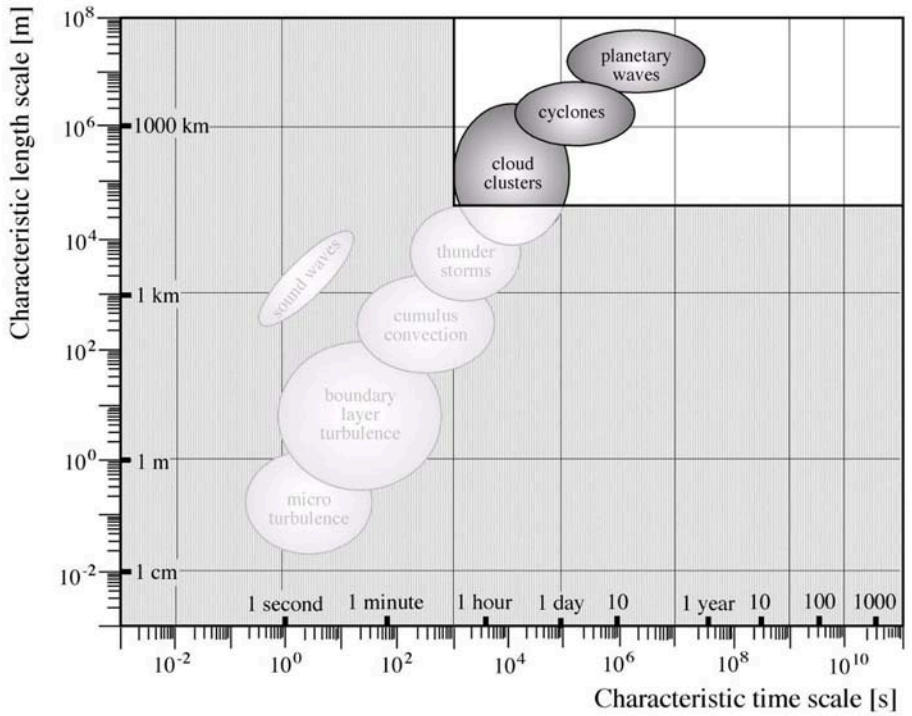

FIGURE 1 | Distribution of atmospheric dynamical processes in the weather system, sorted according to spatial and temporal scales. The stippled part, with small scale processes, is usually not explicitly described in models of the system, but "parametrized." von Storch and Zwiers (1999); ©Cambridge University Press.

entire contiguous US, then the steering of the interior state by the boundaries becomes weak (Castro and Pielke, 2004) and the model shows often tendencies of "divergence in phase space."

Much later, a truly downscaling methodology was developed by introducing a large-scale constraint (e.g., scale-dependent spectral nudging; Waldron et al., 1996; von Storch et al., 2000b) into the LAMs; with this modification, the model was no longer used to solve a boundary value problem but as a data assimilation scheme, which blended dynamical knowledge (the equations of motions etc.) with empirical knowledge (the large-scale state). The success of doing so was illustrated by the case of the contiguous US (Rockel et al., 2008).

Even later, the obvious extension of using the large-scale constraint in a global model (Yoshimura and Kananitsu, 2008; Schubert-Frisius et al., 2017; von Storch et al., 2017) was implemented, which then generates details in all regional states, consistently with the large-scale (global) state. This cannot be done with regular unconstrained global models (GCMs), because there is no way of enforcing a particular large-scale state. This illustrates that conventional unconstrained LAMs are not really "downscaling."

State of the Art

Downscaling has become a household term and hardly needs an explanation when used in scientific papers and reports. Encyclopedias, as well as similar collections of articles, feature accounts of the concept and issues (Rummukainen, 2009, 2015; Wilks, 2010; Ekström et al., 2015; Benestad, 2016), and books have been published (Benestad et al., 2008; Maraun and Widmann, 2018).

While (2) describes "weather downscaling," in most cases by exploiting dynamical models, the relationship (1) represents "climate downscaling," which by using empirical links relates a predictand to a predictor. The advantage of methods based on (2) is that they may be better for studying so far unobserved states, assuming that the considered processes describe the dynamics of the unobserved states well, while (1) allows building links between variables which can hardly be linked dynamically, such as winter mean temperatures and the timing of flowering of a plant (Maak and von Storch, 1997).

THE INTERPOLATION PROBLEM

Today, we are used to present spatial distributions as geographical maps, implicitly assuming that we would have data at all locations—but we have only data at some locations; the rest is achieved by spatial interpolation. It was Alexander von Humboldt, who pioneered this practice in 1817 (e.g., Knobloch, 2018). Humboldt himself saw the introduction of the concept as one of his major achievements (details: Knobloch, p. 21). He explained in a 1853 book: "*Kann man verwickelte Erscheinungen nicht auf eine allgemeine Theorie zurückführen, so ist es schon ein Gewinn, wenn man das erreicht, die Zahlen-Verhältnisse zu bestimmen, durch welche eine große Anzahl zerstreuter Beobachtungen miteinander verknüpft werden können, und*

den Einfluß lokaler Ursachen der Störung rein empirischen Gesetzen zu unterwerfen." [1] (Humboldt 1853, S. 207; quoted after Knobloch, 2018).

Humboldt named these lines "isotherms." Von Storch (1999) noted: "*These contour lines chiefly served the purpose of visualizing the quantitative data. Inside the 20 degree isotherm all stations report temperature larger than 20 degrees, whereas outside the area enclosed by this isoline the temperature at all stations would be less than 20 degrees. The isotherm itself is imaginary; in principle there is such a line, but it can be determined only approximately; it is the art of spatial interpolation to describe this unknown unobservable line.*"

Obviously, the concept can, and was generalized to show "isolines" of other geophysical quantities, such as frequency of winds with gale speeds or amounts of rainfall. Prominent names were Vladimir Köppen and his coworker Rudolf Geiger, who presented their climate classification maps in this way.

However, when more and more mathematical thinking spread in the scientific community, the link to geographical maps weakened, and more general coordinates were introduced. Von Storch (1999) introduced as an example Osborn's et al. (1999) analysis of precipitation in Central England given as a function of vorticity and flow direction (**Figure 2**). We use this example here not because of specific physical interest—this has been dealt with in the original paper by Osborn et al. (1999)—but because it allows to transparently and imply illustrate the issues.

Of course, continuously distributed data did not exit for preparing this map; instead the limited number of scattered data points were binned into a finite number of boxes, and after interpolation isolines were plotted. **Figure 2** informs that a value of −2.5 mm/day for flow strength of 20 m/s and a flow direction of 100° is the mean anomaly (difference from long term mean) of precipitation amounts across all available reports on days with a flow strength of about 20 m/s and a flow direction of about 100°.

Figure 2 shows a 2-dimensional representation, as geographical maps do. But once more general coordinates were introduced, the generalization to more dimensions became possible (even though the graphical presentation is lost, when four and more dimensions are employed).

Von Storch (1999) formalized the concept by asking for an interpolation of K data points, labeled as $\mathbf{G}^k$ at "locations" $\mathbf{x}^k = (\mathbf{x}_1^k, \ldots \mathbf{x}_n^k)$ in an n-dimensional space. The result of the interpolation is a "surface" **I**, with values for all points $\mathbf{x} = (x_1, \ldots x_n)$ in the n-dimensional space, with the property that the difference of this surface at the given data points is limited by some values, say $\| \mathbf{I}(\mathbf{x}^k) - \mathbf{G}^k \| < \delta$. The maximum accepted deviation δ is in most cases zero. In case of kriging, when a "nugget effect" is considered, δ may is non-zero (Wackernagel, 1995).

Implicitly it is assumed that there is a "true" surface *I*, with accurate manifestations $\mathbf{G}^k = \mathbf{I}(\mathbf{x}^k)$ at the locations $\mathbf{x}^k$. This is meaningful in traditional geographical problems, but in some cases $\mathbf{G}^k$ may be considered a random realization of $\mathbf{I}(\mathbf{x}^k)$—for instance, when the data are collected during different times, and the distribution varies in randomly in time. Then I may represent the localized expectation of G, i.e., $\mathbf{I}(\mathbf{x}) = \mathbf{E}(\mathbf{G}|\mathbf{x})$, with the expectation operator **E**.

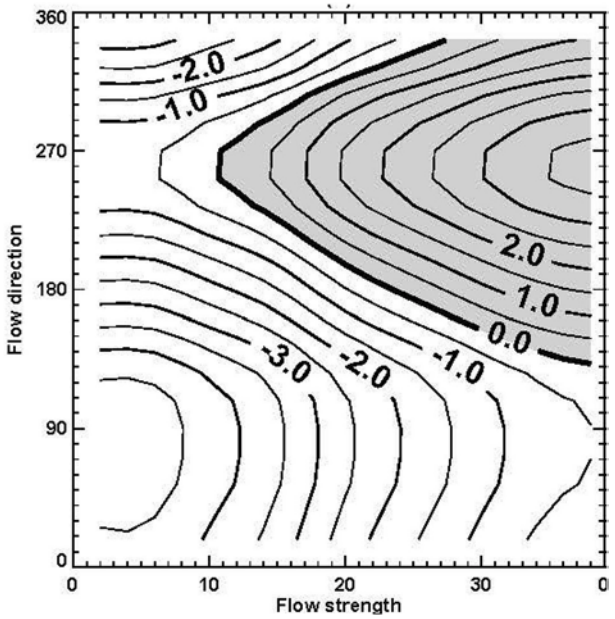

FIGURE 2 | Mean precipitation anomalies (i.e., deviations from the long term mean; in mm/day) in Central England given as function of flow direction (degree) and flow strength (m/s). From Osborn et al., 1999; © Inter-Research 1999.

In **Figure 2** Middle England precipitation is presented as being determined by direction and strength, but there are certainly other factors—thus, precipitation is not determined by the two considered factors, but conditioned, in a stochastic sense.

Von Storch (1999) notes that "the result of the interpolation is an approximate or estimated surface $\mathbf{I}_E$, which differs to some extent from the "true" surface of conditional expectations. The purpose of the spatial interpolation is the determination of the surface $\mathbf{I}(\mathbf{x})$ and not the reproduction of the points $\mathbf{G}_k$. Therefore, the success of $\mathbf{I}_E$ as an estimator of **I** may be determined only by comparing the estimates $I_E(\mathbf{x})$ with the additional $\mathbf{G}(\mathbf{x})$-values at a number of data points **x**, which have not been used in the estimation process."

EXAMPLE: FITTING SURFACES

The question is how such surfaces may be constructed. The interpolation itself can be done in various ways; they differ with respect to a-priori assumptions made about the structure of the surface.

The strongest assumption specifies the global structure. A frequent case refers to multiple regression, which suggests that the surface is a (linear) plane. Often the regression is based on Canonical Correlation Analysis or Redundancy Analysis (cf. von Storch and Zwiers, 1999).

[1] "If complex phenomena cannot be explained by a general theory, then a description is helpful, how a large number of scattered observations are interrelated, and to explain deviations by local empirically formulated causes.

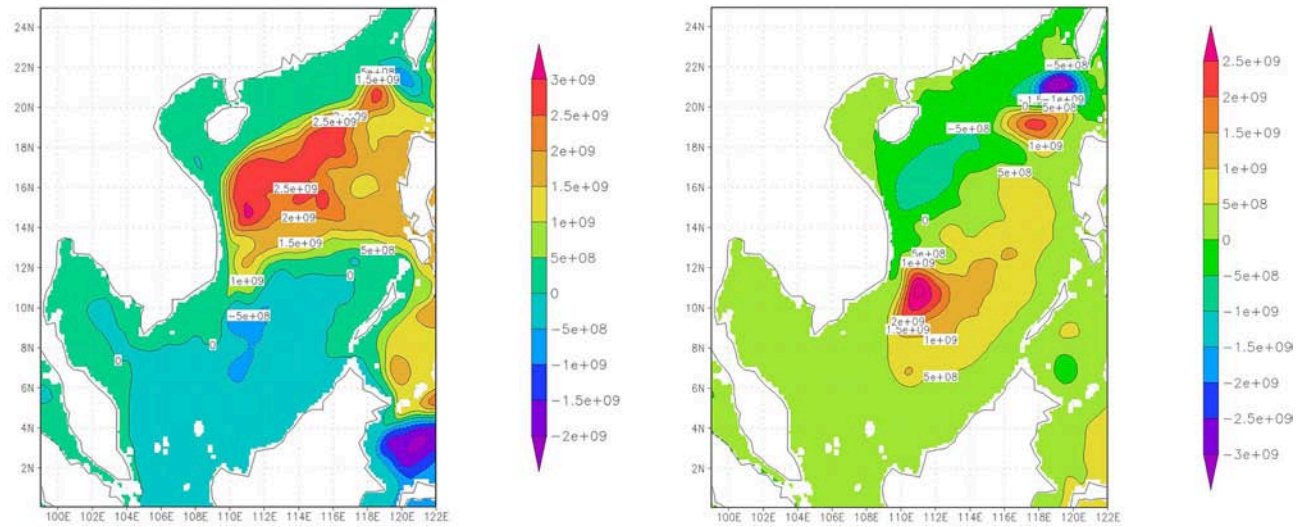

FIGURE 3 | Dominant patterns of interannual variability of summer season barotropic stream function in the South China Sea, the coefficients of which are used in the presentation in **Figure 4** and in the mapping efforts shown in **Figure 5**. Currents follow the gradients of the stream function, clockwise around a center of high (red) values, and counterclockwise around centers with negative (blue) values. Unit: kg s^{-1} (kg/s). Courtesy: Zhang Meng.

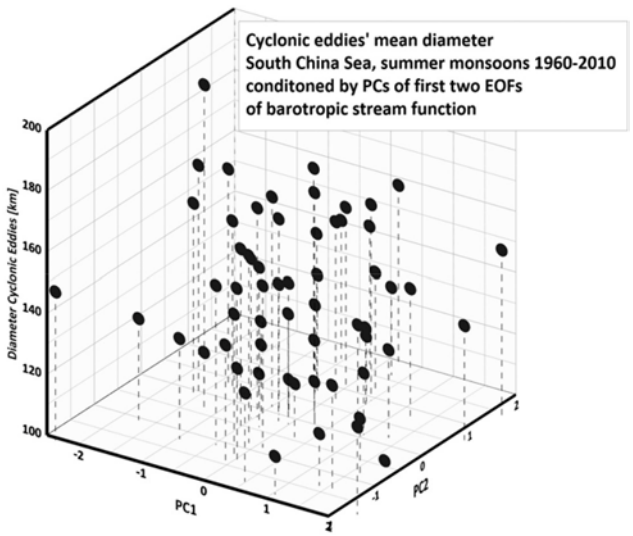

FIGURE 4 | Seasonsal means of cyclonic eddies' diameter in the South China, 1960–2010, given as function of the principal components of the first two EOFs of the barotropic stream function in the South China Sea as shown in **Figure 3**.

If the assumption deals only with local properties, the fitting process is considerably more flexible. Straight forward linear interpolation is an example; Brandsma and Buishand (1997) have used cubic splines for specifying precipitation as a function of temperature. Osborn's example (**Figure 2**) belongs also to this class of interpolations. Geostatistical interpolation, often simply called kriging, is a widely used in mathematical geosciences (e.g., Harff and Davis, 1990), which has also be used for downscaling (e.g., Biau et al., 1999). Fashionable approaches such as neural networks (e.g., Chadwick et al., 2011) and fuzzy logic (e.g., Faucher et al., 1999; Bardossy et al., 2005) are also in use.

The analog, or nearest neighbor, (Zorita et al., 1995; Brandsma and Buishand, 1998; Zorita and von Storch, 1999) represents the surface as piecewise constant plateaus around the data. In geostatistical cricles the method is also known as Voronoi nets (cf. Stoyan et al., 1997).

For illustration, we discuss here three different approaches—bivariate regression, ordinary kriging, and analog—using an example of generalized coordinates in a phase space. We have chosen this example to illustrate that rather abstract problems may be considered.

When preparing a spatial interpolation, some assumptions about the data **G** at locations **x** need to be made. The major assumption is that **G** is representative for a neighborhood of **x**, or that **I** has the same statistical properties in that neighborhood. A correlation length scale may be representative for this neighborhood; this is explicitly so in case of kriging. In that concept, also some spatial discontinuities are permitted ("Nugget effect"; Wackernagel, 1995).

The example employs the displaying the mean summer seasonal cyclonic eddy diameters in the South China Sea (Zhang and von Storch, 2018) as a function of the coefficients of indices of the regional barotropic stream function (the stream function of the vertically averaged flow). Both, the eddy properties as well as the stream function have been constructed using a dynamical ocean model, which was forced with variable atmospheric conditions for the 61 summer seasons 1960–2010 (Zhang and von Storch, 2018). Obviously, the case presented here has no specific significance for the presentation here; it is a mere example, which demonstrates how different interpolating surfaces may be constructed.

The dynamical concept is that some statistics of migrating ocean eddies, in this case the mean seasonal size, may be related to variations in the current patterns. Of course, not all variations in eddy size can be traced back to current anomalies but it is

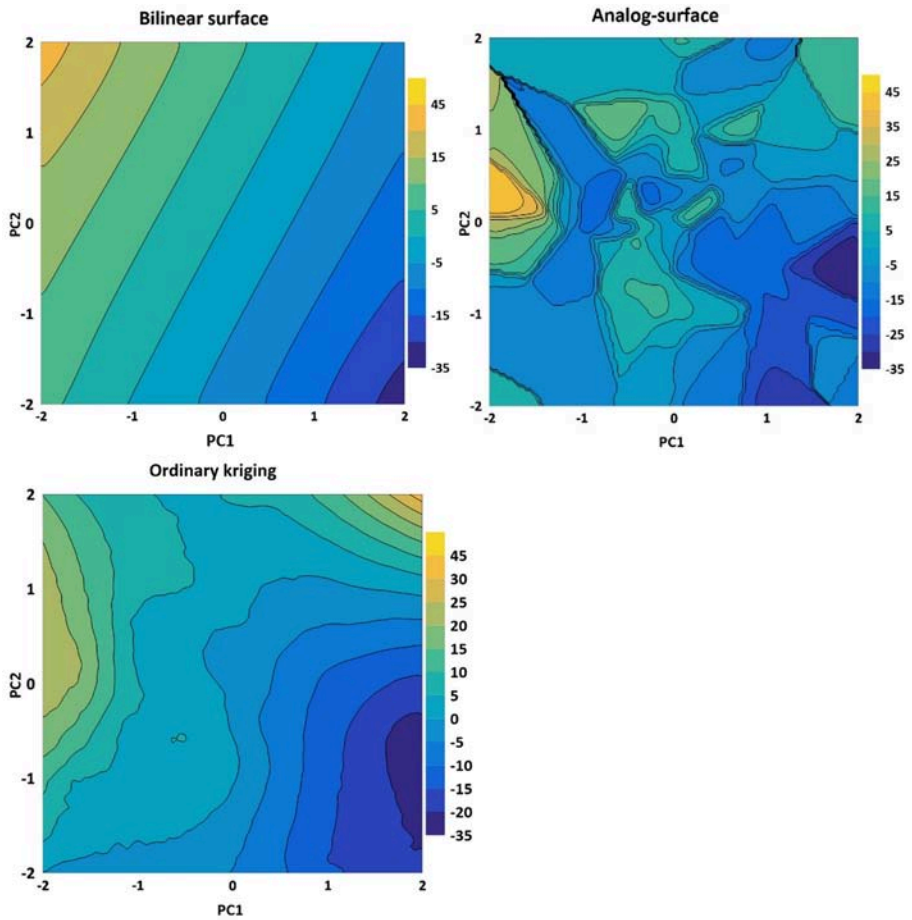

FIGURE 5 | Interpolation of the data points shown in **Figure 4** by means of bivariate regression, by an analog approach, and by ordinary kriging. The coordinates are the principal components of the first two EOFs of the barotropic stream function, shown in **Figure 3**.

reasonable to suggest that eddy size may be seens as a random variable conditioned upon the prevailing currents.

As predictors we use the barotropic stream function In the South China Sea, which is given at 57,750 locations; such large dimension cannot be handled, and therefore the dimension of the problem is reduced in this discussion—to 2. The needed two indices are chosen to be coefficients of the leading Empirical Orthogonal Functions (EOFs; for a detailed introduction, refer to Preisendorfer, 1988; von Storch and Zwiers, 1999) or principal components of the barotropic stream function field. EOFs are a system of orthogonal vectors which are adapted to be most powerful in representing variance of the considered variable, which is here the barotropic streamfunction of the entire South China Sea.

The two indices represent 31.5 and 10.5% of the dominant interannual variations of the barotropic stream function (**Figure 3**).

The seasonal mean diameters of cyclonic eddies in the South China Sea are displayed in **Figure 4** as a function of these first two EOF coefficients; for each summer season (June-August) one dot is plotted, with the vertical coordinate indicting the diameter in km. Obviously the eddy diameters do not constitute a smooth surface; this is meaningful when we consider formation and the intensification of eddies all as a conditional random variable, and each observed mean eddy diameter is considered one realization of a conditional random variable.

We have applied three different interpolation techniques to the anomalies (i.e., deviations from the long term mean) derived from the data displayed in **Figure 4**; the results are shown as "isolines" in **Figure 5** The three techniques are bilinear regression (top left) and nearest neighbors (analog; top right), and ordinary kriging (bottom).

Kriging is a methodology which was developed in geology for mapping structures. At this time, details do not matter so that it may suffice to mention that "ordinary kriging" was used, employing a linear Matheron function and allowing for a nugget effect (cf., Wackernagel, 1995; Maciag, pers. comm.)

The numbers describe the deviation from the overall mean. The two methods of the bivariate regression and of the nearest neighbor are at the opposite ends of complexity. The bilinear regression is smooth, with less variability. The analog, on the other hand, is very noisy, with rather large abrupt changes,

but with a variability which reproduces the variability of the original data, say in terms of variability and skewness, while the krigged surface contains elements of the two other maps, but has a richer structure than the bivariate surface, and is less noisy than the analog-based map. As expected, the krigged map is between the other two, in terms of smoothness and noise.

Seemingly there is no way of deciding which of three maps is "better"; they share a certain basic structure, with high values near the upper left corner, and lower values in the lower right corner. Which map will eventually be chosen depends on how the map will be used. If a general overview is needed, the bivariate may be best; if it is used for weather generators, the analog may be the choice. If details matter, the richer but smooth structure of kriging may be more favorable.

In terms of the link to the barotropic stream function (**Figure 3**), we find the size of cyclonic eddies larger, when both (EOF) patterns prevail in a season, i.e., when there resides an anomalous large and stationary anticyclone in almost the entire northern part of the South China Sea (combination of patterns 1 and 2), and an anomalous outward flow through the Luzon strait. In the same way, smaller eddies are generated on average, when an anomalous counterclockwise flow streams through the South China Sea. Pattern 1 alone goes also with these characteristics, but is associated with a weaker signal, when EOF2, the second pattern, does not contribute. The same holds for pattern 2 in the absence of pattern 1, but with an even weaker signal.

DISCUSSION: APPLICATION OF A MAP IN DOWNSCALING

As mentioned before, the thinking about downscaling is rooted in two different concepts, one in meteorology named "synoptic climatology," the other in "interpolation of data clouds," which was inspired by spatial interpolation.

The basic idea, as introduced the first time likely by Kim et al. (1984), and later by von Storch and Zorita (1990), recognized the limitation of climate modeling, in particular construction of climate change scenarios, in representing small scale phenomena, and many aspects of impacts of climate variability and change.

The aspect of synoptic climatology was employed in the "statistical dynamical method," and was based on building causal (process-based) links between a conditioning large-scale state and a resulting small-scale response; later this method became less and less popular when dynamical downscaling matured and—given the advances of computational power—allowed the simulation of continuous sequences of large-scale forcing.

The other aspect, however, the "interpolation of data clouds," is still in use—it makes use of co-variations, which are not necessarily based on direct causal links. Instead the links may be indirect, such as the emergence of extreme values in a season and the mean state during that season—obviously the mean state does not "make" extremes, but the mean state may favor the formation of synoptic situations which lead to extremes (cf., Branstator, 1995). The example presented in this paper, on the formation of large vortices in the South China Sea, conditioned by mean currents, falls into this category.

Such efforts result in tables, or in maps, which suggest a state of a small-scale or an impact variable, conditional upon some adopted large-scale indicators. When two such variables are used, then the result takes the form of a table, and the method curtails an interpolation, a map-generating effort. The purpose of interpolation is "to guide people in unknown terrain" (Von Storch, 1999), i.e., to guess the state of the system at "locations" not visited no far. Such guesses can be of very different format, depending on the user's needs.

In general, at each point, the method would return a probability interval $I_E(\mathbf{x}) \pm \Delta$, with $I_E(\mathbf{x})$ representing the conditional expectation and Δ a level of uncertainty (say, two standard deviations). In many cases, however, only the conditional expectation will be provided (in the bilinear regression case), whereas sampling from the analog-map will result in random samples including the variability. Thus, the former will be favorable, when dealing with typical conditions, whereas the second gives noisy numbers, but with the right level of variability, as needed in weather generators (cf. Zorita et al., 1995).

AUTHOR CONTRIBUTIONS

All authors listed have made a substantial, direct and intellectual contribution to the work, and approved it for publication.

ACKNOWLEDGMENTS

We thank Łukasz Maciag of the Institute of Marine and Coastal Sciences of the University of Szczecin, Poland, Jan Harff of the University of Sczcecin, Poland, Zhang Meng of the Institute of Coastal Research in Geesthacht, Tim Osborn of Climate Research Unit (CRU) in Norwich and Alexander Kolovos. ŁM prepared the kriging map (**Figure 5**), while JH and AK helped with advice on this matter; Zhang Meng supplied us with the data of the example and with **Figure 4**, and Tim Osborn provided and allowed us the usage of **Figure 2**.

REFERENCES

Bardossy, A., Bogardi, I., and Matyasovszky, I. (2005). Fuzzy rule-based downscaling of precipitation. *Theor. Appl. Climatol.* 82, 119–129. doi: 10.1007/s00704-004-0121-0

Benestad, R. (2016). *Downscaling Climate Information*. New York, NY: Oxford University Press Research Encyclopedia on Climate Science.

Benestad, R. E., Hanssen-Bauer, I., and Chen, D. (2008). *Empirical-Statistical Downscaling*. Hackensack, NJ: World Scientific Publishers.

Biau, G., Zorita, E., von Storch, H., and Wackernagel, H. (1999). Estimation of precipitation by kriging in EOF space. *J. Climate* 12, 1070–1085.

Brandsma, T., and Buishand, T. A. (1997). Statistical linkage of daily precipitation in Switzerland to atmospheric circulation and temperature. *Hydrol. J.* 198, 98–123.

Brandsma, T., and Buishand, T. A. (1998). Simulation of extreme precipitation in the Rhine basin by nearest neighbor resampling. *Hydrol. Earth Sys. Sci.* 2, 195–209.

Branstator, G. (1995). Organization of storm track anomalies by recurring low-frequency circulation anomalies. *J. Atmos. Sci.* 52, 207–226.

Busuioc, A., and von Storch, H. (2003). Conditional stochastic model for generating daily precipitation time series. *Clim. Res.* 24, 181–195. doi: 10.3354/cr024181

Castro, C.L., and Pielke, R. A. Sr. (2004). Dynamical downscaling: assessment of value restored and added using the Regional Atmospheric Modelling System. *J. Geophys. Res.* 110, 1–21. doi: 10.1029/2004JD004721

Chadwick, R., Coppola, E., and Giorgi, F. (2011). An artificial neural network technique for downscaling GCM outputs to RCM spatial scale. *Nonlin. Processes Geophys.* 18, 1013–1028. doi: 10.5194/npg-18-1013-2011

Christensen, J. H., Carter, T., and Giorgi, F. (2002). *PRUDENCE Employs New Methods to Assess European Climate Change*. EOS Transactions of the American Geophysical Union 83, 147.

Christensen, J. H., Christensen, O. B., Rummukainen, G., M., and Jacob, D. (2007). "ENSEMBLES Regional Climate Modeling: a multi-model approach towards climate change predictions for europe and elsewhere," in: *American Geophysical Union, Fall Meeting 2007*. Available online at: http://adsabs.harvard.edu/abs/2007AGUFMGC23B.01C.

Dickinson, R. E., Errico, R. M., Giorgi, F., and Bates, G. T. (1989). A regional climate model for the western United States. *Clim. Change* 15, 383–422.

Ekström, M., Grose, M. R., and Whetton, P. H. (2015). An appraisal of downscaling methods used in climate change research. *WREs Clim. Change 6,* 301–319. doi: 10.1002/wcc.339

Faucher, M., Burrows, W., and Pandolfo, L. (1999). Empirical-Statistical reconstruction of surface marine winds along the western coast of Canada. *Clim. Res.* 11, 173–190.

Frey-Buness, F., Heimann, D., and Sausen, R. (1995). A statistical-dynamical downscaling procedure for global climate simulations. *Theor. Appl. Climatol.* 50, 117–131.

Giorgi, F., and Gutowski, W. J. Jr. (2015). Regional dynamical downscaling and the CORDEX initiative. *Annu. Rev. Environ. Resour.* 40, 467–490. doi: 10.1146/annurev-environ-102014-021217

Harff, J., and Davis, J. C. (1990). Regionalization in geology by multivariate classification. *Math. Geol.* 22, 573–588.

Kim, J. W., Chang, J.-T., Baker, N. L., Wilks, D. S., and Gates, W. L. (1984). The statistical problem of climate inversion: determination of the relationship between local and large-scale climate. *Mon. Wea. Rev.* 112, 2069–2077.

Knobloch, E. (2018). "Zum Verhältnis von Naturkunde/Naturgeschichte und Naturwissenschaft. Das Beispiel Alexander von Humboldt," in *Umgangsweisen mit Natur(en)in der Frühen Bildung III.* Eds M. Rauterberg, and G. Scholz (Über Naturwissenschaft und Naturkunde). Available online at: www.widerstreit-sachunterricht.de Beiheft 12. 13–36.

Maak, K., and von Storch, H. (1997). Statistical downscaling of monthly mean air temperature to the beginning of the flowering of *Galanthus nivalis* L. in Northern Germany. *Intern. J. Biometeor.* 41, 5–12.

Maraun, D., and Widmann, M. (2018). *Statistical Downscaling and Bias Correction for Climate Research.* Cambridge: Cambridge University Press, 360 p.

Osborn, T. J., Conway, D., Hulme, M., Gregory, J. M., and Jones, P. D. (1999). Air flow influences on local climate: observed and simulated mean relationships for the United Kingdom. *Clim. Res.* 13, 173–191. doi: 10.3354/cr013173

Preisendorfer, R.W. (1988). Principal *Component Analysis in Meteorology and Oceanography*. Amsterdam: Elsevier. 426 p.

Rockel, B., Castro, C. L., Pielke, R.A. Sr, von Storch, H., and Leoncini, G. (2008). Dynamical downscaling: Assessment of model system dependent retained and added variability for two different regional climate models. *J. Geophys. Res.* 113:D21107. doi: 10.1029/2007JD009461

Rummukainen, M. (2009). State-of-the-art with regional climate models. *WIREs Clim. Change* 1, 82–96. doi: 10.1002/wcc.8

Rummukainen, M. (2015). Added value in regional climate modeling. *WREs Clim. Change* 7, 145–159. doi: 10.1002/wcc.378

Schubert-Frisius, M., Feser, F., von Storch, H., and Rast, S. (2017). Optimal spectral nudging for global dynamic downscaling. *Mon. Wea. Rev.* 145, 909–927. doi: 10.1175/MWR-D-16-0036.1

Souverijns, N., Gossart, A., Demuzere, M., Lenaerts, J. T. M., Medley, B., Gorodetskaya, I. V., et al. (2019). A new regional climate model for POLAR-CORDEX: evaluation of a 30-year hindcast with COSMO-CLM2 over Antarctica. *J. Geophys. Res. Atmosphere.* doi: 10.1029/2018JD028862. [Epub ahead of print].

Starr, V.P. (1942). *Basic Principles of Weather Forecasting*. New York,NY; London: Harper Brothers Publishers. 299 p.

Stoyan, D., Stoyan, H., and Jansen, U. (1997). *Umweltstatistik: Statistische Verarbeitung und Analyse von Umweltdaten*. Leipzig: Teubner Stuttgart. 348 p.

Von Storch, H. (1999). "Representation of conditional random distributions as a problem of "spatial" interpolation," in *geoENV II - Geostatistics for Environmental Applications,* eds J. Gòmez-Hernàndez, A. Soares and R. Froidevaux (Dordrecht; Boston, MA; London: Kluwer Adacemic Publishers), 13–23.

von Storch, H., Feser, F., Geyer, B., Klehmet, K., Li, D., Rockel, B., et al. (2017). Regional re-analysis without local data - exploiting the downscaling paradigm. *J. Geophys. Res.* 122, 8631–8649. doi: 10.1002/2016JD026332

von Storch, H., Hewitson, B., and Mearns, L. (2000a). "Review of empirical downscaling techniques, "*Regional Climate Development Under Global Warming*, eds T. Iversen, and B. A. K. Høiskar (Torbjørnrud: General Technical Report No. 4. Conf. Proceedings RegClim Spring Meeting Jevnaker), 29–46.

von Storch, H., Langenberg, H., and Feser, F. (2000b). A spectral nudging technique for dynamical downscaling purposes. *Mon. Wea. Rev.* 128, 3664–3673. doi: 10.1175/1520-0493(2000)128<3664:ASNTFD>2.0.CO;2

von Storch, H., and Reichardt, H. (1997). A scenario of storm surge statistics for the German Bight at the expected time of doubled atmospheric carbon dioxide concentration. *J. Climate* 10, 2653–2662.

von Storch, H., and Zorita, E. (1990). *Assessment of regional climate changes with the help of global GCM's: an example.* CAS/JSC Working group on Numerical Experimentation. *WMO Report no. 14, 7.30.*

von Storch, H., Zorita, E., and Cubasch, U. (1991). Downscaling of global climate change estimates to regional scales: an application to Iberian rainfall in Wintertime. *MPI Rep.* 62:36.

von Storch, H., and Zwiers, F. W. (1999). *Statistical Analysis in Climate Research*. Cambridge: Cambridge University Press. 528 p.

Wackernagel, H. (1995). *Multivariate Geostatistics.* Heidelberg: Springer Verlag. 270.

Waldron, K. M., Peagle, J., and Horel, J. D. (1996). Sensitivity of a spectrally filtered and nudged limited area model to outer model options. *Mon. Wea. Rev.* 124, 529–547.

Wilby, R.L., Dawson, C. W., and Barrow, E. M. (2002). SDSM — a deci-sion support tool for the assessment of regional climate change impacts. *Environ Model Softw.* 17, 145–157. doi: 10.1016/S1364-8152(01)00060-3

Wilby, R.L., Hay, L. E., and Leavesley, G. H. (1999). A comparison of downscaled and raw GCM output: implications for climate change scenarios in the San Juan River Basin, Colorado. *J Hydrol.* 225, 67–91.

Wilks, D.S. (2010). Use of stochastic weathergenerators for precipitation downscaling. *WIREs Clim. Change* 1, 898–907. doi: 10.1002/wcc.85

Yoshimura, K., and Kananitsu, M. (2008). Dynamical global downscaling of global reanalysis. *Mon. Wea. Rev.* 136, 2983–2998. doi: 10.1175/2008MWR2281.1

Zhang, M., and von Storch, H. (2018). Distribution features of travelling eddies in the South China Sea. *Res. Activit. Atmosph. Oceanic Model.* 2–31.

Zorita, E., Hughes, J., Lettenmaier, D. P., and von Storch, H. (1995). Stochastic characterization of regional circulation patterns for climate model diagnosis and estimation of local precipitation. *J. Clim.* 8, 1023–1042.

Zorita, E., and von Storch, H. (1997). *A Survey of Statistical Downscaling Techniques*. Geesthacht: GKSS 42 p.

Zorita, E., and von Storch, H. (1999). The analog method - a simple statistical downscaling technique: comparison with more complicated methods. *J. Clim.* 12, 2474–2248.

Conflict of Interest Statement: The authors declare that the research was conducted in the absence of any commercial or financial relationships that could be construed as a potential conflict of interest.

frontiers in Environmental Science

ORIGINAL RESEARCH
published: 10 April 2019
doi: 10.3389/fenvs.2019.00036

Simulating North American Weather Types With Regional Climate Models

Andreas F. Prein, Melissa S. Bukovsky, Linda O. Mearns, Cindy L. Bruyère and James M. Done*

National Center for Atmospheric Research, Boulder, CO, United States

Regional climate models (RCMs) are able to simulate small-scale processes that are missing in their coarser resolution driving data and thereby provide valuable climate information for climate impact assessments. Less attention has been paid to the ability of RCMs to capture large-scale weather types (WTs). An inaccurate representation of WTs can result in biases and uncertainties in current and future climate simulations that cannot be easily detected by standard model evaluation metrics. Here we define 12 hydrologically important WTs in the contiguous United States (CONUS). We test if RCMs from the North American CORDEX (NA-CORDEX) and the Weather Research and Forecasting (WRF) model large physics ensembles (WRF36) can capture those WTs in the current climate and how they simulate changes in the future. Our results show that the NA-CORDEX RCMs are able to simulate WTs more accurately than members of the WRF36 ensemble. The much larger WRF36 domain in combination with not constraining large-scale conditions by spectral nudging results in lower WT skill. The selection of the driving global climate model (GCM) has a large effect on the skill of NA-CORDEX simulations but a smaller impact on the WRF36 runs. The formulation of the RCM is of minor importance except for capturing the variability within WTs. Changing the model physics or increasing the RCM horizontal grid spacing has little effect. These results highlight the importance of selecting GCMs with accurate synoptic-scale variability for downscaling and to find a balance between large domains that can result in biased WT representations and small domains that inhibit the realistic development of mesoscale processes. At the end of the century, monsoonal flow conditions increase systematically by up to 30% and a WT that is a significant source of moisture for the Northern Plains during the growing seasons decreases systematically up to –30%.

Keywords: regional climate models, uncertainties, weather types, North America, CORDEX, domain size, driving data, model quality

OPEN ACCESS

Edited by:
Hans Von Storch,
Helmholtz Centre for Materials and Coastal Research (HZG), Germany

Reviewed by:
Juan Pedro Montávez,
University of Murcia, Spain
Rosmeri Porfirio Da Rocha,
University of São Paulo, Brazil

****Correspondence:***
Andreas F. Prein
prein@ucar.edu

Specialty section:
This article was submitted to Atmospheric Science, a section of the journal Frontiers in Environmental Science

Received: *23 November 2018*
Accepted: *28 February 2019*
Published: *10 April 2019*

Citation:
Prein AF, Bukovsky MS, Mearns LO, Bruyère CL and Done JM (2019) Simulating North American Weather Types With Regional Climate Models. Front. Environ. Sci. 7:36. doi: 10.3389/fenvs.2019.00036

1. INTRODUCTION

Regional climate models (RCMs) are designed to dynamically downscale larger-scale climate data over a region of interest to capture regional-scale processes that are not present in the driving model (Giorgi, 1990; Denis et al., 2002; Rummukainen, 2010). Many studies address the added value of RCM downscaling, which are mainly found on local to regional-scales (Feser et al., 2011; Di Luca et al., 2012; Prein et al., 2016a) in regions with complex orography, areas with strong land-surface heterogeneities, and in atmospheric situations with strong spatial gradients that are often related to extreme events (Rummukainen, 2016). It is more unclear if RCMs can also add value to

the large-scale patterns of their driving model by upscale growth of mesoscale processes. However, there are a few examples in the published literature such as improvements of rain shadow effects due to the better representation of orography (Leung et al., 2003), or downstream effects of mesoscale convective vortices in the US (Clark et al., 2010).

The evaluation of RCMs is typically performed on a seasonal basis using standard atmospheric variables such as near-surface temperature and precipitation (Christensen et al., 2007a; Mearns et al., 2012; Kotlarski et al., 2014; Prein et al., 2016a). While this can provide a broad assessment of model skill it typically does not allow in-depth insights to understand errors in specific modeled processes. This is partly due to combining local- and large-scale errors in the analysis. Addor et al. (2016); for example, showing that a general wet bias of RCM simulated wintertime precipitation in the European Alps can be related to an overestimation of westerly flow regimes.

Weather typing (WTing) was initially developed for weather forecasting (e.g., van Bebber, 1891). In more recent decades, studies used WTing to downscale large scale circulation patterns to local scales (Goodess and Palutikof, 1998; Wood et al., 2016), evaluate global climate model performance (Radić and Clarke, 2011; Gibson et al., 2016), to understand changes in observed climate trends (Paredes et al., 2006; Prein et al., 2016b), and to assess future climate projections in terms of changing large-scale dynamics (Santos et al., 2016).

Here we use hydrologically important WTs to investigate the ability of two ensembles of RCM simulations to capture large-scale atmospheric patterns over the contiguous United States (CONUS). The two ensembles are the North American contributions to the Coordinated Regional Climate Downscaling Experiment (NA-CORDEX; Mearns et al., 2017) and the National Center for Atmospheric Research's (NCAR's) 36 km grid spacing Weather Research and Forecasting (WRF) model physics ensemble (WRF36; Bruyère et al., 2017).

Using WT for model evaluation has two main advantages: (1) We focus solely on the RCM's ability to represent synoptic-scale patterns, which allows separating model biases in large-scale dynamics and thermodynamics and mesoscale components, and (2) RCM errors are typically process-dependent and, therefore, RCMs have different bias characteristics in different seasons (e.g., Mearns et al., 2012; Kotlarski et al., 2014). However, seasons consist of a mix of various weather regimes and atmospheric processes. Seasonally based analyses can be viewed as a zero order approximation of a weather regime-dependent analysis. Performing model evaluation based on WTs helps to separate atmospheric processes more accurately and allows insights into regime-specific model performance.

The goal of this study is 2-fold. (1) We aim to understand which components of an RCM setup affects its capability to simulate WTs over the CONUS. The analyzed components are the driving GCM, the formulation of the RCM, sensitivities to RCM model physics, RCM horizontal grid spacing, and RCM domain size. The goal is to provide guidance for future RCM downscaling studies. (2) We want to understand if there are systematic changes in future climate WT frequencies. Enhancing our understanding of climate impacts on large-scale dynamics is important since almost all confidence that we have regarding future climate projections is based on thermodynamic processes (Shepherd, 2014).

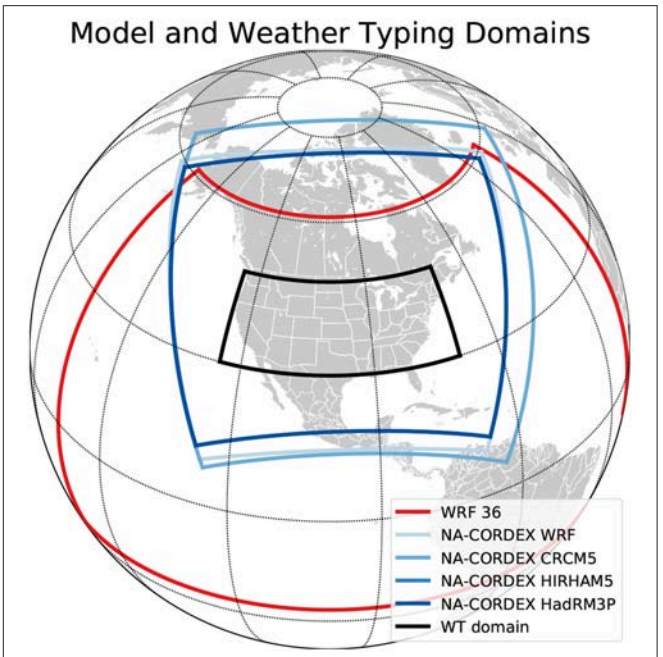

FIGURE 1 | Model (colors) and weather typing domains (black rectangle). The WRF36 domain is shown in red and the NA-CORDEX domains are shown in blue.

The paper is structured as follows. Section 2 summarizes the used RCM simulations and the WT method. Section 3 describes the main characteristics of the derived WTs, presents the results from the RCM evaluation, an assessment of the sources of performance variability, and WT changes in climate projections. Section 4, 5 summarize the findings and conclude the study.

2. DATA AND METHODS

2.1. Regional Climate Models

We use RCM simulations from the NA-CORDEX and the WRF36 ensemble datasets. RCMs participating in the NA-CORDEX ensemble downscale ERA-Interim (Dee et al., 2011) and global climate models (GCMs) from the CMIP5 archive (Taylor et al., 2012) over a common region that covers most of North America (see blue domains in **Figure 1**). The domain sizes vary slightly between the participating RCMs. The ERA-Interim driven simulations cover a common period from 1989 to 2010, while the GCM driven runs at least cover 1951–2099. Most RCMs have a horizontal grid spacing of 0.44°/50 km and the WRF simulations are also available at 0.22°/25 km grid spacing. We only use a subset of the full NA-CORDEX simulations for which the necessary WTing variables are available. We use simulations performed with WRF (Skamarock and Klemp, 2008), the Danish Meteorological Institute's HIRHAM5 model (Christensen et al., 2007b), the UK Met Office's HadRM3P model (Jones et al., 1995;

TABLE 1 | NA-CORDEX simulations used in this manuscript.

Case	GCM	RCM	Institude	Resolution	Time Period
Reanalysis	ERA-Interim	WRF	NCAR	0.44°	1980–2010
Reanalysis	ERA-Interim	WRF	NCAR	0.22°	1980–2010
Reanalysis	ERA-Interim	HIRHAM5	DMI	0.44°	1989–2011
Reanalysis	ERA-Interim	HadRM3P	MOHC	0.44°	1990–2011
Reanalysis	ERA-Interim	CRCM5	UQAM	0.44°	1979–2012
Historical	GFDL-ESM2M	WRF	NCAR	0.44°	1950–2005
Historical	GFDL-ESM2M	WRF	NCAR	0.22°	1950–2005
Historical	MPI-ESM-LR	WRF	NCAR	0.44°	1950–2005
Historical	MPI-ESM-LR	WRF	NCAR	0.22°	1950–2005
Historical	HadGEM2-ES	WRF	NCAR	0.44°	1950–2005
Historical	HadGEM2-ES	WRF	NCAR	0.22°	1950–2005
Historical	CCCma-CanESM2	CRCM5	UQAM	0.44°	1950–2005
Historical	MPI-ESM-LR	CRCM5	UQAM	0.44°	1949–2005
Historical	ICHEC-EC-EARTH	HIRHAM	DMI	0.44°	1951–2005
RCP8.5	GFDL-ESM2M	WRF	NCAR	0.44°	2006–2099
RCP8.5	GFDL-ESM2M	WRF	NCAR	0.22°	2006–2099
RCP8.5	MPI-ESM-LR	WRF	NCAR	0.44°	2006–2099
RCP8.5	MPI-ESM-LR	WRF	NCAR	0.22°	2006–2099
RCP8.5	HadGEM2-ES	WRF	NCAR	0.44°	2006–2099
RCP8.5	HadGEM2-ES	WRF	NCAR	0.22°	2006–2099
RCP4.5	CCCma-CanESM2	CRCM5	UQAM	0.44°	2006–2100
RCP4.5	MPI-ESM-LR	CRCM5	UQAM	0.44°	2006–2100
RCP8.5	MPI-ESM-MR	CRCM5	UQAM	0.44°	2006–2100
RCP4.5	ICHEC-EC-EARTH	HIRHAM	DMI	0.44°	2006–2100
RCP8.5	ICHEC-EC-EARTH	HIRHAM	DMI	0.44°	2006–2100

TABLE 2 | Major characteristics of the NA-CORDEX RCMs.

RCM	Cumulus	Microphysics	Radiation LW–SW	Boundary layer	Land surface model
WRF	Kain-Fritsch (Kain and Fritsch, 1990)	WSM3 (Hong et al., 2004)	RRTM Mlawer et al. (1997) - Goddard	MYJ Janjić (1994)	NOAH (Tewari et al., 2004)
CRCM5	Kain-Fritsch (Kain and Fritsch, 1990)	Sundqvist (Sundqvist, 1978)	Li and Barker - Li and Barker (Li and Barker, 2005)	Delage (Delage, 1997)	CLASS3.5+ (Verseghy, 1991, 2009)
HIRHAM5	Tiedke (Tiedtke, 1989), Nordeng (Nordeng, 1994)	Prognostic liquid water and ice	Morcrette (Morcrette, 1984) - Fouquart and Bonnel (1980)	ECHAM5	ECHAM5
HadRM3P	-	-	-	-	MOSES 2 (Essery and Clark, 2003)

Buonomo et al., 2007), and the Canadian Regional Climate Model version 5 (Caya and Laprise, 1999; Zadra et al., 2008; Martynov et al., 2013; Šeparović et al., 2013, CRCM5;). These RCMs downscale five different GCMs with historical and RCP4.5 and RCP8.5 concentration scenarios (Van Vuuren et al., 2011). The WRF simulations used spectral nudging to constrain synoptic scales according to those of the driving model in the domain interior. This is important since with this setting WTs should not be able to deviate significantly from those in the driving model. No spectral nudging was used in the other RCM simulations. A list of all NA-CORDEX simulations is shown in **Table 1** and more details on the model setup can be found in **Table 2** and online under https://na-cordex.org/rcm-characteristics.

NCAR's WRF36 RCM ensemble (Bruyère et al., 2017) is targeted toward understanding uncertainties from model physics and consists of 24 members of WRF simulations that downscale ERA-Interim within the period from 1990 to 2000 with 36 km horizontal grid spacing. The model domain is substantially larger than the domains used in the NA-CORDEX simulations and covers most of the North and Central Atlantic, the east Pacific, most of North America, central America, and northern South America (**Figure 1**). The motivation for this large domain was to decouple the RCM simulations from their lateral boundary conditions to improve the representation of mesoscale processes. In theory, such improvements should be possible due to the better representation of mesoscale forcing such as orography in

TABLE 3 | The physics combination of the WRF36 ensemble that used ERA-Interim between 1990–2000 as driving data.

		MYJ	YSU	MYJ	YSU
KF	WSM6	CK6M	CK6Y	RK6M	RK6Y
	Thompson	CKTM	CKTY	**RKTM**	RKTY
NSAS	WSM6	CN6M	CN6Y	RN6M	RN6Y
	Thompson	CNTM	CNTY	RNTM	**RNTY**
Tiedke	WSM6	CT6M	CT6Y	RT6M	RT6Y
	Thompson	CTTM	CTTY	RTTM	**RTTY**

The naming convention of individual members follows the rule Radiation—Cumulus—Microphysics—PBL scheme. For example, RNTY uses RRTMG radiation, NSAS cumulus, Thompson microphysics, and YSU PBL schemes. The simulations highlighted with bold font are used for downscaling CESM under current and future conditions. All simulations were produced by NCAR.

addition to atmospheric processes, e.g., tropical cyclones, and teleconnections in the higher resolution RCM (e.g., Erfanian and Wang, 2018).

Table 3 shows the 24 ensemble members that downscale ERA-Interim by systematically varying four physics parameterizations: (1) cumulus [KF: (Kain and Fritsch, 1990); NSAS: (Han and Pan, 2011); and Tiedtke: (Tiedtke, 1989)], (2) radiation [CAM: (Collins et al., 2006) and RRTMG: (Mlawer et al., 1997)], (3) microphysics [WSM6: (Han and Lim, 2006) and Thompson: (Thompson et al., 2004)], and (4) planetary boundary layer [MYJ: (Janjić, 1994) and YSU: (Hong et al., 2006)]. In this study, we abbreviate members of this ensemble by four characters. The first character denotes the radiation scheme, the second the cumulus scheme, the third the microphysics, and the fourth the planetary boundary layer parameterization. For example, the RNTY member uses the RRTMG radiation, NSAS cumulus, Thompson microphysics, and YSU boundary layer scheme. The selected physics are well tested and widely used.

After evaluating the 24-member ensemble, three members were selected to perform additional current and future climate downscaling experiments. These three members are the RKTM, RNTY, and RTTY simulations. They downscale a free running GCM simulation performed by the Community Earth System Model (CESM; Hurrell et al., 2013), which is part of the CMIP5 experiments (Taylor et al., 2012). CESM is one of the best performing models in the CMIP5 ensemble based on its ability to simulate global temperature and precipitation patterns (Knutti et al., 2013). This simulation uses the business as usual RCP8.5 emission scenario for future climate projections (Van Vuuren et al., 2011). To reduce biases in CESM's lateral boundary conditions, a bias correction method described in Bruyère et al. (2014, 2015) was applied prior to the downscaling. This method only bias corrected the mean base state, leaving the synoptic variability, interannual variability, and any climate trend unchanged. The CESM driven WRF36 simulations cover the periods 1990 to 2000, 2020 to 2030, 2030 to 2040, 2050 to 2060, and 2080 to 2090. Additional information about the WRF36 simulations can be found in Bruyère et al. (2017).

The most notable differences between the WRF36 simulations and WRF experiments from the NA-CORDEX are the computational domain size and the use of spectral nudging in the latter (von Storch et al., 2000). The physics in the RK6M simulation are very similar to those used in NA-CORDEX except for the microphysics, which are more simplistic in the latter. The NOAH land surface model (Tewari et al., 2004) is used in both ensembles.

2.2. Reference Data

The variables used for the WTing are derived from daily ERA-Interim data at 12 UTC (Dee et al., 2011). ERA-Interim is a third generation reanalysis, which has very high skill in representing atmospheric processes compared to other reanalysis products (e.g., Decker et al., 2012; Lin et al., 2014).

For precipitation analyses we use the Parameter-elevation Relationships on Independent Slopes Model (PRISM) daily gridded precipitation data within the period from 1980 to 2014 (Daly et al., 1994). PRISM is based on ∼13 000 surface stations for precipitation including USDA NRCS Snow Telemetry (SNOTEL) and snowcourses data (http://www.wcc.nrcs.usda.gov/snow/) to capture mountain snow pack.

2.3. Defining Hydrologically Important Weather Types

The performed WTing is similar to the algorithm used in Prein et al. (2016b) and (Prein, under review). It is a combination of two clustering methods: a hierarchical cluster analysis and a k-means cluster analysis that uses the outcome of the hierarchical clustering as the starting partition (Romesburg, 2004). This approach showed very high skill in classifying WTs in a WT method comparison study over the European Alps (Schiemann and Frei, 2010) and was successfully applied in many weather typing analyses (e.g., García-Valero et al., 2012; Lorente-Plazas et al., 2015). Daily ERA-Interim data from 1979–2014 is used over the CONUS (see black rectangle in **Figure 1**) to define representative WTs capturing the main variability of precipitation in this region. We use a moving average Gaussian high-pass filter of 31-day length to remove variability longer than those of typical synoptic-scale patterns, e.g., the seasonal cycle. This does not affect the spatial patterns of the daily input variables. Afterward, we normalize each input variable to generate fields with equal weights as input for the WT analysis.

We used two metrics to test the skill of the derived WTs. (1) We aim to minimize the intracluster to intercluster variance (Straus and Molteni, 2004) of the daily CONUS wide precipitation patterns in each WT. The goal is to cluster days with similar precipitation patterns within one WT and to obtain WTs having different precipitation patterns when compared to each other. (2) In addition, we want to maximize the average absolute precipitation anomalies of each WT centroid. The WT centroid is the average over each cluster element, e.g., average precipitation anomaly of each day within a WT. This metric ensures that WTs are as different as possible from the climatological average precipitation in the CONUS.

Figure 2 summarizes the results for the WT skill analysis, which is dependent on the number of used WTs and the input variables. We tested a variety of input variable combinations. Horizontal wind speed at 500 hPa (UV500), sea

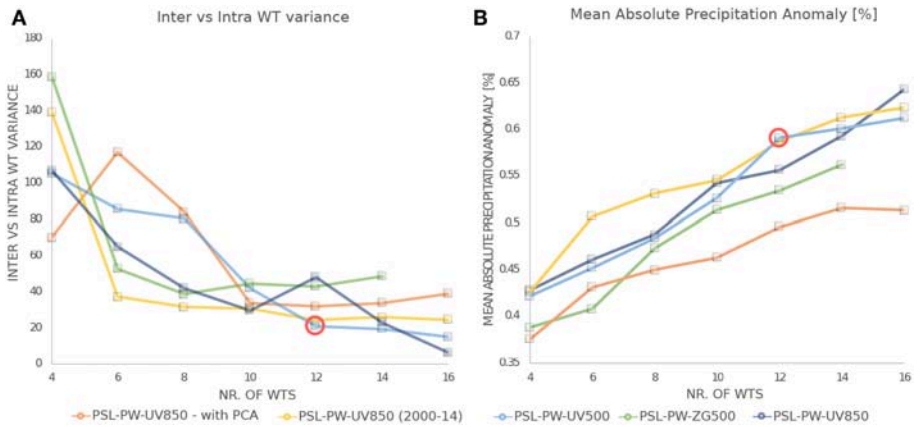

FIGURE 2 | Assessment of the clustering strength of WTs. **(A)** Inter- vs. intra-cluster variance and **(B)** absolute precipitation anomalies averaged over all WTs. Different colors show different WT settings. The tested input variables are sea level pressure (SLP), precipitable water (PW), wind speed at 850 hPa/500 hPa (UV850/UV500), and 500 hPa geopotential height (ZG500). We also test the impacts of using a principal component analysis (PCA) before the WT clustering and the length of the clustering period, which is 1979–2014 unless otherwise denoted. The red circle shows the final WT setup using 12 WTs and SLP, PW, and UV500 as input variables.

level pressure (SLP), and precipitable water (PW) are available on a daily basis for most RCM simulations. These are important variables for many dynamic and thermodynamic processes related to precipitation (Doswell III et al., 1996; Lin et al., 2001). Using 12 WTs with these variables lead to a skillful representation of hydrologically important weather patterns in the CONUS. Twelve WTs seem to be sufficient since adding more WTs only leads to marginal improvements in clustering skill (**Figure 2**). These results are similar to work by Prein et al. (2016b) except that we used 500 hPa instead of 700 hPa wind speed since the latter was not available for many NA-CORDEX simulations.

The WTing on ERA-Interim data results in a WT time series that assigns a WT to each day within the period of 1979–2014. This time series allows us to calculate WT centroids (**Figure 3**), which are used to assign WTs to each day in the RCM output.

2.4. Assigning Weather Types to Climate Model Data

To assign WTs to the RCM output we first conservatively remap daily simulated SLP, UV500, and PW fields to the ERA-Interim grid. Then we apply a 31-day moving average Gaussian high-pass filter to the remapped data and normalize the variables similarly to what we have done to the ERA-Interim data. Thereafter, we calculate the average Euclidean distances of each input variable for each day in the RCM simulations to the 12 ERA-Interim WT centroids that are described above. Each day is assigned to the centroid with the minimum average Euclidean distance.

3. RESULTS

3.1. Description of Observed WTs

The resulting WTs show distinct differences in SLP anomalies, 500 hPa wind speed and direction, and PW values within the CONUS (**Figure 3**). We sorted the WTs from predominantly winter patterns (WT1–4) to shoulder season WTs (WT5–10) and summer WTs (WT11 and WT12). The different flow regimes result in distinct precipitation anomaly patterns (**Figure 4**). WT1 is most frequent in December and January and it is characterized by a strong high-pressure anomaly with dry air advection from the northwest into the central US (**Figure 3A**). This results in anomalous dry conditions in most of the US (**Figure 4A**). In WT2 the high-pressure anomaly is shifted toward the Midwest favoring moisture transport to the west coast (**Figure 3B**), resulting in wetter than average conditions in this region (**Figure 4B**). WT3 has a January maximum and high/low-pressure anomalies in the western/eastern half of the CONUS (**Figure 3C**), which lead to predominantly dry conditions (**Figure 4C**). Very wet conditions in the eastern CONUS occur in WT4 (**Figure 4D**), which has an early winter peak. This is due to strong moist air advection from the Pacific and Gulf of Mexico into the continent (**Figure 3D**). Similar precipitation anomalies are caused by WT5 (**Figure 4E**) as a result of a strong low-pressure anomaly over the Great Lakes region. WT6, WT7, and WT8 occur predominantly in spring and are the main sources of precipitation in the US Southwest (**Figures 4F–H**). They are associated with low-pressure anomalies over the western half of the CONUS and moist air advection from the Pacific (**Figures 3F–H**). WT7 results in anomalously wet conditions in the upper Plains, the Midwest, and the Deep South due to its strong low-pressure anomaly in the central US. Weak flows and predominantly dry conditions are present during the spring WT9 except for parts of Texas and New Mexico (**Figures 3I**, **4I**). Very wet conditions are present in the upper Plains during WT10 conditions due to a low-pressure anomaly and moisture advection into this region (**Figures 3J**, **4J**). WT11 is a typical summer WT with high PW values in the eastern CONUS and wetter than average conditions in this area (**Figures 3K**, **4K**). Monsoonal flow conditions are present in the late summer WT12 with high precipitation anomalies in Arizona and New Mexico (**Figures 3L**, **4L**).

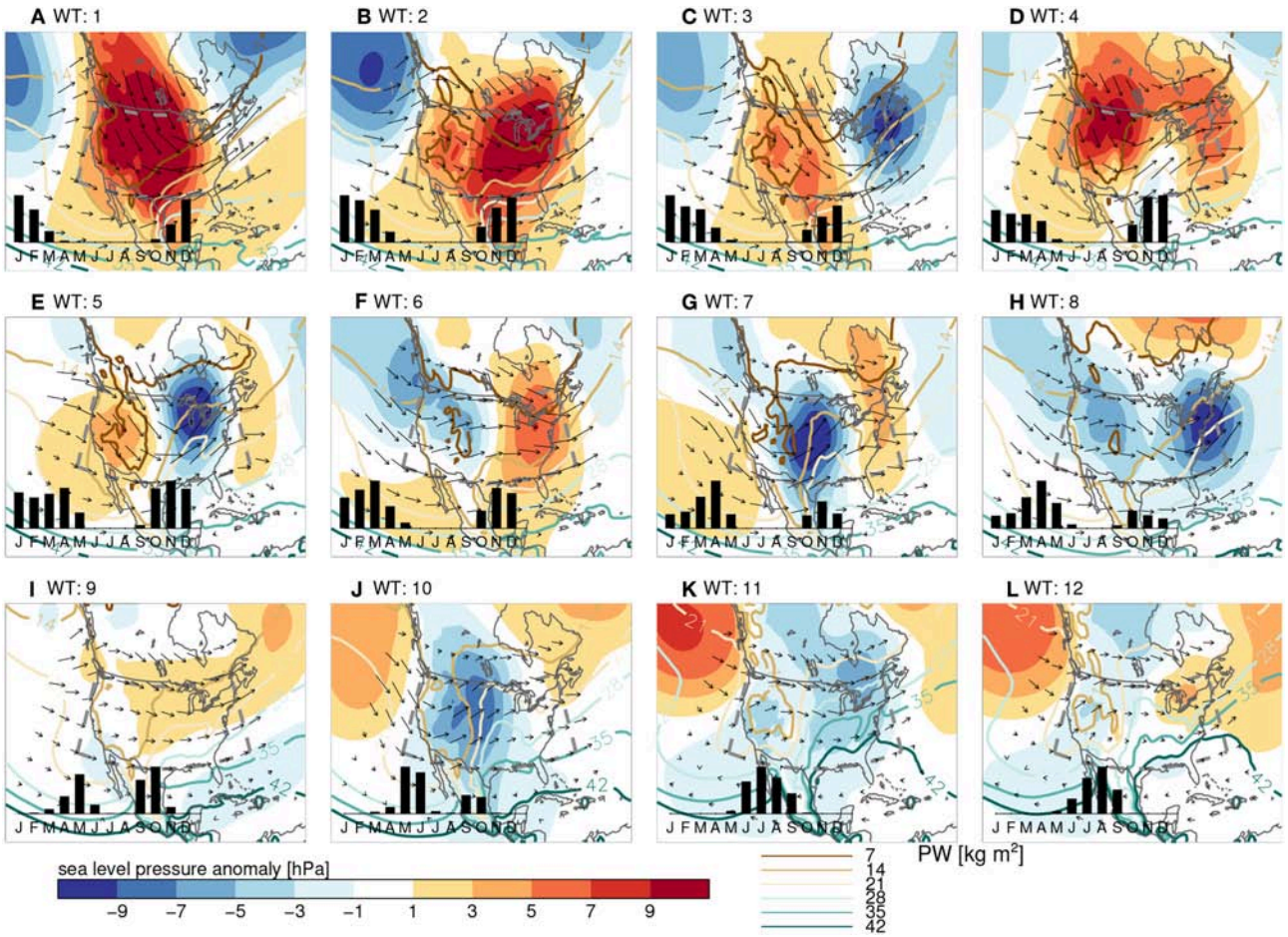

FIGURE 3 | Centroids of the 12 ERA-Interim based WTs **(A–L)** for the period 1979–2014. Filled contours show sea level pressure anomalies, green contour lines show precipitable water (PW), and arrows show 500 hPa wind direction and speed. A histogram of the relative frequency of each WT is shown in the bottom left and the domain used for the WTing is shown in the gray dashed box.

3.2. RCM Evaluation

The following analysis is based on data that cover the common evaluation period of 1990–2000. Due to this rather short period, the results might be affected by internal climate variability. Therefore, we focus our analysis on systematic differences between the two ensembles and their members rather than the performance of individual simulations.

There is a large spread in how well RCMs capture observed WT frequencies (**Figure 5**). The frequencies of WT5 and WT9 are well captured by most simulations whereas other WTs, such as WT4, show systematic low biases. It is important to mention that a high-frequency bias in one WT has to be counteracted in low biases in other WTs. Simulated WT frequency biases will result in precipitation biases since the WTs are associated with pronounced precipitation anomalies. For example, most simulations have a low-frequency bias for WT4 patterns, which results in cold season conditions that are too dry in the Deep South and Appalachian region, since WT4 is one of the main contributors of precipitation in those regions (see **Figure 4D**). Such a bias is frequently found in recent RCM simulations (Mearns et al., 2012).

A more systematic analysis of WT frequency biases is shown in **Figure 6**. The most striking feature is that NA-CORDEX simulations better capture WT frequencies than WRF36 simulations. This is likely related to the much larger domain size and not applying spectral nudging in the WRF36 simulations which allows them to deviate from the large-scale conditions provided by the driving data.

From the WRF36 simulations, we can see that model physics settings only have a small impact on WT frequencies. Simulations that use the NSAS convection scheme and RRTMG radiation scheme have a slightly better performance than the simulations using Tiedtke and CAM. The best ERA-Interim driven WRF36 simulation is the RNTM run, which has an average absolute WT frequency bias of ∼21%. Changing the driving data to CESM results in a slight skill improvement, which is surprising since using CESM should introduce biases that are not present in ERA-Interim. The WRF36 simulations have the largest WT frequency biases during the cold season. WT1 and WT4 frequencies are too

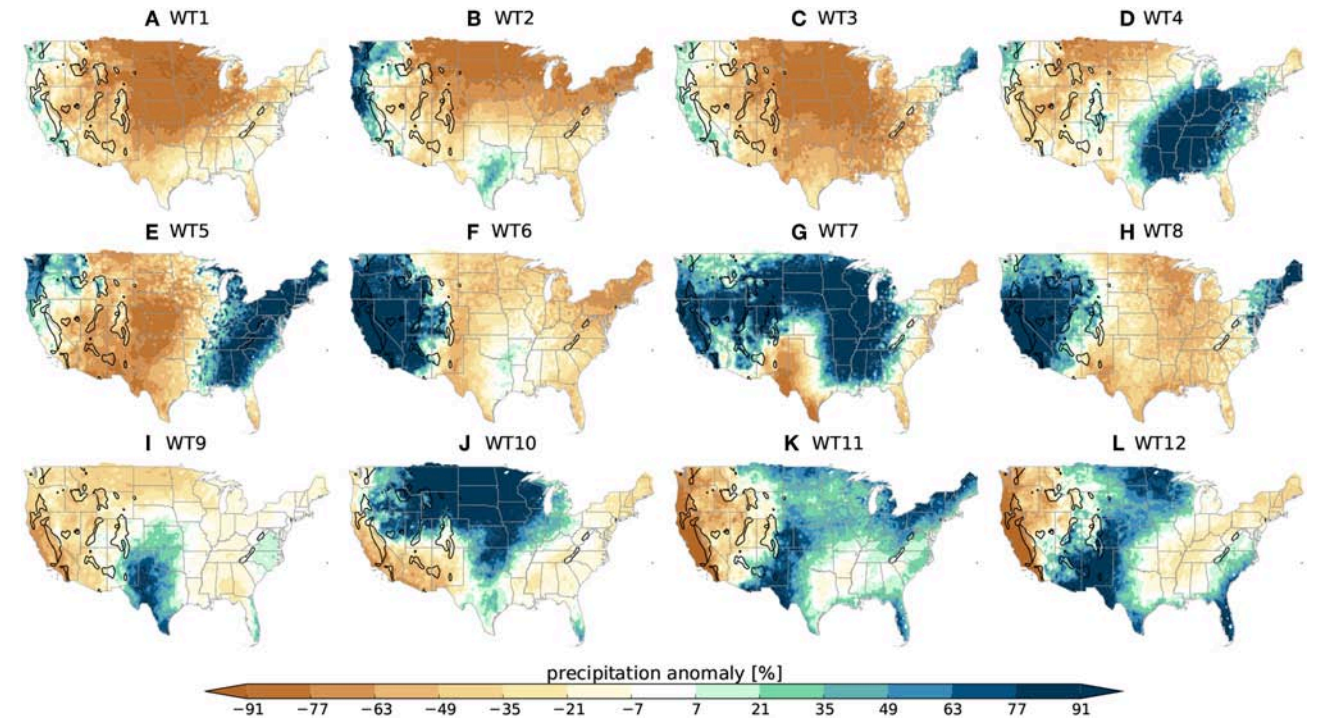

FIGURE 4 | Precipitation anomalies for each WT **(A–L)** based on the PRISM daily gridded observational data between 1981 and 2014 (Daly et al., 1994).

rare, which is counteracted by a too frequent simulation of WT2 and WT3 conditions.

In contrast to the WRF36 simulations, ERA-Interim driven NA-CORDEX runs have generally higher skill than GCM driven NA-CORDEX simulations. The NA-CORDEX ERA-Interim WRF runs have the highest skill of all simulations with average absolute biases lower than 10%. This has to be expected since spectral nudging was only used for the WRF simulations but not for the others. Spectral nudging has been shown to have a positive effect on simulating precipitation in previous North American scale RCM simulations (Mearns et al., 2012). Most NA-CORDEX simulations overestimate the frequency of WT2 and WT3 and underestimate the frequency of WT4 and WT5.

Another way to measure RCMs' quality is to assess their ability in capturing observed intra-WT variability, expressed as the average standard deviation (STDDEV) of normalized SLP, PW, and UV500 patterns from all days within a WT. **Figure 7** shows normalized (modeled divided by ERA-Interim) STDDEVs. A perfect model would have a score of zero, i.e., the same STDDEV as ERA-Interim. Negative values mean that differences between days within a WT are too small whereas positive values mean that they are too large. Very large values could indicate that the RCM simulates WTs that are not observed in ERA-Interim. Such unobserved WTs are assigned the most similar observed WT, resulting in large intra-WT STDDEV.

The WRF36 simulations have less skill in simulating intra-WT STDDEV than the NA-CORDEX runs (**Figure 7**). However, in contrast to the WT frequency analysis above, ERA-Interim driven WRF36 simulations have clearly higher skill than CESM driven simulations. The sensitivity to the used physics options is small. The transition season WT5–8 shows significant and systematically too high STDDEVs whereas too low STDDEVs seldom occur. The largest biases are found for WT8 with some simulations overestimating the observed STDDEV by more than 60%. The same WTs also show too high STDDEVs in the NA-CORDEX simulations, especially for the GCM driven runs, but the biases are smaller and less systematic than in WRF36. The best performance is again found for NA-CORDEX ERA-Interim driven WRF simulations with absolute average biases of <5%.

The third and last skill score that we consider is the WT centroid correlation coefficient, which allows one to assess how well the spatial pattern of each WT variable is reproduced by the RCMs. Values close to one indicate a skillful simulation of observed WT centroid patterns. Also here, the NA-CORDEX simulations outperform the WRF36 runs and the selected physics only have a minor impact on the performance of WRF36 simulations (**Figure 8**). In the WRF36 simulations, the lowest skills are found for simulating PW patterns, which becomes emphasized by changing from ERA-Interim to CESM boundary conditions. Particularly low PW pattern correlations are seen for WT3 and WT8. WT10 has very low correlation coefficients for UV500 when ERA-Interim is downscaled. SLP patterns generally show the highest correlation coefficients.

This is different in the NA-CORDEX simulations where PW patterns are simulated best. Again, ERA-Interim downscaled WRF simulations show the highest skills with average absolute

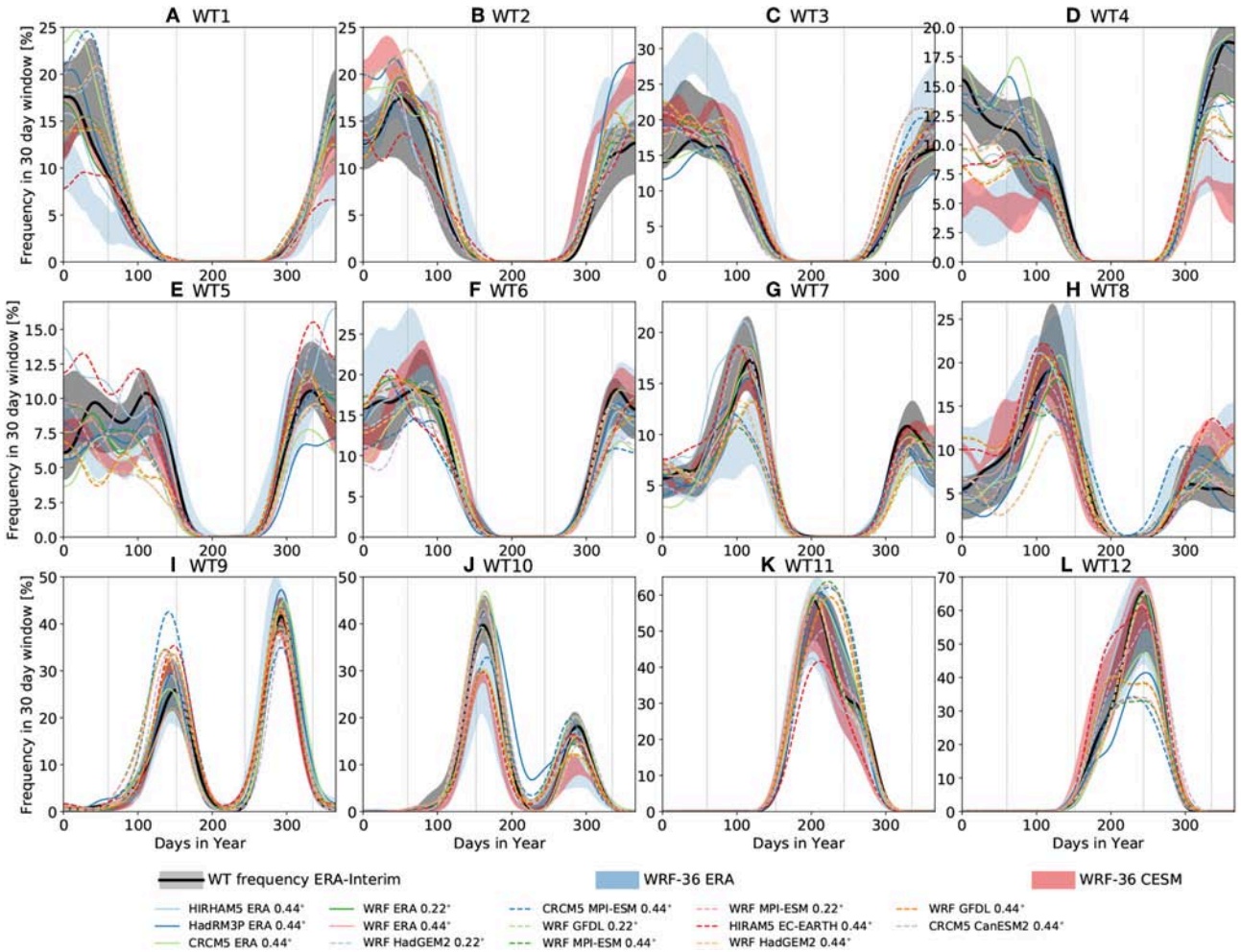

FIGURE 5 | Annual cycle of WT frequencies smoothed by a Gaussian low-pass filter with 10-day standard deviation for each of the 12 WTs **(A–L)**. The thick black line shows ERA-Interim WT frequencies for the period 1990–2000 and the gray contour shows the spread in all possible 11-year contiguous ERA-Interim periods within 1979–2014 as an estimate of climate variability. The blue contour shows the spread in the 24-member WRF36 ensemble that uses ERA-Interim as driving data. The red contour shows the spread within the 3-member CESM driven WRF36 hindcast simulations. Colored solid/dashed lines show WT frequencies in NA-CORDEX hindcast/historical simulations. The RCM results are based on the period 1990–2000. Vertical dashed lines show the end of February, May, August, and November respectively from left to right.

values larger than 0.96. Simulated WT8 patterns have overall the lowest skill but most correlation coefficients are still larger than 0.88.

3.3. Sources of Variability

Here we summarize the origin of different performances in simulating WT characteristics with RCMs. The presented numbers are first-order estimates since a full variance analysis would demand many more simulations than are available, especially for the NA-CORDEX ensemble. **Figure 9** shows the spread in the three assessed skill scores averaged over specific dimensions of the RCM ensembles.

WT frequencies in WRF36 simulations are fairly similar for all ensemble members and only weakly depend on the model physics and driving data (only the RKTM, RNTY, and RTTY are compared for the latter; **Figure 9A**). The NA-CORDEX simulations show higher skill in simulating WT frequencies. The 0.22 horizontal grid spacing WRF NA-CORDEX simulations show 1.9% lower absolute average WT frequency biases compared to their 0.44 counterparts. There is moderate variability (4.4%) concerning the RCM formulation, with CRCM5 showing the highest biases and WRF the lowest. A large variability of 11.1% occurs due to the selected driving data with ERA-Interim clearly resulting in the lowest biases. WRF36 and WRF-NA-CORDEX simulations show substantial variability of 12.7%, which is likely caused by differences in domain size and the application of spectral nudging in the WRF NA-CORDEX, resulting in a more realistic representation of WTs in the latter.

The WRF36 intra-WT STDDEV shows small sensitivity to the model physics but large sensitivity (10.1%) to the driving data with ERA-Interim driven simulations showing clearly higher skill (**Figure 9B**). In the NA-CORDEX ensemble, the

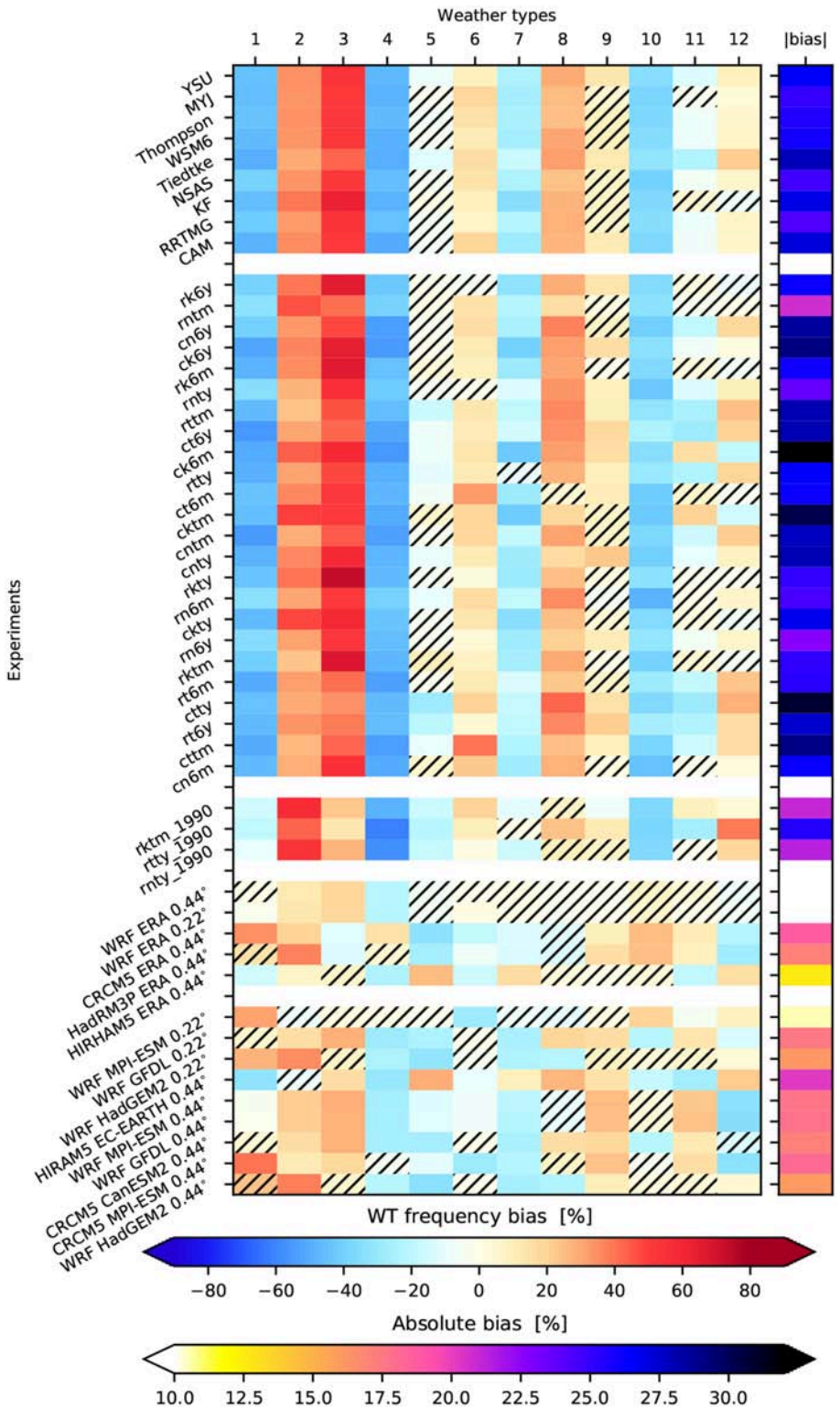

FIGURE 6 | Heatmap showing average WT frequency biases (smaller is better) for simulations (rows) and WTs (columns), and the absolute bias averaged over all WT biases in the rightmost column (lower color bar). The top block shows biases for WRF36 ERA-Interim simulations that use the same physics parameterization, e.g., the biases of all simulations that use the YSU PBL scheme are averaged. The second block from the top shows biases in the WRF36 simulations, and the central block shows biases in the CESM driven WRF36 hindcast runs. The second lowest block shows biases in ERA-Interim driven NA-CORDEX simulation while the lowest block shows NA-CORDEX hindcast driven biases for the period 1990–2000. Hatched rectangles show biases that are within the interannual variability of ERA-Interim WT frequencies.

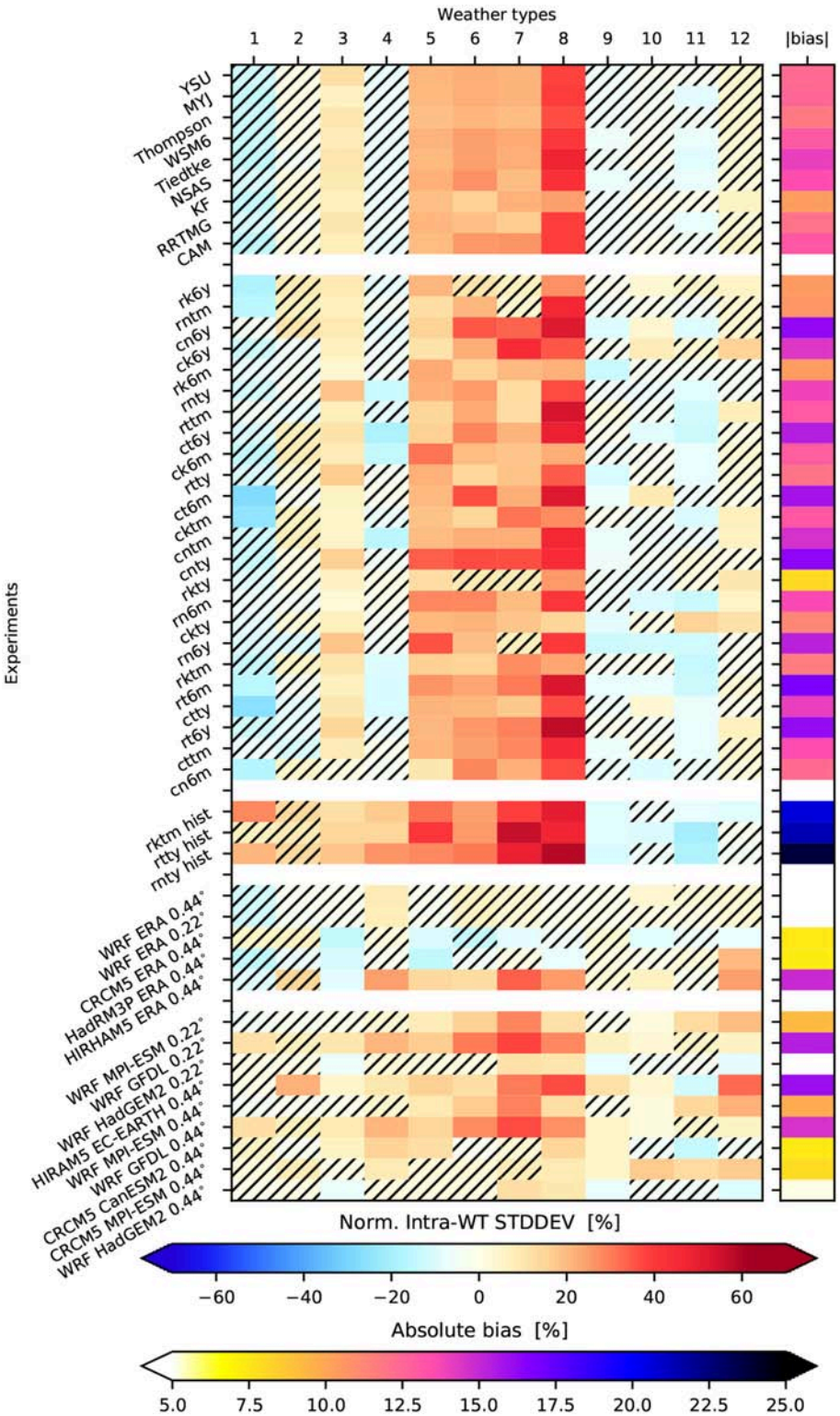

FIGURE 7 | Similar to **Figure 6** but showing the simulated divided by ERA-Interim intra-WT pattern standard deviations. A perfect score is zero and denotes that the model has the same variability than ERA-Interim.

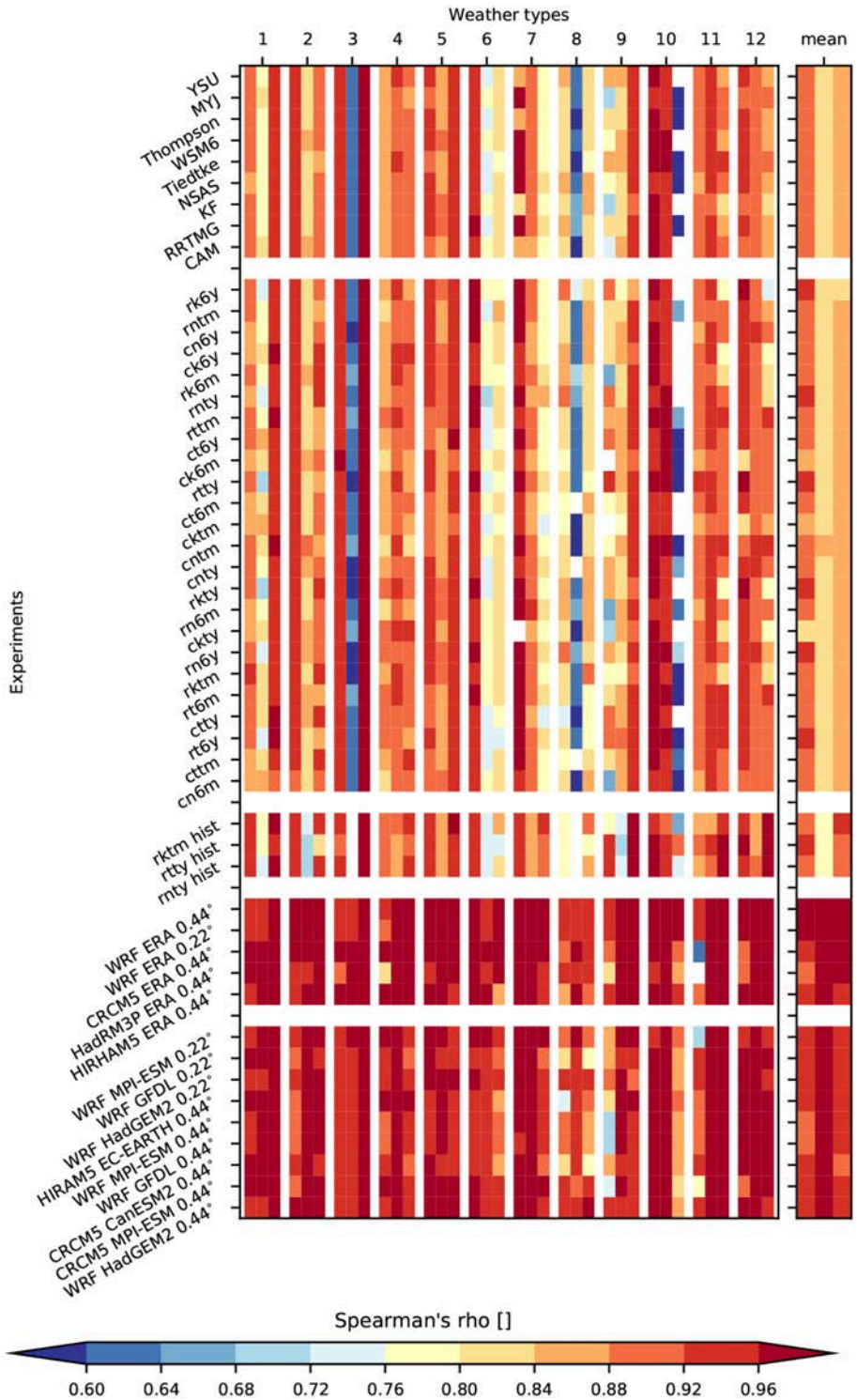

FIGURE 8 | Similar to **Figure 6** but showing correlation coefficients between ERA-Interim and simulated centroids (higher is better). Each column consists of three sub-columns showing correlation coefficients for SLP, PW, and 500 UV from left to right.

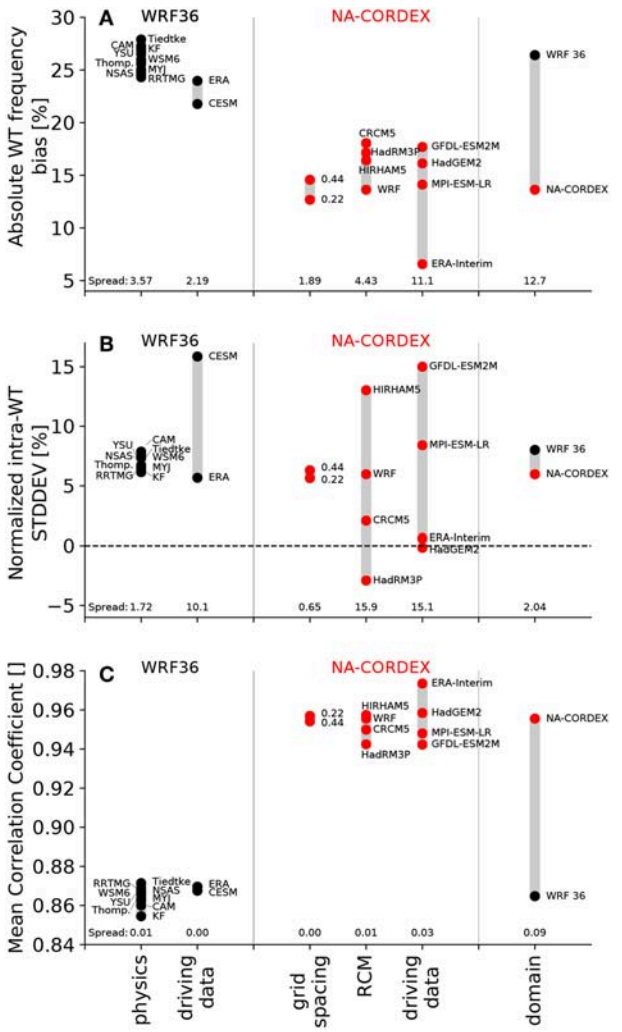

FIGURE 9 | Estimates of WT skill variability for different drivers using three metrics: **(A)** absolute WT frequency biases, **(B)** normalized intra-WT standard deviations, and **(C)** mean centroid pattern correlation coefficients. The impact of model physics and driving data is investigated in the WRF36 simulations (black symbols). The effect of horizontal grid spacing, RCM, and driving data is assessed for the NA-CORDEX simulations (red symbols). The impact of the domain size is estimated comparing WRF simulations in the NA-CORDEX ensemble with WRF36 runs. The maximum minus minimum spread is shown on the bottom of each panel.

WRF model resolution has only minor effects on the skill but the RCM formulation plays a major role (15.9%). The HIRHAM simulations overestimate the STDDEV substantially while HadGEM3P and CRCM5 show high skill. Additionally, the driving GCM has a major impact (15.1%) with ERA-Interim and HadGEM2, resulting in very small biases and GFDL-ESM2M driven simulations resulting in large overestimations of intra-WT STDDEVs. Comparing the WRF simulations from the two ensembles results in similar skills. However, this is mainly due to the larger fraction of ERA-Interim driven members in the WRF36 ensemble (24 out of 27 runs) compared to the NA-CORDEX ensemble (two out of ten).

The average centroid correlation coefficients show very small sensitivities to the WRF36 model physics and driving data (**Figure 9C**). The different sources of variability in the NA-CORDEX simulations lead to only minor sensitivities, with the WRF grid spacing having the smallest impact and the driving GCM having the largest. The major mode of variability in this metric is the RCM domain size and the application of spectral nudging as shown by the difference in correlation coefficients between the WRF36 and WRF-NA-CORDEX simulations.

3.4. Changes in Future WT Frequencies

All GCM driven NA-CORDEX and WRF36 runs also provide future climate data that we use to assess if WT frequencies are projected to change due to climate change. The GCM driven NA-CORDEX simulations are transient climate runs that cover a common period from 1950 to 2099 (see **Table 1**) whereas the GCM driven WRF36 runs are time slice experiments that cover the periods 1990–2000, 2020–2030, 2030–2040, 2050–2060, and 2080–2090.

Most NA-CORDEX simulations show systematic increases in WT7 and WT8 frequencies by mid-century, which, however, are not statistically significant (**Figure 10**). WT2 and WT11 predominantly decrease in their frequency. Six out of the eleven simulations show significant decreases in WT11 frequencies. Most of the NA-CORDEX models still show increases in WT7 frequencies by the end of the century but more systematic and significant are the frequency increases in WT12, which were not obvious at mid-century. WT12 resembles monsoonal flow patterns and it is projected to increase in frequency in ten of eleven models. All NA-CORDEX models agree on a decrease of WT10 patterns by the end of the century, eight of them show systematic decreases, which would indicate a drying of the northern Great Plains during summer (**Figure 4K**). Furthermore, all models show decreases for WT4 frequencies, which are smaller in magnitude and only significant in three models. These systematic changes are likely a result of anthropogenic forcings such as increasing greenhouse gas emissions and changes in aerosol loads. Climate natural variability should have a minor impact because the NA-CORDEX ensemble is forced by various GCMs that each simulate differing phases of, e.g., ENSO or Pacific Decadal Oscillation.

WT frequency changes in the WRF36 ensemble are often not systematic and strongly vary from period to period. This is likely a result of the 11-year long time-slice experiments that are too short to differentiate between climate internal variability and forces climate change (Deser et al., 2012). Differences in the response of the CESM GCM, which is downscaled in the WRF36 ensemble, to the NA-CORDEX GCMs are unlikely but cannot be excluded.

4. SUMMARY AND DISCUSSION

In this study, we use two sets of RCM ensembles, the North American CORDEX (NA-CORDEX) ensemble and a perturbed WRF physics ensemble with 36 km horizontal grid spacing (WRF36). We use a weather typing (WTing) algorithm to investigate if RCM simulations are able to capture hydrologically

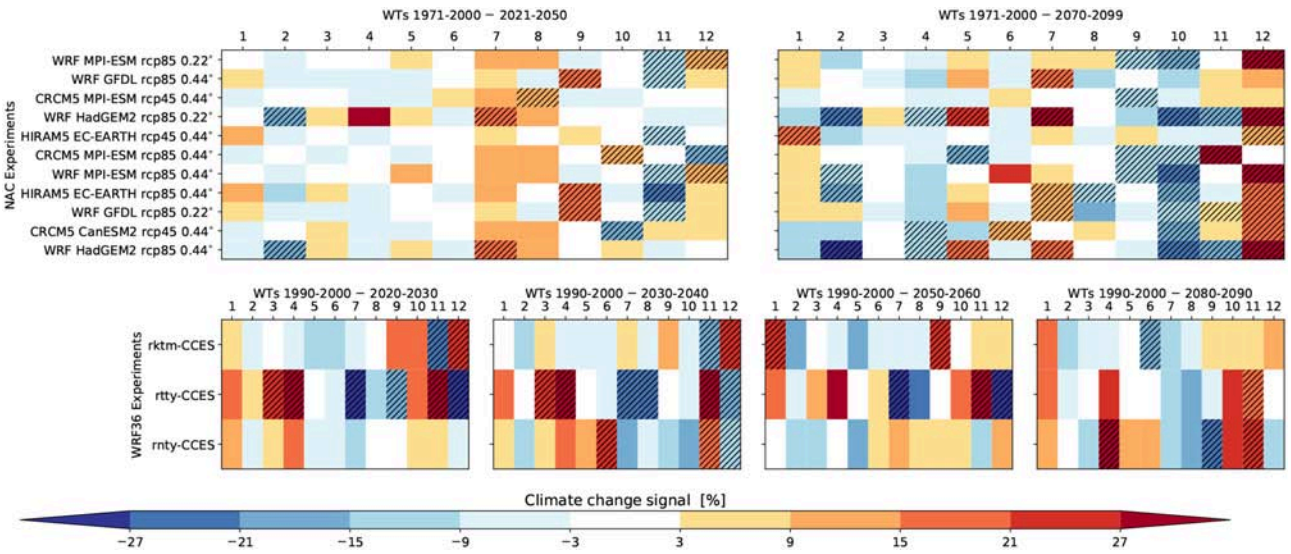

FIGURE 10 | Heatmap showing WT frequency changes in future climate projections. The top panels show results from the NA-CORDEX ensemble using 1979–2000 as the baseline period and 2021–2050 (Left panel) and 2071–2100 (Right panel). The lower panels show results from the WRF36 CESM driven simulations with the baseline period 1990–2000 and the future periods 2020–2030, 2030–2040, 2050–2060, and 2080–2090 from left to right. Hatched boxes show changes that exceed the interannual variability in ERA-Interim.

important weather pattern characteristics over the CONUS. We investigate three metrics: (1) the frequency biases of WT occurrences; (2) the variability of flow patterns within WTs; and (3) the accurate representation of WT spatial patterns.

The NA-CORDEX ensemble clearly outperforms the WRF36 simulations in all three metrics but particularly in the first and third ones. The main source for WRF model skill differences is the size of the RCM domain and the application of spectral nudging. The WRF36 simulations have a much larger domain and do not use spectral nudging, which allows them to significantly deviate from their lateral boundary conditions on synoptic scales. The much smaller NA-CORDEX domains constrain synoptic patterns from the GCM in the RCM domain and result in a more skillful representation of WT characteristics, particularly when they are driven by reanalysis data. Previous research showed that the interior large-scale dynamics can start to depart from the driving data as domain size increases (Alexandru et al., 2007). The second metric shows a larger sensitivity to the driving model and the formulation of the RCM. Also in this metric, however, ERA-Interim driven NA-CORDEX simulations have clearly higher skill than the ERA-Interim driven WRF36 runs. WT characteristics have very little sensitivity to the model physics, which is a robust result from the WRF36 ensemble evaluation. Model physics are, however, very important when it comes to the simulation of mesoscale processes in the RCMs as shown by Mooney et al. (2017) and Bruyère et al. (2017).

Biases that are present in the simulation of WTs directly translate into biases in the representation of the hydrology in RCMs (e.g., Addor et al., 2016). For example, in this study most RCMs underestimate the frequency of WT4 patterns. Days within this pattern result in high precipitation rates in the Deep South and Appalachian region during winter. Too infrequent WT4 conditions result in cold-season conditions that are too dry in these regions. Besides the biases in WT characteristics, RCMs also have biases in the representation of smaller-scale processes such as microphysics or mesoscale dynamics that affect model quality. The presented WT analysis can help to distinguish these two sources of biases, which is not possible when RCMs are evaluated on, for example, a seasonal basis.

WTing applied to climate change projections allows for understanding changes in the synoptic-scale conditions that occur in parallel to thermodynamic changes. A better understanding of changes in the large-scale dynamics is important since almost all climate change signals that we have confidence in originate from thermodynamic changes (Shepherd, 2014). The 11-year-long time slice experiments from the WRF36 ensemble do not allow a robust assessment of climate change in WT frequencies since they are dominated by climate internal variability. However, eight of eleven transient NA-CORDEX simulations show statistically significant increases in North American Monsoonal circulation (WT12) and a statistically significant decrease in patterns that transport moisture into the Northern Plains and Rockies (WT10) during the early warm season. The increase in monsoonal flow is consistent with other studies (Bukovsky et al., 2015, 2017; Prein, under review), which used different types of climate model data and show that the monsoon high strengthens and sets in earlier in the season. The decrease in WT10 seems to be physically linked to the increase in monsoonal flow since southwest monsoon precipitation is anticorrelated with precipitation in the plains. This is due to the modulation of the low pressure influence in the plains (WT10) by the stronger and more persistent monsoon circulation in the future (WT12).

5. CONCLUSION

This study shows that the RCM domain size and the application of spectral nudging can have a significant impact on the model's ability to capture realistic large-scale dynamics in mid-latitudes. Previous work showed that at the very least, RCM lateral boundaries should be sufficiently far removed from the region of interest to minimize spatial spin-up issues (Leduc and Laprise, 2009; Brisson et al., 2015; Matte et al., 2017). In addition, the domain should capture any key contributing regional physical processes missing from the lateral boundary conditions (Giorgi and Mearns, 1999). For example, a regional study of North Atlantic tropical cyclones by Done et al. (2015) required a large domain to capture the development of African easterly waves within the RCM domain. Erfanian and Wang (2018) came to a similar conclusion and showed that including teleconnected oceanic regions in the RCM domain improves its performance. However, too large domains and/or a lack of spectral nudging can lead to biased synoptic-scale patterns as shown here. Therefore, modelers have to find a balance between spinning up mesoscale processes that are not affected by the lateral boundary conditions and simulating large-scale dynamics realistically.

The accurate simulation of synoptic-scale variability in the driving GCM is essential since correcting for such biases in the RCM is challenging (Diaconescu et al., 2007). In contrast, correcting thermodynamic biases in the lateral boundary conditions of the RCM is somewhat easier (Bruyère et al., 2014; Xu and Yang, 2015), although challenges remain (Rocheta et al., 2014). Selecting GCMs with well-simulated large-scale dynamics should be a high priority for RCM downscaling experiments. WTing algorithms, such as the one used here, can support such a model selection.

If the large-scale dynamics are accurately captured in the GCM, spectral nudging can help to constrain synoptic-scale processes in large-domain RCM simulation (von Storch et al., 2000). Care has to be taken that the nudging does not disturb the development of mesoscale structures that are simulated by the RCM.

Another solution would be to use variable resolution GCMs such as the ICOsahedral Non-hydrostatic model (ICON; Zängl et al., 2015) or the Model for Prediction Across Scales (MPAS; Skamarock et al., 2012) instead of limited area modeling for downscaling experiments. These models, in theory, should resolve the domain size dependence of simulating WTs although they are more expensive since they simulate the entire globe instead of a limited area.

Generally, RCMs from both ensembles have larger WT frequency biases for cold season WTs than warm season WTs. The overestimation of variability within shoulder season WTs is also systematic. Future studies should focus on understanding the reason for these systematic biases. Our analyses suggest that these biases are related to the RCM formulation (e.g., model numerics) more so than the model physics.

Future work should also investigate the drivers behind the forced decrease in WT10 and increase in WT12. The consistency of these changes among model projections is surprising since climate change impacts on large-scale dynamics are often uncertain (Shepherd, 2014). Understanding the underlying processes of these changes is important due to their potential impacts on the summertime climate of the U.S. Targeted GCM experiments such as constant soil moisture or constant ice-cover experiments could help to gain insights on the large-scale drivers while additional RCM downscaling could help to understand the regional and local scale impacts.

This study is limited due to the use of existing RCM ensemble datasets, which were not specifically designed to address the impacts of domain size or spectral nudging on large scale circulation patterns. A more systematic analysis that includes the evaluation of WTs in the driving GCMs, the impact of spectral nudging on large domains, and a more systematic perturbation of the RCM domain size would be necessary to fully understand the sources of differences between the NA-CORDEX and WRF36 ensemble. Such an analysis could also help to understand if RCMs are able to add value to the driving GCM's large-scale dynamics by simulating upscale effects of mesoscale processes, or if their added value is constrained to regional scales.

AUTHOR CONTRIBUTIONS

AP designed the study, performed the data analysis, and produced the figures. MB performed data processing of the NA-CORDEX simulations. CB led the development of the WRF36 ensemble. All authors contributed to discussions and helped writing the manuscript.

FUNDING

NCAR is primarily funded by the National Science Foundation. This work was supported by the NCAR Weather and Climate Impacts Assessment Science Program and Regional Climate Uncertainty Program funded by NSF under the NCAR cooperative agreement managed by LM. We are grateful to NCAR's Computational and Information Systems Laboratory (CISL) who granted computational resources on its Yellowstone: IBM iDataPlex System (Climate Simulation Laboratory) http://n2t.net/ark:/85065/d7wd3xhc to perform the WRF36 and parts of the NA-CORDEX simulations. Additionally, CISL provides storage for archiving both RCM ensembles on its GLADE file system.

ACKNOWLEDGMENTS

We acknowledge ECMWF for providing access to its ERA-Interim reanalysis data. We also thank the PRISM Climate Group at Oregon State University for granting access to its daily gridded precipitation product. We acknowledge the World Climate Research Programme's Working Group on Regional Climate, and the Working Group on Coupled Modelling, former coordinating body of CORDEX and responsible panel for CMIP5. We also thank the climate modeling groups (listed in **Table 1** of this paper) for producing and making available their model output. We also acknowledge the U.S Department of Defense ESTCP for its support of the NA-CORDEX data archive.

REFERENCES

Addor, N., Rohrer, M., Furrer, R., and Seibert, J. (2016). Propagation of biases in climate models from the synoptic to the regional scale: implications for bias adjustment. *J. Geophys. Res. Atmos.* 121, 2075–2089. doi: 10.1002/2015JD024040

Alexandru, A., de Elia, R., and Laprise, R. (2007). Internal variability in regional climate downscaling at the seasonal scale. *Mon. Weather Rev.* 135, 3221–3238. doi: 10.1175/MWR3456.1

Brisson, E., Demuzere, M., and Van Lipzig, N. (2015). Modelling strategies for performing convection-permitting climate simulations. *Meteorol. Z.* 25, 149–163. doi: 10.1127/metz/2015/0598

Bruyère, C., Rasmussen, R., Gutmann, E., Done, J., Tye, M., Jaye, A., et al. (2017). *Impact of Climate Change on Gulf of Mexico Hurricanes*. Technical report, Technical Note NCAR/TN-535+ STR. NCAR.

Bruyère, C. L., Done, J. M., Holland, G. J., and Fredrick, S. (2014). Bias corrections of global models for regional climate simulations of high-impact weather. *Clim. Dyn.* 43, 1847–1856. doi: 10.1007/s00382-013-2011-6

Bruyère, C. L., Monaghan, A. J., Steinhoff, D. F., and Yates, D. (2015). *Bias-Corrected CMIP5 CESM Data in WRF/MPAS Intermediate File Format* (Boulder, CO: NCAR Technical Note NCAR/TN-515+STR), 27. doi: 10.5065/D6445JJ7

Bukovsky, M. S., Carrillo, C. M., Gochis, D. J., Hammerling, D. M., McCrary, R. R., and Mearns, L. O. (2015). Toward assessing NARCCAP regional climate model credibility for the North American monsoon: future climate simulations. *J. Clim.* 28, 6707–6728. doi: 10.1175/JCLI-D-14-00695.1

Bukovsky, M. S., McCrary, R. R., Seth, A., and Mearns, L. O. (2017). A mechanistically credible, poleward shift in warm-season precipitation projected for the US southern great plains? *J. Clim.* 30, 8275–8298. doi: 10.1175/JCLI-D-16-0316.1

Buonomo, E., Jones, R., Huntingford, C., and Hannaford, J. (2007). On the robustness of changes in extreme precipitation over Europe from two high resolution climate change simulations. *Q. J. Royal Meteorol. Soc.* 133, 65–81. doi: 10.1002/qj.13

Caya, D., and Laprise, R. (1999). A semi-implicit semi-Lagrangian regional climate model: the Canadian RCM. *Mon. Weather Rev.* 127, 341–362. doi: 10.1175/1520-0493(1999)127<0341:ASISLR>2.0.CO;2

Christensen, J. H., Carter, T. R., Rummukainen, M., and Amanatidis, G. (2007a). Evaluating the performance and utility of regional climate models: the PRUDENCE project. *Clim. Change.* 81, 1–6. doi: 10.1007/s10584-006-9211-6

Christensen, O. B., Drews, M., Christensen, J. H., Dethloff, K., Ketelsen, K., Hebestadt, I., et al. (2007b). *The HIRHAM Regional Climate Model Version 5 (β)*. Techical Report, 6–17.

Clark, A. J., Gallus Jr., W. A., Xue, M., and Kong, F. (2010). Convection-allowing and convection-parameterizing ensemble forecasts of a mesoscale convective vortex and associated severe weather environment. *Weather Forecast.* 25, 1052–1081. doi: 10.1175/2010WAF2222390.1

Collins, W. D., Bitz, C. M., Blackmon, M. L., Bonan, G. B., Bretherton, C. S., Carton, J. A., et al. (2006). The community climate system model version 3 (CCSM3). *J. Clim.* 19, 2122–2143. doi: 10.1175/JCLI3761.1

Daly, C., Neilson, R. P., and Phillips, D. L. (1994). A statistical-topographic model for mapping climatological precipitation over mountainous terrain. *J. Appl. Meteorol.* 33, 140–158. doi: 10.1175/1520-0450(1994)033<0140:ASTMFM>2.0.CO;2

Decker, M., Brunke, M. A., Wang, Z., Sakaguchi, K., Zeng, X., and Bosilovich, M. G. (2012). Evaluation of the reanalysis products from GSFC, NCEP, and ECMWF using flux tower observations. *J. Clim.* 25, 1916–1944. doi: 10.1175/JCLI-D-11-00004.1

Dee, D. P., Uppala, S. M., Simmons, A., Berrisford, P., Poli, P., Kobayashi, S., et al. (2011). The ERA-interim reanalysis: configuration and performance of the data assimilation system. *Q. J. Royal Meteorol. Soc.* 137, 553–597. doi: 10.1002/qj.828

Delage, Y. (1997). Parameterising sub-grid scale vertical transport in atmospheric models under statically stable conditions. *Bound. Layer Meteorol.* 82, 23–48. doi: 10.1023/A:1000132524077

Denis, B., Laprise, R., Caya, D., and Côté, J. (2002). Downscaling ability of one-way nested regional climate models: the Big-Brother experiment. *Clim. Dyn.* 18, 627–646. doi: 10.1007/s00382-001-0201-0

Deser, C., Phillips, A., Bourdette, V., and Teng, H. (2012). Uncertainty in climate change projections: the role of internal variability. *Clim. Dyn.* 38, 527–546. doi: 10.1007/s00382-010-0977-x

Di Luca, A., de Elía, R., and Laprise, R. (2012). Potential for added value in precipitation simulated by high-resolution nested regional climate models and observations. *Clim. Dyn.* 38, 1229–1247. doi: 10.1007/s00382-011-1068-3

Diaconescu, E. P., Laprise, R., and Sushama, L. (2007). The impact of lateral boundary data errors on the simulated climate of a nested regional climate model. *Clim. Dyn.* 28, 333–350. doi: 10.1007/s00382-006-0189-6

Done, J. M., Holland, G. J., Bruyère, C. L., Leung, L. R., and Suzuki-Parker, A. (2015). Modeling high-impact weather and climate: lessons from a tropical cyclone perspective. *Clim. Change.* 129, 381–395. doi: 10.1007/s10584-013-0954-6

Doswell III, C. A., Brooks, H. E., and Maddox, R. A. (1996). Flash flood forecasting: an ingredients-based methodology. *Weather Forecast.* 11, 560–581. doi: 10.1175/1520-0434(1996)011<0560:FFFAIB>2.0.CO;2

Erfanian, A., and Wang, G. (2018). Explicitly accounting for the role of remote oceans in regional climate modeling of South America. *J. Adv. Model. Earth Syst.* 10, 2408–2426. doi: 10.1029/2018MS001444

Essery, R., and Clark, D. B. (2003). Developments in the MOSES 2 land-surface model for PILPS 2e. *Glob. Planet. Change.* 38, 161–164. doi: 10.1016/S0921-8181(03)00026-2

Feser, F., Rockel, B., von Storch, H., Winterfeldt, J., and Zahn, M. (2011). Regional climate models add value to global model data: a review and selected examples. *Bull. Am. Meteorol. Soc.* 92, 1181–1192. doi: 10.1175/2011BAMS3061.1

García-Valero, J. A., Montavez, J. P., Jerez, S., Gómez-Navarro, J. J., Lorente-Plazas, R., and Jiménez-Guerrero, P. (2012). A seasonal study of the atmospheric dynamics over the Iberian Peninsula based on circulation types. *Theor. Appl. Climatol.* 110, 291–310. doi: 10.1007/s00704-012-0623-0

Gibson, P. B., Uotila, P., Perkins-Kirkpatrick, S. E., Alexander, L. V., and Pitman, A. J. (2016). Evaluating synoptic systems in the CMIP5 climate models over the Australian region. *Clim. Dyn.* 47, 2235–2251. doi: 10.1007/s00382-015-2961-y

Giorgi, F. (1990). Simulation of regional climate using a limited area model nested in a general circulation model. *J. Clim.* 3, 941–963. doi: 10.1175/1520-0442(1990)003<0941:SORCUA>2.0.CO;2

Giorgi, F., and Mearns, L. O. (1999). Introduction to special section: regional climate modeling revisited. *J. Geophys. Res. Atmos.* 104, 6335–6352. doi: 10.1029/98JD02072

Goodess, C. M., and Palutikof, J. P. (1998). Development of daily rainfall scenarios for southeast Spain using a circulation-type approach to downscaling. *Int. J. Climatol.* 18, 1051–1083. doi: 10.1002/(SICI)1097-0088(199808)18:10<1051::AID-JOC304>3.0.CO;2-1

Han, J., and Pan, H.-L. (2011). Revision of convection and vertical diffusion schemes in the NCEP global forecast system. *Weather Forecast.* 26, 520–533. doi: 10.1175/WAF-D-10-05038.1

Hong, S.-Y., Dudhia, J., and Chen, S.-H. (2004). A revised approach to ice microphysical processes for the bulk parameterization of clouds and precipitation. *Mon. Weather Rev.* 132, 103–120. doi: 10.1175/1520-0493(2004)132<0103:ARATIM>2.0.CO;2

Hong, S.-Y., and Lim, J.-O. J. (2006). The WRF single-moment 6-class microphysics scheme (WSM6). *J. Korean Meteor. Soc.* 42, 129–151.

Hong, S.-Y., Noh, Y., and Dudhia, J. (2006). A new vertical diffusion package with an explicit treatment of entrainment processes. *Mon. Weather Rev.* 134, 2318–2341. doi: 10.1175/MWR3199.1

Hurrell, J. W., Holland, M. M., Gent, P. R., Ghan, S., Kay, J. E., Kushner, P. J., et al. (2013). The community earth system model: a framework for collaborative research. *Bull. Am. Meteorol. Soc.* 94, 1339–1360. doi: 10.1175/BAMS-D-12-00121.1

Janjić, Z. I. (1994). The step-mountain eta coordinate model: further developments of the convection, viscous sublayer, and turbulence closure schemes. *Mon. Weather Rev.* 122, 927–945. doi: 10.1175/1520-0493(1994)122<0927:TSMECM>2.0.CO;2

Jones, R., Murphy, J., and Noguer, M. (1995). Simulation of climate change over Europe using a nested regional-climate model. I: assessment of control climate, including sensitivity to location of lateral boundaries. *Q. J. Royal Meteorol. Soc.* 121, 1413–1449.

Kain, J. S., and Fritsch, J. M. (1990). A one-dimensional entraining/detraining plume model and its application in convective parameterization. *J. Atmos. Sci.* 47, 2784–2802. doi: 10.1175/1520-0469(1990)047<2784:AODEPM>2.0.CO;2

Knutti, R., Masson, D., and Gettelman, A. (2013). Climate model genealogy: generation CMIP5 and how we got there. *Geophys. Res. Lett.* 40, 1194–1199. doi: 10.1002/grl.50256

Kotlarski, S., Keuler, K., Christensen, O. B., Colette, A., Déqué, M., Gobiet, A., et al. (2014). Regional climate modeling on European scales: a joint standard evaluation of the EURO-CORDEX RCM ensemble. *Geosci. Model Dev.* 7, 1297–1333. doi: 10.5194/gmd-7-1297-2014

Leduc, M., and Laprise, R. (2009). Regional climate model sensitivity to domain size. *Clim. Dyn.* 32, 833–854. doi: 10.1007/s00382-008-0400-z

Leung, L. R., Qian, Y., and Bian, X. (2003). Hydroclimate of the western United States based on observations and regional climate simulation of 1981–2000. Part I: seasonal statistics. *J. Clim.* 16, 1892–1911. doi: 10.1175/1520-0442(2003)016<1892:HOTWUS>2.0.CO;2

Li, J., and Barker, H. (2005). A radiation algorithm with correlated-k distribution. Part I: local thermal equilibrium. *J. Atmos. Sci.* 62, 286–309. doi: 10.1175/JAS-3396.1

Lin, R., Zhou, T., and Qian, Y. (2014). Evaluation of global monsoon precipitation changes based on five reanalysis datasets. *J. Clim.* 27, 1271–1289. doi: 10.1175/JCLI-D-13-00215.1

Lin, Y.-L., Chiao, S., Wang, T.-A., Kaplan, M. L., and Weglarz, R. P. (2001). Some common ingredients for heavy orographic rainfall. *Weather Forecast.* 16, 633–660. doi: 10.1175/1520-0434(2001)016<0633:SCIFHO>2.0.CO;2

Lorente-Plazas, R., Montávez, J., Jimenez, P., Jerez, S., Gómez-Navarro, J., García-Valero, J., et al. (2015). Characterization of surface winds over the Iberian Peninsula. *Int. J. Climatol.* 35, 1007–1026. doi: 10.1002/joc.4034

Martynov, A., Laprise, R., Sushama, L., Winger, K., Šeparović, L., and Dugas, B. (2013). Reanalysis-driven climate simulation over CORDEX North America domain using the Canadian Regional Climate Model, version 5: model performance evaluation. *Clim. Dyn.* 41, 2973–3005. doi: 10.1007/s00382-013-1778-9

Matte, D., Laprise, R., Thériault, J. M., and Lucas-Picher, P. (2017). Spatial spin-up of fine scales in a regional climate model simulation driven by low-resolution boundary conditions. *Clim. Dyn.* 49, 563–574. doi: 10.1007/s00382-016-3358-2

Mearns, L. O., Arritt, R., Biner, S., Bukovsky, M. S., McGinnis, S., Sain, S., et al. (2012). The North American regional climate change assessment program: overview of phase I results. *Bull. Am. Meteorol. Soc.* 93, 1337–1362. doi: 10.1175/BAMS-D-11-00223.1

Mearns, L. O., McGinnis, S., Korytina, D., Arritt, R., Biner, S., Bukovsky, M., et al. (2017). *The NA-CORDEX Dataset, Version 1.0*. NCAR Climate Data Gateway, Boulder CO. doi: 10.5065/D6SJ1JCH

Mlawer, E. J., Taubman, S. J., Brown, P. D., Iacono, M. J., and Clough, S. A. (1997). Radiative transfer for inhomogeneous atmospheres: RRTM, a validated correlated-k model for the longwave. *J. Geophys. Res. Atmos.* 102, 16663–16682. doi: 10.1029/97JD00237

Mooney, P., Broderick, C., Bruyère, C., Mulligan, F., and Prein, A. (2017). Clustering of observed diurnal cycles of precipitation over the United States for evaluation of a WRF multiphysics regional climate ensemble. *J. Clim.* 30, 9267–9286. doi: 10.1175/JCLI-D-16-0851.1

Morcrette, J. J. (1984), Parameterization of radiation in general atmospheric circulation models, Ph.D. thesis, Univ. des Sci. et Technol (Lille), 373.

Nordeng, T. E. (1994). Extended versions of the convective parametrization scheme at ECMWF and their impact on the mean and transient activity of the model in the tropics. *Res. Depart. Tech. Memo.* 206, 1–41.

Paredes, D., Trigo, R. M., Garcia-Herrera, R., and Trigo, I. F. (2006). Understanding precipitation changes in Iberia in early spring: weather typing and storm-tracking approaches. *J. Hydrometeorol.* 7, 101–113. doi: 10.1175/JHM472.1

Prein, A., Gobiet, A., Truhetz, H., Keuler, K., Goergen, K., Teichmann, C., et al. (2016a). Precipitation in the EURO-CORDEX 0.11° and 0.44° simulations: high resolution, high benefits? *Clim. Dyn.* 46, 383–412. doi: 10.1007/s00382-015-2589-y

Prein, A. F., Holland, G. J., Rasmussen, R. M., Clark, M. P., and Tye, M. R. (2016b). Running dry: the US Southwest's drift into a drier climate state. *Geophys. Res. Lett.* 43, 1272–1279. doi: 10.1002/2015GL066727

Radić, V., and Clarke, G. K. (2011). Evaluation of IPCC models' performance in simulating late-twentieth-century climatologies and weather patterns over North America. *J. Clim.* 24, 5257–5274. doi: 10.1175/JCLI-D-11-00011.1

Rocheta, E., Evans, J. P., and Sharma, A. (2014). Assessing atmospheric bias correction for dynamical consistency using potential vorticity. *Environ. Res. Lett.* 9:124010. doi: 10.1088/1748-9326/9/12/124010

Romesburg, C. (2004). *Cluster Analysis for Researchers*. Available online at: Lulu.com

Rummukainen, M. (2010). State-of-the-art with regional climate models. *Wiley Interdiscip. Rev. Clim. Change.* 1, 82–96. doi: 10.1002/wcc.8

Rummukainen, M. (2016). Added value in regional climate modeling. *Wiley Interdiscip. Rev. Clim. Change.* 7, 145–159. doi: 10.1002/wcc.378

Santos, J. A., Belo-Pereira, M., Fraga, H., and Pinto, J. G. (2016). Understanding climate change projections for precipitation over western Europe with a weather typing approach. *J. Geophys. Res. Atmos.* 121, 1170–1189. doi: 10.1002/2015JD024399

Schiemann, R., and Frei, C. (2010). How to quantify the resolution of surface climate by circulation types: an example for Alpine precipitation. *Phys. Chem. Earth.* 35, 403–410. doi: 10.1016/j.pce.2009.09.005

Šeparović, L., Alexandru, A., Laprise, R., Martynov, A., Sushama, L., Winger, K., et al. (2013). Present climate and climate change over North America as simulated by the fifth-generation Canadian regional climate model. *Clim. Dyn.* 41, 3167–3201. doi: 10.1007/s00382-013-1737-5

Shepherd, T. G. (2014). Atmospheric circulation as a source of uncertainty in climate change projections. *Nat. Geosci.* 7:703. doi: 10.1038/ngeo2253

Skamarock, W. C., and Klemp, J. B. (2008). A time-split nonhydrostatic atmospheric model for weather research and forecasting applications. *J. Comput. Phys.* 227, 3465–3485. doi: 10.1016/j.jcp.2007.01.037

Skamarock, W. C., Klemp, J. B., Duda, M. G., Fowler, L. D., Park, S.-H., and Ringler, T. D. (2012). A multiscale nonhydrostatic atmospheric model using centroidal Voronoi tesselations and C-grid staggering. *Mon. Weather Rev.* 140, 3090–3105. doi: 10.1175/MWR-D-11-00215.1

Straus, D. M., and Molteni, F. (2004). Circulation regimes and SST forcing: results from large GCM ensembles. *J. Clim.* 17, 1641–1656. doi: 10.1175/1520-0442(2004)017<1641:CRASFR>2.0.CO;2

Sundqvist, H. (1978). A parameterization scheme for non-convective condensation including prediction of cloud water content. *Q. J. Royal Meteorol. Soc.* 104, 677–690. doi: 10.1002/qj.49710444110

Taylor, K. E., Stouffer, R. J., and Meehl, G. A. (2012). An overview of CMIP5 and the experiment design. *Bull. Am. Meteorol. Soc.* 93, 485–498. doi: 10.1175/BAMS-D-11-00094.1

Tewari, M., Chen, F., Wang, W., Dudhia, J., LeMone, M., Mitchell, K., et al. (2004). "Implementation and verification of the unified NOAH land surface model in the WRF model." in *20th Conference on Weather Analysis and Forecasting/16th Conference on Numerical Weather Prediction* (Seattle, WA). Vol. 1115.

Thompson, G., Rasmussen, R. M., and Manning, K. (2004). Explicit forecasts of winter precipitation using an improved bulk microphysics scheme. Part I: description and sensitivity analysis. *Mon. Weather Rev.* 132, 519–542. doi: 10.1175/1520-0493(2004)132<0519:EFOWPU>2.0.CO;2

Tiedtke, M. (1989). A comprehensive mass flux scheme for cumulus parameterization in large-scale models. *Mon. Weather Rev.* 117, 1779–1800. doi: 10.1175/1520-0493(1989)117<1779:ACMFSF>2.0.CO;2

van Bebber, W. J. (1891). *Die Wettervorhersage: Eine praktische Anleitung zur Wettervorhersage auf Grundlage der Zeitungswetterkarten und Zeitungswetterberichte, für alle Berufsarten*. Enke.

Van Vuuren, D. P., Edmonds, J., Kainuma, M., Riahi, K., Thomson, A., Hibbard, K., et al. (2011). The representative concentration pathways: an overview. *Clim. Change.* 109:5. doi: 10.1007/s10584-011-0148-z

Verseghy, D. (2009). *CLASS–The Canadian Land Surface Scheme (Version 3.4) Technical Documentation (Version 1.1), Environment Canada*. Downsview, ON: Climate Research Division, Science and Technology Branch.

Verseghy, D. L. (1991). CLASS–a Canadian land surface scheme for GCMs. I. Soil model. *Int. J. Climatol.* 11, 111–133. doi: 10.1002/joc.3370110202

von Storch, H., Langenberg, H., and Feser, F. (2000). A spectral nudging technique for dynamical downscaling purposes. *Mon. Weather Rev.* 128, 3664–3673. doi: 10.1175/1520-0493(2000)128<3664:ASNTFD>2.0.CO;2

Wood, J., Harrison, S., Turkington, T., and Reinhardt, L. (2016). Landslides and synoptic weather trends in the European Alps. *Clim. Change.* 136, 297–308. doi: 10.1007/s10584-016-1623-3

Xu, Z., and Yang, Z.-L. (2015). A new dynamical downscaling approach with GCM bias corrections and spectral nudging. *J. Geophys. Res. Atmos.* 120, 3063–3084. doi: 10.1002/2014JD022958

Zadra, A., Caya, D., Côté, J., Dugas, B., Jones, C., Laprise, R., et al. (2008). The next Canadian regional climate model. *Phys. Can.* 64, 75–83.

Zängl, G., Reinert, D., Rípodas, P., and Baldauf, M. (2015). The ICON (ICOsahedral Non-hydrostatic) modelling framework of DWD and MPI-M: description of the non-hydrostatic dynamical core. *Q. J. Royal Meteorol. Soc.* 141, 563–579. doi: 10.1002/qj.2378

Conflict of Interest Statement: The authors declare that the research was conducted in the absence of any commercial or financial relationships that could be construed as a potential conflict of interest.

frontiers in Environmental Science

ORIGINAL RESEARCH
published: 02 July 2019
doi: 10.3389/fenvs.2019.00101

Extreme Orographic Rainfall in the Eastern Andes Tied to Cold Air Intrusions

*Masih Eghdami and Ana P. Barros**

Civil and Environmental Engineering, Duke University, Durham, NC, United States

Long-duration localized heavy rainfall (> 6 h, < 10 km^2) was recorded by raingauges on October 4, 2013 at mid-elevations ($\sim 1,500$ *m*) in the Peruvian Andes, which was not apparent in infrared or microwave measurements from either geostationary or polar orbiting satellites. This spring event is investigated here through a numerical modeling study using the Weather and Research Forecasting (WRF) model, and examined in the context of the climatology of Cold Air Intrusions (CAIs) along the eastern flanks of the tropical Andes. The model results suggest significant precipitation enhancement from intense shallow convection at the CAI frontal boundary amplified by orographic lifting as it propagates northward latched to the slopes of Andes. Analysis of CAI mesoscale dynamics was conducted using four decades of European Center Medium-Range Weather Forecasts (ECMWF) reanalysis, Tropical Rainfall Measurement Mission (TRMM) data products, and rain-gauge observations with emphasis on characterizing year-round CAI frequency, CAI interactions with Andes topography, and their impact on orographic precipitation climatology. The data show a robust enhancement of the diurnal cycle of precipitation during CAI events in all seasons, and in particular increases in surface rainfall rate during early morning at intermediate elevations ($\sim$ 1,500 m), that is the eastern Andes orographic maximum. This link between CAI frequency and rainfall suggests that they play an important role in maintaining the Andes to Amazon year-round terrestrial connectivity through runoff production and transport by the river networks.

Keywords: orographic rainfall, Andes, cold front, extreme events, water cycle

OPEN ACCESS

Edited by:
Frauke Feser,
Helmholtz Centre for Materials and Coastal Research (HZG), Germany

Reviewed by:
Ronny Petrik,
Helmholtz Centre for Materials and Coastal Research (HZG), Germany
Federico Porcu,
University of Bologna, Italy

***Correspondence:**
Ana P. Barros
barros@duke.edu

Specialty section:
This article was submitted to Atmospheric Science, a section of the journal Frontiers in Environmental Science

Received: *29 January 2019*
Accepted: *13 June 2019*
Published: *02 July 2019*

Citation:
Eghdami M and Barros AP (2019) Extreme Orographic Rainfall in the Eastern Andes Tied to Cold Air Intrusions. Front. Environ. Sci. 7:101. doi: 10.3389/fenvs.2019.00101

INTRODUCTION

The Andes mountain range is the most prominent topographic feature of South America and modulates the weather and climate of the continent (Garreaud, 2000, 2009). Orographic effects on synoptic and regional-scale weather and climate (Barros and Lettenmaier, 1994; Houze, 2012) can lead to localized extreme rainfall events causing floods, debris flow, and landslides that reshape the landscape (e.g., Lowman and Barros, 2014). South American Cold Air Intrusions (CAI) (hereafter referred to as CAI) are year-round synoptic scale phenomena that tie the mid-latitudes to the tropics along the eastern slopes of the Andes. The focus of this manuscript is on the role of CAI in the climatology of extreme orographic precipitation in the eastern Andes.

Synoptic-scale cold intrusions of mid-latitude air to the tropics are common along north-south oriented mountain ranges (Garreaud, 2001) including the Rockies (e.g., Schultz et al., 1997), the

Himalayas (e.g., Chen et al., 2002), and the Andes (Garreaud and Wallace, 1998; Garreaud, 1999a,b, 2000; Vera and Vigliarolo, 2000). Garreaud (2000) synthesized the mean synoptic structure of CAI events in the Andes based on 17-years of National Centers for Environmental Prediction-National Center for Atmospheric Research (NCEP-NCAR) reanalysis and satellite measurements of outgoing longwave radiation (OLR) to show how orographic blocking forces geostrophic southerly winds to align with the Andes and transport cold air to the tropics. Earlier studies linked CAI occurrences in the austral winter to light rainfall alone, while estimating that CAI produce 25–50% of summer precipitation over central Amazonia and adjacent plains as a result of the enhanced convective environment ahead of the cold surge (Garreaud and Wallace, 1998). Cold season episodes cause significant temperature drops near the land-surface resulting in widespread freezing conditions in the mid-latitudes and subtropical South America that have severe adverse impacts on agriculture and people. Espinoza et al. (2013) analyzed winter frost episodes (June-July-August, JJA) using *in situ* temperature data from 1975 to 2001, and defined extreme cold events when minimum daily temperature drops below the 10th percentile. They reported different duration and intensities for winter frost events depending on latitude with 60% of the events in the subtropics lasting about 1 day, and 15% of the events in the tropics lasting as long as 3 days. Boers et al. (2014) reported results similar to Espinoza et al. (2013) but focused instead on extreme rainfall events in the Bolivian Andes during the monsoon season (December-January-February, DJF). Hurley et al. (2015) found that most of the snow accumulation on the Quelccaya Ice Cap (QIC) in the Peruvian Andes from $\sim$ 2003 – 2013 occurred during the monsoon, with the heaviest events that account for 70% of total snow accumulation being associated with CAIs' frontal band of enhanced convection. Following Siqueira and Machado (2004), Siqueira et al. (2005) proposed classifying CAIs in three categories: (1) interaction with tropical convection during northward propagation, (2) interaction with tropical convection along a quasi-stationary northeast to southwest convection band, and (3) no interaction with tropical convection, with the first one being most relevant for this work. During the monsoon, CAI events have been linked to emergence of organized mesoscale convective systems (MCSs) over the southern La Plata Basin (Anabor et al., 2008; Boers et al., 2015). Anabor et al. (2008) point out that while the region of convective development typically propagates north and northwestward ahead of the CAI front with MCS activity propagating eastward, occasionally there is upstream southeastward MCS propagation that is tied to the position of the South Atlantic anticyclone. Boers et al. (2015) linked southeasterly propagation of convective precipitation clusters to the Bolivian Andes during the monsoon to pressure anomalies associated with the westerly Rossby Wave (RW) propagating over the Andes as it interacts in the leeside with the northwestern Argentinian low-pressure center (NAL, Seluchi et al., 2003). Besides the different modes of CAI interaction with tropical convection, past CAI climatology studies also focused on trajectory (Lupo et al., 2001) and life-cycle analysis related to westerly RW interactions between the subtropical and polar jets (Müller and Berri, 2007). In particular, Müller and Ambrizzi (2007) linked CAI causing generalized frosts to a double RW train approaching South America (SA) between the subtropical and polar jets. The trajectories of these anomalies may or may not merge as they approach western SA, which subsequently impacts whether they are in-phase (favorable to strong CAI) or out-of-phase on the lee side of the Andes.

The linkages between CAI timing and frequency over long time-scales were investigated by Li and Fu (2006). Specifically, they showed how CAIs played an important role in priming the large-scale environment over the Amazon for the monsoon onset by impacting upper troposphere conditions and low level moist static energy early in the austral spring. Furthermore, they attributed monsoon onset delays to decreased CAI frequency and intensity in the transition season (September, October, November, SON). This finding was confirmed by Yin et al. (2014) who pointed out that poleward displacement of the Southern Hemisphere Subtropical Jets under global warming leads to weaker CAI activity causing late initiation of the monsoon in global climate model (GCM) simulations. Nevertheless, Yin et al. (2013) showed that GCM's handicaps in predicting fully CAI space-time features result in significant simulated rainfall bias, especially in the transition seasons, and more so in the spring (SON). In the austral winter, that is the dry season (May-September), GCM CAI climatology also points to decreases in frequency albeit accompanied by increases in intensity under global warming (Cavalcanti et al., 2013).

An open question following Li and Fu's (2006) work concerns the relative role of local and remote processes. Local processes such as multiscale land-atmosphere interactions depending on land cover and soil moisture conditions can strongly influence the development and organization of the convective activity ahead of the storm. Moreover, telecoupling to remote climatological phenomena such El Niño Southern Oscillation (ENSO) and the Southern Annular Mode (SAM) plays a role in determining favorable or unfavorable SON environmental conditions for CAI's northward propagation (e.g., Siqueira and Machado, 2004). For instance, Medvigy et al. (2012) linked CAI frequency and intensity increases in the western Amazon to deforestation. Likewise, Sun and Barros (2015a) showed that decreases in evapotranspiration from Andean forests up to mid-elevations on the eastern slopes weaken convective activity, modifying the South American Low Level Jet (LLJ), ultimately reducing upslope moisture convergence and orographic precipitation. Besides being critical to moisture recycling in the Amazon proper, evapotranspiration from forests in the Amazon foreland also plays an important role in the dynamics of regional-scale circulations that modulate the diurnal cycle of precipitation in the Andes (Sun and Barros, 2015b). How these feedbacks may be enhanced or weakened in the future due to recent evidence of shifts in forest cover along the Andes foothills is an open question (Aide et al., 2019). Understanding the interplay of large-scale circulation, regional climate, and land-use and land-cover (LULC) change from the Andes to the Amazon, and potential alterations of CAI seasonality and consequently shifts of the timing of monsoon onset requires long-term high-resolution integrated modeling and observations.

Zipser et al. (2006) investigated global storm activity based on Tropical Rainfall Measurement Mission (TRMM) satellite observations: they used the 40-dBZ reflectivity height from the TRMM Precipitation Radar (PR) measurements as an indicator of updraft strength, along with the minimum brightness temperature of precipitation features at 37 and 85 GHz, and the collocated lightning flash rates. Their study shows that the most intense, long lasting, and deepest convection in the world occurs in subtropical South America, a finding replicated by Boers et al. (2016). Rasmussen and Houze (2011) classified Andean convective activity in three types according to their morphology: deep convective cores, wide convective cores, and storms with large stratiform regions, with the second type being the most frequent in the southeastern South America at lower elevations. Due to the challenges of correcting ground-clutter contamination and the complexity of low-level stratiform precipitation systems with embedded convection, the detection and classification of shallow orographic precipitation in mountainous regions is very challenging (Prat and Barros, 2010a,b; Duan et al., 2015; Arulraj and Barros, 2017, 2019) resulting in severe underestimation of precipitation rates in the eastern Andes (Lowman and Barros, 2014). Ground-based precipitation observations are therefore key to detect and measure extreme events such as the isolated ($<$ 10 km^2) torrential event ($\sim$ 30 $mm\ hr^{-1}$ for 6 h) in the Peruvian Andes on October 4, 2013 that motivated this work (**Figure 1**).

Previous CAI studies have focused most often on CAI dynamics and cold season weather such as frost impacts. In this manuscript, the objective is to investigate the link between CAI and extreme orographic precipitation in the eastern Andes. Although a challenging endeavor due to scarce ground-based observations and remote sensing limitations, the integration of long-term reanalysis, satellite data, and rain-gauge observations enables probing the relationship between orographic precipitation extremes and CAIs in the context of regional weather and climate. Specifically, ERA-Interim reanalysis data (39 years) are used to revisit the mean structure and frequency of CAI events in the Peruvian Andes. The data and the methodology used for detecting CAI are presented in section Data and methodology, and the numerical simulations are described and examined vis-à-vis the CAI synoptic scale climatology from reanalysis in section Case study - October 4, 2013. In section Rainfall observations, long-term statistics of CAI are interpreted in the light of rainfall data in the foothills and western Amazon basin toward assessing the role of CAI on orographic precipitation climatology. Discussion and Conclusions follow in section Conclusions and Outlook.

DATA AND METHODOLOGY

Rainfall Data

A torrential rainfall event on October 4, 2013 was recorded by rain-gauges along an altitudinal transect in the Madre de Dios river basin (Barros, 2013) with up to 200 mm of rainfall measured over $\sim$6 h at the orographic maximum ($\sim$ 1,500 *m elevation*) in the eastern Andes comparable to precipitation produced by land-fallen tropical cyclones in the Atlantic Coastal Plain of the US. **Figure 1** shows the geographic setting of all rain-gauges used in this study (right panel and inset) as well as the cumulative rainfall curves (CRCs) for the rain-gauges in the Madre de Dios transect during the event. The rain-gauge locations are provided in **Table 1**.

Precipitation Features (PFs, http://atmos.tamucc.edu/trmm/data/trmm/level_2/rpf/) derived from Tropical Rainfall Measuring Mission (TRMM) measurements after Nesbitt et al. (2000) and Liu et al. (2008) are used here to determine the composite diurnal cycle of rainfall on two altitudinal bands above and below the orographic maximum ($\sim$ *1,500 m*). PFs were classified into five categories for analysis corresponding to 20, 30, 40, 50, 100 ($mm\ hr^{-1}$) average areal rain rate (volumetric rain per unit area) and maximum near surface rain rate from the TRMM 2B31 product (Tropical Rainfall Measuring Mission, 2011). Terrain elevation at the center of each of PF determines the altitudinal band to which the PF belongs for a period of record of more than 16 years (December, 1997—September, 2014). The analysis is centered in the Peruvian Andes ($9^\circ - 17^\circ S, 60^\circ - 80^\circ W$) spanning a distance of about 400 km northward and southward from the Madre de Dios network, and one of the hot-spots region identified by Chavez and Takahashi (2017).

CAI Climatology

The CAI climatology was constructed based on 39 years of European Center for Medium-Range Weather Forecasts (ECMWF) ERA-Interim reanalysis between 1979 and 2017 (Berrisford et al., 2011; Dee et al., 2011). The data consist of 60 vertical levels from the surface to 0.1 hPa with horizontal resolution of $0.75^\circ \times 0.75^\circ$ available daily at 00, 06, 12, and 18 UTC. Mean sea level pressure (MSLP), temperature at 925 hPa (T925), vertically integrated Moisture Convergence (MC) and horizontal wind and specific humidity at 12 pressure levels between 100 and 1,000 hPa (100, 200, 300, 400, 500, 600, 700, 800, 850, 900, 950, 1,000) are used in this study for CAI detection analysis following the methodology described by Garreaud (2000). First, an initial set of events is chosen based on the frequency with which the spatial average 24-h MSLP trends ($\delta MSLP$) in the region between 55.5° - 60° W and 22.50° - 27.00° S exceeds the 10th percentile of its monthly climatology. Next, to ensure the existence of a high pressure system, and therefore a cold front in the domain of study, only events for which the spatial average of *MSLP* exceeds the 10th percentile of its next-day monthly regional value are retained. The median of the time that the conditions for event detection are met is defined as day-0 and the 24 h before and after that time are defined as day-1 and day+1, respectively. For the analysis of rainfall data, the 2 day period between day-1 and day+1 is defined as a CAI event, and other times are considered as non-CAI days. Further, when the inter-event time is $<$2.5 days, only the stronger events are retained for analysis to ensure event independence. This methodology yields the detection of 726 events between 1979 and 2017.

Figure 2 shows 3 months of 24-h MSLP and MLSP trends ($\delta MSLP$), and 925 hPa-air temperature (T925) from the beginning of September until the end of November, 2013.

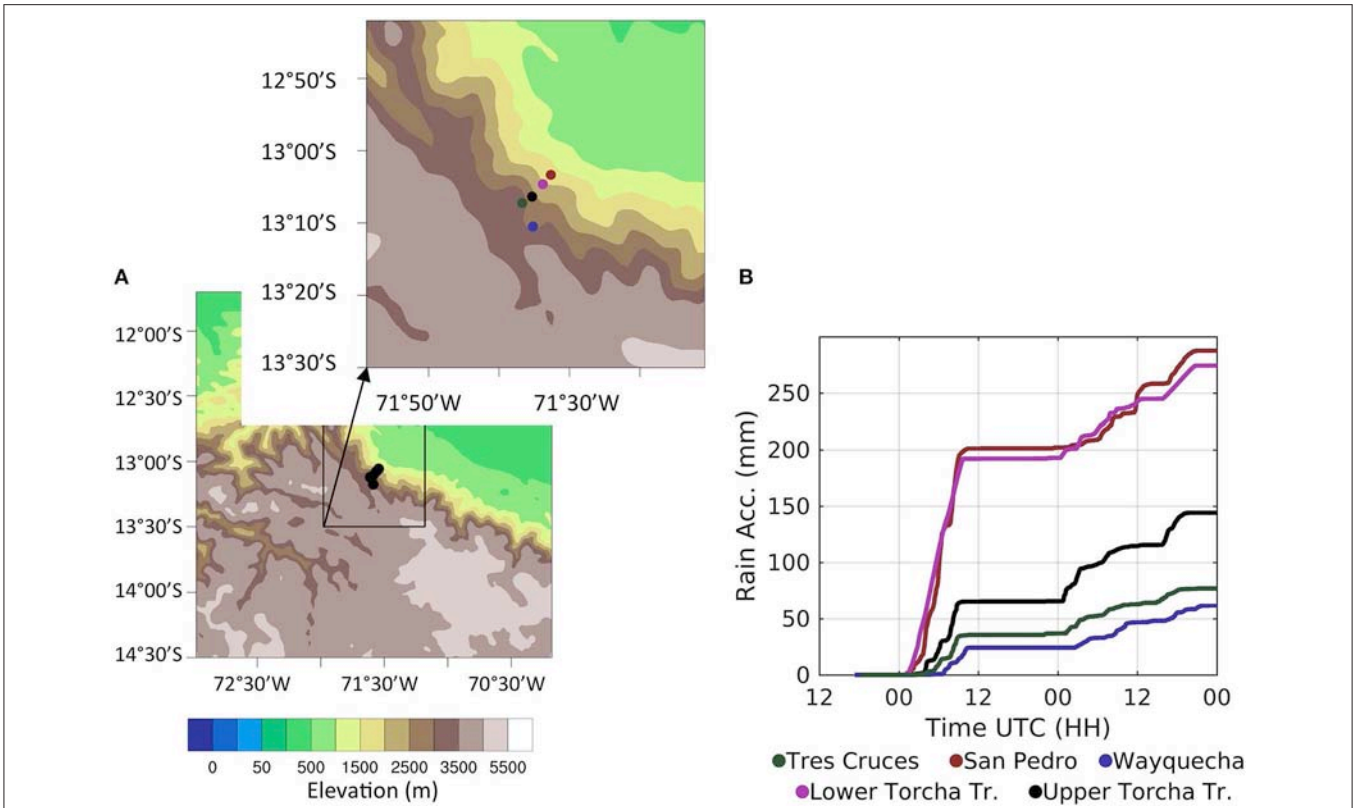

FIGURE 1 | (A) Location of the rain-gauges used in this study and Madre de Dios Transect (inset) in the Peruvian Andes. **(B)** Cumulative rainfall curves (CRCs) from 2013-10-03 12:00 Local Time (LT) to 2013-10-06 00:00 LT for all rain-gauges. The CRC color is the same as the corresponding rain-gauge mark in the inset map.

TABLE 1 | Rain gauge location and time in service.

Gauge Location	Latitude	Longitude	Elevation (m)	Period
Upper trocha	13.1062°S	71.5883°W	2,690	Nov-2011 to Oct-2017*
Posada san pedro	13.0559°S	71.5441°W	1,401	Jun-2011 to Oct-2017
Lower trocha	13.0775°S	71.5630°W	2,125	Apr-2012 to Oct-2017
Wayquecha	13.1749°S	71.5865°W	2,896	Jun-2011 to Oct-2017
Tres cruces	13.1207°S	71.6116°W	3,639	Oct-2011 to Oct 2017

**For Upper Trocha, Posada San Pedro, Lower Trocha, and Tres Cruces, 622, 189, 39, 27 days are missing.*

The seven events detected during this period are identified by vertical lines. CAI intensity expressed in terms of pressure increase and temperature drop varies significantly from event to event. In particular, note that the pressure changes for the extreme event on October 4th, 2013 are not distinct from all the others. This suggests that beyond synoptic–scale forcing, there is an important role for regional—(moisture convergence, atmospheric stability) and local-scale conditions (orographic forcing) to determine the location and magnitude of extreme events.

CASE STUDY—OCTOBER 4, 2013

Previously, moist orographic processes over the Andes were simulated using the Weather and Research Forecasting (WRF, Skamarock et al., 2008) model by Sun and Barros (2015a,b) and de la Torre et al. (2015) among others. The WRF simulation of the October 2013 event presented here relies on these and other orographic precipitation studies with regard to selection of model physical parameterizations, numerical grid design, as well as specification of initial and boundary conditions.

A 3-domain one-way nested grid is set-up (**Figure 3**) with 18, 6, and 1.2 *km* grid-spacing following Sun and Barros (2014, 2015a) who successfully investigated interactions between strong synoptic systems and complex topography. Simulations were conducted using WRF 3.8.1 to solve the non-hydrostatic and fully compressible flow equations with a 6-h spin-up time in the outer domain and one-way coupling between nested grids. The grid-spacing ratio between the outer ($D01$, 18 *km*) and intermediate ($D02$, 6 *km*) domains is 1:3 with 316 × 496 and

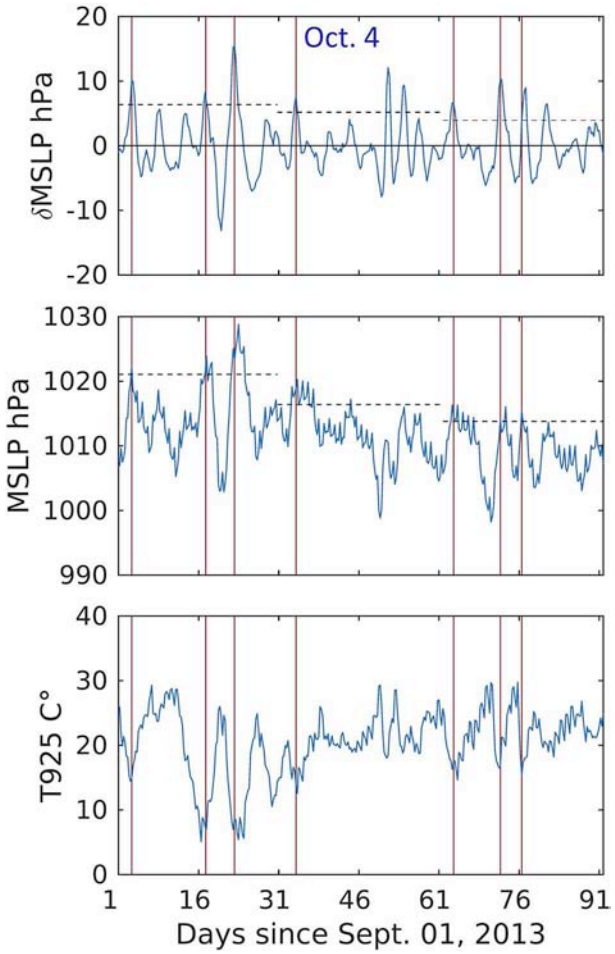

FIGURE 2 | Time series of (top) 24-h Sea Level Pressure tendencies (δ*MSLP*), (middle) averaged Sea Level Pressure (*MSLP*) and (bottom) 925-hPa air temperature averaged in the area between 55.5° - 60°*W* and 22.50°-27.00°*S* coordinates, starting from the beginning of Sept. until the end of Nov. 2013. The vertical lines mark CAI events detected during this period. The horizontal dashed lines show the monthly 10th percentile of δ*MSLP* and *MSLP* in the top and middle panels, respectively.

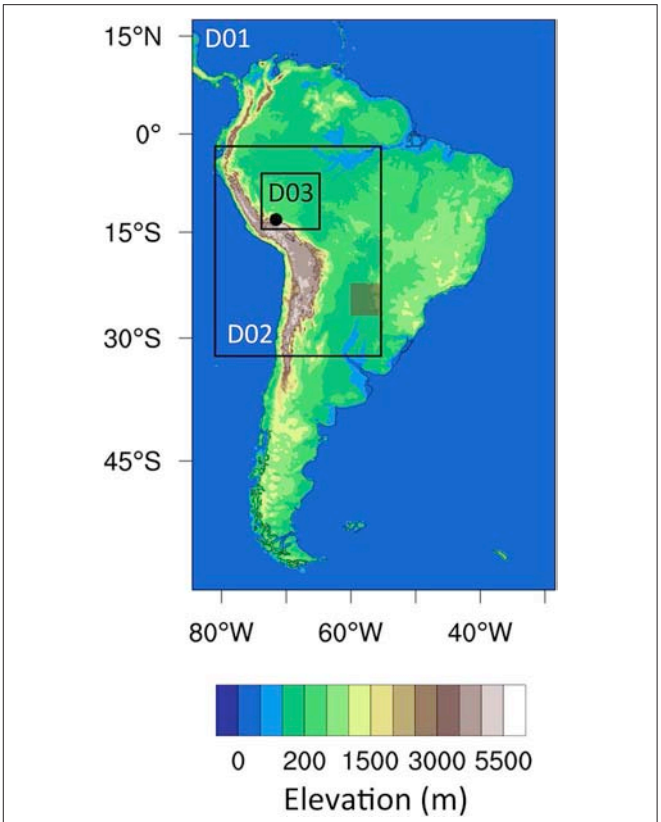

FIGURE 3 | Domain setup for numerical simulations with 3 nested domains with increasingly higher grid resolution: D01 (*18 km*), D02 (*6 km*), and D03 (*1.2 km*). The small shaded box shows the region where the ECMWF reanalysis data are used for detecting the events. The black circle marks the region highlighted in **Figure 1** where the rain-gauges are installed.

433 × 547 horizontal grid points, respectively (**Figure 3**). The grid-spacing ratio between the intermediate and inner domains (*D*03, 1.2 *km*) with 756 × 726 horizontal grid points is 1:5. All the domains have 90 vertical atmospheric layers with top at 50 hPa, and 4 soil layers. Initial and boundary conditions are extracted from the National Centers for Environmental Prediction Final Operational Global Analysis (NCEP-FNL) available at 1° × 1° resolution every 6 h (Kalnay et al., 1996) with 26 vertical layers between 1,000 to 10 hPa in addition to the surface layer following Sun and Barros (2015a,b).

The selection of physical parameterizations was informed by recent studies of orographic precipitation (e.g., Wilson and Barros, 2015, 2017) and includes the Mellor–Yamada–Nakanishi–Niino (MYNN level 2.5; Nakanishi and Niino, 2006) planetary boundary layer scheme, the Milbrandt microphysics scheme (Milbrandt and Yau, 2005a,b), and the Noah land surface model (Ek et al., 2003). The Rapid Radiative Transfer Model (RRTM) (Mlawer et al., 1997) and the Dudhia scheme (Dudhia, 1989) are used to describe longwave and shortwave radiation at 1-min intervals. The Kain-Fritsch cumulus parameterization (Kain, 2004) scheme is applied in the outer and intermediate domains, whereas in the inner domain, convective processes are explicitly resolved.

Figure 4 shows simulated fields of MSLP, and 850 hPa winds and geopotential heights every 6 h starting on October 3 at 06Z. Synoptic scale context is provided by movies of the evolution of 500 and 850 hPa geopotential heights and winds in **Supplemental Informations S1a,b**. For reference, composite *MSLP*, and 850 hPa level horizontal winds for all CAI events in the austral spring (September, October, and November, SON) 1979–2017 are also provided for day-1, day-0, and day+1 (**Supplemental Information S1c**). The main driver of the October 2013 event is the migratory high-pressure system that moves eastward from the South Pacific associated with eastward mid-latitude wave propagation along the subtropical jet consistent with climatology (e.g., Garreaud, 2009). The large-scale structure shows poleward orientation of mid-latitude trajectories west of south SA due to orographic blocking by the Andes (**Supplemental Informations S1a,b**). The MSLP of the

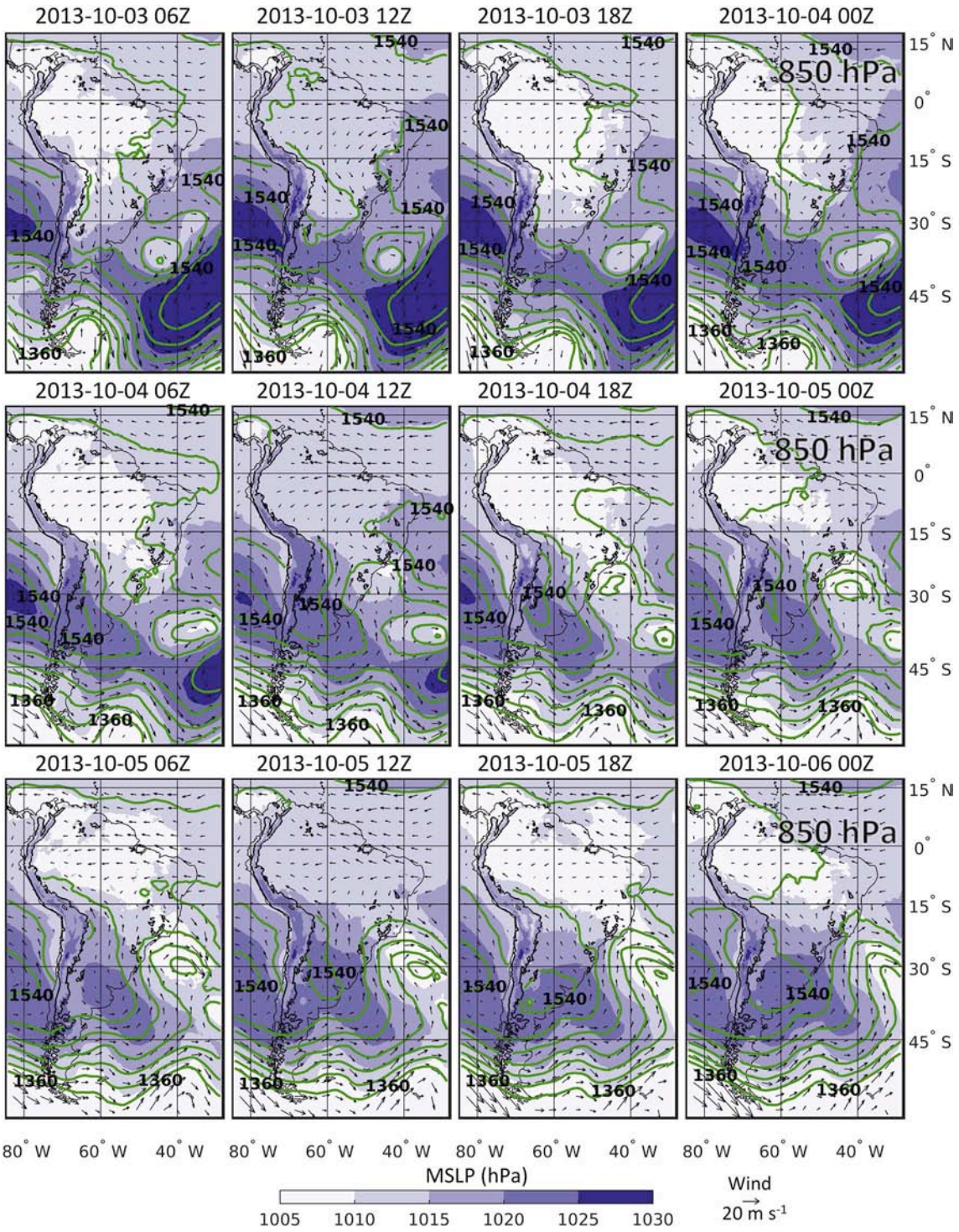

FIGURE 4 | WRF simulation (*D*01, 18 *km*) of the October 4, 2013 CAI case study. The maps show Mean Sea Level Pressure (*MSLP*, shaded), 850 hPa level horizontal winds (arrows), and 850 hPa geopotential heights (green contours, 30 m interval) every 6 h starting on October 3 at 06Z. The black contour line shows the 2000 *m* elevation.

case study is about 5 hPa lower than climatology in the subtropics both for the day before (day-1) and the day of the event (day-0), which is favorable to convective activity. More interestingly, early on in the development of the October 4, 2013 event (day-1), a strong high-pressure system is present in the South Atlantic (∼ 40°W, 50°S) that forms a stationary mid-latitude dipole with a

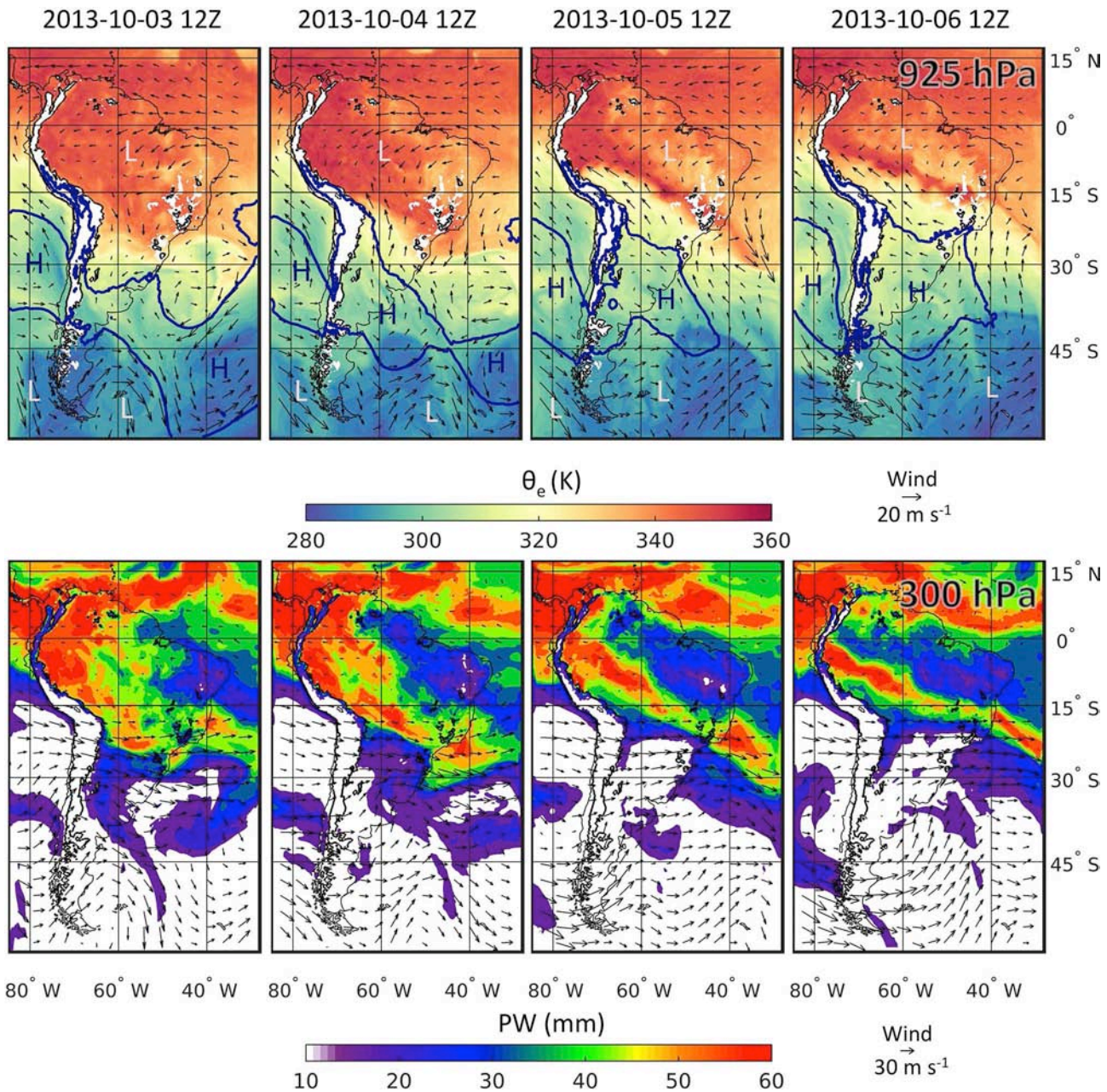

FIGURE 5 | WRF simulation (*D*01, 18 *km*) of the CAI event on October 3–7, 2013. Top row shows the equivalent potential temperature and 925 hPa level horizontal wind fields. The blue contour line delineates the 1,020 hPa sea level pressure. Areas of high and low pressure are marked with H and L, respectively. Bottom row shows the Precipitable Water (PW) overlain on the 300 hPa level horizontal wind fields. A movie showing the temporal evolution of PW during the event duration is available as **Supplemental Information S2**.

low pressure center to the north (∼40°S) at the same longitude. The dipole moves slowly eastward after 18Z on day-1 (October 3) and is out of the domain by day+1 (October 5). As the westerly migratory high-pressure system moves over the Andes (∼ 45°*S*), atmospheric blocking by the mid-latitude pressure dipole enhances counterclockwise geostrophic circulation on the lee-side of the Andes, thus favoring the development of a mid-latitude anticyclone confined to continental SA (∼60°*W*). Orographic blocking in the lower troposphere (< 700 hPa) to the west along the eastern slopes of the Andes forces the development of ageostrophic southerly winds pushing CAI that are further enhanced by cyclonic circulation over the Rio de la Plata (∼55°W, 35°S) on day-0 and into day+1. Persistent southerly winds during this period reach the tropics fueling convective activity along the frontal boundary between the CAI air mass and warm moist tropical air well into day+2 (October

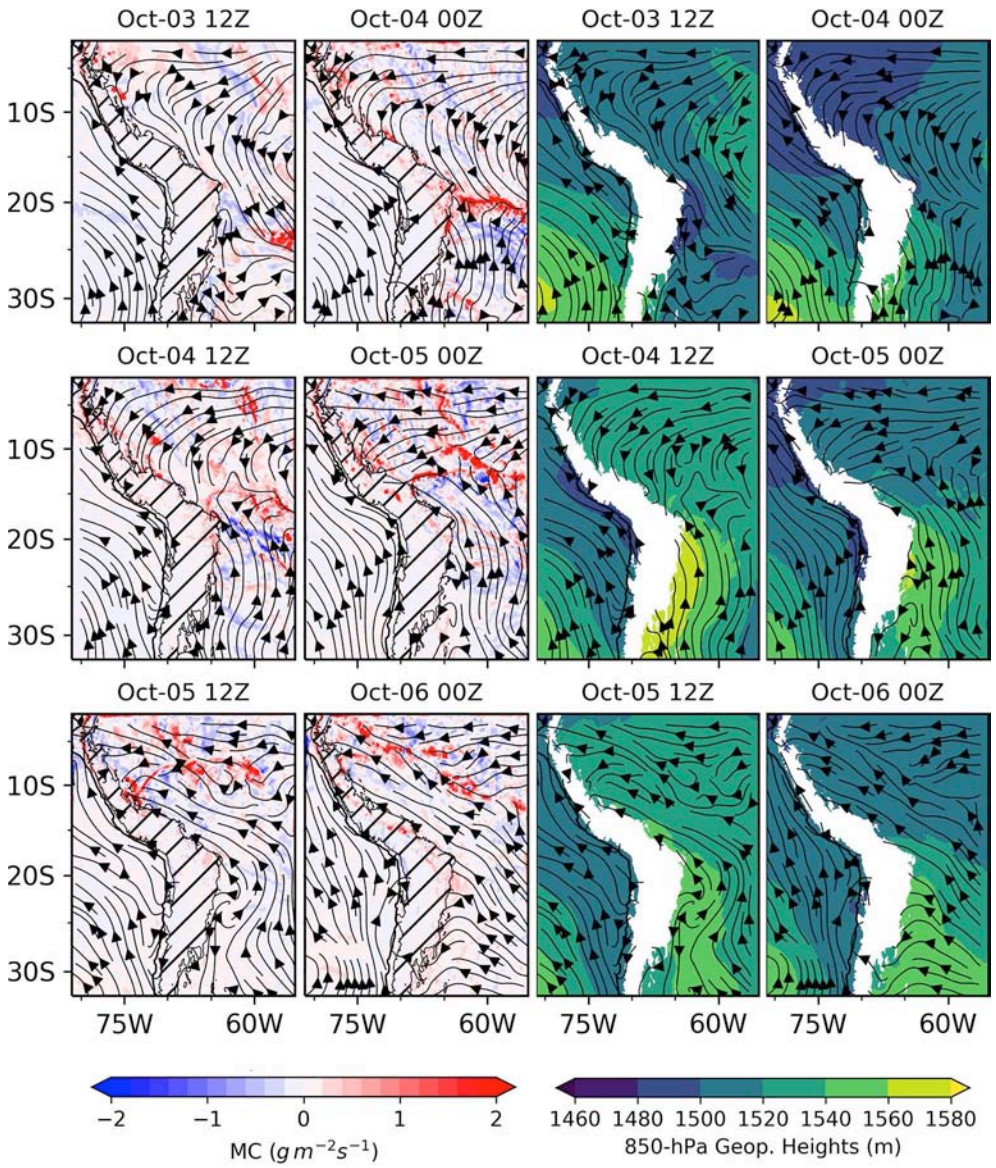

FIGURE 6 | WRF simulation (*D*02, 6 *km*) of the CAI event on October 3–7, 2013. The first two columns show the integrated moisture convergence (MC) and 850 *hPa* level horizontal wind streamlines. The 1500 *m* orography is shown by southwest-northeast hatching. The second two columns show the 850 *hPa* level geopotential heights and horizontal wind streamlines. The white region is the area with pressures lower than 850 *hPa*.

6, **Figure 4**). After the high-pressure system passes over the mountains, regional circulation changes returning to non-CAI conditions with northerly winds toward the South Atlantic Convergence Zone (SACZ) by day+3 (October 7, not shown).

Figure 5 shows the simulated synoptic scale evolution of near the surface equivalent potential temperature (925 *hPa*) and Precipitable Water (PW) fields overlain the 300 hPa winds every 24 h October 3–7, 2013. There is a large contrast between very high PW (>50 mm) over the Amazon due to easterly advection of warm moist air from the tropical Atlantic and that piles up against the eastern Andes initially (bottom row, left panels) and subsequently becomes organized ahead of the CAI front, and PW (< 20 mm) in southern SA associated with low level cold advection behind the front. Easterly moisture transport from the Atlantic piles unstable moist air (60 mm PW) against the terrain ahead of the CAI front north of 15°*S* as it can be seen from the co-evolution of PW and 850 hPa winds (**Supplemental Information S2**).

The mesoscale evolution of the storm described by the vertically integrated Moisture Convergence ($MC = -\nabla \cdot \frac{1}{g}\int qUdp$, where q is specific humidity and U is horizontal wind, p is pressure and g is the acceleration due to gravity), geopotential heights and horizontal winds at 850 *hPa* is presented in **Figure 6**. Initially, regional conditions are consistent with the

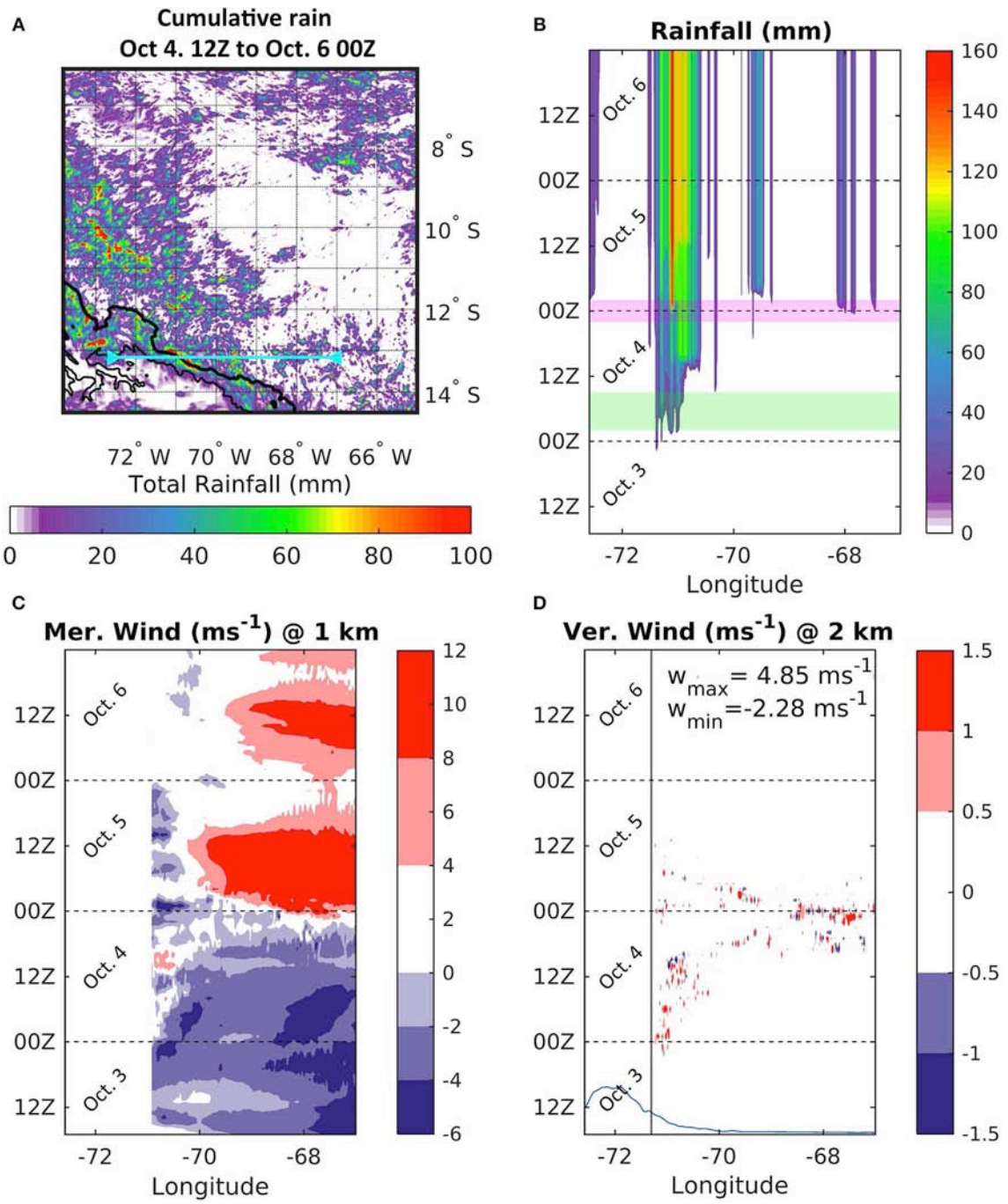

FIGURE 7 | (A) Simulated cumulative rainfall from the high resolution domain (*D*03, 1.2 *km*) between Oct. 4, 12Z and Oct. 6, 00Z, 2013. The thick and thin black contour lines show the 1 *km* and 3.5 *km* topographic elevations, respectively; the cyan straight horizontal line marks the cross-section used in **(B–D)**. **(B)** Total cumulative rainfall in the cross section, purple shading in **(B)** indicates time of maximum rainfall intensity in model simulations, green shading in **(B)** indicates time of maximum rainfall intensity in the Madre de Dios network; **(C)** longitude-time diagram of meridional wind interpolated to 1 *km* AMSL; and **(D)** longitude-time diagram of vertical wind at 2 *km* AMSL. Blue line in **(D)** represents the terrain cross-section, and the black line is marked on the 2 *km* elevation contour.

typical wind patterns associated with the SACZ with streamlines in the NE-SE direction (Oct-03, 12Z). The color-scale is chosen to show the average behavior of MC. However, the maximum values can locally assume values as high as 30 ($g\ m^{-2}\ s^{-1}$). Note evidence of a low-level mesoscale cyclonic vortex centered at 25°*S* and 65°*W* (consistent with the NAL) and high-pressure to the right (top row). Blocking of the easterly geostrophic flow as discussed above in the context of **Figure 4** forces the alignment of northward low level flow along the eastern Andes, and the development of a cold front (e.g., the CAI front) as southerly air

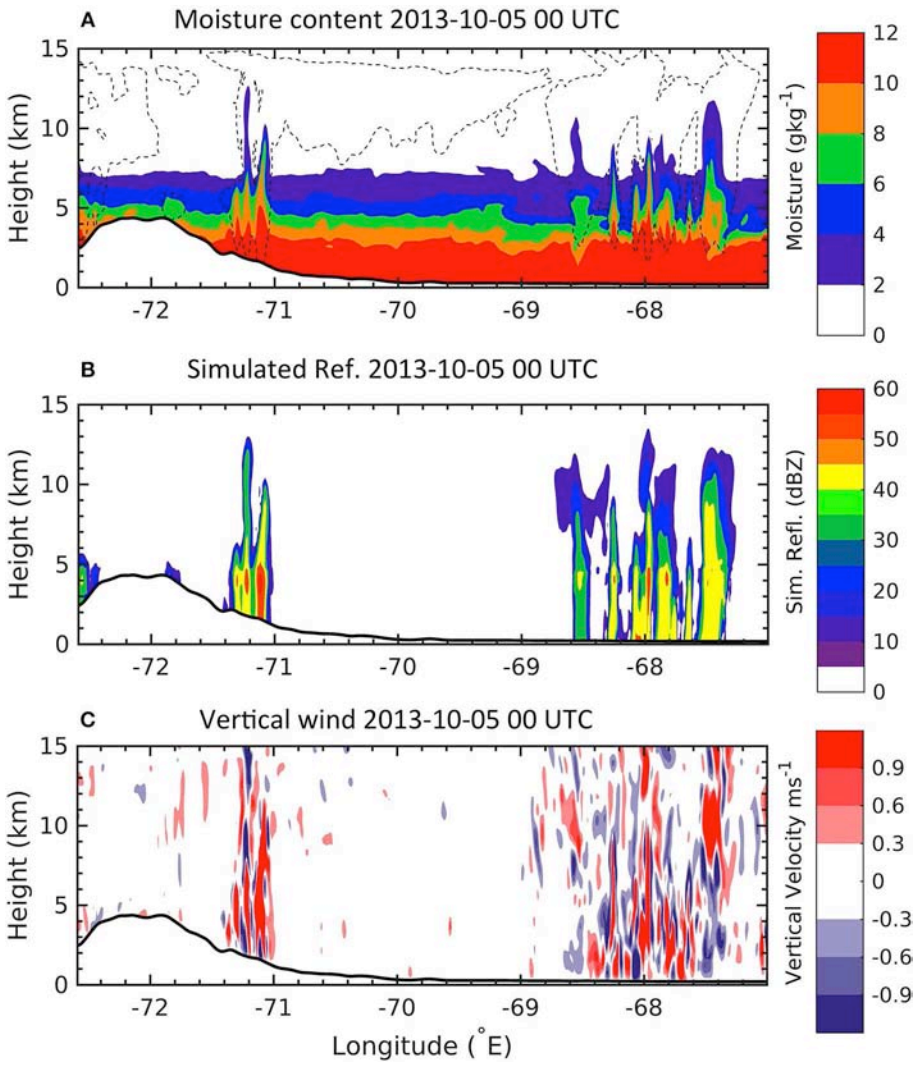

FIGURE 8 | Cross section of **(A)** moisture content and frozen hydrometeors **(B)** simulated reflectivity and **(C)** vertical velocities at 2013-10-05 00:00 UTC. The dashed contour lines in **(A)** show the $3 \times 10^{-3} gkg^{-1}$ value of frozen phases. The cross section is shown in **Figure 7A** with cyan line at 13.16°S.

interacts with tropical moist air. Behind the front, an orographic blocking high forms in the subtropics that expands northward and strengthens with time eventually reaching the tropics in day-0 and into day+1.The cold front propagates northward reaching the subtropics (Oct-04, 00Z) with a well-defined region of strong convergence forming ahead of the cold front consistent with the PW patterns in **Figure 5**. The leading moist convergence zone (MCZ) advances with the CAI front along the Andes until it reaches ∼6°S (Oct-06, 00Z).

Figure 7 shows the spatial distribution of simulated rainfall **(Figures 7A,B)** in the inner domain just as the CAI reaches its northernmost excursion and begins to retreat as per the meridional wind changes in **Figure 7C**. The model predicts localized precipitation accumulations of up to 172 mm **(Figure 7B)** against the 1,000 m elevation contour along a cross-section (cyan) at the latitude of the raingauge network in **Figure 1**. Note the rapid change in rainfall accumulations in **Figure 7B** from 50 to 160 mm over a period of 6 h as the CAI front arrives. **Figure 7C** suggests that low level northerly meridional winds are blocked by the terrain and by the southerly cold front over the low topography of the Amazon foreland basin. This blocking effect and change in wind regime that is accompanied by moisture convergence ahead of the storm can also be seen in **Figure 6** (starting from Oct-4, 00Z). Convection initiates where northerly warm moist air piles against the terrain forcing localized upward motion to develop in the lower 1-2 km AMSL (2 km AMSL shown in **Figure 7D**; negligible at 1 km AMSL, not shown) producing heavy precipitation (purple shade in **Figure 7B**). Simulated updrafts can reach 35 $m\ s^{-1}$ at higher altitudes ($10 - 15\ km$). The model captures rainfall initiation with a 12–24 h delay in peak rainfall intensity relative to the Madre de Dios network (approximate time difference between

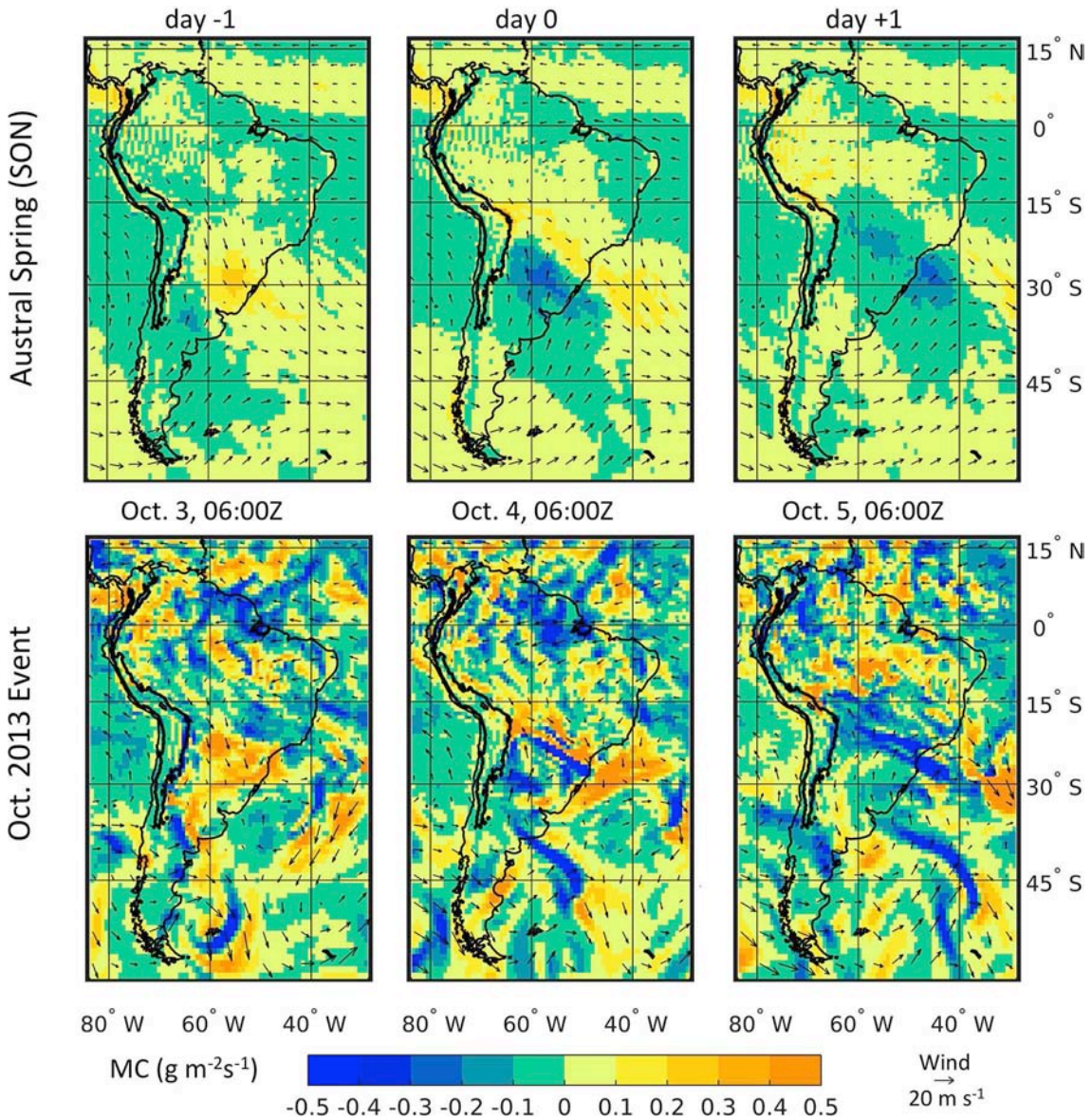

FIGURE 9 | Top row: Composite vertically integrated Moisture Convergence (*MC*) patterns overlain on 850 hPa horizontal winds in the austral spring (SON) between 1979 and 2017 from ERA-Interim. The black contour line marks the 2000 *m* elevation. Bottom row: similar plots for the case-study CAI.

purple and green shades in **Figure 7B**), but well within the time of arrival and movement of the CAI front along the Central Andes hot-spot region. Simulated rainfall intensities (*1.2 km* grid-spacing) are 3–4 times lower than rain-gauges (point scale), with rainfall occurring intermittently throughout the day in contrast with the observations that exhibit a mid-day rainfall break. Overall, the simulated rainfall accumulations at 1,500 m elevation vary between 131 and 172 mm in contrast with accumulations of 270–280 mm measured by the rain-gauges (**Figure 1**). Nevertheless, the spatial organization of simulated precipitation (**Figure 7A**) is consistent overall with the spatial distribution of precipitation features from the TRMM satellite climatology along the eastern slopes of the Andes with negligible precipitation or very light rainfall at higher elevations above the tree line (e.g., ∼3,500 m) along the headwaters of the Amazon basin (Lowman and Barros, 2014).

The vertical distribution of moisture content and frozen hydrometeors **(Figure 8A)**, simulated reflectivity **(Figure 8B),** and vertical winds **(Figure 8C)** are shown in **Figure 8** for the period of maximum simulated rainfall intensity along the cross-section marked in **Figure 7A**. The moisture content is the sum of water vapor, rain water, cloud water, and frozen phase (ice, snow, graupel, and hail) mixing ratios. The contour lines highlight the spatial distribution of frozen hydrometeors as a proxy for convective activity that extends to the higher levels in the atmosphere. Note the spatial alignment of high

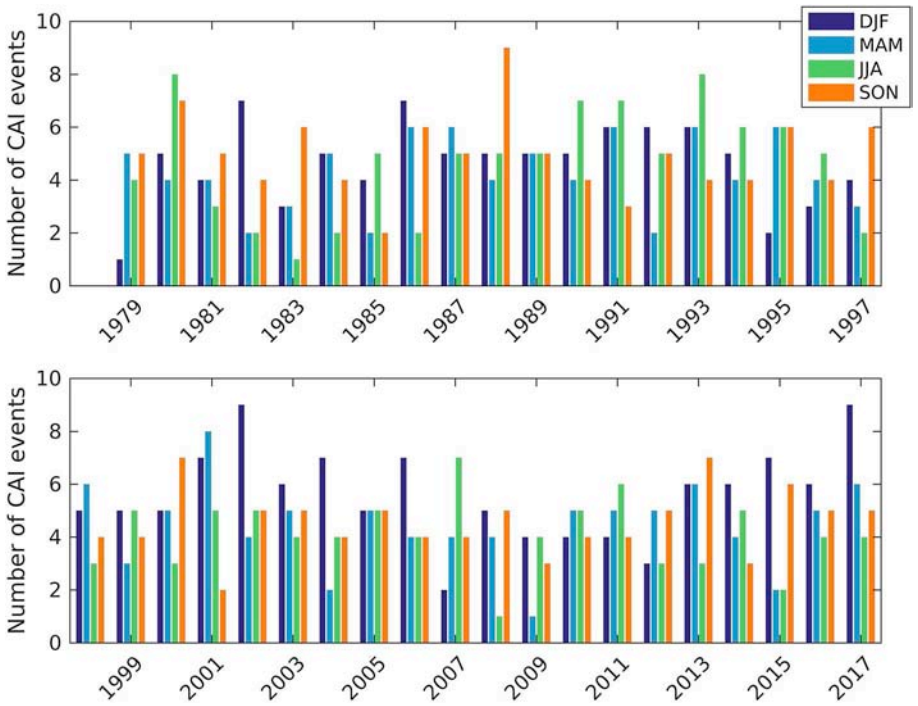

FIGURE 10 | Seasonal time series of CAI events detected from ERA-Interim data 1979–2017 for the eastern side of the Andes cordillera.

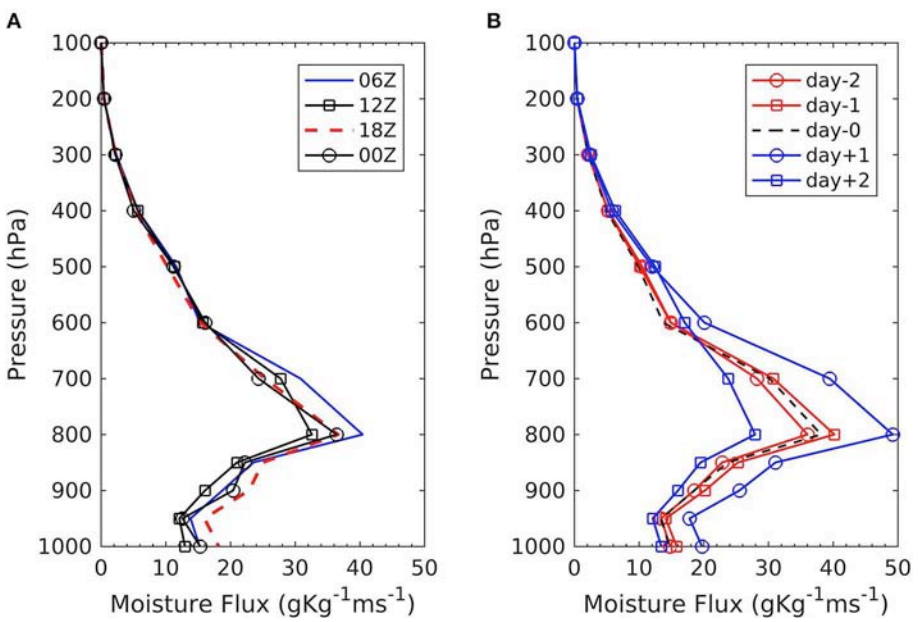

FIGURE 11 | Vertical profile of moisture flux ($q \times \sqrt{u^2 + v^2}$) from ERA-Interim: **(A)** climatological values at different times of the day **(B)** during CAI in September-October-November (SON) at (71.25°W, 12.75°S).

reflectivity cores of heavy precipitation (reflectivity up to 60 dBZ at 5 km AMSL) with the updrafts and downdrafts associated with localized orographic convection at mid-elevations (< 2 km) over the eastern slopes of the Andes. Furthermore, the region of well-developed convection to the east over the low topography of the Amazon is consistent with the position of the front and the spatial distribution of precipitable water (PW) west of 60°W in **Figure 5**. Orographic convection initiation takes place at the

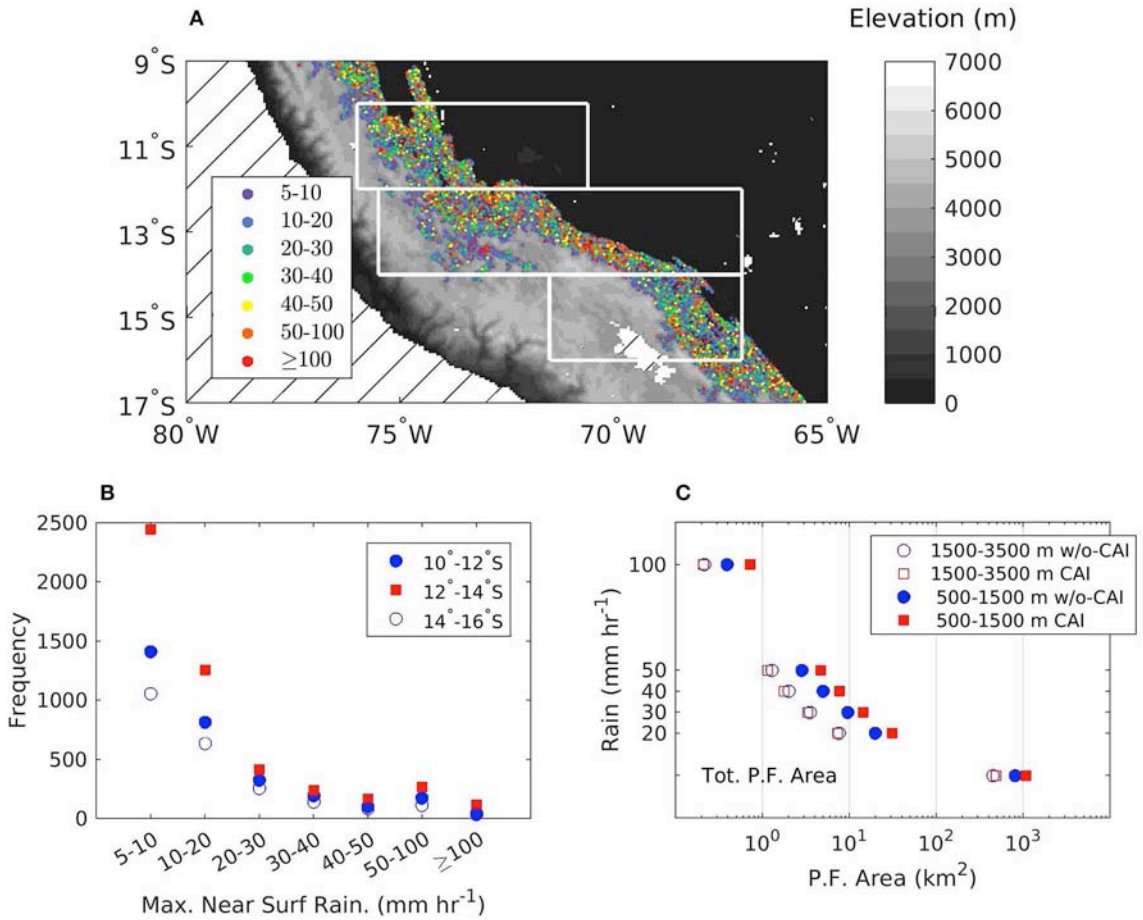

FIGURE 12 | (A) Map of maximum near surface rain rate for the 16-year composite of TRMM Precipitation Features discussed in section Data and methodology overlaying the topography of the Central Andes and adjacent regions. The white boxes delimit three latitude bands including the Andes hot-spot area (central box, also the Madre de Dios rain-gauge network **Figure 1**) used for analysis in **Figure 13**. **(B)** The frequency of TRMM PFs binned with maximum near-surface rainfall rates for each latitude band. **(C)** Distribution of PF areal extent as a function of average rainfall rate for two elevation bands with and without CAI conditions.

geographic intersection of the cold front with the terrain. This enhances localized low level stationary blocking by the terrain inducing a sloshing-like behavior along the front and spatially and temporally intermittent convective activity (**Figure 7B**). The convective cores shown in **Figure 8** move zonally up and down (back-and-forth) along the slopes of the Andes and into the Amazon foreland throughout the day. The peak of simulated rainfall is delayed until the CAI frontal boundary pushes northward beyond the reference cross-section in **Figure 7** with localized rainfall intensification tied to on-and-off convective activity against the terrain. The development of terrain-following convective activity along the CAI trajectory against the eastern slopes of the Peruvian Andes is in keeping with the spatial layout of precipitation hot-spots mapped by Chavez and Takahashi (2017) along elevation bands suitable for optimum orographic enhancement of precipitation (e.g., Sun and Barros, 2015a,b). Easterly moisture transport from the Atlantic piles unstable moist air (60 mm PW) against the terrain ahead of the CAI front north of 15°*S* as it can be seen from the co-evolution of PW and 850 hPa winds (**Supplemental Information S2**). Consumption of low level entropy supports upslope flow and enables convective initiation at elevations 1–2 km at the intersection of the terrain and the CAI front that results in the highly localized precipitation features in **Figures 7**, **8**.

Figure 9 contrasts the mean structure of vertically integrated Moisture Convergence (MC) from reanalysis for austral spring (SON, top row) CAIs with simulated MC for the October 2013 event (bottom rows, see also **Figure 6**). Before the event begins (day-1, **Figure 4**) the convective area extends to the subtropics along with northwesterly winds associated to the SACZ. In the second day (day-0), MC from the Amazon and the tropical Atlantic is organized ahead of the CAI front with divergence trailing behind it. This large-scale arrangement maintains the spatial pattern and magnitude of tropical moisture convergence against the mountains before it detaches in the eastern Andes of Bolivia and turns southeastward guided by the CAI front. During day-0, the MCZ moves with the frontal boundary as it progresses northward while easterly winds weaken in the western

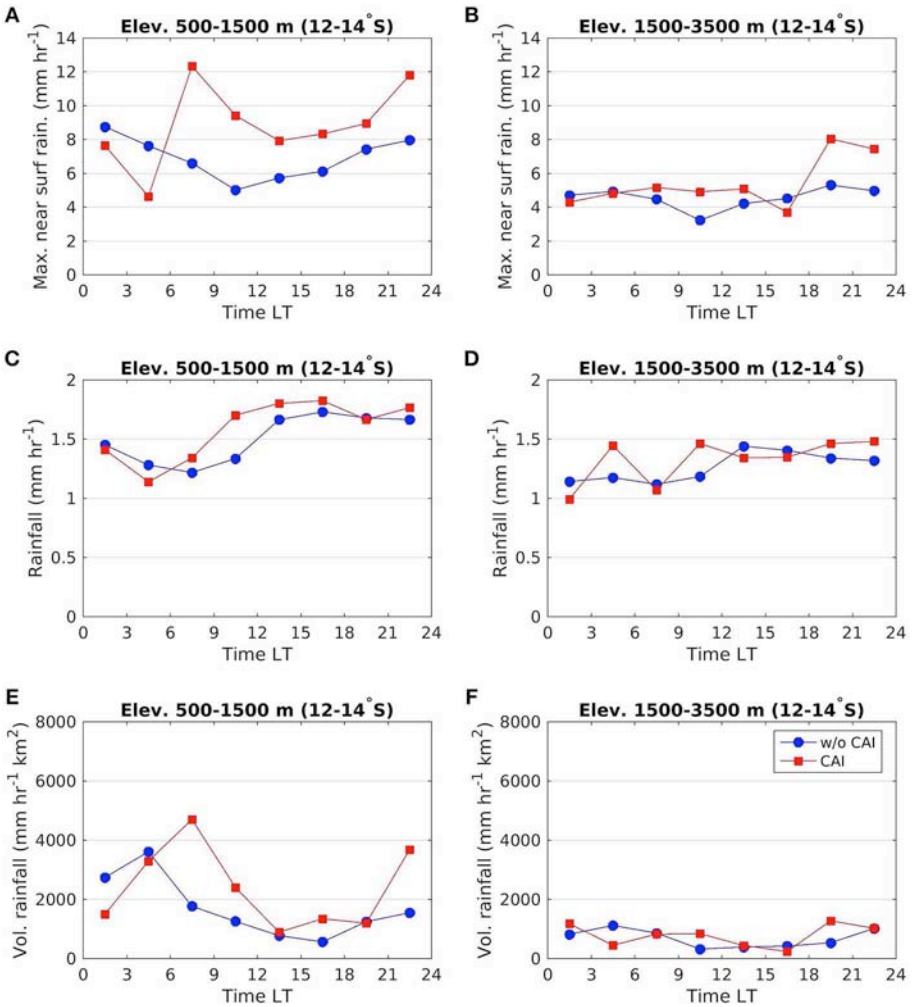

FIGURE 13 | Diurnal cycle of **(A,B)** maximum near surface rain, **(C,D)** spatially averaged rain, and **(E,F)** volumetric rain associated with TRMM PFs over the Andes during ONDJFM between 12° and 14°*S* latitude (see **Figure 12**) for two elevation bands 500–1,500 m and 1,500–3,500 m. Circles show non-CAI climatology. Squares show the mean values between 1 day before (day-1) and 1 day after (day+1) the detected CAI events according to the methodology described in section Data and methodology.

Amazon basin. Day+1 circulation features are similar for the SON composite and the simulated event. Over northern SA, the wind fields are generally much weaker than climatology, with weak low level jet (WLLJ) conditions that favor MC and accumulation of moist unstable warm air ahead of the front, thus favorable to high precipitation in the Central Andes hot-spot region (Sun and Barros, 2015a,b; Chavez and Takahashi, 2017).

RAINFALL OBSERVATIONS

In this section long-term statistics of CAI from reanalysis are interpreted in the context of rainfall measurements in the foothills and western Amazon basin.

The season time series of detected CAI events using the pressure data from ERA reanalysis is presented in **Figure 10**. The data show high-frequency of CAI in all seasons, albeit with large inter-annual variability. Interestingly, the range of inter-annual variability is higher in the austral summer (DJF) and fall (MAM) seasons compared to winter (JJA) and spring (SON) with increased summer activity in the last two decades. The reliability of CAI in the spring (SON) supports the argument for their important role in providing antecedent precipitation and atmospheric humidity necessary to condition the atmosphere for the monsoon season (Li and Fu, 2006; Yin et al., 2013, 2014).

The vertical profile of southerly moisture flux at an ERA-Interim grid-point in the Peruvian Andes close to the rain-gauge network used here (71.25°*W*, 12.75°*S*) is shown in **Figure 11**. Note how the average moisture flux significantly increases on day+1 (**Figure 11B**) compared to the average daily values for non-CAI conditions (**Figure 11A**), especially between ∼800 and 600 hPa where most precipitation is produced. The maximum moisture flux is concurrent with

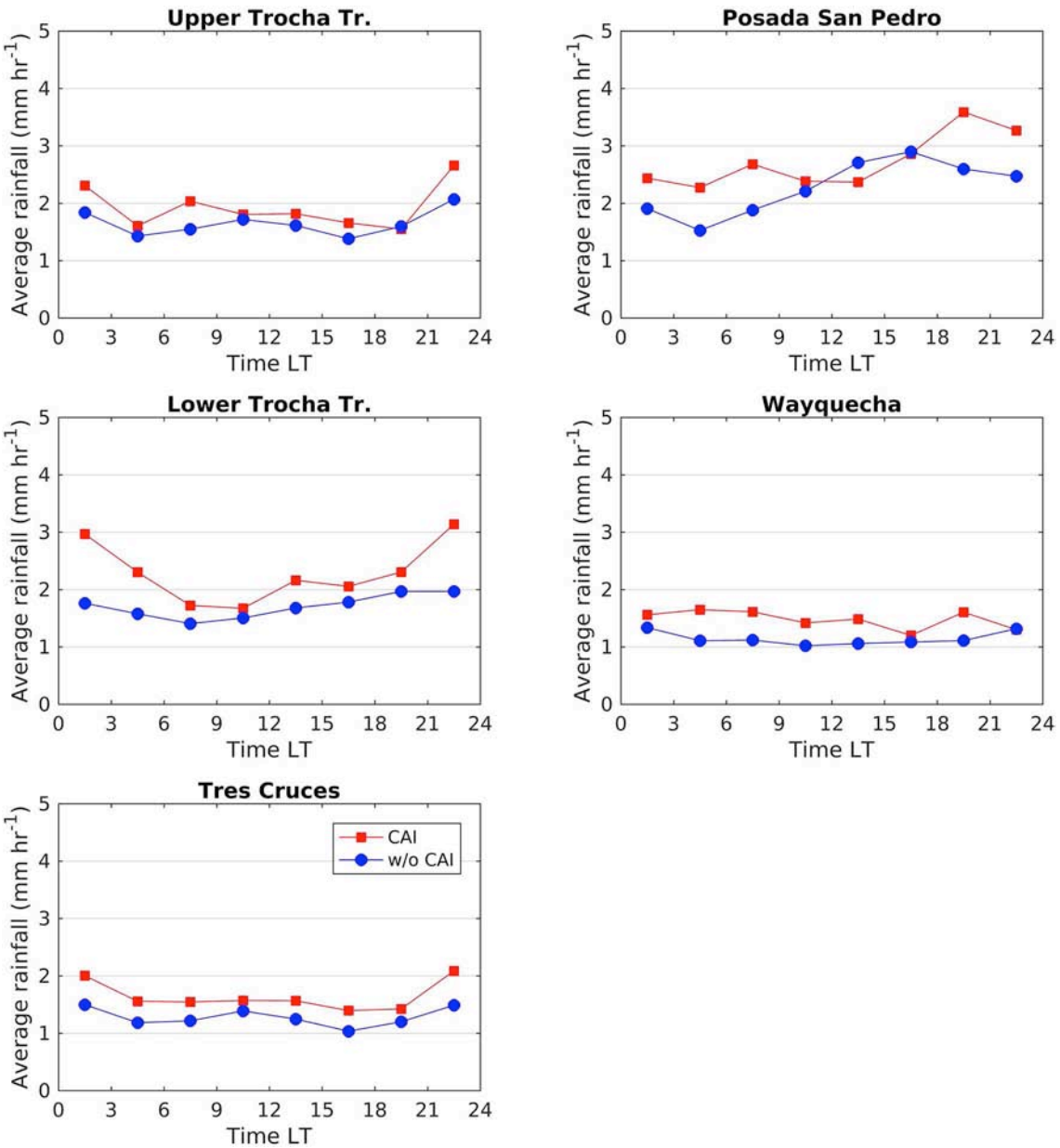

FIGURE 14 | Diurnal cycle of mean rainfall intensity from five gauges in the Madre de Dios network from April 2012–2017. Mean value calculations do not include times without rain. Circles show non-CAI climatology and squares show the mean values between 1 day before and after the detected CAI events.

CAI progression northward along the slopes of the eastern Andes to reach the rain-gauge network latitude in day+1 consistent with the simulation of the October 2013 CAI event (see **Figure 6**).

Figure 13 shows the diurnal cycle of rainfall metrics obtained from TRMM precipitation features below and above 1,500 *m* terrain elevation in the Peruvian Andes hot-spot region [12° − 14°*S*, **Figure 12**] for different elevation bands between December, 1997 and September, 2014 for CAI and non-CAI days, during the extended spring-summer rainy season (ONDJFM). The diurnal cycle of CAI maximum rainfall intensity shows increases up to 100% (**Figure 13A**) and higher values of volumetric rainfall (**Figure 13E**) in the early morning compared to non-CAI conditions in the orographic envelope between 500 and 1,500 m. The early morning peak in the *500–1,500 m* elevation band is consistent with findings by Giovannettone and Barros (2009) who showed that nighttime and early morning convection in the central Andes is constrained to low elevations including inner mountain valleys and the foothills. This suggests enhancement of interactions among cold air pooling processes and low-level convergence of warm moist air at the CAI frontal boundary. Because TRMM products severely

underestimate orographic precipitation (e.g., Prat and Barros, 2010a,b; Duan et al., 2015), the CAI signal on rainfall is likely underestimated (**Figures 13C,D**). The coefficients of variation (not shown) are similar for CAI and non-CAI conditions during the TRMM period of record with high values (2–3) for the near surface maximum rainfall and low (<1) for the areal average rain rate. Coefficients of variation are very high for volumetric rainfall as expected because of large event-to-event variability in convective activity, and thus rainfall intensity, as well as areal extent, and more so at higher elevations for non-CAI conditions reflecting the decrease in rainfall frequency and amount with altitude above the orographic precipitation maximum.

Likewise, the diurnal cycle of rainfall at the gauges on the Madre de Dios altitudinal transect corresponding to 100 CAI events (during the period of record) is presented in **Figure 14**. Although each station shows a different diurnal cycle, there is a systematic increase of the rainfall intensity at all times of the day in all seasons during CAI events with maximum enhancement at San Pedro ($\sim 1,500\ m$). The rainfall enhancement at Tres Cruces is remarkable given that this gauge is located at very high elevation above the tree line in the inner region of the Central Andes, which indicates for the first time that CAI events may play an important role in the water cycle of puna ecosystems in the High Andes beyond the negative impacts of frost reported in the literature. This implies that sustainability of puna ecosystems may be tied at least in part to the reliability of CAI activity. Note the significant difference in the spatial representativeness gap between the rain-gauge data (point scale) and the TRMM PFs (pixel scale $\sim 25\ km^2$). Consequently, to enable interpretation and analysis, it is proposed that the diurnal cycle of orographic rainfall by altitude based on TRMM PFs captures the most frequent timing of maximum rainfall during CAI events, whereas the raingauges capture significant localized enhancement of orographic precipitation by a factor of about 2 during CAI events.

CONCLUSIONS AND OUTLOOK

Cold Air Intrusions are a key synoptic scale feature of South American climate and weather. In the present study, *in situ* rainfall measurements are used for the first time together with the longest period of available climatology from ECMWF ERA-Interim reanalysis (1979–2017) to investigate the connection between the CAI and orographic precipitation on the eastern flanks of the tropical Andes. An extreme precipitation event in October 2013 was selected for simulation and analysis. The simulated synoptic scale structure agrees well with the classic definition of CAI in previous studies. The model, although underestimating the rainfall amounts and intensities, produces the extreme localized rainfall patterns near the orographic maximum ($\sim$ *1,000–2,000 m*) in the Central Andes suggested by the raingauge measurements for this case study. A careful study of the vertical structure of atmospheric moisture content and vertical winds shows strong shallow convection associated with high values of precipitation at the intersection of the CAI front with the Andes terrain explaining the localized enhancement of surface rainfall. The trajectory of shallow convection following the terrain as the CAI front propagates northward is in agreement with the orographic precipitation maximum on the Andes slopes inferred from rain-gauge observations, and the hot-spot clusters of precipitation features from satellite observations). The reanalysis climatology reveals that the moisture flux increases significantly at all heights during CAI events with a maximum of up to 50% between 800 and 600 hPa. The enhanced moisture flux is necessary to sustain strong shallow convection that translates into increased rainfall intensity and accumulations on the eastern slopes of Andes ($\sim\ 1000 - 2000\ km$) in TRMM products and *in situ* measurements. Specifically, analysis of the rain-gauge data shows strong precipitation enhancement (up to 100%) tied to CAI events. This behavior is also evident in the climatology of TRMM precipitation features that show enhancement of precipitation up to 100% in the early morning in the Peruvian Andes tied to enhance convective activity at low elevations. The multi-decadal record of CAI events derived from ERA-Interim indicates that CAIs are year-round phenomena, with frequency, intensity, and latitudinal excursion amplitude that exhibit variability at both seasonal and inter-annual scales. Nevertheless, reliability of CAI events in the spring season supports the notion that CAI precipitation makes an important contribution to priming the low-level troposphere over the Amazon basin prior to monsoon onset similar to previous studies. Localized very high orographic rainfall intensity in the region of study drives regional landslide activity consistent with the association of landform, precipitation, and erosion in the region of study.

AUTHOR CONTRIBUTIONS

AB proposed the research idea and the research plan. ME implemented the research plan, performed the WRF simulations, and conducted the climatology analysis and interpretation of the results under the guidance of the AB. The two authors worked collaboratively in the preparation of the manuscript.

ACKNOWLEDGMENTS

We would like to acknowledge high-performance computing support from Yellowstone (http://n2t.net/ark:/85065/d7wd3xhc) provided by NCAR's Computational and Information Systems Laboratory, sponsored by the National Science Foundation. We thank two Reviewers for helpful comments and constructive suggestions. This research was funded by NASA grant NNX16AL16G and NSF EAR0711430 with AB.

SUPPLEMENTARY MATERIAL

The Supplementary Material for this article can be found online at: https://www.frontiersin.org/articles/10.3389/fenvs.2019.00101/full#supplementary-material

REFERENCES

Aide, T. M., Grau, H. R., Graesser, J., Andrade-Nunez, M. J., Araoz, E., Barros, A., et al. (2019). Woody vegetation dynamics in the tropical and subtropical Andes from 2001 to 2014: the impacts of land use change and climate. *Glob. Change Biol.* 25, 2112–2116. doi: 10.1111/gcb.14618

Anabor, V., Stensrud, D. J., and de Moraes, O. L. L. (2008). Serial upstream-propagating mesoscale convective system events over southeastern South America. *Monthly Weather Rev.* 136, 3087–3105. doi: 10.1175/2007MWR2334.1

Arulraj, M., and Barros, A. P. (2017). Shallow precipitation detection and classification using multifrequency radar observations and model simulations. *J. Atmosphere. Oceanic Technol.* 34, 1963–1983. doi: 10.1175/JTECH-D-17-0060.1

Arulraj, M., and Barros, A. P. (2019). Improving quantitative precipitation estimates in mountainous regions by modelling low-level seeder-feeder interactions constrained by Global Precipitation Measurement Dual-frequency Precipitation Radar measurements. *Remote Sens. Environ.* 231:111213. doi: 10.1016/j.rse.2019.111213

Barros, A. P. (2013). "Orographic precipitation, freshwater resources, and climate vulnerabilities in mountainous regions," in *Climate Vulnerability: Understanding and Addressing Threats to Essential Resources*, Vol. 1, eds J. Adegoke and C. Y. Wright (Waltham, MA: Elsevier Inc.; Academic Press), 57–78. doi: 10.1016/B978-0-12-384703-4.00504-9

Barros, A. P., and Lettenmaier, D. P. (1994). Dynamic modeling of orographically induced precipitation. *Rev. Geophys.* 32, 265–284. doi: 10.1029/94RG00625

Berrisford, P., Dee, D., Poli, P., Brugge, R., Fielding, K., Fuentes, M., et al. (2011). *The ERA-Interim 76 Archive, Version 2.0*. Technical report, ECMWF.

Boers, N., Barbosa, H. M. J., Bookhagen, B., Marengo, J. A., Marwan, N., and Kurths, J. (2015). Propagation of strong rainfall events from southeastern South America to the central andes. *J. Clim.* 28, 7641–7658. doi: 10.1175/JCLI-D-15-0137.1

Boers, N., Bookhagen, B., Barbosa, H. M., Marwan, N., Kurths, J., and Marengo, J. (2014). Prediction of extreme floods in the eastern central Andes based on a complex networks approach. *Nat. Commun.* 5:5199. doi: 10.1038/ncomms6199

Boers, N., Bookhagen, B., Marwan, N., and Kurths, J. (2016). Spatiotemporal characteristics and synchronization of extreme rainfall in South America with focus on the Andes mountain range. *Clim. Dynam.* 46, 601–617. doi: 10.1007/s00382-015-2601-6

Cavalcanti, I. F., Müller, G. V., Andrade, K. M., and Long, M. E. F. (2013). Cold air intrusions over southeastern South America – GFDL model behavior regarding climate simulations in the 20th century and future projections. *Glob. Planet. Change* 111, 31–42. doi: 10.1016/j.gloplacha.2013.08.006

Chavez, S. P., and Takahashi, K. (2017). Orographic rainfall hot spots in the Andes-Amazon transition according to the TRMM precipitation radar and in situ data. *J. Geophys. Res.* 122, 5870–5882. doi: 10.1002/2016JD026282

Chen, T.-C., Yen, M.-C., Huang, W.-R., and Gallus, W. A. Jr. (2002). An east asian cold surge: case study. *Monthly Weather Rev.* 130, 2271–2290. doi: 10.1175/1520-0493(2002)130<2271:AEACSC>2.0.CO;2

de la Torre, A., Pessano, H., Hierro, R., Santos, J., Llamedo, P., and Alexander, P. (2015). The influence of topography on vertical velocity of air in relation to severe storms near the southern Andes mountains. *Atmospher. Res.* 156, 91–101. doi: 10.1016/j.atmosres.2014.12.020

Dee, D. P., Uppala, S. M., Simmons, A. J., Berrisford, P., Poli, P., Kobayashi, S., et al. (2011). The ERA-interim reanalysis: configuration and performance of the data assimilation system. *Quart. J. R. Meteorol. Soc.* 137, 553–597. doi: 10.1002/qj.828

Duan, Y., Wilson, A. M., and Barros, A. P. (2015). Scoping a field experiment: error diagnostics of TRMM precipitation radar estimates in complex terrain as a basis for IPHEX2014. *Hydrol. Earth Syst. Sci.* 19, 1501–1520. doi: 10.5194/hess-19-1501-2015

Dudhia, J. (1989). Numerical study of convection observed during the winter monsoon experiment using a mesoscale two-dimensional model. *J. atmosphere. Sci.* 46, 3077–3107. doi: 10.1175/1520-0469(1989)046<3077:NSOCOD>2.0.CO;2

Ek, M. B., Mitchell, K. E., Lin, Y., Rogers, E., Grunmann, P., Koren, V., et al. (2003). Implementation of NOAH land surface model advances in the national centers for environmental prediction operational mesoscale eta model. *J. Geophys. Res.* 108:8851. doi: 10.1029/2002JD003296

Espinoza, J. C., Ronchail, J., Lengaigne, M., Quispe, N., Silva, Y., Bettolli, M. L., et al. (2013). Revisiting wintertime cold air intrusions at the east of the Andes: propagating features from subtropical Argentina to Peruvian Amazon and relationship with large-scale circulation patterns. *Clim. Dynam.* 41, 1983–2002. doi: 10.1007/s00382-012-1639-y

Garreaud, R. (1999a). Cold air incursions over subtropical and tropical South America: a numerical case study. *Monthly Weather Rev.* 127, 2823–2853. doi: 10.1175/1520-0493(1999)127<2823:CAIOSA>2.0.CO;2

Garreaud, R. (1999b). Multiscale analysis of the summertime precipitation over the Central Andes. *Monthly Weather Rev.* 127, 901–921. doi: 10.1175/1520-0493(1999)127<0901:MAOTSP>2.0.CO;2

Garreaud, R. (2000). Cold air incursions over subtropical South America: mean structure and dynamics. *Monthly Weather Rev.* 128, 2544–2559. doi: 10.1175/1520-0493(2000)128<2544:CAIOSS>2.0.CO;2

Garreaud, R., and Wallace, J. M. (1998). Summertime incursions of midlatitude air into subtropical and tropical South America. *Monthly Weather Rev.* 126, 2713–2733. doi: 10.1175/1520-0493(1998)126<2713:SIOMAI>2.0.CO;2

Garreaud, R. D. (2001). Subtropical cold surges: regional aspects and global distribution. *Int. J. Climatol.* 21, 1181–1197. doi: 10.1002/joc.687

Garreaud, R. D. (2009). The Andes climate and weather. *Adv. Geosci.* 22, 3–11. doi: 10.5194/adgeo-22-3-2009

Giovannettone, J. P., and Barros, A. P. (2009). Probing regional orographic controls of precipitation and cloudiness in the central Andes using satellite data. *J. Hydrometeorol.* 10, 167–182. doi: 10.1175/2008JHM973.1

Houze, R. A. (2012). Orographic effects on precipitating clouds. *Rev. Geophys.* 50:RG1001. doi: 10.1029/2011RG000365

Hurley, J. V., Vuille, M., Hardy, D. R., Burns, S. J., and Thompson, L. G. (2015). Cold air incursions, δ^{18}O variability, and monsoon dynamics associated with snow days at Quelccaya Ice Cap, Peru. *J. Geophys. Res.* 120, 7467–7487. doi: 10.1002/2015JD023323

Kain, J. S. (2004). The Kain-Fritsch convective parameterization: an update. *J. Appl. Meteorol.* 43, 170–181. doi: 10.1175/1520-0450(2004)043<0170:TKCPAU>2.0.CO;2

Kalnay, E., Kanamitsu, M., Kistler, R., Collins, W., Deaven, D., Gandin, L., et al. (1996). The NCEP/NCAR 40-year reanalysis project. *Bull. Am. Meteorol. Soc.* 77, 437–471. doi: 10.1175/1520-0477(1996)077<0437:TNYRP>2.0.CO;2

Li, W., and Fu, R. (2006). Influence of cold air intrusions on the wet season onset over Amazonia. *J. Clim.* 19, 257–275. doi: 10.1175/JCLI3614.1

Liu, C., Zipser, E. J., Cecil, D. J., Nesbitt, S. W., and Sherwood, S. (2008). A cloud and precipitation feature database from nine years of TRMM observations. *J. Appl. Meteorol. Climatol.* 47, 2712–2728. doi: 10.1175/2008JAMC1890.1

Lowman, L. E. L., and Barros, A. P. (2014). Investigating links between climate and orography in the Central Andes: coupling erosion and precipitation using a physical-statistical model. *J. Geophys. Res.* 119, 1322–1353. doi: 10.1002/2013JF002940

Lupo, A. R., Nocera, J. J., Bosart, L. F., Hoffman, E. G., and Knight, D. J. (2001). South american cold surges: types, composites, and case studies. *Monthly Weather Rev.* 129, 1021–1041. doi: 10.1175/1520-0493(2001)129<1021:SACSTC>2.0.CO;2

Medvigy, D., Walko, R. L., and Avissar, R. (2012). Simulated links between deforestation and extreme cold events in South America. *J. Clim.* 25, 3851–3866. doi: 10.1175/JCLI-D-11-00259.1

Milbrandt, J. A., and Yau, M. K. (2005a). A multimoment bulk microphysics parameterization. part I: Analysis of the role of the spectral shape parameter. *J. atmosphere. Sci.* 62, 3051–3064. doi: 10.1175/JAS3534.1

Milbrandt, J. A., and Yau, M. K. (2005b). A multimoment bulk microphysics parameterization. part II: A proposed three-moment closure and scheme description. *J. atmosphere. Sci.* 62, 3065–3081. doi: 10.1175/JAS3535.1

Mlawer, E. J., Taubman, S. J., Brown, P. D., Iacono, M. J., and Clough, S. A. (1997). Radiative transfer for inhomogeneous atmospheres: RRTM, a validated correlated-k model for the longwave. *J. Geophys. Res.* 102, 16663–16682. doi: 10.1029/97JD00237

Müller, G. V., and Ambrizzi, T. (2007). Teleconnection patterns and Rossby wave propagation associated with generalized frosts over southern South America. *Clim. Dynam.* 29, 633–645. doi: 10.1007/s00382-007-0253-x

Müller, G. V., and Berri, G. J. (2007). Atmospheric circulation associated with persistent generalized frosts in central-southern South America. *Monthly Weather Rev.* 135, 1268–1289. doi: 10.1175/MWR3344.1

Nakanishi, M., and Niino, H. (2006). An improved Mellor–Yamada level-3 model: its numerical stability and application to a regional prediction of advection fog. *Bound. Layer Meteorol.* 119, 397–407. doi: 10.1007/s10546-005-9030-8

Nesbitt, S. W., Zipser, E. J., and Cecil, D. J. (2000). A census of precipitation features in the tropics using TRMM: Radar, ice scattering, and lightning observations. *J. Clim.* 13, 4087–4106. doi: 10.1175/1520-0442(2000)013<4087:ACOPFI>2.0.CO;2

Prat, O. P., and Barros, A. P. (2010a). Assessing satellite-based precipitation estimates in the southern Appalachian Mountains using rain gauges and TRMM PR. *Adv. Geosci.* 25, 143–153. doi: 10.5194/adgeo-25-143-2010

Prat, O. P., and Barros, A. P. (2010b). Ground observations to characterize the spatial gradients and vertical structure of orographic precipitation experiments in the inner region of the Great Smoky Mountains. *J. Hydrol.* 391, 141–156. doi: 10.1016/j.jhydrol.2010.07.013

Rasmussen, K. L., and Houze, R. A. (2011). Orogenic convection in subtropical South America as seen by the TRMM satellite. *Monthly Weather Rev.* 139, 2399–2420. doi: 10.1175/MWR-D-10-05006.1

Schultz, D. M., Bracken, W. E., Bosart, L. F., Hakim, G. J., Bedrick, M. A., Dickinson, M. J., et al. (1997). The 1993 superstorm cold surge: frontal structure, gap flow, and tropical impact. *Monthly Weather Rev.*125, 5–39. doi: 10.1175/1520-0493(1997)125<0005:TSCSFS>2.0.CO;2

Seluchi, M. E., Saulo, A. C., Nicolini, M., and Satyamurty, P. (2003). The northwestern argentinean low: a study of two typical events. *Mon. Wea. Rev.* 131, 2361–2378. doi: 10.1175/1520-0493(2003)131<2361:TNALAS>2.0.CO;2

Siqueira, J. R., and Machado, L. A. T. (2004). Influence of the frontal systems on the day-to-day convection variability over South America. *J. Clim.* 17, 1754–1766. doi: 10.1175/1520-0442(2004)017<1754:IOTFSO>2.0.CO;2

Siqueira, J. R., Rossow, W. B., Machado, L. A. T., and Pearl, C. (2005). Structural characteristics of convective systems over South America related to cold-frontal incursions. *Monthly Weather Rev.* 133, 1045–1064. doi: 10.1175/MWR2888.1

Skamarock, W., Klemp, J., Dudhia, J., Gill, D., Barker, D., Duda, M., et al. (2008). *A Description of the Advanced Research Wrf Version 3, Ncar Technical Note, Mesoscale and Microscale Meteorology Division*. National Center for Atmospheric Research, Boulder, Colorado, USA.

Sun, X., and Barros, A. P. (2014). High resolution simulation of tropical storm Ivan (2004) in the Southern Appalachians: role of planetary boundary-layer schemes and cumulus parametrization. *Q. J. R. Meteorol. Soc.* 140, 1847–1865. doi: 10.1002/qj.2255

Sun, X., and Barros, A. P. (2015a). Impact of Amazonian evapotranspiration on moisture transport and convection along the eastern flanks of the tropical Andes. *Quart. J. R. Meteorol. Soc.* 141, 3325–3343. doi: 10.1002/qj.2615

Sun, X., and Barros, A. P. (2015b). Isolating the role of surface evapotranspiration on moist convection along the eastern flanks of the tropical Andes using a quasi-idealized approach. *J. atmosphere. Sci.* 72, 243–261. doi: 10.1175/JAS-D-14-0048.1

Tropical Rainfall Measuring Mission. (2011). *TRMM Combined Precipitation Radar and Microwave Imager Rainfall Profile L2 1.5 hours V7,* Greenbelt, MD, Goddard Earth Sciences Data and Information Services Center (GESDISC): Available online at: https://disc.gsfc.nasa.gov/datacollection/TRMM_2B31_7.html

Vera, C. S., and Vigliarolo, P. K. (2000). A diagnostic study of cold-air outbreaks over South America. *Monthly Weather Rev.* 128, 3–24. doi: 10.1175/1520-0493(2000)128<0003:ADSOCA>2.0.CO;2

Wilson, A. M., and Barros, A. P. (2015). Landform controls on low level moisture convergence and the diurnal cycle of warm season orographic rainfall in the southern Appalachians. *J. Hydrol.* 531, 475–493. doi: 10.1016/j.jhydrol.2015.10.068

Wilson, A. M., and Barros, A. P. (2017). Orographic land-atmosphere interactions and the diurnal cycle of low-level clouds and fog. *J. Hydrometeorol.* 18, 1513–1533. doi: 10.1175/JHM-D-16-0186.1

Yin, L., Fu, R., Shevliakova, E., and Dickinson, R. E. (2013). How well can CMIP5 simulate precipitation and its controlling processes over tropical South America? *Clim. Dynam.* 41, 3127–3143. doi: 10.1007/s00382-012-1582-y

Yin, L., Fu, R., Zhang, Y., Arias, P. A., Fernando, D. N., Li, W., et al. (2014). What controls the interannual variation of the wet season onsets over the Amazon? *J. Geophys. Res.* 119, 2314–2328. doi: 10.1002/2013JD021349

Zipser, E. J., Cecil, D. J., Liu, C., Nesbitt, S. W., and Yorty, D. P. (2006). Where are the most intense thunderstorms on Earth? *Bull. Am. Meteorol. Soc.* 87, 1057–1072. doi: 10.1175/BAMS-87-8-1057

Conflict of Interest Statement: The authors declare that the research was conducted in the absence of any commercial or financial relationships that could be construed as a potential conflict of interest.

frontiers in Earth Science

ORIGINAL RESEARCH
published: 06 December 2019
doi: 10.3389/feart.2019.00294

Evaluation of CORDEX Regional Climate Models in Simulating Extreme Dry Spells in Southwest China

Tao Feng[1,2,3], Zachary Tipton[4], Lan Xia[1,2] and Youli Chang[1,2]**

[1] Department of Atmospheric Sciences, Yunnan University, Kunming, China, [2] Key Laboratory of Atmospheric Environment and Processes in the Boundary Layer Over the Low-Latitude Plateau Region, Yunnan University, Kunming, China, [3] State Key Laboratory of Numerical Modeling for Atmospheric Sciences and Geophysical Fluid Dynamics (LASG), Institute of Atmospheric Physics, Chinese Academy of Sciences, Beijing, China, [4] Department of Biological Sciences, University of Arkansas, Fayetteville, AR, United States

OPEN ACCESS

Edited by:
Martin Stendel, Danish Meteorological Institute (DMI), Denmark

Reviewed by:
Rosane Rodrigues Chaves, Federal University of Rio Grande do Norte, Brazil
Myoung-Seok Suh, Kongju National University, South Korea
Merja H. Tölle, University of Giessen, Germany

***Correspondence:**
Tao Feng
taofeng@ynu.edu.cn
Youli Chang
ylchang@ynu.edu.cn

Specialty section:
This article was submitted to Atmospheric Science, a section of the journal Frontiers in Earth Science

Received: *31 October 2018*
Accepted: *28 October 2019*
Published: *06 December 2019*

Citation:
Feng T, Tipton Z, Xia L and Chang Y (2019) Evaluation of CORDEX Regional Climate Models in Simulating Extreme Dry Spells in Southwest China. Front. Earth Sci. 7:294. doi: 10.3389/feart.2019.00294

In recent decades, Southwest China (SWC) has experienced a series of severe and extensive droughts resulting in tremendous socioeconomic losses. The annual maximum dry spell length (AMDSL), which refers to the number of consecutive days without rainfall, or days with rainfall below a threshold, plays an important role in triggering drought. The main objective of this study is to provide a comparison of the capabilities of current regional climate models (RCMs) in simulating extreme dry spell characteristics in mountainous SWC. Five available RCM simulations utilized in the Coordinated Regional Climate Downscaling Experiment (CORDEX)-East Asia project over 1981–2005 were employed in this study; the RCMs being NIMR-HadGEM3, SNU-MM5, SNU-WRF, KNU-RegCM4, and YSU-RSM. First, it was found that all of the RCMs reasonably simulate the main seasonality features of rainfall and dry days in SWC. Furthermore, four of the RCMs, excepting YSU-RSM, can accurately capture the spatial pattern of dry-day occurrence based on Taylor diagram diagnosis. Second, we assessed the performance of the five RCMs to detect and reproduce the climatology and variability of the AMDSL. In general, the RCMs simulate the spatial pattern of long-term mean and interannual variability of the AMDSL in SWC well. Based on Taylor diagram evaluation, NIMR-HadGEM3 was the best among the five in simulating the AMDSL characteristics. Third, the generalized extreme value (GEV) distribution is considered the most suitable model for fitting the AMDSL in both observation and RCM experimental data in comparison to other three-parameter probabilistic models. Higher value centers of the scale parameter and the location parameter indicate a wider and amplified distribution of the AMDSL over the low-latitude highlands (LLH) region against other areas in SWC, which is consistent with the spatial patterns of climatological AMDSL. In addition, sensitivity analysis of different thresholds for dry days shows that the 1 mm threshold is suitable for this study and that different threshold

choices have little effect on simulation ability. Overall, the results show that although significant differences are found between RCMs, the RCMs excepting YSU-RSM can reasonably reveal extreme dry spell occurrence and amplitude, along with the spatial distribution of the AMDSL at a 20-year return period in SWC. This information is useful for model evaluation and improvement, future climate projections, and water resource risk management.

Keywords: regional climate models, annual maximum dry spell length, CORDEX East Asia, generalized extreme value, *L*-moments

INTRODUCTION

Southwest China (SWC), as shown in **Figure 1**, covers an area of approximately 1.23 million km^2, or 12.9% of China, containing four provinces and one municipality. SWC is one of the most densely populated and highest grain-producing regions in China and also contains the headwaters of many important rivers for supplying water to Chinese agriculture and the Mekong River Basin (MRB). Droughts have had significant impacts on economic growth, water scarcity, crop failure, and the daily lives of millions of people in this area (Qin et al., 1997; Cheng et al., 2009). In recent decades, droughts, as defined by National Climate Center, have been widespread and frequent in SWC and have been associated with 60% of the economic losses from all meteorological disasters (Qin et al., 1997; Cheng et al., 2009; Wang et al., 2015). Severe droughts were observed more frequently in the area during the last decade, with the summer of 2006, the autumn of 2009 to the spring of 2010 (Yang et al., 2011; Barriopedro et al., 2012), and the summer of 2011 (Sun and Yang, 2012; Wang et al., 2014) being most notable. Considerable efforts have been expended on surveying the drought characteristics as well as establishing the possible physical causes and mechanisms of droughts in SWC, which have been reviewed by Wang et al. (2015).

To assess drought characteristics and impacts, it is necessary to study hydro-meteorological variables that affect water availability, including precipitation frequency and intensity, evaporation, and dry spells (Vicente-Serrano et al., 2010; Spinoni et al., 2019). In particular, the number of consecutive dry days (CDD) without rainfall, or days with rainfall below a specific threshold, is defined as a dry spell. This variable can show the effect of long periods of precipitation deficit on soil moisture conditions, ground water levels, and available water in reservoirs (Tebaldi et al., 2006; Modarres, 2010; Sushama et al., 2010; Sarhadi and Heydarizadeh, 2014; Saaroni et al., 2015; Raymond et al., 2016; Tramblay and Hertig, 2018). Exceptionally long dry spell periods play an important role in the occurrence and intensity of drought and have strong environmental and social impacts. SWC is comprised of complex terrain including the low-latitude highlands (LLH), Sichuan basin (SB), southeastern Tibetan Plateau (SETP), and Traverse Mountain Chain (TMC), as shown in **Figure 1C**. In addition, SWC is located in the interface area between the Indian Summer Monsoon (ISM) and the East Asian Summer Monsoon (EASM). Both the combination of the two monsoons and the complex terrain make the interannual variability of the AMDSL stronger and harder to simulate with state-of-art climate models.

Regional climate models (RCMs) are our primary tool for understanding how extreme local-scale precipitation characteristics may change in the future under global warming scenarios (Wang et al., 2004; Christensen and Christensen, 2007; Giorgi et al., 2009; von Storch and Zorita, 2019). RCMs have a higher resolution than earth system models (ESMs) but span a limited area. To improve the confidence of an RCM on extreme precipitation or extreme dry spell representation, the added value from downscaled physical processes is the key challenge in regional climate modeling (Maraun et al., 2010; Rummukainen, 2015). In general, two factors have the largest contribution to a model's ability to simulate extremes: horizontal grid resolution and physical parameterization schemes (Christensen and Christensen, 2007; Chan et al., 2013, 2014). The horizontal grid resolution has been considered the most important factor in simulating extremes (Pope and Stratton, 2002; Roeckner et al., 2006; Salathé et al., 2008; Shaffrey et al., 2009; Wehner et al., 2010). With finer-scale physical processes and better representation of the orographic effect, increasing the horizontal grid resolution could give better representation of small-scale processes affecting precipitation extremes and lead to increasing model ability to simulate extremes like the AMDSL (Pope and Stratton, 2002; Roeckner et al., 2006; Chan et al., 2013, 2014). Previous studies have reported an improved confidence in simulating extreme precipitation and extreme dry spells over continental Europe and Canada (Boberg et al., 2010; Rauscher et al., 2010; Sushama et al., 2010; Wehner et al., 2010; Kopparla et al., 2013).

Recently, an international collaborative program known as the Coordinated Regional Climate Downscaling Experiment (CORDEX) project has provided a quality-controlled dataset of downscaled precipitation for the historical past and future climate changes as well as a model evaluation framework over East Asia (Giorgi et al., 2009)[1]. Several previous studies have examined the performance of a single RCM or ensemble RCMs in simulating precipitation climatology and precipitation extremes over CORDEX-East Asia (CORDEX-EA) (Huang et al., 2015; Park et al., 2016; Li et al., 2018). Although RCMs have shown systematic bias in mean and extreme precipitation, those models have been able to reproduce spatiotemporal characteristics of

[1]http://www.cordex.org/

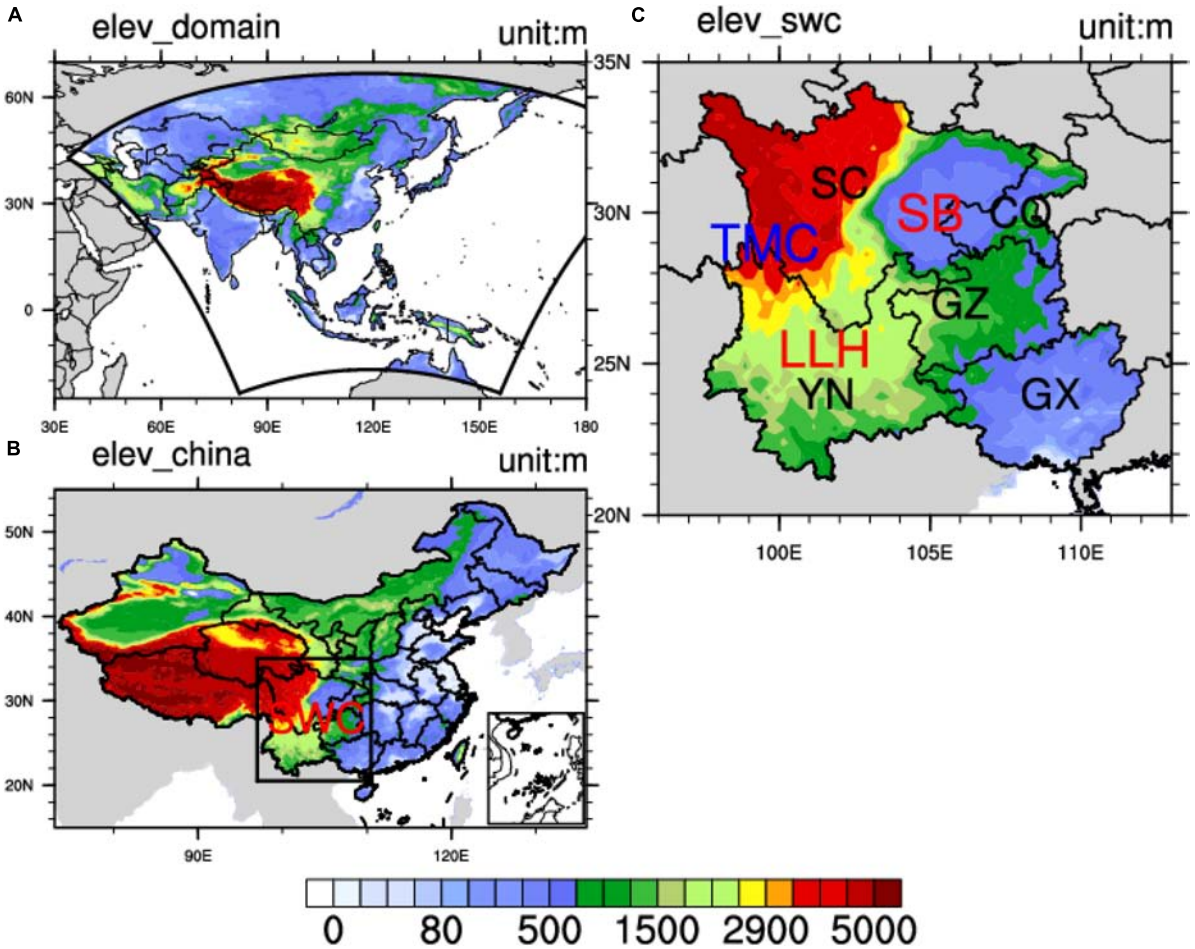

FIGURE 1 | (A) The entire CORDEX East Asia domain (within the outer black line). **(B)** The analysis sub-region, Southwest China (SWC), with latitudes and longitudes ranging from 21°N to 35°N and 98°E to 112°E, respectively. **(C)** Zoomed view of SWC with administrative divisions (black font) and main terrain elements (colored font) marked. Shading indicates topography.

TABLE 1 | Detailed information on RCMs used in this study.

	SNU-WRF	SNU-MM5	YSU-RSM	KNU-RegCM4	NIMR-HadGEM3
Horizontal resolution (no. of grid points lat × lon)	50 km (197 × 233)	50 km (197 × 233)	50 km (198 × 241)	50 km (197 × 243)	0.44° (183 × 220)
Vertical levels	σ-27	σ-24	σ-22	σ-18	Hybrid-60
Dynamic framework	Non-hydrostatic	Non-hydrostatic	Hydrostatic	Hydrostatic	Non-hydrostatic
Convection scheme	Kain-Fritch II	Kain-Fritch II	Simplified Arakawa–Schubert	MIT-Emanuel	Revised mass flux scheme
Land surface	Unified Noah	CLM3	NOAH LSM	CLM3	MOSES-II
PBL scheme	YSU	YSU	YSU	Holtslag	MOSES-II non-local
Spectral nudging	Yes	Yes	Yes	Yes	No
References	Skamarock et al., 2005	Cha and Lee, 2009	Hong et al., 2013	Giorgi et al., 2012	Davies et al., 2005
Initial and boundary conditions	HadGEM2-AO historical simulation				
Simulation period	HIST: 1979–2005				

The dataset was accessed at https://www.cordex.org/domains/region-7-east-asia/.

extreme precipitation over China and East Asia (Park et al., 2016; Li et al., 2018).

Previous studies have already evaluated the capacity of RCMs to reproduce the spatiotemporal characteristics of dry spells. For example, Herrera et al. (2010) and Domínguez et al. (2013) use RCMs from the ENSEMBLES/ESCENA project to assess the ability of the simulations to reproduce the mean and maximal annual number of CDDs in Spain. They found that the models tend to have negative CDD number bias compared to observations. López-Franca et al. (2015) also used five RCMs from the ESCENA project to detect the annual average of dry spells length (AADSL) index in Spain. In their study, they found that the five RCM simulations reproduced the observed AADSL pattern in Spain well. Fantini et al. (2016) used nine RCMs from the Euro-CORDEX and Med-CORDEX experiments to assess the ability of the RCMs to reproduce the frequency of dry days or dry spells. They also found those RCMs tend to underestimate the extreme dry spell frequency over wetter regions of the Mediterranean Basin. Raymond et al. (2018) used HyMeX/Med-CORDEX experiments to detect very long dry spells (VLDS) over the Mediterranean Basin. They found that at least 51% of the observed VLDS were reproduced by the RCM simulations and that those RCMs accurately simulated spatiotemporal characteristics. Nevertheless, studies on the frequency and intensity of extreme dry spells, especially the interannual change in extreme dry spells, have rarely been conducted over complex terrain and different climate type area like SWC, for which area the ability of RCMs to simulate extreme dry spells is worth studying. Here we present the evaluation results of the CORDEX-EA project using an ensemble of five RCM simulations driven by the HadGEM2-AO global model (Lee et al., 2014; Oh et al., 2014). The AMDSL distribution characteristics were analyzed based on GEV theory in both observation and RCM simulations.

This paper is arranged as follows into five sections. Observations and model simulations are described in section "Observations and Model Simulations." In section "Methodology," we present the methodology of distribution parameter estimation and return value calculation. In section "Results," RCM performances are assessed for dry day occurrence,

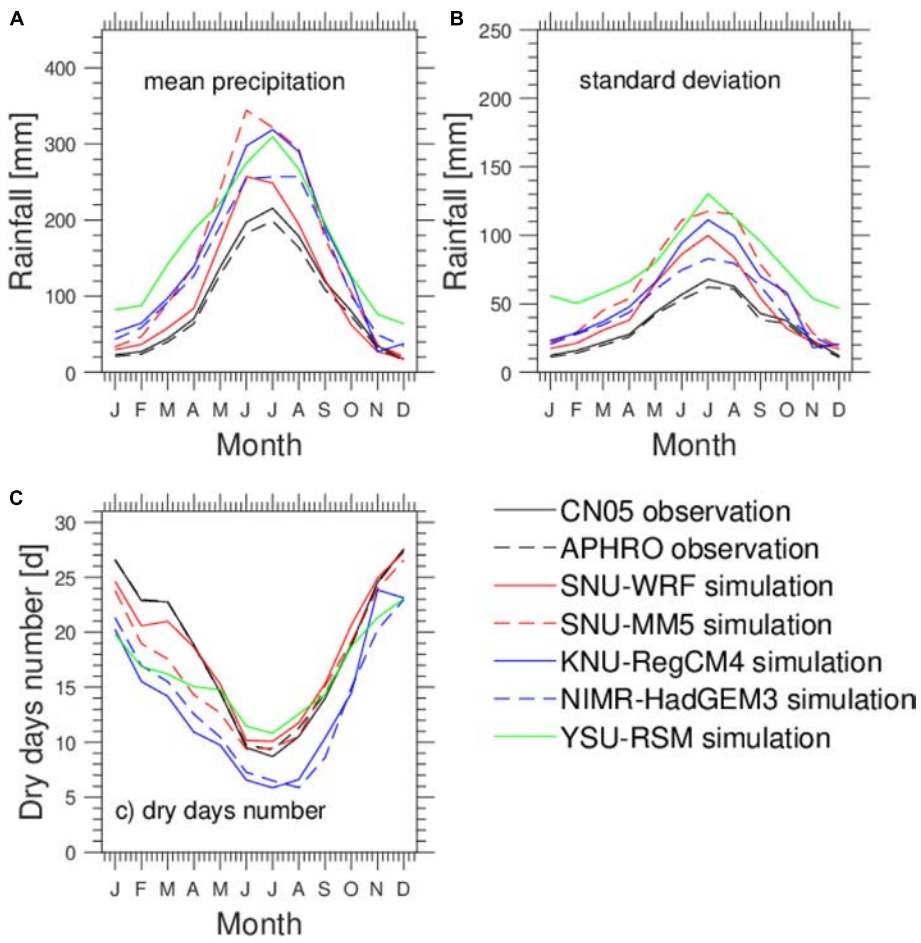

FIGURE 2 | (A) Annual cycle of area-averaged monthly mean precipitation over SWC. **(B)** Annual cycle of area-averaged monthly standard deviation of monthly mean precipitation. **(C)** Annual cycle of area-averaged monthly mean number of dry days. The different line types represent two observations (CN05 and APHRO) and five RCM simulations (SNU-WRF, SNU-MM5, YSU-RSM, KNU-RegCM4, and NIMR-HadGEM3), respectively.

dry spell frequency, AMDSL climatology, and the GEV fitted AMDSL return value. In section "Discussion and Conclusion," we conclude and discuss our results.

OBSERVATIONS AND MODEL SIMULATIONS

Observational Datasets

Among the sets of high-resolution gridded precipitation data such as the multi-source weighted ensemble precipitation product (Beck et al., 2017a,b), Version 1.2 of the Global Precipitation Climatology Project (GPCP) daily precipitation estimates (Huffman et al., 2001), the CN05 daily precipitation data for China (CMA; Wu and Gao, 2013), and the APHRODITE (APHRO) gridded precipitation data (Yatagai et al., 2012), we chose the appropriate observation data based on two principles: one is having finer horizontal resolution than the RCM simulation data and the other is that the data are widely used for RCM evaluation over the East Asia domain (Oh et al., 2014; Huang et al., 2015; Li et al., 2018).

The simulated results for mean AMDSL and extremes for the historical period (1981–2005) were validated against two widely used daily high-resolution gridded observational datasets, namely, the CN05 and APHRO gridded daily precipitation data. The CN05 product was developed and distributed by the National Climate Centre of China and contains daily precipitation at a horizontal resolution of 0.25° × 0.25°. APHRO is also a high-resolution daily precipitation dataset developed by the Meteorological Research Institute of the Japan Meteorological Agency (MRI/JMA). In this study, we used the latest and improved version of the daily dataset for Monsoon Asia (APHRO_MA_V1101R1), covering 60.0°E–150.0°E, 15.0°S–55.0°N at a high spatial resolution of 0.25° × 0.25°. The dataset was accessed at the official website of the APHRODITE project: http://www.chikyu.ac.jp/precip/english/products.html.

RCM Simulations

Five RCMs are utilized in CORDEX-East Asia climate experiments. RCMs include three nonhydrostatic RCMs (NIMR-HadGEM3, SNU-MM5, and SNU-WRF) and two hydrostatic RCMs (KNU-RegCM4 and YSU-RSM). Here, SNU-WRF and SNU-MM5 stand for simulation data from WRF (Skamarock et al., 2005) and MM5 (Cha and Lee, 2009) from Seoul National University, respectively. KNU-RegCM4 stands for simulation data from RegCM4 (Giorgi et al., 2012) from Kongju National University. NIMR-HadGEM3 stands for simulation data from HadGEM3_RA (Davies et al., 2005) from the National Institute of Meteorological Research in South Korea. YSU-RSM represents simulation data from RSM (Hong et al., 2013) from Yonsei University. Following the modeling framework of the CORDEX project (Giorgi et al., 2009), the simulations are driven by boundary and initial conditions from the historical simulation of HadGEM2-AO GCM with 1.875° × 1.25° longitude–latitude horizontal resolution, and are integrated from 1981 to 2015 over the East Asia domain, which includes East Asia, India, the Western Pacific Ocean, and the northern part of Australia, as shown in **Figure 1**. All RCM simulations have a spatial horizontal resolution of 0.44° (∼50 km). Different physical schemes including convection scheme, land surface, and the planetary boundary layer (PBL) scheme are applied across RCMs, as summarized in **Table 1**. The dataset was accessed at https://www.cordex.org/domains/region-7-east-asia/.

As mentioned above, the two observational datasets have finer spatial resolution than RCM simulations. In this study, both observations and RCM simulations were interpolated onto the standard CORDEX-EA grids (Giorgi et al., 2009) by applying the nearest-neighbor interpolation method (Kotlarski et al., 2014)

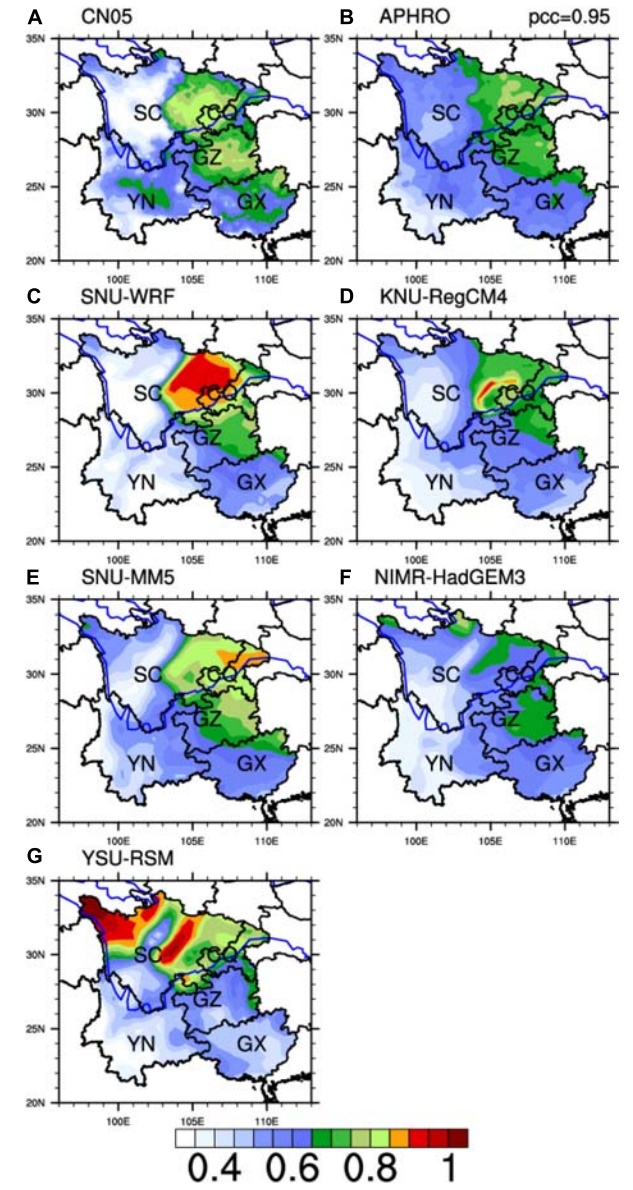

FIGURE 3 | Spatial distributions of dry day occurrence (unit:%) from two observations, **(A)** CN05 and **(B)** APHRO, and five RCM simulations, **(C)** SNU-WRF, **(D)** KNU-RegCM4, **(E)** SNU-MM5, **(F)** NIMR-HadGEM3, and **(G)** YSM-RSM.

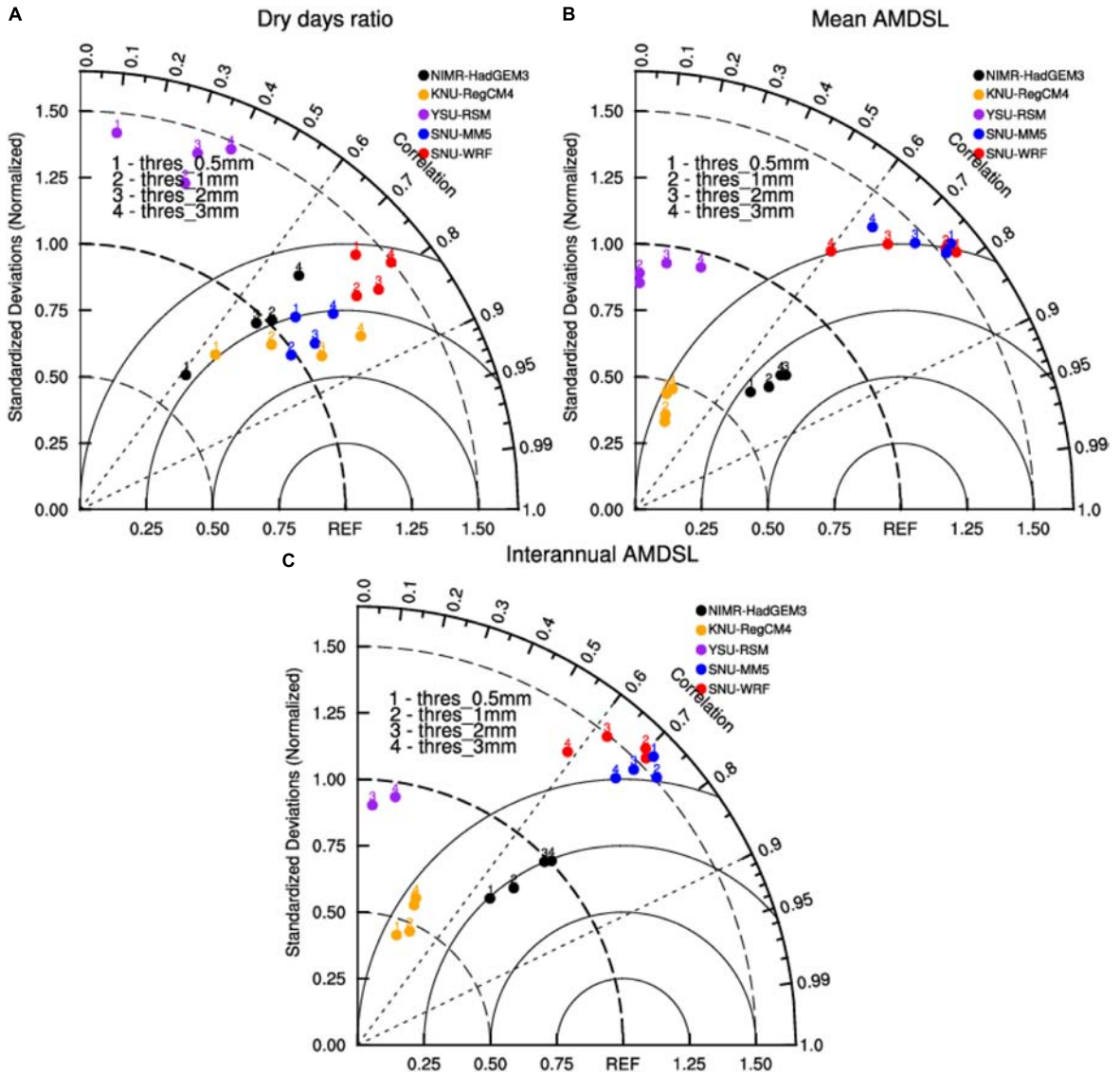

FIGURE 4 | Multivariable Taylor diagram displaying normalized statistical comparisons of SNU-WRF (red), SNU-MM5 (blue), YSU-RSM (purple), KNU-RegCM4 (orange), and NIMR-HadGEM3 (black) simulated climatological dry days ratio **(A)**, mean AMDSL **(B)**, and interannual variability of the AMDSL **(C)**, respectively. Numbers indicate four different thresholds for dry days.

before conducting comparative analysis. Furthermore, in order to avoid the influence of the interpolation method on the analysis results, a bilinear interpolation algorithm was also applied to the same datasets as a comparative analysis. The results of analysis with Taylor diagrams show that the conclusions obtained by the two interpolation methods are basically consistent.

METHODOLOGY

Threshold for the AMDSL

In this study, following previous studies (Frich et al., 2002; Sushama et al., 2010; Raymond et al., 2016, 2018; Tramblay and Hertig, 2018), an annual maximum dry spell length (AMDSL) is defined as the largest number of consecutive days without precipitation or with precipitation less than 1 mm/day, a threshold also adopted to identify CDD by the Expert Team on Climate Change Detection and Indices (ETCCDI) (Zhang et al., 2011). The choice of this threshold is subjective and has been used in most previous studies on CDD or AMDSL on a global and regional scale (Sushama et al., 2010; Donat et al., 2016; Raymond et al., 2016; Herold et al., 2017). Thus, the AMDSL is mostly defined as a punctual measure through a pure statistical approach rather than a physical approach. To avoid the effect of threshold selection on the results, a threshold sensitivity analysis was also applied in this study. Another three thresholds, 0.5, 2, and 3 mm/d, are considered for comparative analysis.

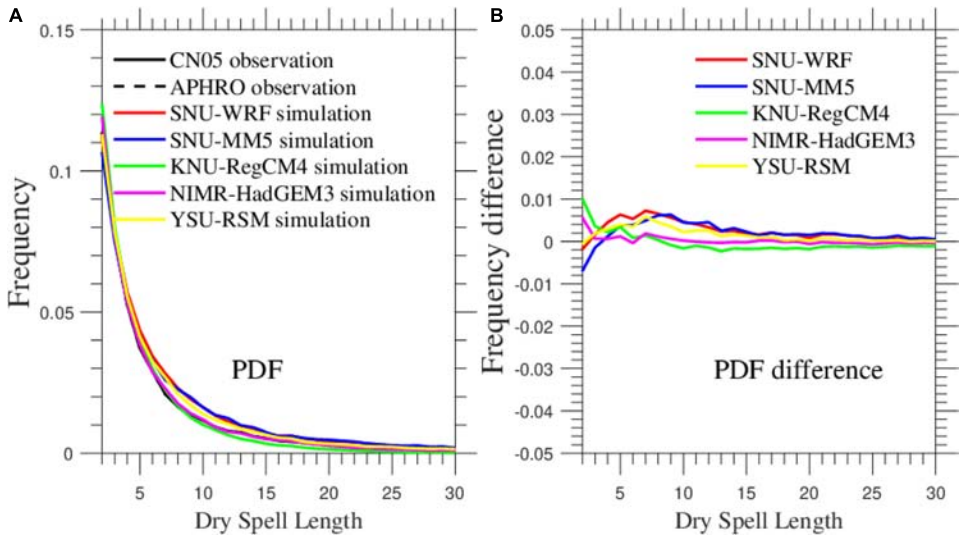

FIGURE 5 | (A) Probability distribution functions of dry spell length (days), for rainfall in two observational datasets and five RCM simulations. **(B)** PDF differences of five RCMs against CN05 observational data. The different line colors represent two observations (CN05 and APHRO) and five RCM simulations (SNU-WRF, SNU-MM5, YSU-RSM, KNU-RegCM4, and NIMR-HadGEM3), respectively.

Extreme Value Modeling

An important part of event extreme statistics is to identify the suitable distribution from which the extremes extracted from an observed period were drawn. Extreme events are computed using two different approaches: block maxima (like the AMDSL) and peaks-over-threshold (POT). Coles et al. (2001) demonstrated that the distribution of POT asymptotically converges to generalized Paredo (GPD) (Dominguez-Castro et al., 2019). Similarly, that of block maxima like the AMDSL converges to GEV.

The location, scale, and shape parameter of the GEV distribution can be estimated from a time series of block maxima (e.g., the AMDSL). Several estimation approaches are available including the *L*-moment method (Hosking and Wallis, 2005), probability-weighted moments, and maximum-likelihood estimator (MLE) (Coles et al., 2001). As linear combinations of order statistics, *L*-moments are resistant to the effects of outliers and thus provide robust estimates of distribution parameters (Hosking and Wallis, 2005; Sushama et al., 2010). In this study, we used the *L*-moment method for estimating GEV distribution parameters.

To further explore the best fitting model for the AMDSL in both observation and RCM simulations, the best-fit distribution is identified following the steps of *L*-moment theory proposed by Hosking (1990) (see details in **Supplementary Material**). Four commonly used three-parameter distributions are considered to the AMDSL, which include GEV, three-parameter lognormal distribution (LN3), Pearson type 3 distribution (PIII), and GPD, as given in **Supplementary Table S1**. The theoretical relationship between the empirical L-*skewness* (τ_3) and L-*kurtosis* ($\tau_4^{(GEV)}$, $\tau_4^{(LN3)}$, $\tau_4^{(PE3)}$, and $\tau_4^{(GPD)}$ for the considered GEV, LN3, PE3, and GPD models, respectively) are presented in **Supplementary Table S2**. After the theoretical τ_4 value was calculated for the considered extreme distributions, the goodness-of-fit measure of minimum absolute difference ($|D|$) proposed by Hosking and Wallis (1993) was used to identify the best-fit distribution function. The optimum fitted distribution functions can be chosen by comparing the difference $|D|$ between empirical and theoretical *L-kurtosis* based on a given empirical *L-skewness* value. The best choice of distribution is the one with minimum difference $|D|$.

There are several conventional methods for identifying the most suitable extreme distribution, including probabilistic-probabilistic plots, quantile–quantile plots, and *L*-moment relationships. This is more easily achieved by using *L*-moments than via conventional moments and other goodness-of-test methods (Kroll and Vogel, 2002; Sushama et al., 2010).

RESULTS

Annual Cycles of Rainfall and Dry Days

Based on the spatial distribution of annual rainfall, SWC has abundant precipitation of 1200–1800 mm per year on the long-term average (Wang et al., 2015). Rainfall in the SWC area also has a distinct seasonal character. The wet season is from May to September, and the dry season is from October to April of the following year. **Figure 2A** illustrates the performance of the CORDEX RCMs in simulating area-averaged annual rainfall cycles for the SWC. Grid cells in two sets of gridded observations and model simulations are averaged for the comparison over SWC. The two gridded observations have substantially similar annual cycles of monthly mean precipitation, standard deviation, and monthly mean dry days. All of the five RCMs capture the shape of the monthly mean rainfall seasonality well but with a certain degree of overestimation, 1.5–2.5 mm/day, in the wet

season. As shown in **Figure 2B**, all five RCMs also simulate the standard deviation of the annual cycle of monthly rainfall well, which indicates that RCMs show relatively good performance in simulating the interannual variability of rainfall in each month but with 0.8–1.5 mm/day overestimation of the variability. Furthermore, the area-averaged climatology of dry days is also presented in **Figure 2C**. All of the RCMs can simulate the shape of the seasonal cycle of dry days for each month well. Three models, KNU-RegCM4, YSU-RSM, and NIMR-HadGEM3, have an overall underestimation of the annual cycle of dry days by 2–4 days/month. SNU-MM5 captured dry day seasonality well but with a relative underestimation by 2.5 days/month during the dry season. SNU-WRF reproduced the annual cycle of dry days very well.

Spatial Pattern of Dry Days and Dry Spell Distribution

Figure 3 shows the spatial pattern of the proportion of dry days in the two rainfall observation datasets and in the five

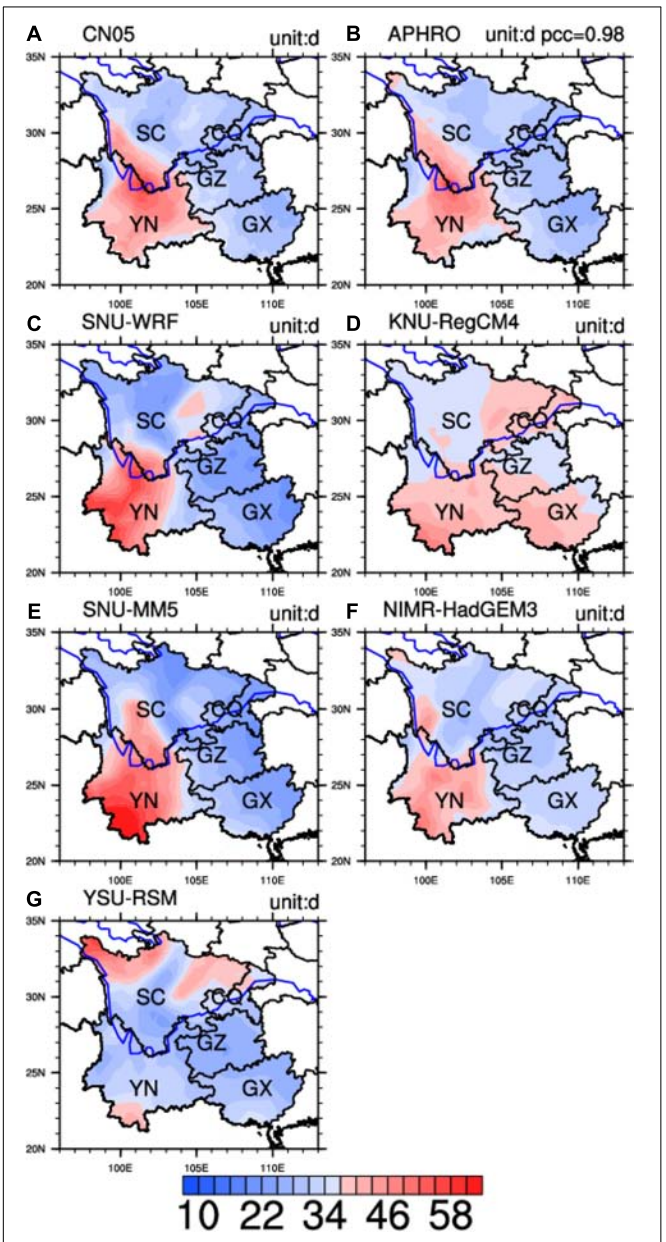

FIGURE 6 | Spatial distributions of mean annual maximum dry spell length (AMDSL) (unit: day) from two observations: **(A)** CN05, **(B)** APHRO; and five RCM simulations: **(C)** SNU-WRF, **(D)** KNU-RegCM4, **(E)** SNU-MM5, **(F)** NIMR-HadGEM3, and **(G)** YSM-RSM.

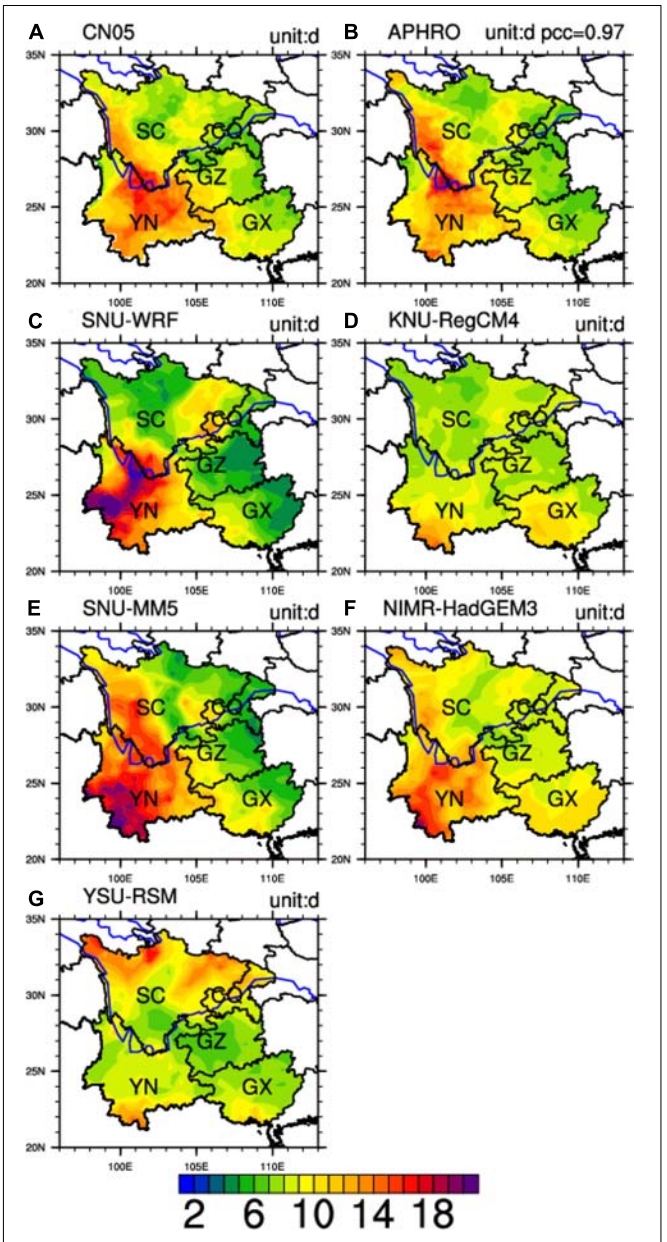

FIGURE 7 | Spatial distributions of interannual variability of the annual maximum dry spell length (AMDSL) (unit: day) from two observations: **(A)** CN05, **(B)** APHRO; and five RCM simulations: **(C)** SNU-WRF, **(D)** KNU-RegCM4, **(E)** SNU-MM5, **(F)** NIMR-HadGEM3, and **(G)** YSM-RSM.

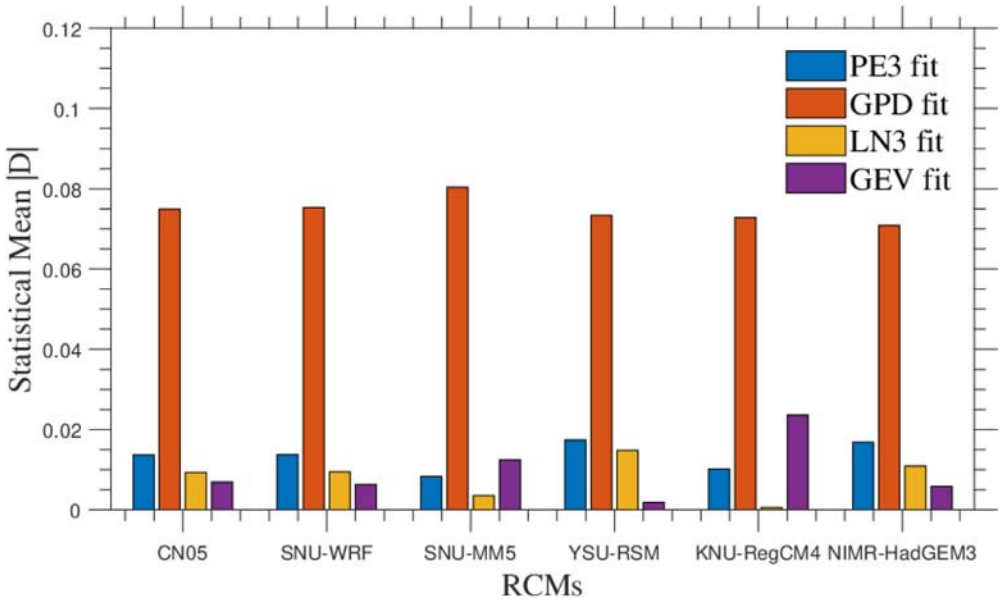

FIGURE 8 | Statistical mean values of absolute differences (|D|) of fitted L-kurtosis values from different probabilistic models against theoretical L-kurtosis values in the CN05 observational dataset and five RCM simulations (SNU-WRF, SNU-MM5, YSU-RSM, KNU-RegCM4, and NIMR-HadGEM3). Probabilistic models include the generalized extreme value (GEV) (purple bar), three-parameter lognormal (LN3) (orange bar), generalized Pareto (GPD) (red bar), and Pearson Type III (PE3) (blue bar).

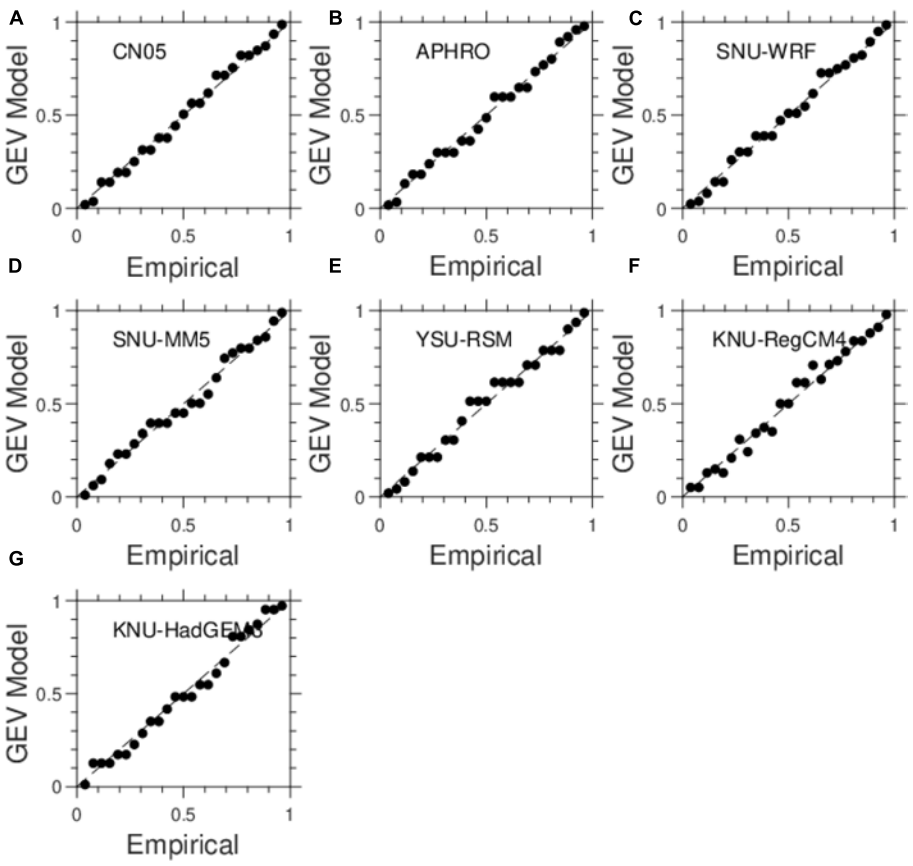

FIGURE 9 | Probabilistic–probabilistic plots of the annual AMDSL time series for cell grid at 101.75°E, 23.25° from two observations, **(A)** CN05 and **(B)** APHRO, and five RCMs, **(C)** SNU-WRF, **(D)** SNU-MM5, **(E)** YSM-RSM, **(F)** NIMR-HadGEM3, and **(G)** KNU-RegCM4.

RCM simulations. The climatological mean proportion of dry days tends to be much larger in the northeastern part of SWC, including CQ and GZ, where the distance of water vapor transport from the tropical ocean is higher and the number of precipitation days is lower. A smaller proportion of dry days is identified in SB and is mainly affected by the mesoscale geographical convergence induced by the SETP and the Southwest Low Vortex (SLV). Another low dry ratio area is the southern part of YN, an area mainly influenced by the tropical monsoon at ground altitudes. The results of the spatial pattern regarding the proportion of dry days from the two different sources were consistent, indicating the reliability of the results. For RCMs, besides YSU-RSM, the other four RCMs reasonably reproduced the spatial distribution pattern for the proportion of dry days. SNU-MM5 had the best correlation in simulating the spatial pattern of the mean ratio of dry days, with a PCC of 0.81. SNU-WRF reproduced a center with a larger proportion of dry days in CQ, the northeastern part of SWC. Simultaneously, SNU-WRF and NIMR-HaDGEM3 simulations showed a negative bias in the LLH region, with a lower proportion of dry days. The terrain in the two areas mentioned above is complex due to influences by the TMC and Wushan Mountain Chain (WMC), and this has a significant impact on the simulation ability of RCMs. YSU-RSM exhibited the worst performance in simulating dry day characteristics.

Using Taylor diagrams (Taylor, 2001, see details in **Supplementary Material**), **Figure 4A** presents a concise statistical summary of RCM performances in simulating the dry day ratio over SWC. The pattern correlation, root-mean-square difference, and amplitude of variation of the dry day ratio of each RCM are presented. In general, the closer the colored dots are to the reference point, the better the model's utility. Apart from YSU-RSM, the RCMs presented good spatial correlations with the observations for the proportion of dry days, ranging from 0.7 to 0.85. SNU-WRF showed a strong correlation but with larger spatial variance, which led to decreased model utility compared to the other three RCMs. Spatial correlations are significant at the 95% confidence level except for the YSU-RSM simulation. As we expected, for the four precipitation thresholds, the spread of points is larger for the lower threshold compared to those for the higher threshold due to the larger sample size for the latter (Sushama et al., 2010). However, threshold sensitivity analysis based on the Taylor diagrams indicates that choosing different thresholds for dry days does not significantly affect ability to simulate the dry day ratio pattern. In addition, among all threshold values used in the sensitivity study, the 1 mm/day threshold used to identify the AMDSL in this study provided the best model simulation ability.

Another important characteristic of dry spells is the PDF of dry spells as a function of different dry spell lengths, which is shown in **Figure 5**. The area covered by the curve is 1. All five RCMs showed similar area-averaged probability distribution functions of dry spells, including KNU-RegCM4 and YSU-RSM, two models with lower ability to simulate dry day occurrence. NIMR-HadGEM3 and KNU-RegCM4 agree well with the observational datasets but tended to overestimate dry spells of less than 5 days. SNU-WRF and SNU-MM5 underestimate the 2–5-day dry spell frequency but tended to overestimate the 5–15-day dry spell frequency.

Climatology and Interannual Variability of AMDSL

The climatological AMDSLs in two observational datasets and five RCM simulations are shown in **Figure 6**. Larger mean AMDSL is identified over the east side of the LLH and the TMC

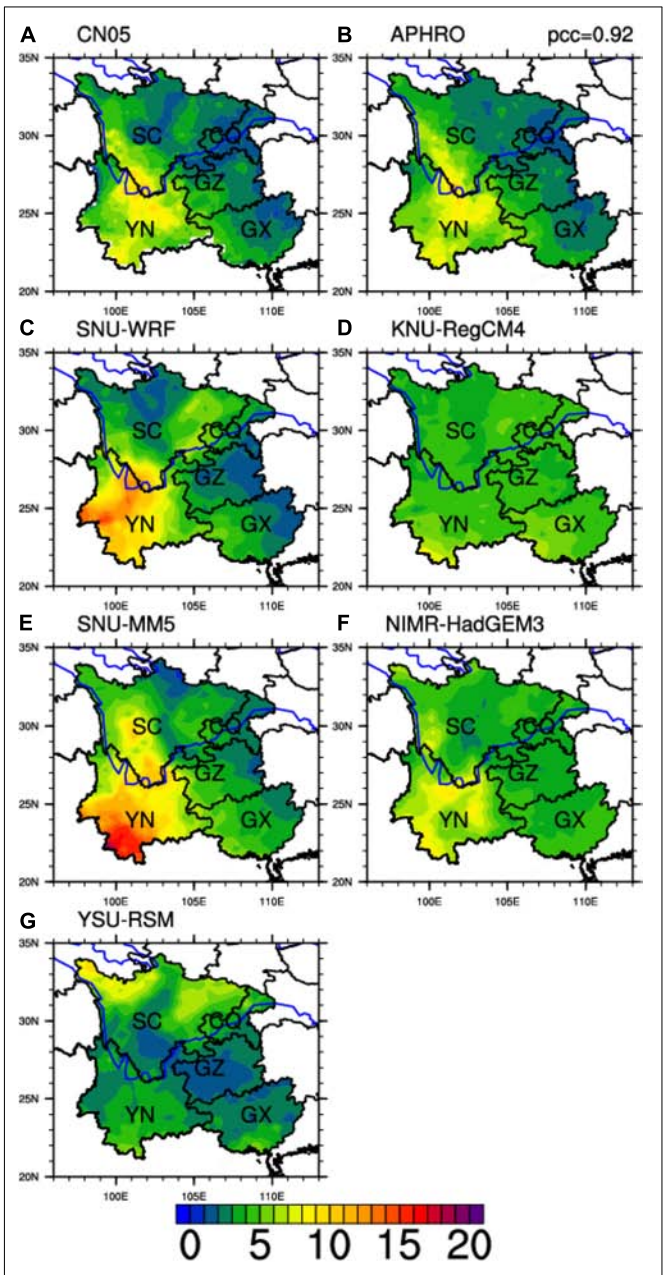

FIGURE 10 | Spatial distributions of the GEV scale parameter of the AMDSL. **(A)** CN05, **(B)** APHRO, and five RCMs: **(C)** SNU-WRF, **(D)** KNU-RegCM4, **(E)** SNU-MM5, **(F)** NIMR-HadGEM3, and **(G)** YSM-RSM.

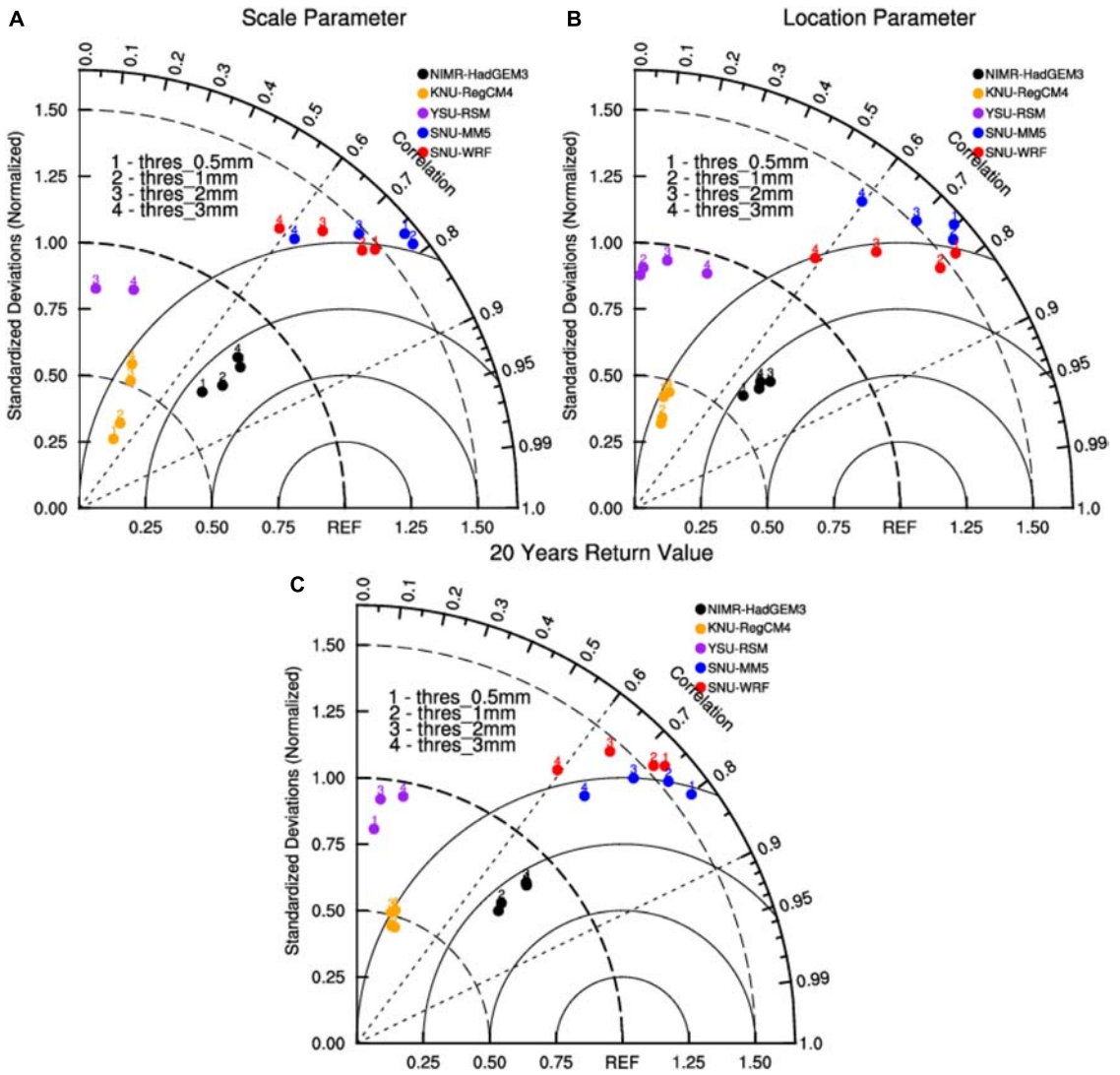

FIGURE 11 | Multivariable Taylor diagram displaying normalized statistical comparisons of the SNU-WRF (red), SNU-MM5 (blue), YSU-RSM (purple), KNU-RegCM4 (orange), and NIMR-HadGEM3 (black) simulated GEV **(A)** scale parameter, **(B)** location parameter, and **(C)** 20-year return value of the AMDSL, respectively. Numbers indicate four different thresholds for dry days.

despite the lower proportion of dry days in this region compared to CQ. These results show that dry days in the LLH tended to appear more concentrated, although the proportion of dry days is lower than that in CQ, which leads to a higher risk of longer dry spells or meteorological drought. In contrast, a smaller mean AMDSL is located on the west side of the TMC, SB, and most of the CQ and GX regions. For the spatial distribution of the average intensity of AMDSL, the observation data of the two sets of grid points are more consistent with a PCC of 0.98. The four RCMs besides YSU-RSM reasonably reproduced the spatial distribution pattern of the mean AMDSL except in some areas with large changes in terrain such as the two sides of the TMC and the edge of SB. NIMR-HadGEM3 had better ability to simulate the spatial pattern of the mean AMDSL with a PCC of 0.70. The KNU-RegCM4 simulation exhibited positive model bias with higher simulated intensity of the AMDSL in CQ and GX regions but showed negative model bias with lower intensity of the AMDSL over the LLH, indicating that KNU-RegCM4 has limited ability to simulate the climatology of AMDSL over complex terrain areas.

Figure 4B presents a Taylor diagram summary of the RCMs performances in simulating the mean AMDSL over SWC. Spatial correlations are significant at the 95% confidence level except for the YSU-RSM simulation. Although there are four RCMs that reasonably reproduced the observed AMDSL spatial pattern, the spatial variability between RCMs is quite different. NIMR-HadGEM3 had better ability than the other three RCMs in simulating the mean AMDSL. The correlation coefficients of SNU-WRF and SNU-MM5 were higher, but the root-mean-square error was also large. Therefore, these two RCMs are comparable to KNU-RegCM's simulation ability. Threshold

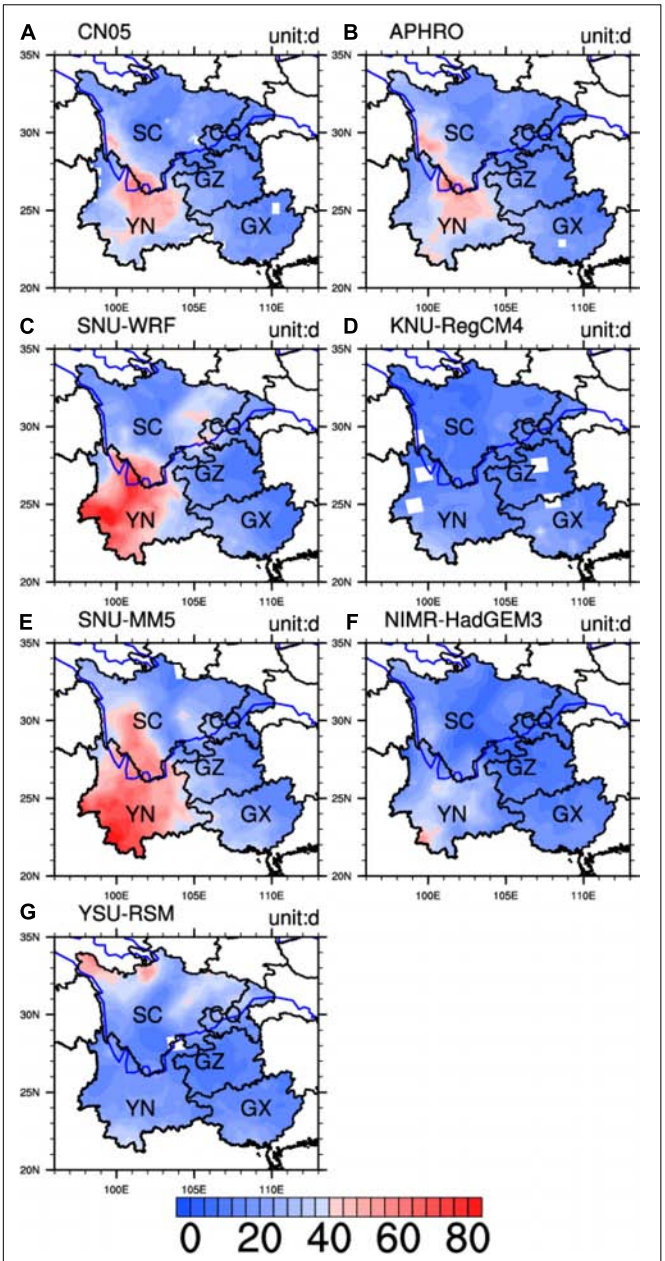

FIGURE 12 | Spatial distributions of the GEV 20-yr return value of the AMDSL. **(A)** CN05, **(B)** APHRO; and five RCMs: **(C)** SNU-WRF, **(D)** KNU-RegCM4, **(E)** SNU-MM5, **(F)** NIMR-HadGEM3, and **(G)** YSM-RSM.

sensitivity analysis indicated that choosing different thresholds for dry days does not significantly affect the ability to simulate the AMDSL spatial pattern.

Figure 7 shows the spatial distribution pattern of standard deviation of the AMDSL. Larger interannual variability is identified over the east side of the LLH and TMC. These results show that interannual fluctuation of the AMDSL is very high and the magnitude of the AMDSL may vary from year to year in this region, which lead to continuously observed very long dry periods (10–15 days) and severe meteorological droughts in the area. This area also corresponds to the interface area between the ISM and the EASM, where the combination of the two monsoons makes the interannual variability of the AMDSL stronger than the northeastern part of SWC and the west side of the TMC. The four RCMs excepting YSU-RSM reproduced the spatial distribution pattern of AMDSL interannual variations relatively well, with PCCs of 0.5, 0.71, 0.78, and 0.71, respectively. SNU-WRF reproduced smaller interannual variability in the SETP and GX areas. For NIMR-HadGEM3, positive discrepancies lie in the northeastern part of SWC, which corresponds to the area where NIMR-HadGEM3 simulated a larger proportion of dry days. KNU-RegCM4 showed less ability to simulate the spatial variability of AMDSL interannual variations, which is consistent with the previous results regarding mean AMDSL. Since the terrain is very complex, the area also has a diverse climate ranging from tropical to temperate; KNU-RegCM4's ability to simulate AMDSL characteristics with complex terrain still needs improvement.

Figure 4C presents a Taylor diagram summary of RCM performances in simulating the interannual variability of AMDSL over SWC. Compared to **Figure 4B**, there are four RCMs, excepting YSU-RSM, that have simulation abilities close to the model abilities to simulate AMDSL.

Identification of Extreme Distribution for the AMDSL

An important part of extreme event statistics is to identify a suitable distribution from which the extremes extracted from an observed period were drawn. In particular, several conventional methods are used to identify the most suitable extreme distribution, including probabilistic–probabilistic plots, quantile–quantile plots, and *L*-moment relationships.

Figure 8 compares the empirical *L*-kurtosis with theoretical *L*-kurtosis of the GEV, LN3, PE3, and GPD models for a given empirical *L*-skewness value of the AMDSL series from CN05 observations, and corresponding series in the five RCM simulations. Comparing the yellow column representing the GEV distribution in **Figure 8**, the GEV model offers a better fit compared to the other probability models for the AMDSL series in the CN05 dataset and three RCM simulations, SNU-WRF, YSU-RSM, and NIMR-HadGEM3. The LN3 model is the best-fitted model in SNU-MM5 and KNU-RegCM4 simulations. Conversely, the GPD model showed a bad fit compared with other extreme models, with a very large $|D|$ value.

Figure 9 compares the empirical probability with the theoretical probability of GEV for the AMDSL time series with a cell grid at 101.75°E, 23.25°. The probability–probability plots indicate that the GEV model offers a relatively good fit to the AMDSL time series.

Simulated GEV Distribution Parameters

After fitting the GEV model to the AMDSL time series, three GEV parameters were estimated at each model gird cell for the five RCM simulations and also for the CN05 dataset. An explanation of the parameters in the GEV model is given in

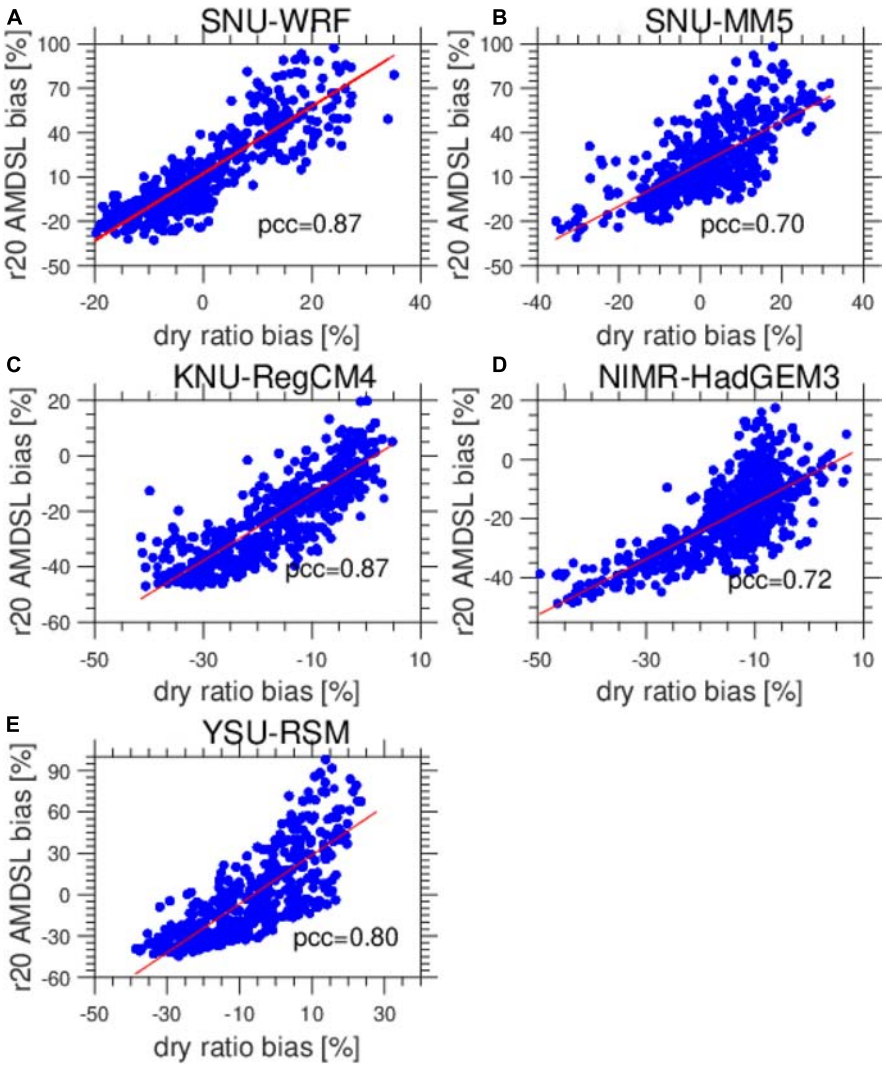

FIGURE 13 | Scatter plots of relative model bias of the 20-year return value of the AMDSL against relative model bias of dry day occurrence. **(A)** SNU-WRF, **(B)** SNU-MM5, **(C)** KNU-RegCM4, **(D)** NIMR-HadGEM3, and **(E)** YSM-RSM.

Supplementary Figure S1. Since both scale parameter α and location parameter ξ in GEV fitting contribute to the estimation of the 20-year return value, further analysis of model ability in simulating individual GEV parameters is needed for assessment of RCM performance.

The GEV scale parameter α, as characterized by the width of the probability distribution function, is a general measurement of the interannual variability of the AMDSL. In general, higher scale parameter values lead to a wider distribution and higher variability of the rarely occurring AMDSL. The spatial distribution pattern of scale parameter α for observed AMDSL over SWC is shown in **Figure 10A**. The distribution pattern is similar to the spatial pattern of the standard deviation of the AMDSL, which indicates that the scale parameter reasonably reflects the interannual variability of the AMDSL. The most dramatic center of AMDSL interannual change was found in the LLH region, which reflects the interaction of the EASM and the ISM. The spatial patterns of AMDSL scale parameter values in the five RCM simulations are also shown in **Figure 10**. The SNU-WRF, SNU-MM5, and NIMR-HadGEM3 simulations captured the large α value center in the LLH region and a northeast–southwest contrast dipole mode, with PCCs of 0.75, 0.80, and 0.77, respectively. In addition, SNU-WRF and SNU-MM5 produced positive bias, with overestimated interannual variation of the AMDSL in the southern part of YN, an area that is significantly affected by the tropical summer monsoon.

Figure 11A presents a Taylor diagram summary of RCM performances in simulating the scale parameter over SWC. Spatial correlations are significant at the 95% confidence level except for the YSU-RSM simulation. Similar to **Figure 4B**, four RCMs, except for YSU-RSM, reasonably reproduce the interannual variation of the AMDSL, but the spatial variability between RCMs is still different. Threshold sensitivity analysis indicated that choosing different thresholds for dry days does not

significantly affect the ability of RCMs to simulate the AMDSL spatial pattern.

The GEV location parameter ξ is characterized by the position of the probability distribution function, which is a measurement of the averaged amplitude of the AMDSL. The spatial distribution patterns of the location parameter ξ for observed and simulated AMDSL over SWC are shown in **Supplementary Figure S2**. The distribution pattern is similar to that of the mean AMDSL. Both a larger location parameter and mean AMDSL are identified over the east side of the LLH and TMC, indicating a higher amplitude of the AMDSL and higher risk of drought in this region.

Figure 11B presents a Taylor diagram summary of RCM performances in simulating the location parameter over SWC. Spatial correlations are significant at the 95% confidence level except for the YSU-RSM simulation. Similar to **Figure 4C**, four RCMs, excepting YSU-RSM, reasonably reproduce the interannual variation of the AMDSL, but the spatial variability between RCMs is still different.

Based on equations in **Supplementary Material Part B**, the 20-year return values in each model grid were derived by inverting the GEV cumulative distribution function. In general, spatial maps of AMDSLs (**Figure 12**) revealed that the 20-year return value of the AMDSL increases gradually from the northeast to the southwest over SWC. The spatial pattern is similar to both the GEV scale parameter and location parameter. Higher values of the scale parameter over the LLH indicated a wider distribution of the AMDSL, and higher values of the location parameter led to an amplified distribution of the AMDSL. The interaction of two parameters resulted in an intensified northeast–southwest spatial contrast dipole mode of 20-year return values of the AMDSL. NIMR-HadGEM3 showed better simulation ability than the other three models based on **Figure 11C**.

Figure 13 presents the linear relationship between relative model bias of the 20-year return value of the AMDSL and the dry day occurrence. Obviously, the simulated relative error of the RCMs for the occurrence of dry days is the main source for the simulated model bias of the mean AMDSL (**Supplementary Figure S3**) and 20-year return values of the AMDSL.

Overall, based on the spatial distribution of the AMDSL in climatological mean and in distribution return values, higher values of the AMDSL were more likely to appear in the LLH, an area affected by both the EASM and the ISM. This region can also be considered as at higher risk of drought conditions (Wang et al., 2014). As most of SWC is used for agriculture and is more often subjected to soil moisture deficits due to longer lasting droughts, any increase in dry spell duration, particularly during the spring, can affect the agricultural sector significantly.

DISCUSSION AND CONCLUSION

In this study, we comprehensively evaluated the performance of five CORDEX-EA RCMs in simulating AMDSL characteristics in an area of complex terrain. The focus of this paper is not on unveiling the physical processes of the AMDSL nor on assessing its robust projection results but on providing a comparison of the capabilities of five RCMs in simulating the intensity and interannual variability of the AMDSL in SWC. This evaluation will provide insight to determine whether the AMDSL can be reasonably reproduced on a regional scale with RCMs.

The monthly variation in precipitation, interannual variability of precipitation, and mean dry days was well identified in both the CN05 and APHRO data. The five RCMs also reproduced the annual cycle of monthly mean precipitation, interannual variability, and monthly mean dry days but tended to overestimate the monthly mean precipitation and underestimate the monthly mean dry days. In addition, the five RCMs all simulated the probability distribution of dry spells over SWC reasonably well.

For the five RCMs used in this study, the four RCMs besides YSU-RSM reproduced the spatial pattern of the proportion of dry days and the climatology of the AMDSL over the SWC region. This is consistent with the previous results of RCM simulations on different regional scales (Tebaldi et al., 2006; Sushama et al., 2010; Wehner et al., 2010; Raymond et al., 2016, 2018; Tramblay and Hertig, 2018). It should be noted that large spatial variability differences are found among different RCM simulations. This variability can be attributed to the variance of RCMs in simulating extreme dry spells over complex terrain areas (Herrera et al., 2010; López-Franca et al., 2015). It is also worth noting that the RCMs reasonably simulate the spatial distribution of the interannual variability of AMDSL. Based on Taylor diagram evaluations, the four RCMs besides YSU-RSM show comparable ability to simulate the interannual variability of AMDSL compared to the climatology of AMDSL.

The generalized extreme value (GEV) distribution is considered the most suitable model for fitting the AMDSL in both observations and model experiments. The simulation of GEV scale parameters and location parameters is consistent with the simulation of the interannual variability and climatology of AMDSL by the RCMs. This is consistent with the previous results for RCMs simulating the probability distribution of the AMDSL (Tebaldi et al., 2006; Sushama et al., 2010; Wehner et al., 2010; Tramblay and Hertig, 2018).

The limitation of our study is the use of only five RCM simulations driven by one GCM. This meant that the full range of variability was not assessed. Additional RCM simulations are gradually becoming available, and these will be considered in the future. Furthermore, though dry spells can be indicators of drought (Tebaldi et al., 2006), other indicators, including temperature, soil moisture, and evaporation, were not well addressed in the present study.

Overall, the main findings on the performances of the five RCM simulations in reproducing various features of the AMDSL can be summarized as follows:

(a) Though the results show large spatial variability differences among different RCMs, four RCM simulations among five reasonably reproduced the AMDSL climatology and interannual variability. In addition, these four RCMs showed an ability to simulate the interannual variability of AMDSL that was comparable to that for simulation of the climatology of AMDSL. The results may provide references

for choosing preferential RCMs in studies of the AMDSL and drought events in areas of complex terrain like SWC.

(b) The GEV distribution of the AMDSL could reveal the spatial distribution of the intensity and variability of the AMDSL, which would be helpful for longer-period return value estimation under present climate conditions and would be applicable to extreme dry spell prevention and mitigation.

(c) Probabilistic distribution analysis of the AMDSL over a range of precipitation thresholds was performed in the present study, and it is notable that, based on Taylor diagram summaries, the different threshold values did not influence the abilities of RCMs.

(d) The performance of RCMs in simulating the intensity and extreme distribution of the AMDSL is highly influenced by the ability of the model to simulate the occurrence of dry days.

DATA AVAILABILITY STATEMENT

Publicly available datasets were analyzed in this study. This data can be found here: https://www.cordex.org/domains/region-7-east-asia/.

AUTHOR CONTRIBUTIONS

TF designed the work, finished regional model data analysis, and wrote the manuscript. LX contributed to model evaluation and manuscript writing. YC designed the work and wrote the manuscript. ZT contributed to further analysis of regional climate model data.

FUNDING

This work was supported by the National Natural Science Foundation of China (41875109), the Natural Science Foundation of Yunnan Province (Grant No. 2018FB074), the Educational Foundation of Yunnan Province (Grant No. 2018JS014), the Yunnan Excellent Youth Fund Development Project (2018YDJQ012), and the Project of Power Construction Corporation of China (DJ-ZDZX-2016-02).

ACKNOWLEDGMENTS

The authors thank all the scientists and crew members who were involved in the program. The authors also thank the reviewers for their valuable comments, which helped to improve the manuscript a lot.

SUPPLEMENTARY MATERIAL

The Supplementary Material for this article can be found online at: https://www.frontiersin.org/articles/10.3389/feart.2019.00294/full#supplementary-material

REFERENCES

Barriopedro, D., Gouveia, C. M., Trigo, R. M., and Wang, L. (2012). The 2009/10 drought in China: possible causes and impacts on vegetation. *J. Hydrometeor.* 13, 1251–1267. doi: 10.1175/JHM-D-11-074.1

Beck, H. E., Van Dijk, A. I., Levizzani, V., Schellekens, J., Gonzalez Miralles, D., Martens, B., et al. (2017a). MSWEP: 3-hourly 0.25 global gridded precipitation (1979-2015) by merging gauge, satellite, and reanalysis data. *Hydrol. Earth Syst. Sci.* 21, 589–615. doi: 10.5194/hess-21-589-2017

Beck, H. E., Vergopolan, N., Pan, M., Levizzani, V., van Dijk, A. I., Weedon, G. P., et al. (2017b). Global-scale evaluation of 22 precipitation datasets using gauge observations and hydrological modeling. *Hydrol. Earth Syst. Sci.* 21, 6201–6217. doi: 10.5194/hess-21-6201-2017

Boberg, F., Berg, P., Thejll, P., Gutowski, W. J., and Christensen, J. H. (2010). Improved confidence in climate change projections of precipitation further evaluated using daily statistics from ENSEMBLES models. *Clim. Dym.* 35, 1509–1520. doi: 10.1007/s00382-009-0683-8

Cha, D. H., and Lee, D. K. (2009). Reduction of systematic errors in regional climate simulations of the summer monsoon over East Asia and the western North Pacific by applying the spectral nudging technique. *J. Geophys. Res.* 114:D14108. doi: 10.1029/2008JD011176

Chan, S. C., Kendon, E. J., Fowler, H. J., Blenkinsop, S., Ferro, C. A. T., and Stephenson, D. B. (2013). Does increasing the spatial resolution of a regional climate model improve the simulated daily precipitation? *Clim. Dyn.* 41, 1475–1495. doi: 10.1007/s00382-012-1568-9

Chan, S. C., Kendon, E. J., Fowler, H. J., Blenkinsop, S., Roberts, N. M., and Ferro, C. A. T. (2014). The value of high-resolution Met Office regional climate models in the simulation of multi-hourly precipitation extremes. *J. Clim.* 27, 6155–6174. doi: 10.1175/JCLI-D-13-00723.1

Cheng, J. G., Yan, H. M., and Yan, H. S. (2009). *Analysis on Characteristic and Cause of Severe Climate Disaster in Yunnan*. Beijing: China Meteorology Press.

Christensen, J. H., and Christensen, O. B. (2007). A summary of the PRUDENCE model projections of changes in European climate by the end of this century. *Clim. Change* 81, 7–30. doi: 10.1007/s10584-006-9210-7

Coles, S., Bawa, J., Trenner, L., and Dorazio, P. (2001). *An Introduction to Statistical Modeling of Extreme Values*, Vol. 208. London: Springer.

Davies, T., Cullen, M. J. P., Malcolm, A. J., Mawson, M. H., Staniforth, A., White, A. A., et al. (2005). A new dynamical core for the Met Office's global and regional modeling of the atmosphere. *Q. J. R. Meteorol. Soc.* 131, 1759–1782. doi: 10.1256/qj.04.101

Domínguez, M., Romera, R., Sánchez, E., Fita, L., Fernández, J., Jiménez-Guerrero, P., et al. (2013). Present-climate precipitation and temperature extremes over Spain from a set of high resolution RCMs. *Clim. Res.* 58, 149–164. doi: 10.3354/cr01186

Dominguez-Castro, F., Vicente-Serrano, S. M., Tomas-Burguerra, M., Pena-Gallardo, M., Begueria, S., El Kenawy, A., et al. (2019). High-spatial-resolution probability maps of drought duration and magnitude across Spain. *Nat. Hazards Earth Syst. Sci.* 19, 611–628. doi: 10.5194/nhess-19.611-2019

Donat, M. G., Alexander, L. V., Herold, N., and Dittus, A. J. (2016). Temperature and precipitation extremes in century-long gridded observations, reanalyses, and atmospheric model simulations. *J. Geophys. Res. Atmos.* 121, 11174–11189. doi: 10.1002/2016JD025480

Fantini, A., Raffaele, F., Torma, C., Bacer, M., Coppola, E., Giorgi, F., et al. (2016). Assessment of multiple daily precipitation statistics in ERA-Interim driven Med-CORDEX and Euro-CORDEX experiments against high resolution observations. *Clim. Dyn.* 51, 877–900. doi: 10.1007/s00382-016-3453-3454

Frich, P., Alexander, L. V., Della-Marta, P., Gleason, B., Haylock, M., Tank, A. M. G. K., et al. (2002). Observed coherent changes in climatic extremes during the second half of the twentieth century. *Clim. Res.* 19, 193–212. doi: 10.3354/cr019193

Giorgi, F., Coppola, E., Solmon, F., Mariotti, L., Sylla, M. B., Bi, X., et al. (2012). RegCM4: model description and preliminary tests over multiple CORDEX domains. *Clim. Res.* 52, 7–29. doi: 10.3354/cr01018

Giorgi, F., Jones, C., and Asrar, G. R. (2009). Addressing climate information needs at the regional level: the CORDEX framework. *WMO Bull.* 58, 175–183.

Herold, N., Behrangi, A., and Alexander, L. V. (2017). Large uncertainties in observed daily precipitation extremes over land. *J. Geophys. Res. Atmos.* 122, 668–681. doi: 10.1002/2016JD025842

Herrera, S., Fita, L., Fernández, J., and Gutiérrez, J. M. (2010). Evaluation of the mean and extreme precipitation regimes from the ENSEMBLES regional climate multi model simulation over Spain. *J. Geophys. Res. Atmos.* 115:D21117. doi: 10.1029/2010JD013936

Hong, S.-Y., Park, H., Cheong, H.-B., Kim, J.-E. E., Koo, M.-S., Jang, J., et al. (2013). The global/regional integrated model system (GRIMs). *Asian Pac. J. Atmos. Sci.* 49, 219–243. doi: 10.1007/s13143-013-0023-0

Hosking, J. R. M. (1990). L-moments: analysis and estimation of distributions using linear combinations of order statistics. *J. R. Statist. Soc. B* 52, 105–124. doi: 10.1111/j.2517-6161.1990.tb01775.x

Hosking, J. R. M., and Wallis, J. R. (1993). Some statistics useful in regional frequency analysis. *Water Resour. Res.* 29, 271–281. doi: 10.1029/92WR01980

Hosking, J. R. M., and Wallis, J. R. (2005). *Regional Frequency Analysis: An Approach Based on L-Moments*. Cambridge: Cambridge University Press.

Huang, B., Polanski, S., and Cubasch, U. (2015). Assessment of precipitation climatology in an ensemble of CORDEX-East Asia regional climate simulations. *Clim. Res.* 64, 141–158. doi: 10.3354/cr01302

Huffman, G. J., Adler, R. F., Morrissey, M. M., Bolvin, D. T., Curtis, S., Joyce, R., et al. (2001). Global precipitation at one-degree daily resolution from multisatellite observations. *J. Hydrometeor.* 2, 36–50. doi: 10.1175/1525-75412001002<0036:GPAODD<2.0.CO;2

Kopparla, P., Fischer, E. M., Hannay, C., and Knutti, R. (2013). Improved simulation of extreme precipitation in a high-resolution atmosphere model. *Geophys. Res. Lett.* 40, 5803–5808. doi: 10.1002/2013GL057866

Kotlarski, S., Keuler, K., Christensen, O. B., Colette, A., Déqué, M., Gobiet, A., et al. (2014). Regional climate modeling on European scales: a joint standard evaluation of the EURO-CORDEX RCM ensemble. *Geosci. Model Dev.* 7, 1297–1333. doi: 10.5194/gmd-7-1297-2014

Kroll, C. N., and Vogel, R. M. (2002). Probability distribution of low streamflow series in the United States. *ASCE J. Hydrol. Eng.* 7, 137–146. doi: 10.1061/(ASCE)1084-069920027:2(137)

Lee, J.-W., Hong, S.-Y., Chang, E.-C., Suh, M.-S., and Kang, H.-S. (2014). Assessment of future climate change over East Asia due to the RCP scenarios downscaled by GRIMs-RMP. *Clim. Dyn.* 42, 733–747. doi: 10.1007/s00382-013-1841-6

Li, H. X., Chen, H. P., Wang, H. J., and Yu, E. T. (2018). Future precipitation changes over China under 1.5°C and 2.0°C global warming targets by using CORDEX regional climate models. *Sci. Total. Environ*. 640-641, 543–554. doi: 10.1016/j.scitotenv.2018.05.324

López-Franca, N., Sánchez, E., Losada, T., Domínguez, M., Romera, R., and Gaertner, M. A. (2015). Markovian characteristics of dry spells over the Iberian Peninsula under present and future conditions using ESCENA ensemble of regional climate models. *Clim. Dyn.* 45, 661–677. doi: 10.1007/s00382-014-2280-8

Maraun, D., Wetterhall, F., Ireson, A. M., Chandler, R. E., Kendon, E. J., Widmann, M., et al. (2010). Precipitation downscaling under climate change: recent developments to bridge the gap between dynamical models and the end user. *Rev. Geophys.* 48:RG3003. doi: 10.1029/2009RG000314

Modarres, R. (2010). Regional dry spells frequency analysis by L-moment and multivariate analysis. *Water Resour. Manage.* 24, 2365–2380. doi: 10.1007/s11269-009-9556-5

Oh, S.-G., Park, J.-H., Lee, S.-H., and Suh, M.-S. (2014). Assessment of the RegCM4 over East Asia and future precipitation change adapted to the RCP scenarios. *J. Geophys. Res. Atmos.* 119, 2913–2927. doi: 10.1002/2013JD020693

Park, C., Min, S.-K., Lee, D., Cha, D.-H., Suh, M.-S., Kang, H.-S., et al. (2016). Evaluation of multiple regional climate models for summer climate extremes over East Asia. *Clim. Dyn.* 46, 2469–2486. doi: 10.1007/s00382-015-2713-z

Pope, V., and Stratton, R. (2002). The processes governing horizontal resolution sensitivity in a climate model. *Clim. Dyn.* 19, 211–236. doi: 10.1007/s00382-001-0222-8

Qin, J., Ju, J. H., and Xie, M. E. (1997). *Weather and Climate in Low Latitudes Plateau (in Chinese)*. Beijing: China Meteorology Press, 210.

Rauscher, S. A., Coppola, E., Piani, C., and Giorgi, F. (2010). Resolution effects on regional climate model simulations of seasonal precipitation over Europe. *Clim. Dyn.* 35, 685–711. doi: 10.1007/s00382-009-0607-7

Raymond, F. A., Drobinski, C., Ullmann, P., and Camberlin, P. (2018). Extreme dry spells over the Mediterranean Basin during the wet season: assessment of HyMeX/Med-CORDEX regional climate simulations (1979-2009). *Int. J. Climatol.* 38, 3090–3105. doi: 10.1002/joc.5487

Raymond, F. A., Ullmann, P., Camberlin, P., Drobinski, C., and Chateau Smith, C. (2016). Extreme dry spell detection and climatology over the Mediterranean Basin during the wet season. *Geophys. Res. Lett.* 43, 7196–7204. doi: 10.1002/2016GL069758

Roeckner, E., Brokopf, R., Esch, M., Giorgetta, M., Hagemann, S., Kornblueh, L., et al. (2006). Sensitivity of simulated climate to horizontal and vertical resolution in the ECHAM5 atmosphere model. *J. Clim.* 19, 3771–3791. doi: 10.1175/JCLI3824.1

Rummukainen, M. (2015). Added value in regional climate modeling. *WREs Clim. Change* 7, 145–159. doi: 10.1002/wcc.378

Saaroni, H., Ziv, B., Lempert, J., Gazit, Y., and Morin, E. (2015). Prolonged dry spells in the Levant region: climatologic-synoptic analysis. *Int. J. Climatol.* 35, 2223–2236. doi: 10.1002/joc.4143

Salathé, E. P., Steed, R., Mass, C. F., and Zah, P. H. (2008). A high-resolution climate model for the U.S. Pacific Northwest: mesoscale feedbacks and local responses to climate change. *J. Clim.* 21, 5708–5726. doi: 10.1175/2008JCLI2090.1

Sarhadi, A., and Heydarizadeh, M. (2014). Regional frequency analysis and spatial pattern characterization of Dry Spells in Iran. *Int. J. Climatol.* 34, 835–848. doi: 10.1002/joc.3528

Shaffrey, L., Stevens, I., Norton, W. A., Roberts, M. J., Vidale, P. L., Harle, J. D., et al. (2009). U.K. HiGEM: the new U.K. high-resolution global environment model—Model description and basic evaluation. *J. Clim.* 22, 1861–1896. doi: 10.1175/2008jcli2508.1

Skamarock, W. C., Klemp, J. B., Dudhia, J., Gill, D. O., Barker, D. M., Wang, W., et al. (2005). *A Description of the Advanced Research WRF Version 2*. NCAR Technical note NCAR/TN-4681STR.

Spinoni, J., Barbosa, P., De Jager, A., McCormick, N., Naumann, G., Vogt, J. V., et al. (2019). A new global database of meteorologcial dorught events from 1951 to 2016. *J. Hydrol. Reg. Stud.* 22:100593. doi: 10.1016/j.ejrh.2019.100593

Sun, C., and Yang, S. (2012). Persistent severe drought in southern China during winter–spring 2011: large-scale circulation patterns and possible impacting factors. *J. Geophys. Res.* 117:D10112. doi: 10.1029/2012JD017500

Sushama, L., Khaliq, N., and Laprise, R. (2010). Dry spell characteristics over Canada in a changing climate as simulated by the Canadian RCM. *Glob. Planet. Chang* 74, 1–14. doi: 10.1016/j.gloplacha.2010.07.004

Taylor, K. E. (2001). Summarizing multiple aspects of model performance in a single diagram. *J. Geophys. Res.* 106, 7183–7192. doi: 10.1029/2000JD900719

Tebaldi, C., Hayhoe, K., Arblaster, J. M., and Meehl, G. A. (2006). An intercomparison of model-simulated historical and future changes in extreme events. *Clim. Change* 79, 185–211. doi: 10.1007/s10584-006-9051-4

Tramblay, Y., and Hertig, E. (2018). Modelling extreme dry spells in the mediterranean region in connection with atmospheric circulation. *Atmos. Res* 202, 40–48. doi: 10.1016/j.atmosres.2017.11.015a

Vicente-Serrano, S. M., Beguería, S., and López-Moreno, J. I. (2010). A multiscalar drought index sensitive to global warming: the standardized precipitation evapotranspiration index. *J. Clim.* 23, 1696–1718. doi: 10.1175/2009JCLI2909.1

von Storch, H., and Zorita, E. (2019). The history of ideas of downscaling—from synoptic dynamics and spatial interpolation. *Front. Environ. Sci.* 7:21. doi: 10.3389/fenvs.2019.00021

Wang, L., Chen, W., and Zhou, W. (2014). Assessment of future drought in Southwest China based on CMIP5 multimodel projections. *Adv. Atmos. Sci.* 31, 1035–1050. doi: 10.1007/s00376-014-3223-3

Wang, L., Chen, W., Zhou, W., and Huang, G. (2015). Drought in Southwest China: a review. *Atmos. Ocean. Sci. Lett.* 8, 339–344. doi: 10.3878/AOSL20150043

Wang, Y., Leung, L. R., McGregor, J. L., Lee, D.-K., Wang, W. C., Ding, Y. H., et al. (2004). Regional climate modeling: progress, challenges and prospects. *J. Meteorol. Soc. Jpn.* 82, 1599–1628. doi: 10.2151/jmsj.82.1599

Wehner, M. F., Smith, R. L., Bala, G., and Duffy, P. (2010). The effect of horizontal resolution on simulation of very extreme US precipitation events in a global atmosphere model. *Clim. Dyn.* 32, 241–247. doi: 10.1007/s00382-009-0656-y

Wu, J., and Gao, X. (2013). A gridded daily observation dataset over China region and comparison with the other datasets (in Chinese). *Chin. J. Geophys.* 56, 1102–1111. doi: 10.6038/cjg20130406

Yang, Y. L., Du, Y., Chen, H. S., and Zhang, Y. S. (2011). Influence of ENSO event on rainfall anomaly over Yunnan Province and its neighboring regions during late spring-early summer (in Chinese). *Chin. J. Atmos. Sci.* 35, 729–738. doi: 10.3878/j.issn.1006-9895.2011.04.12

Yatagai, A., Kaminguchi, K., Arakawa, O., Hamada, A., Yasutomi, N., and Kitoh, A. (2012). APHRODITE: constructing a long-term daily gridded precipitation dataset for Asia based on a dense network of rain gauges. *Bull. Am. Meteor. Soc.* 93, 1401–1415. doi: 10.1175/BAMS-D-11-00122.1

Zhang, X., Alexander, L., Hegerl, G. C., Jones, P., Tank, A. K., Peterson, T. C., et al. (2011). Indices for monitoring changes in extremes based on daily temperature and precipitation data. *WIREs. Clim. Change* 2, 851–870. doi: 10.1002/wcc.147

Conflict of Interest: The authors declare that the research was conducted in the absence of any commercial or financial relationships that could be construed as a potential conflict of interest.

Advantages of publishing in Frontiers

OPEN ACCESS
Articles are free to read for greatest visibility and readership

FAST PUBLICATION
Around 90 days from submission to decision

HIGH QUALITY PEER-REVIEW
Rigorous, collaborative, and constructive peer-review

TRANSPARENT PEER-REVIEW
Editors and reviewers acknowledged by name on published articles

Frontiers
Avenue du Tribunal-Fédéral 34
1005 Lausanne | Switzerland

Visit us: www.frontiersin.org
Contact us: info@frontiersin.org | +41 21 510 17 00

REPRODUCIBILITY OF RESEARCH
Support open data and methods to enhance research reproducibility

DIGITAL PUBLISHING
Articles designed for optimal readership across devices

FOLLOW US
@frontiersin

IMPACT METRICS
Advanced article metrics track visibility across digital media

EXTENSIVE PROMOTION
Marketing and promotion of impactful research

LOOP RESEARCH NETWORK
Our network increases your article's readership